Pascal Jerôme Gunkel

Hadronic effects in the QCD phase diagram

Dissertation

Zur Erlangung des akademischen Grades

Doktor der Naturwissenschaften (Dr. rer. nat.)

verfasst am Institut für Theoretische Physik der

Justus-Liebig-Universität Giessen

Juni 2021

Dekan:	Prof. Dr. Kai-Thomas Brinkmann
Erstgutachter:	Prof. Dr. Christian S. Fischer
Zweitgutachter:	Prof. Dr. Lorenz von Smekal
3. Prüferin:	Prof. Dr. Claudia Höhne
4. Prüfer:	Prof. Dr. Markus Thoma
Tag der Einreichung:	30. Juni 2021
Tag der mündlichen Prüfung:	.....

Abstract

In this thesis, we investigate meson properties at finite chemical potential and vanishing temperature and study the influence of mesonic and baryonic backcoupling effects on the chiral order parameters and different parts of the QCD phase diagram. For this purpose, we solve a coupled set of (truncated) Dyson-Schwinger equations for the Landau gauged quark and gluon propagators with $\mathrm{N_f} = 2\,(+1)$ dynamical quark flavors and the two cases of including and neglecting the backcoupling of hadrons. The corresponding quark-meson Bethe-Salpeter vertices and bound state properties, i.e. the meson masses and decay constants, of multiple light- and strange-quark mesons are explicitly calculated from their homogeneous Bethe-Salpeter equations at finite chemical potential and vanishing temperature. Since the baryon backcoupling is calculated in the quark-diquark approximation, the necessary baryon and diquark wave-functions and properties are approximated by corresponding results explicitly calculated in vacuum.

At vanishing temperature, we study the changes of the quark dressing functions and meson Bethe-Salpeter wave-functions with chemical potential and thereby trace charge-conjugation parity breaking. For the light and strange quarks, we observe two separate first-order coexistence regions. From zero chemical potential up to the end of these coexistence regions, we find constant masses and decay constants for every considered meson and the quark condensate. Thereby, we explicitly verify the Silver-Blaze property of QCD. Inside the light- and strange-quark coexistence region, the Pion and the $\bar{K}$ meson, respectively, become more massive while their decay constants decrease. The corresponding quantities for the (axial-)vector and scalar mesons and the K meson remain (almost) perfectly constant.

For the backcoupling of the Pion and/or Sigma meson as well as for the backcoupling of the nucleon and/or scalar diquark, we find similar chiral-restoration effects. Considering backcoupled baryons, oscillations of the quark propagator at finite chemical potential and vanishing temperature prevent a clear statement regarding the liquid-gaseous phase transition. For Pion and Sigma meson backcoupling, we observe a (small) shift of the critical endpoint towards smaller chemical potentials and a reduced curvature of the chiral crossover line. We conclude that the location of the critical endpoint in the phase diagram is mainly determined by microscopic degrees of freedom of QCD (quarks and gluons) while its critical properties are dominated by macroscopic degrees of freedom (especially the Sigma meson).

Zusammenfassung

In dieser Arbeit untersuchen wir einerseits die Eigenschaften von Mesonen bei endlichem chemischem Potential und verschwindender Temperatur und andererseits den Einfluss von mesonischen und baryonischen Rückkopplungseffekten auf die chiralen Ordnungsparameter und verschiedene Bereiche des QCD-Phasendiagramms. Zu diesem Zweck lösen wir einen gekoppelten Satz von (trunkierten) Dyson-Schwinger Gleichungen für die Landau-eichfixierten Quark- und Gluonpropagatoren, für die wir $\mathrm{N_f} = 2\,(+1)$ dynamische Quark-Flavor und den Fall von inkludierten und nicht inkludierten hadronische Rückkopplungen in die Rechnung eingehen lassen. Die entsprechenden Quark-Meson-Bethe-Salpeter-Vertizes, Mesonenmassen und elektroschwachen Zerfallskonstanten der verschiedenen leichten und strange Quark Mesonen werden explizit von ihren homogenen Bethe-Salpeter-Gleichungen bei endlichem chemischem Potential und verschwindender Temperatur ermittelt. Da die Baryonen-Rückkopplung in der Quark-Diquark-Approximation berechnet wird, werden die notwendigen Baryon- und Diquark-Wellenfunktionen und -Eigenschaften durch entsprechende, speziell dafür im Vakuum berechnete Ergebnisse approximiert.

Bei verschwindender Temperatur untersuchen wir die Änderungen der Quark-Dressingfunktionen und Bethe-Salpeter Wellenfunktionen, welche durch eine Änderung des chemischen Potentials induziert werden. Dadurch können wir die Brechung der Ladungskonjugationsinvarianz durch ein nichtverschwindendes chemisches Potential untersuchen. Für die leichten und strange Quarks beobachten wir zwei disjunkte Koexistenz-Gebiete der chiralen Symmetriebrechung. Außerdem finden wir konstante Massen und Zerfallskonstanten für jedes betrachtete Meson sowie ein konstantes Quarkkondensat, meist fast bis zum Ende des jeweiligen Koexistenz-Gebiets. Dies impliziert weiterhin, dass unsere Berechnungen die Silver-Blaze-Eigenschaft der QCD erfüllen. Innerhalb des Koexistenz-Gebiet der leichten (des strange) Quarks wird das Pion (das $\bar{K}$-Meson) massiver, während die zugehörigen Zerfalls-konstanten abnehmen. Währenddessen bleiben die entsprechenden Größen für die (axial-)vektor- und skalaren Mesonen und das K-Meson (fast) perfekt konstant.

Wenn wir die Rückkopplung der Pionen- und Sigma-Mesonen oder die Rückkopplung des Nukleons und des skalaren Diquarks betrachten, finden wir ähnliche chirale Restaurierungseffekte für die einzelnen Komponenten. Bei verschwindender Temperatur und endlichem chemischen Potential verhindern Oszillationen des

Quark-Propagators eine klare Aussage über den Phasenübergang von flüssiger zu gasförmiger Kernmaterie, wenn wir die Rückkopplung der Baryonen (und der Diquarks) mit in die Berechnung einbeziehen. Für die Rückkopplung von Pionen und des Sigma-Mesons beobachten wir eine (kleine) Verschiebung des kritischen Endpunktes zu kleineren chemischen Potentialen und eine reduzierte Krümmung der chiralen Koexistenzslinie. Wir schließen daraus, dass die Lage des kritischen Endpunktes im Phasendiagramm hauptsächlich durch die mikroskopische Freiheitsgrade der QCD (Quarks und Glu-onen) bestimmt wird, während seine kritischen Eigenschaften durch makroskopische Freiheitsgrade (insbesondere das Sigma-Meson) dominiert werden.

Abbreviations

AxWTI axial-vector Ward-Takahashi identity

BC Ball-Chiu

BSA Bethe-Salpeter amplitude

BSE Bethe-Salpeter equation

CEP critical endpoint

dof degrees of freedom

DSE Dyson-Schwinger equation

DχSB dynamical chiral symmetry breaking

FRG functional renormalization group

hBSE homogeneous Bethe-Salpeter equation

nPI n particle irreducible

QCD quantum chromodynamics

QED quantum electrodynamics

QFT quantum-field theory

QGP quark-gluon plasma

SBP Silver-Blaze property

STI Slavnov-Taylor identity

VEV vacuum expectation value

WTI Ward-Takahashi identity

YM Yang-Mills

Contents

1. Introduction

In the last two decades, the phase diagram of strongly interacting matter has become a hot topic in particle physics. Especially the quest of the existence, the location, and the properties of a putative critical endpoint (CEP) is an important goal for various heavy-ion-collision experiments like the Beam Energy Scan (BES) program [1] at the Relativistic Heavy Ion Collider (RHIC) at the Brookhaven National Laboratory or the present HADES (FAIR Phase-0) [2] as well as the future Compressed Baryonic Matter (CBM) experiment [3] at the Facility for Antiproton and Ion Research (FAIR).

In these experiments, heavy ions are accelerated to large fractions of the speed of light before they are collided. When colliding, the particles produce a zone of hot and dense matter which is, under certain conditions, equal to a so-called quark-gluon plasma (QGP) predicted from theoretical calculations at high temperatures and densities/ chemical potentials. The zone then expands, cools down and ends in a phase of ordinary hadrons which are finally detected. With this procedure the existing operations like RHIC or the large hadron collider (LHC) at CERN (Conseil européen pour la recherche nucléaire) were able to study parts of the phase diagram. While an analytic crossover at vanishing chemical potential [4–7] (from lattice) and a liquid-gaseous first-order phase transition of nuclear matter are settled, there is no experimental reassurance of the theoretically predicted CEP so far. Due to technical limitations of the experiments, it is still difficult to reach the high density region needed for the CEP.

On the theoretical side, we describe the interaction of all particles by the quantum mechanical local gauge groups $\mathrm{SU_C}(3) \times \mathrm{SU_L}(2) \times \mathrm{U_Y}(1)$ where the first group describes the strong and the latter two the electroweak interaction. Thereby, the electroweak interaction represents the unification of weak and electromagnetic interactions and includes effects like the decay of particles and the attraction or repulsion of particles due to the electromagnetic and weak charges. The strong interaction, on the other hand, explains the binding of fundamental particles to composite objects which are necessary for more complex structures. The building elements of these complex structures are the quarks which carry a so-called color charge and interact via the color-force by emitting and absorbing gluons. This color-force is stronger than the other three fundamental interactions, acts only on length scales of the elementary particles (quark and gluons) and can only be described by

a non-Abelian, non-perturbative gauge theory, namely quantum chromodynamics (QCD). While the theory of electromagnetic interactions, quantum electrodynamics (QED), can generally be described in a perturbative expansion in terms of the electromagnetic coupling constant e, the self interaction of the gluons in QCD leads to a strong coupling constant g_s at low momenta which is too large for an expansion and makes a non-perturbative treatment necessary. At high momenta, however, the strong coupling decreases enabling a perturbative description.

In QCD, two important non-perturbative phenomena appear: Color confinement and dynamical chiral symmetry breaking (DχSB) which is connected to dynamical mass generation. While the color confinement describes the absence of any colored particle in the experimental detectors, the DχSB states that the mass of colorless bound states cannot result from the Higgs mechanism alone but has to be explained through dynamical mass generations and anomalies of the strong interaction instead. In some cases, the Higgs mechanism even represents only a small percentage of the actual mass. It is important to note that quarks and gluons carry color (charge) and are bound to colorless bound states which in turn are bound to nuclei by the residual force. While colored particles are confined at low momenta, the observed decrease of the strong coupling with higher momenta leads to an asymptotic freedom [8, 9] of the elementary particles. In addition, the two non-perturbative effects depend on thermodynamic circumstances. If used as classification for different states of the strongly interacting matter, we can collect the thermodynamic information to these phenomena into the QCD phase diagram.

In this QCD phase diagram, we summarize the thermodynamic properties (chemical potential and temperature dependencies) of the chiral [10] and center [11] symmetry (in a graphical way) for the two non-perturbative phenomena of DχSB and color confinement, respectively. The QCD phase diagram as it is presently believed to look like is shown schematically in Fig. 1.1. Corresponding comprehensive reviews to this topic can be found in Refs. [12, 13] and references therein. Three (kinds of) phases, i.e. states of strongly interacting matter, can be found:

(i) A quark-gluon plasma (QGP) at high temperature and chemical potential where the chiral symmetry is (approximately) restored and quarks and gluons move as quasi-free particles since they are asymptotically free and no longer confined.

(ii) A hadronic phase at small temperatures and chemical potentials where the chiral symmetry is spontaneously broken due to the formation of a quark condensate and the quarks and gluons are confined to bound states.

(iii) Different manifestations of color superconducting phases at small temperatures and high chemical potentials where the chiral symmetry is again

spontaneously broken since the quarks form Cooper pairs in certain combinations of color and flavor.

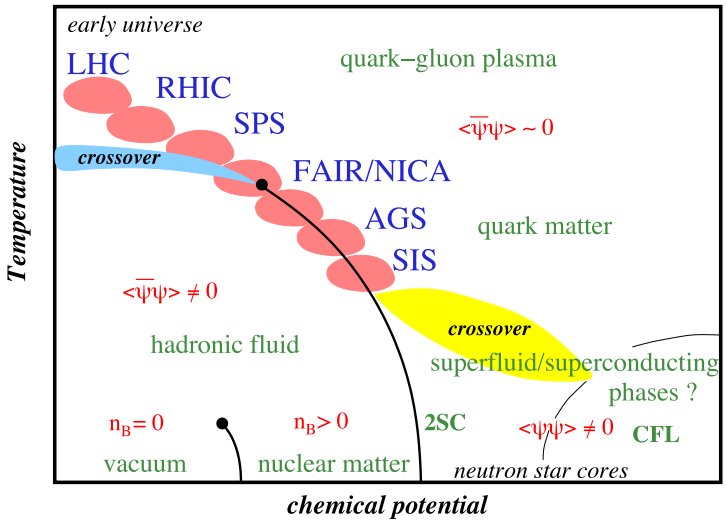

Figure 1.1.: Sketch of the QCD phase diagram taken from Ref. [14].

The existence of these three phases is largely accepted or proven but the coexistence lines in between are still matter of intense studies, theoretically and experimentally. For the experimental side, see for example the different experimental facilities shown in the figure which probe the phase diagram. For the coexistence lines, it is expected from functional methods and model calculations [15–17] that we find a continuous crossover at low chemical potential which turns, for increasing chemical potentials, into a second-order CEP and a sharp first-order phase transition above it. In the hadronic phase, there furthermore is a liquid-gaseous first-order phase transition [18] which indicates the appearance of nuclear matter.

For the theoretical determination of the QCD phase diagram, there exist different approaches. The method of choice is the ab initio lattice QCD approach where we discretize the theory on a finite space-time grid and use Monte-Carlo simulations to obtain results. This method is well established at vanishing chemical potential but suffers from the so called Fermion sign-problem [19] at non-vanishing chemical potentials. Due to the sign-problem, we have to resort to extrapolations which are valid up to a certain chemical potential to temperature ratio. For a review of this method see the Refs. [20, 21]. Also effective theories like the (Polyakov-loop extended) Nambu-Jona-Lasinio ((P)NJL) or the quark meson ((P)QM) model are convenient tools for many applications associated with the QCD phase diagram and its relations to heavy-ion collisions [15]. But, especially the versions with

added Polyakov-loop potential in the functional renormalization group (FRG) approach [22–26], have a certain success. However, using these models, we have to keep in mind that they do not treat the gluon as an active degree of freedom and are only valid in a certain limit of the theory. Finally, functional methods like the Dyson-Schwinger (DS) or FRG approach can map the whole phase diagram and are, in general, equivalent to the generating functional and consequently ab initio. Furthermore, since they are based on the representation of the generating functional in terms of correlation functions, they have access to the fundamental degrees of freedom and derived observables and composite particles, too. However, due to this representation, they constitute an infinite tower of coupled integral (DS approach) and differential (FRG approach) equations for Green functions which relies on truncations to be solved. But these truncations are less controlled than Monte-Carlo simulations. Reviews to the DS and FRG approach can be found in Refs. [17, 27, 28] and [29, 30], respectively. In this work, we will apply the Dyson-Schwinger approach and will build upon a series of works dealing with (i) the bound state phenomenology in vacuum [31–34], (ii) the influence of quark flavors on the QCD phase diagram [35–37] and (iii) the critical scaling of the CEP of QCD [38] as well as (iv) the calculation of thermodynamic quantities like the pressure, the quark number density and baryon number fluctuations in medium [39–43].

Applications include the determination of simplified baryon backcoupling effects on the QCD phase diagram [44], too. In this work, we will enhance this baryon backcoupling study towards the chemical potential axis of the QCD phase diagram to check the applied calculation for any indications of a liquid-gaseous nuclear matter phase transition. The observed baryonic effects result from the quark-gluon vertex which represents the crucial element coupling the Yang-Mills sector with its quark sector. While propagators have been determined from their Dyson-Schwinger or FRG equations in vacuum and medium [37, 45–49], the corresponding vertices (including the quark-gluon vertex) have not been determined with comparable precision, especially in medium. For this purpose, recent attention has focused on the medium fluctuations of this vertex and their effect on the location of the CEP. In the DS approach, Ref. [50] calculated the quark-gluon vertex Dyson-Schwinger equation (DSE) semi-perturbatively whereas Ref. [49] studied effects due to nonprimitively-divergent vertex structures. In addition, mesonic medium effects have been taken into account in the FRG approach in Refs. [46, 47, 51] and are naturally present in quark-meson type effective theories [22, 52–54]. Due to the inherent complementarity of truncations in the DS and FRG approach, it is highly desirable to complement these studies by a corresponding one in the DS approach which is one of the main topics in this work.[55]

To be more precise, based on the studies in Refs. [56–58], we will determine the

influence of explicitly calculated and backcoupled Pion and Sigma mesons onto the QCD phase diagram. We restrict ourselfs to the (pseudo-)Goldstone Bosons (Pions) and their chiral partner (Sigma) since we expect them to be dominant, not only for the universal behavior [52, 59, 60] but also compared to the backcoupling of other mesons. As input for the backcoupling, we will calculate and study the properties and wave-functions of these backcoupled mesons together with multiple vector and axial-vector mesons on the chemical potential axis of the QCD phase diagram. With this procedure, we take important chemical-potential effects for the meson backcoupling into account which are mandatory to preserve the Silver-Blaze property (SBP) [61, 62] but neglect temperature effects. In addition, we complement meson bound state calculations at finite temperature [63–67]. Furthermore, we are able to trace the breaking of the charge conjugation parity through the chemical potential and to check the validity of the SBP: all dependencies of colored quantities on chemical potential cancel out in observables.

In particular, the determination of the meson properties of the vector mesons are interesting since especially the light vector (ρ, ω and ϕ) mesons play an important role for the observed dilepton spectrum [3, 68, 69] and due to their quantum numbers they couple to the electromagnetic current. Since the electromagnetic radiation from the hot and dense fireball of the experimental heavy-ion collisions escapes the medium almost undistorted, this radiation and the light vector mesons (though the observed dilepton spectrum) can serve as a probe for the state of matter in the early stages of the collision. In consequence, it is important to know the medium properties of these vector mesons. So far, the impact of non-vanishing chemical potential on the bound state properties and the quark and gluon structure of the ρ, its chiral partner a_1, and the ϕ meson (covered in this work) is less studied. Instead, mainly the properties of vector mesons like the spectral function have been studied in a range of approaches with focus on the medium effects of their Pion cloud and medium effects due to the coupling of ρ mesons to the nucleons via resonance excitations [3, 68, 69].

This work is structured as follows: In Chaps. 2 and 3, we will derive and discuss the properties and the truncation of the Dyson-Schwinger and Bethe-Salpeter equations for the fundamental and mesonic bound state particles, respectively. In Chap. 4, we present the quark and meson property and wave-function results as well as the chiral observable results at finite chemical potential. These are used in Chap. 5 to determine the influence of Pion and Sigma meson backcoupling effects onto the quark, the chiral observables and the QCD phase diagram. Before we conclude in Chap. 7, we study the backcoupling effects of baryons onto the quark and chiral observables in Chap. 6 in a simplified manner and for finite chemical potential and vanishing temperature.

2. Fundamental particles of QCD

In this chapter, we will discuss the theoretical background for the properties of the fundamental particles of quantum chromodynamics (QCD): the quarks and their gauge Bosons the gluons which mediate the strong interaction. We will begin by deriving equations to calculate these properties. For this purpose, we introduce the functional approach of Dyson-Schwinger equations (DSEs) and discuss the necessary approximations for this framework to be implemented numerically. At the end, we will show some first results.

To begin, we describe the theory of strong interactions via the generating functional of QCD, which contains all information of the considered strong interaction. From this quantity, we are able to derive the equations of motion for each of the elementary particles. To be more general, we will do so for arbitrary actions first, before we apply the procedure to the QCD action. By using the path integral formalism, the generating functional for partially connected Green functions in vacuum is given by

$$Z[J] = \mathcal{N} \int \mathcal{D}\varphi \, e^{i\left(S[\varphi] - \int_x \varphi(x) J(x)\right)} \tag{2.1}$$

with the arbitrary action $S[\varphi] = \int_x \mathscr{L}(\varphi(x), \partial_\mu \varphi(x))$, the integral abbreviation $\int_x = \int d^4x$, the Lagrangian density $\mathscr{L}$ and the super-field φ which contains all fields of the system. We add the external source field $J(x)$ to the action for the ability to derive all Green functions $G_n(x_1, \ldots, x_n)$ of the order n by simply applying a functional derivative w.r.t $J(x)$ to the generating functional $Z[J]$ and ultimately setting $J(x) = 0$. In equations this means:

$$\begin{aligned} G_n(x_1, \ldots, x_n) &= \langle 0 | \, \hat{T} \left\{ \hat{\varphi}(x_1) \ldots \hat{\varphi}(x_n) \right\} | 0 \rangle = \frac{\int \mathcal{D}\varphi \, \varphi(x_1) \ldots \varphi(x_n) e^{iS[\varphi]}}{\int \mathcal{D}\varphi \, e^{iS[\varphi]}} \\ &= \frac{1}{Z[J]} \frac{i^n \delta^n}{\delta J(x_1) \ldots \delta J(x_n)} Z[J] \Big|_{J=0} . \end{aligned} \tag{2.2}$$

Here, $\hat{T}$ represents the time ordering operator. Next, we will use this relation to derive the master equation of the Dyson-Schwinger framework.

2.1. Dyson-Schwinger framework

The Dyson-Schwinger framework is based on the representation of the generating functional in terms of correlation functions which can be demonstrated by

$$Z[J] = Z[0] \sum_{n=0}^{\infty} \frac{(-i)^n}{n!} \int d^4x_1 \dots d^4x_n J(x_1) \dots J(x_n) G_n(x_1, \dots, x_n) \,. \tag{2.3}$$

Due to this identity, the Dyson-Schwinger framework is an ab initio approach if it is solved completely and self-consistently. The framework is given by an infinite tower of coupled integral equations, the Dyson-Schwinger equations (DSEs). These equations are the quantum equations of motion for all n-point Green functions of the theory. Every equation is self-consistent which means that the quantity which is defined by the equation depends on itself. In consequence, we need a fixpoint iteration to solve the equation. See App. C.1.2 for more information of this procedure.

In general, the solutions of the quantum equations of motion are the Green functions of the elementary particles of the considered theory or the Green functions of n-particle bound states consisting of these elementary particles. The two-particle (mesonic) bound states described by the Bethe-Salpeter equations (BSEs) will be discussed in the next Chap. 3. In the next sections, however, we will discuss the elementary particles as fundamental degrees of freedom described by the Dyson-Schwinger equations.

2.1.1. Derivation of the Dyson-Schwinger equations

The DSEs result from the local translation invariance of the generating functional. We describe this local translation by the field transformation $\mathcal{T}$: $\varphi(x) \to \varphi'(x) = \varphi(x) + \delta\varphi(x)$. Since we integration over all filed configurations, the field transformation $\mathcal{T}$ only represents a redefinition of the integral variable. Consequently, the path integral is not affected, implying

$$\begin{aligned} \mathcal{T}(Z[J]) &= \mathscr{N} \int \mathcal{D}\varphi' \, e^{i(S[\varphi'] - \int_x \varphi'(x) J(x))} \\ &= \mathscr{N} \int \mathcal{D}\varphi \, e^{i \int_x \delta\varphi(x) \left[\frac{\delta S[\varphi]}{\delta\varphi(x)} - J(x)\right]} e^{i(S[\varphi] - \int_x \varphi(x) J(x))} \\ &\overset{(2.2)}{=} Z[J] \left\langle e^{i \int_x \delta\hat{\varphi}(x) \left[\frac{\delta S[\hat{\varphi}]}{\delta\hat{\varphi}(x)} - J(x)\right]} \right\rangle_{J \neq 0} \overset{!}{=} Z[J] \,. \end{aligned} \tag{2.4}$$

In this derivation, we used the Taylor-expansion $S[\varphi'] = S[\varphi] + \int_x \delta\varphi(x) \delta S[\varphi]/\delta\varphi(x)$ and the fact that the integral measure $\mathcal{D}\varphi$ is invariant under transformation $\mathcal{T}$.

The expression $\langle f(\hat{\varphi})\rangle_{J\neq 0}$ represents the vacuum expectation value (VEV) of the function f depending on the field operator $\hat{\varphi}$ with intact dependency from external source J. From Eq. (2.4), we can deduce the so-called master DSE for partially connected Green functions which is defined via

$$\left\langle \frac{\delta S[\hat{\varphi}]}{\delta\hat{\varphi}(x)} \right\rangle_{J\neq 0} = J(x) \tag{2.5}$$

and describes the quantum mechanical expectation value of the classical equation of motion. So far, we considered partially connected Green functions, but we are interested in the n-point one-particle irreducible (1PI)[1] Green functions since we can derive all other kinds of Green functions from them, e.g. the (partially) connected Green functions. The 1PI Green functions represent the irreducible contribution to the n-point interaction vertex without redundancies and can be derived from the so-called effective action $\Gamma[\tilde{\varphi}]$. This generating functional is connected to the other generating functionals via

$$\frac{Z[J]}{Z[0]} = e^{iW[J]} = e^{i\left(\Gamma[\tilde{\varphi}] - \int_z \tilde{\varphi}(z)J(z)\right)} \tag{2.6}$$

where $W[J]$ is related to the effective action by Legendre transformation and generates all connected n-point Green functions which enter into the scattering-matrix. $\tilde{\varphi}(x) = \langle\varphi(x)\rangle_{J\neq 0}$ is the so-called averaged field and defined as the vacuum expectation value of the field operator $\hat{\varphi}$. Resulting from the definition of the effective action as a Legendre transformation, we can identify $J(x) = \partial\Gamma[\tilde{\varphi}]/\partial\tilde{\varphi}(x)$ and $\tilde{\varphi}(x) = \partial W[J]/\partial J(x)$ as conjugated sources. This implies that $\tilde{\varphi}$ vanishes if J vanishes[2]. To be able to express the Master-DSE in Eq. (2.5) also with connected and 1PI Green functions, we consider the definition of $\langle f(\hat{\varphi})\rangle_{J\neq 0}$ for the different kinds of Green functions and get the following relations:

$$\begin{aligned}
\langle f(\hat{\varphi})\rangle_{J\neq 0} &:= \frac{\int \mathcal{D}\varphi\, f(\varphi) e^{i(S[\varphi] - \int_x \varphi(x)J(x))}}{\int \mathcal{D}\varphi\, e^{i(S[\varphi] - \int_x \varphi(x)J(x))}} = \frac{1}{Z[J]} f\left(\frac{i\delta}{\delta J}\right) Z[J] \\
&= e^{-iW[J]} f\left(\frac{i\delta}{\delta J}\right) e^{iW[J]} = f\left(-\frac{\delta W[J]}{\delta J} + \frac{i\delta}{\delta J}\right) 1 \\
&= f\left(\tilde{\varphi}(\bullet) + \int_y \Delta_{\bullet y}[\tilde{\varphi}] \frac{\delta}{\delta\tilde{\varphi}(y)}\right) 1\,.
\end{aligned} \tag{2.7}$$

Here, we used the relation $e^{-x} f(\partial/\partial y) e^{x} = f(\partial x/\partial y + \partial/\partial y)$ and the definition of the conjugated variables. In the last line, $\Delta_{xy}[\tilde{\varphi}] = \left(\frac{\partial^2\Gamma[\tilde{\varphi}]}{\partial\tilde{\varphi}(x)\partial\tilde{\varphi}(y)}\right)^{-1} = -\frac{\partial^2 W[J]}{\partial J(x)\partial J(y)}$

[1] 1PI diagrams stay connected if one internal line is cut.

[2] In case of dynamical chiral symmetry breaking (DχSB), $\tilde{\varphi}$ is generally finite but can be redefined to zero.

describes the 1PI two-point function or inverse propagator with non-vanishing external source. In the limit of a vanishing external source, we obtain the 1PI two-point Green function: $G_2(x,y) = \Delta_{xy}[\tilde{\varphi}]|_{J,\tilde{\varphi}\to 0}$.

With Eq. (2.7), we are now able to translate classical relations between fields $f(\varphi) = 0$ into quantum-mechanical identities $\langle f(\hat{\varphi})\rangle = 0$. For this purpose, we exchange the classical fields φ by field operators $\hat{\varphi}$ and take the vacuum expectation value. If we do so for Eq. (2.5), we finally get the Master-DSE for 1PI Green functions which is given by

$$\frac{\delta\Gamma}{\delta\tilde{\varphi}(x)}[\tilde{\varphi}] = \frac{\delta S}{\delta\varphi(x)}\left[\tilde{\varphi}(\bullet) + \int_y \Delta_{\bullet y}[\tilde{\varphi}]\frac{i\delta}{\delta\tilde{\varphi}(y)}\right]1\,. \tag{2.8}$$

Now, we can apply this Master-DSE to the QCD action and derive all necessary DSEs. But first we will discuss the different components of the QCD action.

QCD in vacuum

Analog to quantum electrodynamics (QED), the QCD action has to obey Poincaré invariance, renormalizability and P- or T-invariance[3] but also local $\mathrm{SU_C(N_c)}$ gauge invariance. The only action in vacuum and Minkowski space-time that fulfills these requirements is given by

$$S[A,\bar{\Psi},\Psi] = \int_x \left\{\bar{\Psi}_f(x)\left(i\gamma^\mu D_\mu(x) - \mathbb{1}_\mathrm{D}\mathbb{1}_\mathrm{C} m_\mathrm{q}^f\right)\Psi_f(x) - \frac{1}{4}F^g_{\mu\nu}(x)F_g^{\mu\nu}(x)\right\} \tag{2.9}$$

with the Dirac spinor for quark $\Psi_f(x)$ and antiquark $\bar{\Psi}_f(x) = \Psi_f^\dagger(x)\gamma_0$ fields and the quark flavor f. The field strength tensor $F_{\mu\nu}(x) = \frac{i}{g_\mathrm{s}}\left[D_\mu(x), D_\nu(x)\right]$ is defined through the covariant derivative $D_\mu(x) = \mathbb{1}_\mathrm{C}\partial_\mu - ig_\mathrm{s}\mathcal{A}_\mu(x)$ and the $\mathrm{SU_C(N_c)}$ gauge fields $\mathcal{A}_\mu(x) = A^g_\mu(x)t^g$ describing the gluon. g_s and m_q^f are the unrenormalized strong coupling constant and the current quark mass of quark flavor f, generated by the Higgs mechanism. Under the local gauge transformation $\mathcal{G}$:

$$\begin{aligned}
\mathcal{G}(\Psi_f(x)) &= U_\mathcal{G}(x)\Psi_f(x)\,,\\
\mathcal{G}(\bar{\Psi}_f(x)) &= \bar{\Psi}_f(x)U^\dagger_\mathcal{G}(x)\,,\\
\mathcal{G}(\mathcal{A}_\mu(x)) &= U_\mathcal{G}(x)\left(\mathcal{A}_\mu(x) + \frac{i}{g_\mathrm{s}}\mathbb{1}_\mathrm{C}\partial_\mu\right)U^\dagger_\mathcal{G}(x)\,,\\
U_\mathcal{G}(x) &= e^{i\epsilon(x)} = e^{i\sum_g \epsilon_g(x)t^g}
\end{aligned} \tag{2.10}$$

[3] In general, an additional $\epsilon_{\alpha\beta\mu\nu}F_g^{\alpha\beta}F_g^{\mu\nu}$ term can appear, but this term breaks the P- and T-invariance [70]. Here, $\epsilon_{\alpha\beta\mu\nu}$ represents the totally antisymmetric tensor.

the (anti-)quark and gluon fields transform as elements of the fundamental and adjoint representation of the $\mathrm{SU_C(N_c)}$-group, respectively. Furthermore, $U_{\mathcal{G}}(x)$ is the unitary local gauge transformation matrix acting on the color part of the elementary fields. The $\mathrm{SU_C(N_c)}$ gauge-group generators t^g fulfill the Lie algebra $\left[t^g, t^h\right] = if^{ghl}t^l$, but the actual representation of the generators depend on the fields they are acting on. Further relations and the possible representation of the "color" generators can be found in App. A.2. Naturally, we consider $\mathrm{N_c} = 3$ colors. The corresponding Dirac matrix representation is shown in App. A.1. By using the Lie algebra of the color gauge group generators, the field strength tensor can be rewritten as

$$\begin{aligned} F_{\mu\nu}(x) &= \partial_\mu \mathcal{A}_\nu(x) - \partial_\nu \mathcal{A}_\mu(x) - ig_\mathrm{s}\left[\mathcal{A}_\mu(x), \mathcal{A}_\nu(x)\right] \\ &= \left(\partial_\mu A^g_\nu(x) - \partial_\nu A^g_\mu(x) + g_\mathrm{s} f^{ghl} A^h_\mu(x) A^l_\nu(x)\right) t^g = F^g_{\mu\nu}(x) t^g \end{aligned} \tag{2.11}$$

where f^{ghl} are the totally antisymmetric and real structure constants. The last term results from the non-Abelian character of the strong interaction and leads to gluon self-interaction.[4]

From Eq. (2.10), we can deduce that a subset of gauge fields is connected by the gauge transformation $\mathcal{G}$. Since they all have the same physical content, we encounter an over-counting in the generating functional. Due to this problem, we have to reduce the integration to a subset where the gauge fields can no longer be transformed into each other via the gauge transformation $\mathcal{G}$. This procedure is called gauge fixing. One possible method for this procedure is the Faddeev-Poppov gauge fixing from Ref. [71]. As result of this procedure, an additional gauge fixing action term appears in the QCD action which depends on the so-called Faddeev-Poppov ghost $c(x)$ and antighost $\bar{c}(x)$ auxiliary fields. If we consider a generalized linear covariant gauge fixing condition $f[A] = \partial^\mu A^g_\mu(x) - \omega = 0$ with arbitrary ω the additional action term then is given by

$$S_\mathrm{GF}[A, c, \bar{c}] = -\int_x \frac{\left(\partial^\mu A^g_\mu(x)\right)^2}{2\xi} + \int_x \bar{c}(x)\partial^\mu D_\mu(x) c(x) \tag{2.12}$$

where ξ is the unrenormalized gauge parameter. Under the local gauge transformation $\mathcal{G}$ the ghost fields $c(x) = c_a(x)t^a$ are elements of the adjoint representation of $\mathrm{SU_C(N_c)}$, too.

So far, all fields and constants in the QCD action are unrenormalized. To cancel appearing infinities, we introduce the regulator Λ and renormalization constants.

[4] In the Abelian QED, this last term vanishes and there are no self-interacting Photons in the QED U(1) gauge group.

The regulator removes the appearing infinities by introducing a regulator dependency, while the renormalization constants are fixed through the renormalization conditions. Through this renormalization procedure, we no longer have a regulator dependency but need the constants ($m_{\mathrm{q}}^f(\xi_{\mathrm{q}})$, $g_{\mathrm{s}}(\xi_{\mathrm{i}})$) as input from experimental data at the renormalization points ξ_{x}. In the QCD action, we introduce renormalization constants for the quark wave-function Z_2^f and the quark mass Z_m^f of quark flavor f, as well as for the strong coupling constant Z_g, the gluon wave function Z_3, the ghost wave function $\tilde{Z}_3$, and the gauge fixing parameter Z_ξ. The corresponding connection of the unrenormalized to the renormalized quantities is defined via

$$\begin{aligned}
\Psi_f(\Lambda) &= \left(Z_2^f(\Lambda,\xi_{\mathrm{q}})\right)^{1/2}\Psi_f(\xi_{\mathrm{q}}), & m_{\mathrm{q}}^f(\Lambda) &= Z_m^f(\Lambda,\xi_{\mathrm{q}})m_{\mathrm{q}}^f(\xi_{\mathrm{q}}),\\
\mathcal{A}_\mu(\Lambda) &= \left(Z_3(\Lambda,\xi_{\mathrm{g}})\right)^{1/2}\mathcal{A}_\mu(\xi_{\mathrm{g}}), & g_{\mathrm{s}}(\Lambda) &= Z_g(\Lambda,\xi_{\mathrm{i}})g_{\mathrm{s}}(\xi_{\mathrm{i}}),\\
c(\Lambda) &= \left(\tilde{Z}_3(\Lambda,\xi_{\mathrm{gh}})\right)^{1/2}c(\xi_{\mathrm{gh}}), & \xi(\Lambda) &= \left(Z_\xi(\Lambda,\xi_{\mathcal{G}})\right)^{-1}\xi(\xi_{\mathcal{G}})
\end{aligned} \tag{2.13}$$

where Λ is the regulator and ξ_{x} with $\mathrm{x}\in\{\mathrm{q},\mathrm{g},\mathrm{gh},\mathrm{i},\mathcal{G}\}$ are the renormalization points. From now on, we use renormalized quantities and suppress the renormalization point and regulator dependency for the rest of this work. Furthermore, we transform some renormalization constants in more convenient vertex renormalization constants using so-called Slavnov-Taylor identities (STIs). This re-expression yields

$$Z_1 = Z_g\left(Z_3\right)^{3/2}, \quad \tilde{Z}_1 = \tilde{Z}_3 Z_g\left(Z_3\right)^{1/2}, \quad Z_{1\mathrm{F}}^f = Z_2^f Z_g\left(Z_3\right)^{1/2}, \quad Z_4 = \left(Z_g\right)^2\left(Z_3\right)^2 \tag{2.14}$$

with the vertex renormalization constants for the three-gluon vertex Z_1, the ghost-gluon vertex $\tilde{Z}_1$, the quark-gluon vertex $Z_{1\mathrm{F}}^f$ of quark flavor f, and the four gluon vertex Z_4. Finally, we can write the renormalized, Lorentz gauge fixed QCD action in vacuum and Minkowski space-time by

$$\begin{aligned}
S_{\mathrm{QCD}}[A,\bar{\Psi},\Psi,c,\bar{c}] = \int_x \Big[& Z_2^f\bar{\Psi}^f(x)\left(i\gamma^\mu\mathbb{1}_{\mathrm{C}}\partial_\mu - Z_m^f\mathbb{1}_{\mathrm{D}}\mathbb{1}_{\mathrm{C}}m_{\mathrm{q}}^f\right)\Psi^f(x) +\\
& + Z_{1F}^f g_{\mathrm{s}}\bar{\Psi}^f(x)\gamma^\mu t_g A_\mu^g(x)\Psi^f(x) + Z_3\frac{1}{2}A_\mu^g(x)\left(\Box g^{\mu\nu} + \left[\frac{Z_\xi}{\xi}-1\right]\partial^\nu\partial^\mu\right)A_\nu^g(x) +\\
& - Z_1\frac{g_{\mathrm{s}}}{2}f_{ghl}\left[\partial^\mu A_g^\nu(x) - \partial^\nu A_g^\mu(x)\right]A_\mu^h(x)A_\nu^l(x) + \tilde{Z}_3\bar{c}(x)\Box c(x) +\\
& - Z_4\frac{g_{\mathrm{s}}^2}{4}f_{gko}f_{ghl}A_k^\mu(x)A_o^\nu(x)A_\mu^h(x)A_\nu^l(x) + g_{\mathrm{s}}\tilde{Z}_1\left(\partial_\mu\bar{c}(x)\right)\mathcal{A}^\mu(x)c(x)\Big] .
\end{aligned} \tag{2.15}$$

Now, we want to derive the necessary DSEs from this QCD action. But to derive the DSEs for quarks, gluons, ghosts and all vertices from the generating functional,

it is more convenient to transform the QCD action into the Euclidean momentum space first. This is done in Apps. A.4 and A.5. For the derivation we, furthermore, use a graphical notation, apply the derivation explained in Ref. [73] and get the

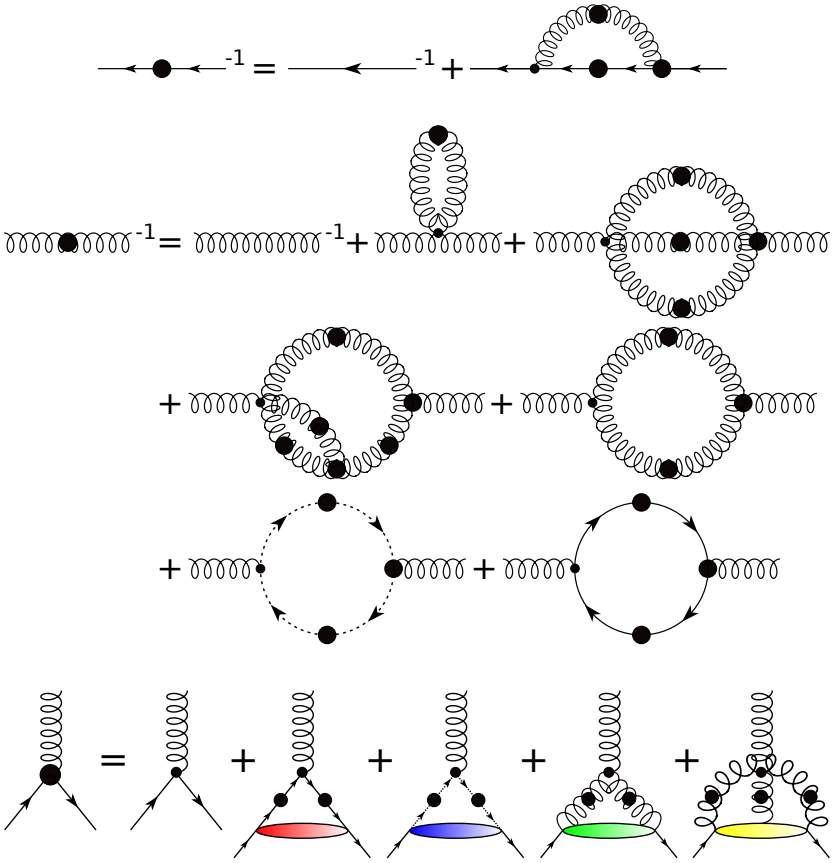

Figure 2.1.: Full, untruncated Dyson-Schwinger equations for the inverse quark (upper) and gluon (center) propagator as well as the quark-gluon vertex (lower). Quark, gluon and ghost propagators are denoted by solid, curly and dotted lines, respectively. The intersection of different line types or three or four curly lines represent different kinds of vertices. Dressed quantities are indicated by big black dots. The remaining ones are bare. The arrows indicate the direction of the quark or ghost flavor and the momentum. The differently colored symbols in the quark-gluon vertex DSE represent higher dressed vertices. Note that the upper vertex in all diagrams of the quark-gluon vertex DSE are bare. The shown vertex representation is adopted from Refs. [44, 72]. The signs and prefactors are absorbed into the diagrams.

full quark, gluon and quark-gluon vertex DSEs shown in Fig. 2.1 as well as all further vertices and ghost DSEs. The quark-gluon vertex DSE shown in this figure is one possible representation. Another is given in Ref. [74].

2.1.2. Quark and gluon equations

In this section, we consider and discuss only the quark and gluon DSEs. A diagrammatic representation of the considered quark and gluon DSEs with the appropriate momentum routing is shown in Fig. 2.2. The first term on the right side

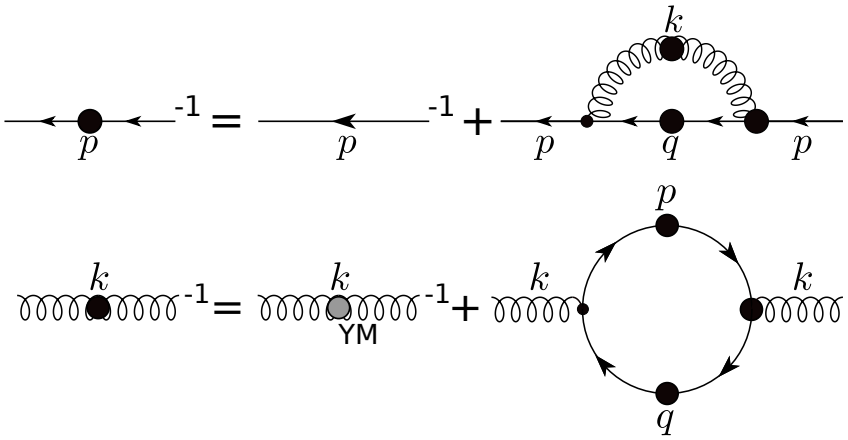

Figure 2.2.: Dyson-Schwinger equations for the inverse quark (upper) and gluon (lower) propagator with the corresponding momentum routing. The intersection of quark and gluon lines represent quark-gluon vertices. The first gluon term marked by a gray dot and a YM subscript summaries all Yang-Mills diagrams of the gluon DSE shown in Fig. 2.1. The remaining quantities are defined in the same way as in Fig. 2.1.

of the gluon DSE, marked by a gray dot, summarizes all diagrams already present in Yang-Mills theory. In equations we indicate this term as $D_{\mu\nu}^{\mathrm{YM}}$. It includes the bare gluon propagator, gluon self-interactions and gluon-ghost interactions. The quark loop term in the gluon DSE couples the matter sector of QCD back onto the gluon and includes an implicit sum over all $\mathrm{N_f}$ considered quark flavor. In this work, we mostly consider $\mathrm{N_f} = 2 + 1$. Through this sum, the quark loop term furthermore yields a non-trivial coupling between the quark flavors.

In algebraic equations, the DSEs for the quark and gluon propagators for real p

momenta[5] are given by

$$\left[S^f(p)\right]^{-1} = \left[S_0^f(p)\right]^{-1} - \int_q \Gamma^{f,\epsilon,h}_{\mathrm{qg},0} S^f(q) \Gamma^{f,\nu,h}_{\mathrm{qg}}(p,q,k) D_{\epsilon\nu}(k)\,, \tag{2.16}$$

$$[D_{\epsilon\nu}(k)]^{-1}_{hg} = \left[D^{\mathrm{YM}}_{\epsilon\nu}(k)\right]^{-1}_{hg} + \int_q \mathrm{Tr}_{\mathrm{DCF}}\left[\Gamma^{\epsilon,h}_{\mathrm{qg},0} S(q) \Gamma^{\nu,g}_{\mathrm{qg}}(p,q,k) S(p)\right]\,. \tag{2.17}$$

For each quark flavor f, there is a quark DSE. In the quark self energy $\Sigma_f(p)$ and the quark loop $\Pi^{\mathrm{QL}}_{\mu\nu}(k)$ terms of the quark and gluon DSEs (second term on the RHS), we use the integral abbreviation $\int_q \equiv \int d^4q/(2\pi)^4$ and consider $\mathrm{N_f}$ quark and $\mathrm{N_c} = 3$ colors. Additionally, the quark loop includes a trace over the Dirac, color and flavor part. The fermionic quark momenta p and q and the bosonic gluon momentum k are connected by the momentum routing $p = q - k$ with momenta of the form $q = (\vec{q}, q_4)$.

The quark self energy and the quark loop depend on the bare $\Gamma^{f,\epsilon,h}_{\mathrm{qg},0} = ig_{\mathrm{s}} Z^f_{1\mathrm{F}} \gamma^\epsilon t^h$ and dressed $\Gamma^{\nu,h,f}_{\mathrm{qg}}(p,q,k) = ig_{\mathrm{s}} t^h \Gamma^{\nu,f}_{\mathrm{qg}}(p,q,k)$ quark-gluon vertex of the quark flavor f. The representations and relations of the contained Dirac γ_μ and color matrices t^h are given in Apps. A.1 and A.2, respectively. In the quark self energy, the color matrices sum up to $\sum_h t^h t^h = C_{\mathrm{F}}$ with the quadratic Casimir factor $C_{\mathrm{F}} = (\mathrm{N_c^2} - 1)/(2\mathrm{N_c})$ in the fundamental representation, while the color trace of the quark-loop yields $\mathrm{Tr_C}[t^h t^g] = \delta_{hg}/2$. The appearing strong coupling constant is defined by $g_{\mathrm{s}}^2 = 4\pi\alpha_{\mathrm{s}}(\xi_{\mathrm{v}})$ where $\alpha_{\mathrm{s}}(\xi_{\mathrm{v}}) = 0.3$ is the running coupling at a scale fixed by the quenched gluon from lattice (see Refs. [75, 76] for details). In the renormalization constant for the quark-gluon vertex $Z^f_{1\mathrm{F}} = Z^f_2 \tilde{Z}_1/\tilde{Z}_3$, the ghost-gluon vertex renormalization constant $\tilde{Z}_1$ is set to one since the corresponding vertex is ultraviolet finite in the Landau gauge (see Ref. [77]) which we will apply throughout this work. $\tilde{Z}_3$ furthermore is the ghost wave function renormalization constant.

The dressed quark propagator also depends on the inverse bare quark propagator which is, in vacuum, given by

$$\left[S_0^f(p)\right]^{-1} = Z_2^f \left(i\not{p} + \mathbb{1}_{\mathrm{D}} Z_m^f m_{\mathrm{q}}^f(\xi_{\mathrm{q}})\right) \mathbb{1}_{\mathrm{C}} \tag{2.18}$$

with Z_2^f and Z_m^f being the quark wave-function and quark mass renormalization constants of the quark flavor f. $m_{\mathrm{q}}^f(\xi_{\mathrm{q}})$ is the renormalized current quark mass of the quark flavor f at the quark renormalization point $\xi_{\mathrm{q}} = 80\,\mathrm{GeV}$.[6]

[5] The discussion of the quark DSEs for complex momenta is done in App. C.1.3.

[6] We use such a high value for the renormalization point to be sufficiently far in the perturbative regime.

To solve the coupled set of quark and gluon equations, we need an ansatz for the dressed quark and gluon propagators. For the dressed quark propagator S^f of quark flavor f in vacuum, this ansatz can be displayed by

$$S^f(p) = \frac{-i\not{p}\,\mathrm{A}_f(p) + \mathbb{1}_\mathrm{D}\,\mathrm{B}_f(p)}{\mathrm{N}_f(p)}\mathbb{1}_\mathrm{C}\,, \tag{2.19}$$
$$\mathrm{N}_f(p) = p^2\,\mathrm{A}_f^2(p) + \mathrm{B}_f^2(p)\,.$$

The dressed quark propagators of the different quark flavors can be written in a diagonal flavor matrix $S = \mathrm{diag}\left(S^\mathrm{u}, S^\mathrm{d}, \ldots\right)$ which will be important for a compact notation in the bound state approach and is used in the gluon DSE. Since we consider the isospin-symmetric limit of equal up- and down-quark masses $m_\mathrm{q}^\mathrm{u} = m_\mathrm{q}^\mathrm{d}$, the up- and down-quark propagators are identical $S^\mathrm{u} = S^\mathrm{d}$, too. From now on, we will no longer differentiate between these two quark flavors and will call them light quark mesons ($f = \ell$). The dressed gluon propagator $D_{\mu\nu}$ in vacuum (still with an arbitrary gauge) is given by

$$D_{\mu\nu}(k) = \left(\frac{\mathrm{Z}(k)}{k}T_{\mu\nu}(k) + \frac{\xi}{k^2}L_{\mu\nu}(k)\right)\mathbb{1}_\mathrm{C} \tag{2.20}$$

with the projectors

$$T_{\mu\nu}(k) = \delta_{\mu\nu} - \frac{k_\mu k_\nu}{k^2}\,, \tag{2.21}$$
$$L_{\mu\nu}(k) = \frac{k_\mu k_\nu}{k^2} \tag{2.22}$$

transversal ($T_{\mu\nu}$) and longitudinal ($L_{\mu\nu}$) to the gluon momentum k. The dressing function of the gluon (Z) as well as those of the quark (A_f, B_f) have non-trivial momentum dependence and encode the non-perturbative information. Normally, these dressing functions and the renormalization constants all depend on the gauge parameter ξ, but the dependence is suppressed here and further on. In all calculations, we apply the so-called Landau gauge $\xi = 0$. Details to the renormalization procedure of the quark and gluon equations as well as details to the general numerical setup in the DSE are noted in Apps. C.1.1 and C.1.2, respectively.

This leaves us with the quark-gluon vertex $\Gamma_\mathrm{qg}^{\nu,f}(p,q,k)$ and Yang-Mills part of the gluon $D_{\mu\nu}^\mathrm{YM}(k)$ which are still to define. In Sec. 2.2, we will introduce truncations to the set of equations and will discuss these two quantities in more detail. But before, we will consider the changes introduced by considering the system in medium.

2.1.3. Introduction of the medium

In this section, we are interested in the connection between the system describing quantities of thermodynamics and quantum field theory (QFT). Consequently, we search for a connection between the appropriate thermodynamic potential or partition function of a certain set of natural variables and the generating functional. Since we need a system which is in contact with the heat bath and allows particle and energy exchange, we consider the grand canonical ensemble. Here, the particle number and energy are only known on average and the system is defined by the natural variables of temperature T and a set of quark chemical potentials μ_{q}^{f} for the quark flavors $f \in \{\mathrm{u}, \mathrm{d}, \mathrm{s}\}$. The grand canonical ensemble is described by the partition function[7]

$$Z_{\mathrm{GC}}(T, \mu_{\mathrm{q}}^{f}) = \mathrm{Tr}\left(e^{-(\hat{H}-\mu_{\mathrm{q}}^{f}\hat{N}_{f})/T}\right) . \tag{2.23}$$

In this expression, $\hat{N}_f = \int d^3x \hat{\Psi}_f^{\dagger}(x)\hat{\Psi}_f(x) = \int d^3x \hat{\bar{\Psi}}_f(x)\gamma_0\hat{\Psi}_f(x)$ represents the quark particle number operator with $\hat{\Psi}_f(x)$ and $\hat{\bar{\Psi}}_f(x)$ as quark and antiquark spinor field operators of the quark flavor f. In the following expressions, the Hamiltonian will be redefined such that the particle number term is included.

For the connection between thermodynamics and QFT, we now use the Euclidean Matsubara or imaginary time formalism. A review to this topic can be found in Ref. [78]. First we consider the generating functional in Eq. (2.1) in Euclidean space-time (transformation see App. A.4) and for the special case of a finite time interval as shown by

$$\begin{aligned} Z_{\mathrm{Eucl.}}[J=0](\varphi_f(\tau_f), \varphi_i(\tau_i)) &= \langle \varphi_f(\tau_f)|\, \varphi_i(\tau_i)\rangle = \left\langle \varphi_f \left| e^{-\hat{H}(\tau_f-\tau_i)} \right| \varphi_i \right\rangle = \\ &= \mathcal{N} \int_{\varphi_i(\tau_i)}^{\varphi_f(\tau_f)} \mathcal{D}\varphi\, e^{-S_{\mathrm{Eucl.}}[\varphi](\tau_i,\tau_f)} \end{aligned} \tag{2.24}$$

where $S_{\mathrm{Eucl.}}[\varphi](\tau_i, \tau_f) = \int_{\tau_i}^{\tau_f} d\tau \int d^3x \mathscr{L}_{\mathrm{Eucl.}}(\varphi(x,\tau), \partial_\mu\varphi(x,\tau))$ defines the corresponding Euclidean action and $\tau = -it$ is the imaginary time. By comparing this expression of the Euclidean generating functional with finite time interval and the

[7] The connected grand canonical potential is given by $\Omega = -T/V \log Z_{\mathrm{GC}}(T, \mu_{\mathrm{q}}^{f})$ with the volume of the system V, the temperature T and the quark chemical potentials μ_{q}^{f} of the quark flavor f.

grand canonical ensemble, we get the desired connection in the from

$$Z_{\mathrm{GC}}(T,\mu_q) = \int d\varphi \left\langle \varphi \left| e^{-\left(\hat{H}-\mu_{\mathrm{q}}^f \int d^3x \hat{\bar{\Psi}}_f(x)\gamma_0\hat{\Psi}_f(x)\right)/T} \right| \varphi \right\rangle = \\ = \mathscr{N} \int_{\varphi(0)=\pm\varphi(1/T)} \mathscr{D}\varphi e^{-S_{\mathrm{Eucl.}}[\varphi](0,1/T)+\mu_{\mathrm{q}}^f \int_0^{1/T} d\tau \int d^3x \bar{\Psi}_f(x)\gamma_0\Psi_f(x)} \tag{2.25}$$

As consequence from this connection and the spin-statistic theorem, we can deduce antisymmetric and symmetric periodicity conditions for Fermion fields Ψ and Boson fields Φ, respectively. These conditions are given by

$$\begin{aligned} \Psi(\vec{x},\tau+1/T) &= -\Psi(\vec{x},\tau)\,, \\ \Phi(\vec{x},\tau+1/T) &= +\Phi(\vec{x},\tau)\,. \end{aligned} \tag{2.26}$$

Due to the periodicity conditions and the finite integration interval in the temporal component, the energy component of the four-momentum becomes discrete. For this purpose, we introduce the bosonic (B) and fermionic (F) Matsubara frequencies:

$$\omega_p^{\mathrm{F}} = \pi T(2n_p+1)\,, \quad \omega_p^{\mathrm{B}} = 2\pi T n_p \quad \text{with } n_p \in \mathbb{Z}\,. \tag{2.27}$$

At finite temperature, we consequently have to replace all integrations $\int_q$ by $\not\int_q \equiv T\sum_{n_q}\int d^3q/(2\pi)^3$ which includes a sum over the discrete (fermionic) Matsubara frequencies. If we additionally consider finite chemical potential, the quark chemical potential is added to the Matsubara frequency via $\tilde{\omega}_p = \omega_p + i\mu_{\mathrm{q}}^f$ for each considered quark.

In this work, however, we mostly consider the case of finite chemical potential but vanishing temperature. Turning down the temperature to zero, there is no longer a discrete energy component, no periodicity conditions, and no summation over Matsubara frequencies but the quark chemical potential still has to be included into the energy component of the quark four momentum. In the following, we will discuss the quark and gluon propagator representation at finite chemical potential and vanishing temperature but the finite temperature case is easily obtainable by exchanging the fourth momentum component by a discrete Matsubara frequency. The inverse bare quark propagator of the quark flavor f at finite chemical potential and vanishing temperature is given by

$$\left[S_0^f(p)\right]^{-1} = Z_2^f\left(i\vec{\not p} + i\tilde{p}_4^f\gamma_4 + \mathbb{1}_{\mathrm{D}} Z_m^f m_{\mathrm{q}}^f(\xi_{\mathrm{q}})\right)\mathbb{1}_{\mathrm{C}} \tag{2.28}$$

with the abbreviation $\tilde{p}_4^f = p_4 + i\mu_{\mathrm{q}}^f$. In medium, the O(4) symmetry of the propagator is broken to a O(3) symmetry by the appearance of an assigned

direction of the medium $v_{\text{med}} = (\vec{0}, 1)$. This assigned direction results from a non-vanishing chemical potential in the energy component of the momentum or from the introduction of a heat bath. Due to this O(4) symmetry breaking, the corresponding dressed quark propagator S^f of the quark flavor f for finite quark chemical potential μ_{q}^f but vanishing temperature T now has to be represented by

$$S^f(p) = \frac{-i\vec{\not{p}}\,\mathrm{A}_f(p) + \mathbb{1}_{\mathrm{D}}\,\mathrm{B}_f(p) - i\tilde{p}_4^f\gamma_4\,\mathrm{C}_f(p) + i\tilde{p}_4^f\gamma_4\vec{\not{p}}\,\mathrm{D}_f(p)}{\mathrm{N}_f(p)}\mathbb{1}_{\mathrm{C}}\,, \tag{2.29}$$

$$\mathrm{N}_f(p) = \vec{p}^{\,2}\,\mathrm{A}_f^2(p) + \mathrm{B}_f^2(p) + (\tilde{p}_4^f)^2\,\mathrm{C}_f^2(p) + \vec{p}^{\,2}(\tilde{p}_4^f)^2\,\mathrm{D}_f^2(p)\,.$$

The fourth dressing function D_f has no perturbative counterpart in the bare quark propagator, its contribution is negligible in principle (see Refs. [79, 80]), and since it is explicitly zero for a Rainbow-Ladder interaction vertex in the quark DSE, we will not use it in this work. In the dressed gluon propagator $D_{\mu\nu}$ for finite quark chemical potential μ_{q}^f but vanishing temperature T, the assigned direction of the medium has a similar effect as in the quark. In Landau gauge, the dressed gluon propagator is now represented by

$$D_{\mu\nu}(k) = \left(\frac{\mathrm{Z}_{\mathrm{L}}(k)}{k^2}\mathcal{P}_{\mu\nu}^{\mathrm{L}}(k) + \frac{\mathrm{Z}_{\mathrm{T}}(k)}{k^2}\mathcal{P}_{\mu\nu}^{\mathrm{T}}(k)\right)\mathbb{1}_{\mathrm{C}} \tag{2.30}$$

with the medium projectors

$$\mathcal{P}_{\mu\nu}^{\mathrm{T}}(k) = \left(\delta_{\mu\nu} - \frac{\vec{k}_\mu\vec{k}_\nu}{\vec{k}^2}\right)(1-\delta_{\mu 4})(1-\delta_{\nu 4})\,, \tag{2.31}$$

$$\mathcal{P}_{\mu\nu}^{\mathrm{L}}(k) = T_{\mu\nu}(k) - \mathcal{P}_{\mu\nu}^{\mathrm{T}}(k) \tag{2.32}$$

taking into account the transversality w.r.t. the momentum k and the assigned direction of the medium $v_{\text{med}} = (\vec{0}, 1)$. In vacuum or for momenta scales much higher than the temperature and chemical potential, the gluon dressing functions Z_{L} and Z_{T} as well as the quark vector dressing functions A_f and C_f degenerate while they can become distinguishable in medium.

In previous works [44, 81] at finite temperature and chemical potential, we worked with non-zero light-quark chemical potential but set the strange quark chemical potential explicitly to $\mu_{\text{q}}^{\text{s}} = 0$. In principle, the strange quark chemical potentials should be adjusted such that the strangeness neutrality (as encountered in heavy ion collisions) is fulfilled [82, 83]. In this way, we could derive the appropriate dependence on the isospin- (μ_{I}), strangeness- (μ_{S}) and baryon- (μ_{B}) chemical potential. But since a variation of the strange quark chemical potential in the interval $\mu_{\text{q}}^{\text{s}} \in \{0, \mu_{\text{q}}^{\ell}\}$ only has a small influence on location of CEP as shown by Ref. [80], we work with equal light- (μ_{q}^{ℓ}) and strange-quark ($\mu_{\text{q}}^{\text{s}}$) chemical

potentials for the most parts of this work. If this is not the case, it will explicitly be mentioned. Throughout the remaining work, we will express all chemical potential dependencies by the baryon chemical potential $\mu_\mathrm{B} = 2\mu_\mathrm{q}^\ell + \mu_\mathrm{q}^\mathrm{s} = 3\mu_\mathrm{q}^f$.

2.1.4. Dynamical chiral symmetry breaking observables

In the following chapters, we often discuss the reaction of the chiral symmetry on different circumstances. For this purpose, we need reliable observables for the chiral symmetry. But first, we have to define the chiral symmetry, its breaking and possible observables for the dynamical chiral symmetry breaking (DχSB).

Chirality is the property of left- and right-handed quarks to transform separately under the chiral symmetry group $\mathrm{SU_R(N_f)} \times \mathrm{SU_L(N_f)}$. The invariance under this symmetry group is called chiral symmetry and implies that the differently handed quarks decouple from each other and do not mix or transform into each other anymore. The right- or left-handed representation of the flavor group $\mathrm{SU_{R/L}(N_f)}$ only transforms right-/left-handed particles. These left- Ψ_- and right-handed Ψ_+ quarks are particles with negative and positive helicity[8] $h = \frac{\vec{p}\cdot\vec{s}}{|\vec{p}||\vec{s}|}$, which is defined by the projection of the spin vector onto the momentum vector of the particle. Thereby, the differently handed quarks are defined via $\Psi_\pm = P_\pm \Psi$ with the chiral projector[9]

$$P_\pm = \frac{1}{2}(\mathbb{1}_\mathrm{D} \pm \gamma_5)\,. \tag{2.33}$$

Since we are interested in the chiral properties, we have to use the Weyl representation of the Dirac matrices (mentioned in App. A.1) for this section and especially for this projector. If we use the chiral projector and consider the different Dirac structures

$$\bar{\Psi}\Gamma^{(\mu)}\Psi = \begin{cases} \sum\limits_{\omega=\pm} \bar{\Psi}_\omega \Gamma^{(\mu)} \Psi_\omega & \Gamma^\mu \in \{\gamma^\mu, \gamma^\mu\gamma_5\} \\ \sum\limits_{\omega=\pm} \bar{\Psi}_{-\omega} \Gamma^{(\mu)} \Psi_\omega & \Gamma \in \{\mathbb{1}_\mathrm{D}, \gamma_5\} \end{cases}, \tag{2.34}$$

we can deduce that mass terms break the chiral symmetry[10] since they induce a mixing or interaction of left- and right-handed quarks in the QCD action. If we,

[8] The helicity is only a conserved quantum-number for mass-less particles, since there always is an inertial system which is faster than a massive particle yielding a sign-flip for the helicity.

[9] The chiral projector fulfills the rules of a general projector P_λ. This includes the idempotency $P_\lambda^2 = P_\lambda$ and the existence of an orthogonal projector $P_\lambda + P_\lambda^\perp = \mathbb{1}$ ($\rightarrow P_\lambda P_\lambda^\perp = 0$). Furthermore, the chiral projector has the properties: $P_\pm \gamma_\mu = \gamma_\mu P_\mp$ and $P_\pm \gamma_5 = \gamma_5 P_\pm$.

[10] As shown in Tab. B.3, the introduction of a mass term breaks the symmetry of the $\mathrm{SU_A(N_f)}$ flavor group and therefore also the chiral symmetry.

consequently, consider the chiral limit of vanishing static quark masses ($m_\mathrm{q} = 0$), the flavor symmetry groups $\mathrm{SU_V(N_f)} \times \mathrm{SU_A(N_f)}$ of the QCD action are classically conserved since the action is invariant under the symmetry transformations. However, dynamically generated quark masses can still break the chiral symmetry (group) $\mathrm{SU_R(N_f)} \times \mathrm{SU_L(N_f)}$ back to $\mathrm{SU_V(N_f)} \times \mathrm{SU_A(N_f)}$. In the following, we will therefore take a closer look at the spontaneous symmetry breaking.

For this purpose, we have to consider the charge of the $\mathrm{SU_A(N_f)}$ flavor group $Q_a^\mathrm{A} = \int d^3x \Psi^\dagger(x)\gamma_5\tau_a\Psi(x) = n_+^a - n_-^a$ which represents the "particle number" $n_\pm^a = \int d^3x \Psi_\pm^\dagger(x)\tau_a\Psi_\pm(x)$ difference between the right- (+) and left-handed (-) contributions. Here, we used $\gamma_5 = P_+ - P_-$. If this charge is a constant of motion (not time dependent), we immediately know that there cannot be a transition between particles of different helicities. By considering the vacuum expectation value of an infinitesimal symmetry transformation $\left[\hat{Q}_a, \hat{\varphi}_i\right] = -(\hat{\tau}_a)_{ij}\hat{\varphi}_i$ (see App. B.1 for more information) with the charge operator $\hat{Q}_a = \hat{Q}_a^\mathrm{A}$ of the flavor symmetry group $\mathrm{SU_A(N_f)}$ and a pseudo-scalar density for the field $\hat{\varphi}_i = \hat{\mathrm{P}}_b(0)$, we get

$$\begin{aligned}\left\langle 0 \left| \left[\hat{Q}_a^\mathrm{A}, \hat{\mathrm{P}}_b(0)\right] \right| 0 \right\rangle &= -i \left\langle 0 \left| \hat{\bar{\Psi}} \left\{\tau_a, \tau_b\right\} \hat{\Psi} \right| 0 \right\rangle \\ &= -i\frac{\delta_{ab}}{\mathrm{N_f}} \left\langle \bar{\Psi}\Psi \right\rangle - id_{abc} \left\langle 0 \left| \hat{\mathrm{S}}_c(0) \right| 0 \right\rangle \overset{m_\mathrm{q}\propto \mathbb{1}_\mathrm{D}}{=} -i\frac{\delta_{ab}}{\mathrm{N_f}} \left\langle \bar{\Psi}\Psi \right\rangle\end{aligned} \tag{2.35}$$

where we used the bilinear operator commutation relation in Eq. (B.6) and considered the flavor matrices $\tau_a = \lambda_a/2$ for the three quark flavors. For the last equality we have to mention that if we consider the limit $m_\mathrm{q} = m_\mathrm{q}^f \mathbb{1}_\mathrm{D}$, the symmetry under the flavor group $\mathrm{SU_V(N_f)}$ is exact, implying that the charge operator annihilates the vacuum $\hat{Q}_a^\mathrm{V} |0\rangle = 0$ (compare with the discussion in App. B.1). Since the non-singlet scalar condensate $if_{abc}\hat{\mathrm{S}}_c(x) = \left[\hat{Q}_a^\mathrm{V}, \hat{\mathrm{S}}_b(x)\right]$ is connected with the Noether charge operator $\hat{Q}_a^\mathrm{V}$ of the flavor group $\mathrm{SU_V(N_f)}$, all non-singlet scalar condensates $\left\langle 0 \left| \hat{\mathrm{S}}_c(0) \right| 0 \right\rangle$ must vanish.

Finally, from Eq. (2.35), we can deduce that (even) if we consider the chiral limit $m_\mathrm{q} = 0$ the flavor symmetry group $\mathrm{SU_A(N_f)}$ (and consequently the chiral symmetry too) is classically conserved but spontaneously broken by the quark condensate $\left\langle \bar{\Psi}\Psi \right\rangle$ which represents the transition probability of a right-handed quark to become a left-handed one and vice versa.[11] Note that the spontaneous symmetry breaking is also present for finite quark masses.

[11] In App. B.1, we discuss that the charge operator does not annihilate the vacuum in this case. Instead it produces another energy-degenerated vacuum state.

In our calculations, we will consider two different chiral symmetry observables: The dynamical quark mass and the quark condensate. The dynamical quark mass $\mathrm{M}_f(p) = \frac{\mathrm{B}_f(p)}{\mathrm{A}_f(p)}$ is a renormalization point invariant but not renormalization scheme invariant observable for the dynamical chiral symmetry breaking (DχSB) and depend on the scalar B_f and first vector A_f quark dressing function. The quark condensate, on the other hand, represents the transition probability of right-handed quarks to become left-handed quarks and vice versa and is defined by

$$\langle \hat{\bar{\Psi}}\hat{\Psi}\rangle_f(T,\mu_\mathrm{B}) = -Z_2^f Z_m^f \sum\!\!\!\!\!\!\int_q \mathrm{Tr}_\mathrm{DC}\left[S^f(q)\right] \tag{2.36}$$

with a Dirac and color trace. Since this property shows a quadratically divergent behavior proportional to the quark mass, we define a regularized quark condensate $\Delta_{\ell\mathrm{s}}$ by subtracting the primarily static quark condensate of a heavier quark[12] weighted by the corresponding mass ratio as shown by

$$\Delta_{\ell\mathrm{s}}(T,\mu_\mathrm{B}) = \langle \hat{\bar{\Psi}}\hat{\Psi}\rangle_\ell(T,\mu_\mathrm{B}) - \frac{m_\mathrm{B}^\ell}{m_\mathrm{B}^\mathrm{s}}\langle \hat{\bar{\Psi}}\hat{\Psi}\rangle_\mathrm{s}(T,\mu_\mathrm{B})\,. \tag{2.37}$$

Here $m_\mathrm{B}^f = Z_m^f m_\mathrm{q}^f$ is the bare quark mass of flavor f.

2.2. Truncation

As mentioned earlier, the DSEs represent an infinite tower of coupled integral equations and only if we solve this tower completely, the DSEs are equivalent to the generating functional. But in order to be able to solve it, we need truncations (approximations) rendering the infinite tower finite. Thereby, we have to chose the truncation carefully to conserve all important properties of the theory, e.g. the thermodynamic properties. The truncations are furthermore guided by symmetries, constrains and other methods, e.g. lattice QCD. In general, the truncation can be improved systematically by adding n-point Green functions order by order and using ansätze for the missing Green functions. In vacuum, this was done e.g. in Refs. [34, 84–88]. At finite temperature, however, the truncation does not have reached this level of sophistication.

In the following section, we will first introduce hadronic contributions in the quark-gluon vertex before we discuss the truncation of the non-hadronic part and the QCD phase diagram resulting from this non-hadronic part only. The truncation that will be presented hereinafter is mainly detailed in Ref. [44] but with more attention to the mesonic backcoupling in Refs [38, 89].

[12] For high masses the dynamic part is negligible relative to the static part.

2.2.1. Hadronic contributions in the quark-gluon vertex

In this section, we will take a closer look at the untruncated full quark-gluon vertex DSE shown in Fig. 2.1. We will express parts of the vertex by hadronic contributions and will introduce an approximation for the quark-gluon vertex based on the differentiation into hadronic and non-hadronic contributions.

Besides the tree-level term, the full quark-gluon vertex DSE contains three one-loop diagrams with fully dressed quark, ghost and gluon propagators running through the loop and connected to the external gluon by a corresponding bare vertex. It remains a gluonic two-loop diagram with a bare four gluon vertex. The one- and two-loop diagrams contain four- and five-point 1PI Green functions, which are expendable in skeleton diagrams with fully dressed internal 1PI propagators and vertices [72]. If we now consider the first non-trivial and Abelian diagram of the quark-gluon vertex DSE in Fig. 2.1 (first loop diagram indicated by a red blob and a dressed quark running through the loop[13]), we can re-express parts of the skeleton diagrams of the contained four-point quark vertex in a resonance expansion. If we do so for the lowest orders of this quark-antiquark scattering kernel, the Abelian diagram of the quark-gluon vertex DSE can be represented by Fig. 2.3 as discussed in Refs. [44, 56].

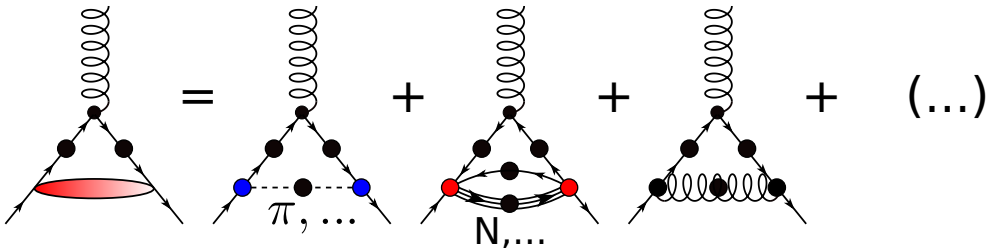

Figure 2.3.: Resonance expansion of the quark-antiquark scattering kernel in the Abelian diagram of the quark-gluon vertex in terms of Bethe-Salpeter and Faddeev-type vertices as well as propagators for mesons and baryons. Quark, gluon, meson and baryon propagators are denoted by solid, curly, dashed and triple lines, respectively. The intersection of two quarks and a gluon or a meson represents a quark-gluon or a Bethe-Salpeter vertex, respectively. The analogon for three quarks and a baryon is called Faddeev-type vertex. Dressed quantities are indicated by big colored dots. The remaining ones are bare. The arrows indicate the direction of the quark or baryon flavor and the momentum. Note that the upper vertex in all diagrams is bare. The shown expansion is adopted from Ref. [44]. The signs and prefactors are absorbed into the diagrams.

[13]The other non-trivial diagrams are non-Abelian.

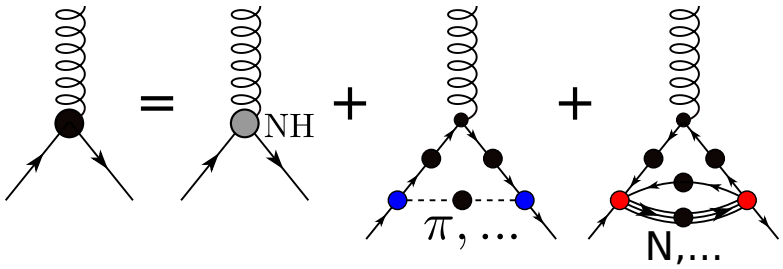

Figure 2.4.: Separation of the full quark-gluon vertex into non-hadronic contributions (first term) and lowest order hadronic contributions resulting from a resonance expansion of the quark-antiquark scattering kernel. The first term represents a summary of all non-hadronic contributions. Thereby the non-hadronic part is mostly given by pure Yang-Mills diagrams. For the hadronic contribution we consider an one-meson exchange (second term) and a baryon two-loop diagram (third term). The components are defined in the same way as in Fig. 2.3. The shown expansion is again adopted from Refs. [44].

The first and last contributions represent the off-shell one meson and one gluon exchanges between a quark and an antiquark. The second contribution is much more complicated since the off-shell baryon is included via a two loop diagram. In these diagrams, the mesons and baryons are no actual degrees of freedom but composite particles. They interact with their constituents via the Bethe-Salpeter and Faddeev-type vertices. Double counting of diagrams is easily avoided in this expansion due to the different quantum numbers of the hadrons. If we summarize all non-hadronic contributions of the quark-gluon vertex into one quantity and only consider the lowest order of the hadronic contributions, the full quark-gluon vertex then takes the form shown in Fig. 2.4. We assume the summary term of all non-hadronic contributions to consist basically of pure Yang-Mills diagrams since we expect the diagrams to be only mildly quark dependent. The hadronic terms then represent unquenching effects in form of the backcoupling of hadron degrees of freedom onto the quark-gluon interaction.[14]

In this work, we will not solve the quark-gluon vertex DSE, but instead we will insert the different parts of the vertex into the other considered equations (quark, gluon, mesons). Consequently, we will approximate the different parts of the vertex by solving them separately. This separation of the hadronic and non-hadronic parts can be motivated by two considerations: (i) a $1/N_c$-expansion and (ii) the tensor-structures to which the hadronic part in comparison to the non-hadronic

[14] Hadronic contributions in the quark-gluon vertex are generated by the inclusion of dynamical sea quarks in the quark-gluon interaction and are therefore only present in unquenched QCD.

part contributes. We discuss the effects of the Pion, since the other hadronic diagrams are suppressed by a factor $\Lambda_{\mathrm{QCD}}^2/m_{\mathrm{x}}^2$ relative to the Pion. The effects, however, are similar.

(i) If we consider a $1/\mathrm{N_c}$-expansion[15] of the quark-gluon vertex, the hadronic part contributes maximally to the next-to-leading order (NLO) corrections in the order of $\mathrm{O}(1/\mathrm{N_c})$. The leading order (LO) corrections result from the non-Abelian diagrams and are of the order of $\mathrm{O}(1)$. Since the hadronic terms are suppressed relative to the non-hadronic part we can motivate a separation of the two contributions.

(ii) In general, the quark-gluon vertex can be decomposed into twelve tensor-structures. See e.g. Ref. [92] for a basis decomposition. All these tensor-structures can be important in the intermediate momentum regime, as explored in lattice simulations in Ref. [93] and DSE calculations in Refs. [74, 94]. Ref. [56] shows that the one-Pion exchange diagram contributes to all of these tensor-structures. Our ansatz for the non-hadronic part of the quark-gluon vertex, on the other hand, is based on the leading vertex tensor-structure with a tree-level counterpart. Due to this different tensor structure decomposition necessary for the hadronic part, it makes sense to separate the two interactions in our calculation.

In the next section, an ansatz for the non-hadronic part of the quark-gluon vertex is introduced. In the remaining chapter and Sec. 4, we neglect the hadronic contributions and define and use two corresponding truncations. But in Sec. 5 we will introduce the one-meson exchange in addition to the non-hadronic part and discuss its implication. In Sec. 6, we do the same for the baryon.

2.2.2. Fischer-Maas-Müller model/ The non-hadronic part

For the full quark-gluon vertex, we now take only the first term in Fig. 2.4 into account and discuss a truncation for the remaining set of equations build upon i) a truncation of the gluon DSE and ii) an ansatz for the quark-gluon vertex. This truncation evolved from the quenched case [75, 76] to different numbers of backcoupled quark flavors [35–37]. Applications also exist for color superconductivity [95, 96]. An overview can be found in Ref. [17].

[15] The large $\mathrm{N_c}$ expansion originates from the Refs. [90, 91] and arranges the appearing diagrams in orders of the color number $\mathrm{N_c}$. For this purpose, the strong coupling constant g_{s} is replaced by $g_{\mathrm{s}}^0/\sqrt{\mathrm{N_c}}$, where g_{s}^0 is kept fixed. In Dyson-Schwinger diagrams, the $\mathrm{N_c}$-order can easily be determined by matching the color structure on the LHS and RHS of the equation, using the rules given in App. A.2 and exchanging the strong coupling constant as described before.

Table 2.1.: Temperature dependent fit parameter of the quenched gluon fit function shown in Eq. (2.38) below and above the transition temperature $T_c = 277\,\mathrm{MeV}$ for the quenched $\mathrm{SU_C(N_c)}$ theory. $t = T/T_c$ represents the reduced temperature.

Parameter	$t < 1$	$t > 1$
$a_L(T)$	$0.595 - 0.9025\,t + 0.4005\,t^2$	$3.6199\,t - 3.4835$
$a_T(T)$	$0.595 + 1.1010\,t^2$	$0.8505\,t - 0.2965$
$b_L(T)$	$1.355 - 0.5741\,t + 0.3287\,t^2$	$0.1131\,t + 0.9319$
$b_T(T)$	$1.355 + 0.5548\,t^2$	$0.4296\,t + 0.7103$

For the truncation of the gluon DSE, we use a temperature-dependent fit $D^{\mathrm{fit}}_{\mu\nu}(k)$ to quenched lattice data [76, 97] for the Yang-Mills diagrams $D^{\mathrm{YM}}_{\mu\nu}(k)$ indicated in Fig. 2.2 as gray dot with subscript YM. The quark-loop term $\Pi^{\mathrm{QL}}_{\mu\nu}(k)$ in this equation then leads to the unquenching of the gluon.[16] The fit function to the quenched gluon is given in terms of transversal and longitudinal gluon dressing functions (relation to gluon propagator in Eq. (2.30)) which are represented by

$$\mathrm{Z}^{\mathrm{fit}}_{\mathrm{T/L}}(k^2) = \frac{x}{(x+1)^2}\left[\left(\frac{\hat{c}}{x + a_{\mathrm{T/L}}(T)}\right)^{b_{\mathrm{T/L}}(T)} + x\left(\frac{\beta_0 \alpha_s}{4\pi}\ln(1+x)\right)^{\gamma}\right]. \quad (2.38)$$

In this fit function, we use the momentum variable $x = k^2/\Lambda^2$ together with the gluon momentum k. $\hat{c} = 5.87$ and $\Lambda = 1.4\,\mathrm{GeV}$ are temperature independent parameters and α_s is the running coupling defined in Sec. 2.1.2. The logarithmic term represents the perturbative running with the anomalous dimension of the quenched gluon $\gamma = \frac{-13\mathrm{N_c}+4\mathrm{N_f}}{22\mathrm{N_c}+4\mathrm{N_f}} \overset{\text{que.}}{=} -\frac{13}{22}$ at high momenta. It includes the leading-order coefficient of the beta function $\beta_0 = (11\mathrm{N_c} - 2\mathrm{N_f})/3 \overset{\text{que.}}{=} 11\mathrm{N_c}/3$. Since we consider a fit for a quenched gluon, $\mathrm{N_f}$ vanishes in these two parameters. The remaining temperature dependent fit parameters $a_{\mathrm{T/L}}(T)$ and $b_{\mathrm{T/L}}(T)$, appearing in the first term, are shown in Tab. 2.1.

Since we split the YM part and the quark-loop and calculate them separately, we neglect sub-leading (compared to quark loop) second order (in a $1/\mathrm{N_c}$ expansion) unquenching effects in YM diagrams. But due to the unquenching process of

[16] In the quenched case, the YM sector decouples from the matter sector and can be calculated without the knowledge of the quark. The quark, however, uses the quenched gluon as input. A quark or hadronic backcoupling onto the gluon leads to a coupling of the two sectors and unquenches the system of equations. Infinitely heavy quarks decouple from the YM part.

this truncation, we achieve a non-trivial coupling of different quark flavors and introduce implicit flavor, chemical potential and temperature dependencies to the quark and gluon. Consequently, we can state that the gluon is controlled by QCD dynamics instead of just modeling. Since the quenched gluon is chemical potential independent, the chemical potential dependence of the gluon only results from the quark loop.

For the considered dressed quark-gluon vertex $\Gamma^{\nu,h,f}_{\mathrm{qg}}(p,q,k)$, we use an infrared enhanced perturbative ansatz with a tensor structure which is guided by the Slavnov-Taylor identity. In previous works [36, 37, 44] the ansatz was fully determined by the construction

$$\begin{aligned}\Gamma^{\nu,h,f}_{\mathrm{qg}}(p,q,k) &= i g_{\mathrm{s}} t^h \tilde{Z}_3 \gamma^\nu \Gamma_{\mathrm{qg}}(x) \Gamma^f_{\mathrm{BC}}(p,q)\,,\\ \Gamma_{\mathrm{qg}}(x) &= \frac{d_1}{d_2 + x\Lambda^2} + \frac{x}{1+x}\left(\frac{\beta_0 \alpha_{\mathrm{s}}}{4\pi}\ln(1+x)\right)^{2\delta}\,,\\ \Gamma^f_{\mathrm{BC}}(p,q) &= (1-\delta_{\nu 4})\frac{\mathrm{A}_f(p)+\mathrm{A}_f(q)}{2} + \delta_{\nu 4}\frac{\mathrm{C}_f(p)+\mathrm{C}_f(q)}{2}\,.\end{aligned} \tag{2.39}$$

In this work, we will modify this construction, as will be shown in the next Sec. 2.2.3. In the following, we will, however, discuss the original construction. Except for $\Gamma^f_{\mathrm{BC}}(p,q)$ in the quark DSE, everything else is still valid for the modified construction.

In the self energy Σ of the quark DSE, the momentum variable x is represented by the gluon momentum $x = k^2/\Lambda^2$ whereas in the quark loop Π^{QL} of the gluon DSE it is defined via the sum over the squared quark momenta $x = (p^2+q^2)/\Lambda^2$. This distinction is necessary to maintain the multiplicative renormalizability of the gluon DSE [98]. $\beta_0 = (11\mathrm{N_c} - 2\mathrm{N_f})/3$ is again the leading-order coefficient of beta function and the temperature-independent parameters $d_2 = 0.5\,\mathrm{GeV}^2$ and $\Lambda = 1.4\,\mathrm{GeV}$ are fixed to match the scales in the quenched gluon propagator from the lattice. The only free parameter d_1 represents the effective infrared vertex interaction strength. We will discuss its fixing in Sec. 2.2.3. g_{s}, t^h, and $\tilde{Z}_3$ are defined in the same way as in Sec. 2.1.2.

Overall, $\Gamma_{\mathrm{qg}}(x)$ describes a phenomenological vertex dressing function ansatz capturing the well known perturbative running of the vertex at large momenta and parametrizing the non-perturbative enhancement at small momenta, which is known from explicit solutions of the vertex DSE in vacuum (see Refs. [34, 84] and references therein for more information). It accounts for non-Abelian effects and due to the second term, it describes the correct logarithmic running with the anomalous dimension of the vertex $2\delta = \frac{-9\mathrm{N_c}}{22\mathrm{N_c}-4\mathrm{N_f}}$. The first term is a phenomenological infrared ansatz with the two parameters d_1 and d_2.

$\Gamma^f_{\mathrm{BC}}(p,q)$ together with the Dirac matrix γ^ν represent the leading term of the Abelian Ball-Chiu vertex construction [99] in medium. We will refer to it as leading-order BC term. This term satisfies the Abelian Ward-Takahashi identity (WTI), which is used as approximation for the non-Abelian Slavnov-Taylor identity (STI). In App. B.4, we discuss the STI and the resulting construction in full glory. Due to the quark propagator in the leading-order BC term, a non-trivial temperature and chemical potential dependence is introduced into the vertex. This chemical potential and temperature dependence, however, is not sufficient. In Ref. [42], we studied the baryon number fluctuations and discussed the necessity of an improvement of the vertex truncation by using more terms of the Ball-Chiu vertex construction.

For a measure of this truncation concerning the gluon DSE and the quark-gluon vertex, we can discuss two different comparisons:

1. In vacuum, the comparison of this truncation with a more elaborated truncation in Ref. [98] where the quark, gluon and ghost are calculated explicitly, showed a difference below the five-percent level. Furthermore, the vertex dressing together with the gluon dressing fulfills the perturbative renormalization-group running at large momenta.

2. At finite temperature and vanishing chemical potential, the comparison of DSE results for an unquenched gluon [36, 45] with corresponding lattice results [100] showed very good agreement in the range of $5\% - 10\%$. The results are summarized and discussed in Ref. [17]. It is worth mentioning that the DSE results were published before the lattice results.

Due to the complexity of the calculation of fundamental particles and mesons, we now modify the vertex construction and introduce a further approximation.

2.2.3. Additional approximations

Because of (i) the numerical complexity of the additional study of mesons (in medium) and (ii) the calculation of gluons for finite chemical potential but vanishing temperature, we will introduce two additional approximations in this section.

The first approximation (i) concerns the tensor structure of the quark-gluon vertex. In Sec. 3.1.1, it will be discussed that the quark self energy has to fulfill the axial-vector Ward-Takahashi identity (AxWTI) to ensure the correct implementation of the chiral symmetry and its breaking in the bound state approach. This further implies that we have to chose between a Rainbow-Ladder like vertex in the quark DSE and a more complex bound state kernel construction. To keep the (medium)

bound state calculation simple and fast, we strive for a Rainbow-Ladder like vertex in the quark DSE. The discussion how the more complex bound state kernel is constructed is detailed in Sec. 3.1.1 and Ref. [82].

A Rainbow-Ladder like vertex means that the quark-gluon vertex construction in Eq. (2.39) should not depend on the quark propagator. For this purpose, we have to replace $\Gamma^f_{\mathrm{BC}}(p,q)$ by the quark wave-function renormalization constant Z_2^f. If we do so in the quark and gluon DSE, the calculation is no longer converging. The problem emerges in the quark loop, where $\Gamma^f_{\mathrm{BC}}(p,q)$ seems to have a stabilizing role. In Refs. [95, 96] the same calculation converged, but a Nambu-Gorkov formalism and another regularization of the gluon were used to calculate color superconductivity. The gluon regularization used in this work and the previous works mentioned above is detailed in App. C.1.1.

In this work, we want to keep contact to previous calculations as much as possible. Therefore, we introduce a quark-gluon vertex truncation which we will refer to as Hybrid (Hyb) truncation from now on. In this truncation, we replace $\Gamma^f_{\mathrm{BC}}(p,q) \to Z_2^f$ in the quark-gluon vertex construction (2.39) of the quark DSE together with an appropriate change of the vertex interaction strength $d_1 \to d_1^{\mathrm{q}}$ to compensate the missing interaction strength resulting from the omission of the quark dressing functions (d_2 and Λ remain unchanged). Consequently, we use a Rainbow-Ladder like vertex term

$$\Gamma^{\nu,h,f}_{\mathrm{qg}}(p,q,k) = ig_{\mathrm{s}}t^h Z_2^f \tilde{Z}_3 \gamma^\nu \tilde{\Gamma}_{\mathrm{qg}}(x) \tag{2.40}$$

with a modified vertex interaction strength in the quark DSE while we keep the full (leading-order BC) quark-gluon vertex construction as discussed in the previous section for the gluon DSE. This includes an unchanged vertex interaction strength d_1 in the gluon DSE. What unchanged means will become clear in the next section, where we discuss the parameter fixing of the truncation.

The second approximation (ii) concerns the tensor structure of the gluon propagator in case of vanishing temperatures and finite chemical potential. In this case, we neglect the chemical-potential dependence of the gluon (which results solely from the quark backcoupling) by setting the gluon propagator to its vacuum state.[17] This further implies that the quark flavors do not influence each other anymore. The reason is purely numerical and discussed in App. C.1.2. We use this approximation for first qualitative results but strive to improve upon it. To quantify the error, we will study the chemical potential dependency of the gluon at small temperatures and baryon chemical potentials up to 1 GeV in Sec. 2.2.4.

[17] Other works (see e.g. Refs. [101, 102]) used this approximation too, since the gluon is only implicitly chemical potential dependent through the quark in the quark loop.

Fixing parameters

In this section, we discuss the fixing of parameters for two truncations: The one used in previous works [42] without the additional approximations (1BC) and the one with those approximations (Hyb). We introduced the Hyb truncation with an 'unchanged' d_1 in the gluon vertex. Unchanged means that we use the d_1 value from the 1BC truncation as input for the Hyb truncation. Since we additionally determine the quark mass ratio between the light and strange quarks for both truncations by fixing the Pion and Kaon masses in the Hyb truncation, it is necessary to determine the trunaction and QCD parameters of both truncations simultaneously in an iterative procedure. This iterative procedure is shown in Fig. 2.5. The converged parameters for both truncations, i.e. the vertex strengths and quark masses, are shown in Tab. 2.2 together with the corresponding pseudocritical temperature at vanishing chemical potential. The resultant meson masses in vacuum are given in Tab. 3.3. In Fig. 2.6 we furthermore show the vacuum-normalized, regularized quark condensate results of both truncations compared to the corresponding continuum extrapolated lattice result for finite temperature and vanishing chemical potential.

At low temperatures, the results of both truncation are almost indistinguishable and within the error bars they agree well with the lattice results. For moderate temperatures, the slope of the lattice data is reproduced satisfactorily by both truncations. We have to emphasize that this is a non-trivial result since the parameter fixing only influences the pseudocritical temperature not the slope of our results. At high temperatures, however, the Hyb truncation produces slightly too large condensate values while the 1BC truncation shows good agreement with the lattice results. In the following, we will discuss that this behavior of the Hyb truncation is not connected to the additional approximations but is due to missing contributions in the quark-gluon vertex.

Table 2.2.: Vertex strength parameter(s) $d_1^{(\mathrm{q})}$, quark masses m_{q}^f, light-to-strange quark mass ratio $r_{\ell\mathrm{s}}$ and the pseudocritical temperature T_{pc} at vanishing chemical potential for the truncations 1BC and Hyb. The error of the pseudocritical temperature is purely numerical and its determination from the vacuum-normalized, regularized quark condensate is discussed in App. C.1.2.

	d_1^{q} [GeV^2]	d_1 [GeV^2]	m_{q}^{ℓ} [MeV]	$m_{\mathrm{q}}^{\mathrm{s}}$ [MeV]	$r_{\ell\mathrm{s}}$	T_{pc} [MeV]
1BC	8.49		0.80	20.6	25.7	156(1)
Hyb	12.85	8.49	1.47	37.8	25.7	155(1)

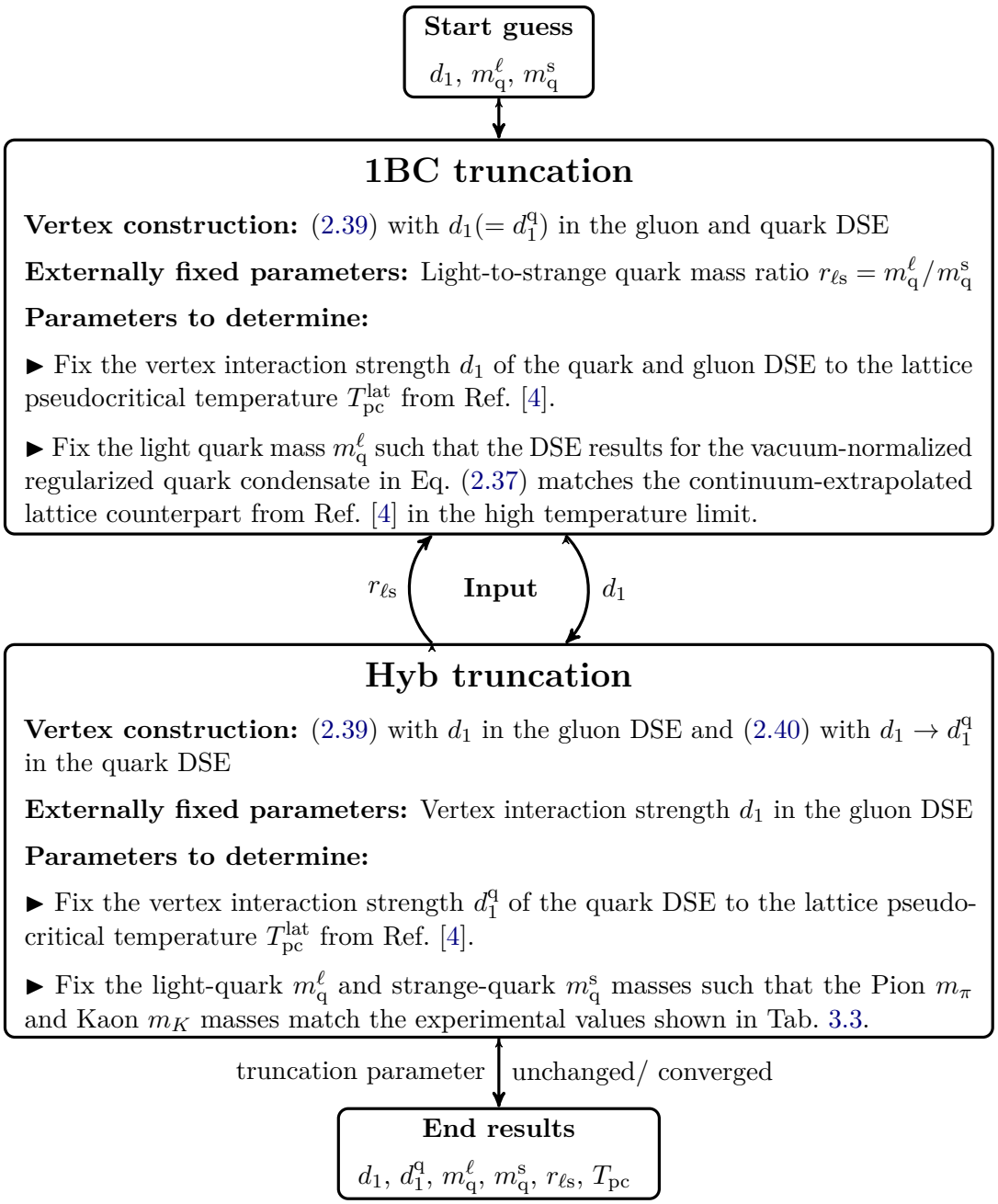

Figure 2.5.: Iterative procedure to fix the truncation parameters of the 1BC and Hyb truncations simultaneously. In this iterative procedure, we determine the parameters of the two truncations repeatedly with the input from the other truncation until the parameters of both truncations converged. For the lattice pseudocritical temperature we used the same value as in previous works [4] but values between 154.0 MeV and 157.0 MeV with errors between 1.5 MeV and 9.0 MeV are found in Refs. [4, 5, 103, 104].

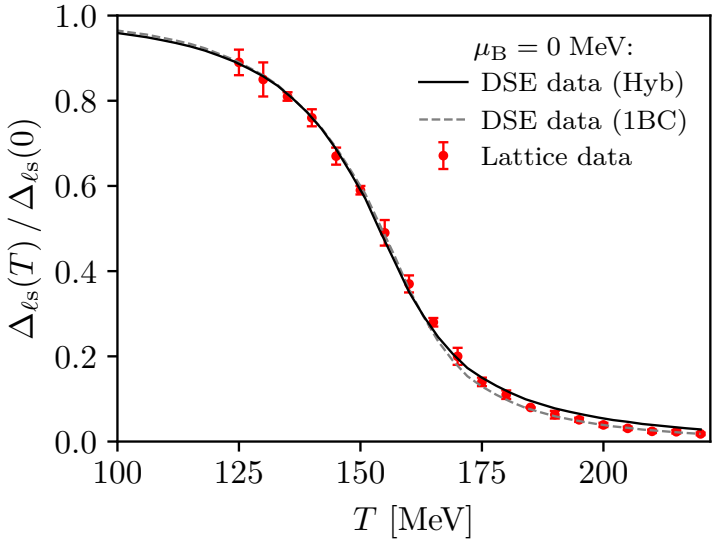

Figure 2.6.: Comparison of the vacuum-normalized regularized quark condensate (2.37) of the 1BC (dashed gray) [42] and Hyb (solid black) [105] DSE truncation with the corresponding continuum-extrapolated lattice results (solid red circles) from Ref. [4]. The results are considered at finite temperature and vanishing chemical potential.

First, it has to be mentioned that at high temperature the normalized regularized quark condensate is mainly controlled by the static part of the quark masses. Consequently, the overshooting of the Hyb truncation results from too high current quark masses. But where do these high quark masses come from? In this work, the quark masses in the 1BC truncation are fixed to the correct large temperature limit of the quark condensate (w.r.t lattice data) and therefore to the correct thermodynamics, while the quark masses of the Hyb truncation are fixed to reproduce the correct meson masses. Applying the latter fixing procedure to the 1BC truncation, too, we also observe the same overestimation of chiral symmetry breaking as shown in Ref. [37]. Consequently, it is reasonable to assume that the additional approximations do not lead to the observed overestimation of chiral symmetry breaking at high temperature. The reason, however, is an artifact of the Fischer-Maas-Müller truncation. More precisely, it is an artifact of the quark-gluon vertex ansatz since the gluon compares satisfactorily with the lattice results. Unfortunately, the artifact makes it impossible to describe meson properties and thermodynamics equally well at the same time.

In general, in the high-temperature phase, a vertex construction with more Ball-Chiu components is advisable. This is also visible in sensitive thermodynamic

observables like the baryon number fluctuations studied in Ref. [42], where we argued that terms reacting strongly on the chiral restoration (they are only present if chiral symmetry broken) are missing in the vertex ansatz. We guess that the simultaneous description of thermodynamics and meson properties will improve if we improve the used vertex construction.

Since we are mostly interested in describing mesons in medium in this work, we fix our quark masses to the meson masses and do not worry about the artifact. Next, it is interesting how the QCD phase diagram reacts on the modified interaction in the quark DSE.

2.2.4. QCD phase diagram

In this section, we will compare the chiral symmetry QCD phase diagram for the Hyb and 1BC truncation. The comparison is presented in Fig. 2.7. The 1BC truncation phase diagram was only calculated for a reduced chemical potential interval due to the necessary additional computational effort. In both truncations, we find a crossover at low chemical potential which becomes steeper and turns at the second-order critical endpoint (CEP) into a metastable phase. This metastable phase thereby represents a phase-coexistence area where the coexisting phases exist simultaneously but locally separated. This first-order coexistence region is defined by the area between the so-called Nambu-Goldstone and Wigner-Weyl first-order spinodals which are represented by the upper and lower strait line in Fig. 2.7, respectively. The physical first-order phase transition is located inside this coexistence region and has to be determined by thermodynamic considerations. In Ref. [43], the thermodynamic quantities of the 1BC truncation were evaluated and discussed, but due to the lack of lattice data for the pressure difference between the Nambu and Wigner phase, it is not possible to determine the physical first-order phase transition, yet.

The Nambu and Wigner spinodals are defined by two types of stable solutions of the quark DSE: The chirally broken (Nambu) and the chirally symmetric (Wigner) solution. A more detailed description can be found in Apps. B.1 and Sec. 2.1.4. For chemical potentials above the CEP, the appearance and disappearance of these solutions mark three regions in the plot: At low temperature and chemical potential, only the Nambu solution is found in the numerical iteration. The Wigner solution is also present but neither iteratively attractive nor thermodynamically favored. At high temperature and/or chemical potential, the Nambu solution disappears and the Wigner solution remains, now as the only stable solution. In between, there is an area where we find both solutions as stable solutions.[105] In the text above, we already indicated this area as metastable phase or coexistence

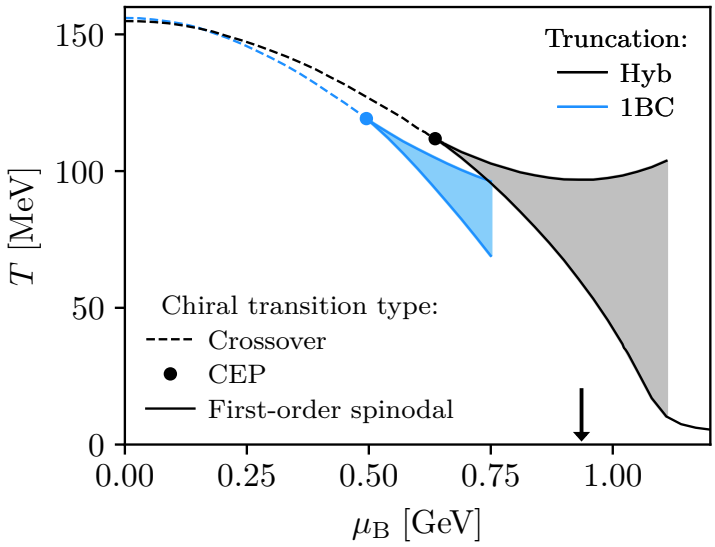

Figure 2.7.: Chiral symmetry QCD phase diagram for the Hyb (black) and 1BC (blue) truncation introduced in Sec. 2.2.3. Dashed lines correspond to crossover transitions while strait lines represent a first-order spinodal. The physical first-order phase transition happens in the coexistence region indicated by the shaded areas. The big dots show the location of the second order critical endpoint of the corresponding truncation. In case of the Hyb truncation, the arrow towards the chemical potential axis displays the zero-temperature limit of the Wigner spinodal. This point was calculated neglecting the chemical potential dependency of the gluon. More information can be found in the text. The transition lines are obtained from the inflection point of the quark condensate. More information to the definition and the determination of the (pseudo)critical temperatures can be found in App. C.1.2. For the calculation of both phase diagrams the strange quark chemical potential was set to $\mu_q^s = 0$ for comparability with previous results, e.g. Ref. [42]. The phase diagram was first published in Ref. [106].

region. The Nambu and Wigner spinodals are therefore defined by the chemical potential, temperature tuple of the upper and lower borders of the latter region. See Ref. [107] for a proper definition and Ref. [12] for a comprehensive introduction to the QCD phase diagram. More details and explanations on the appearance and disappearance of the different solutions in the quark DSE can be found in Refs. [57, 108, 109].

The phase diagram of the Hyb truncation resembles the one of the 1BC truncation but the CEP is shifted to higher chemical potentials. This is mainly due to the high

vertex interaction strength d_1^{q} value in the quark DSE and shows the necessity to carefully take all the temperature and chemical potential effects of the quark-gluon vertex into account. The corresponding critical endpoints (CEPs) of the two truncations are located at

$$\begin{aligned}(\mu_{\mathrm{B}}\,, T)^{\mathrm{CEP}}_{\mathrm{Hyb}} &= (636(1)\,, 111.9(1))\,\mathrm{MeV}\,,\\ (\mu_{\mathrm{B}}\,, T)^{\mathrm{CEP}}_{\mathrm{1BC}} &= (495(1)\,, 119.2(1))\,\mathrm{MeV}\,.\end{aligned} \tag{2.41}$$

The errors of the CEPs are purely numerical.[18] Another considerable feature of the phase diagram is the transition temperature $T_{\mathrm{pc}}(\mu_{\mathrm{B}})$ at low baryon chemical potentials μ_{B} which can be described by the expansion

$$\frac{T_{\mathrm{pc}}(\mu_{\mathrm{B}})}{T_{\mathrm{pc}}(0)} = 1 - \kappa \left(\frac{\mu_{\mathrm{B}}}{T_{\mathrm{pc}}(0)}\right)^2 + \lambda \left(\frac{\mu_{\mathrm{B}}}{T_{\mathrm{pc}}(0)}\right)^4 \tag{2.42}$$

and represents the curvature of the chiral phase boundary at low chemical potential. With the corresponding pseudocritical temperature values at vanishing chemical potential $T_{\mathrm{pc}}(0)$ shown in Tab. 2.2, we obtain the associated curvature coefficients

$$\begin{aligned}\kappa_{\mathrm{Hyb}} &= 0.017331\,, \quad \lambda_{\mathrm{Hyb}} = -0.000796\,,\\ \kappa_{\mathrm{1BC}} &= 0.024626\,, \quad \lambda_{\mathrm{1BC}} = -0.000532\end{aligned} \tag{2.43}$$

by fitting the expansion up to a baryon chemical potential of $\mu_{\mathrm{B}} = 240\,\mathrm{MeV}$. In comparison to FRG [47] ($\kappa = 0.0142(2)$) and extrapolated lattice results [104, 110, 111] ($\kappa = 0.0144(26) - 0.0153(18)$) as well as results for a FRG-DSE combined framework [48, 49] ($\kappa = 0.0147(5) - 0.0150(7)$), the curvatures of both truncations are too high. But interestingly, the less consistent Hyb truncation is closer to the $\mathrm{N_f} = 2 + 1$ curvature values of FRG, lattice and the FRG-DSE combined framework. Also, for the CEP, we find a better agreement to the FRG and FRG-DSE combined framework when considering the Hyb truncation instead of the 1BC truncation. We expect that this is due to missing effects in the quark-gluon vertex, e.g. further Ball-Chiu terms. In the following, we will mention some other possible optimizations of the calculation before we will do a quality check of the Hyb truncation.

So far, we did not include the hadronic backcoupling as introduced in Sec. 2.2.1. This can possibly improve the agreement with the extrapolated lattice results and will be done in Chaps. 5 and 6. Eventually, in Chap. 5, we will discuss the

[18] An estimation of the systematic error due to truncation assumptions could be done by the comparison with other truncations, e.g. the combined framework of the functional renormalization-group (FRG) together with DSE in Ref. [49].

influence of mesonic backcoupling on the QCD phase diagram, the location of the CEP and the curvature. In Ref. [44], this was already done for the baryonic backcoupling effects but in a simplified manner. As we will, unfortunately, see later, both effects improve the agreement with the lattice extrapolations only marginally. But the description of the respective backcoupling can and should still be improved. Another possibility to improve the phase diagram and the agreement of the curvature in a future work is the introduction of a backcoupled background gauge field. This further allows us to simultaneously investigate the confinement via the Polyakov loop potential. See e.g. Ref. [112] for the determination of the Polyakov loop potential from a background gluon field in the FRG and DSE approach and Refs. [113, 114] for basics to the background gluon field.

Quality check of the truncation

In this section, we will mainly discuss the Hyb truncation results, but in preliminary calculations with slightly modified numerics we found indications for a similar behavior for the coexistence lines of the 1BC truncation. At first, we will consider the flaws of the QCD phase diagram, before we discuss the validity of the second approximation (vacuum gluon approximation).

Considering the QCD phase diagram for chiral symmetry in Fig. 2.7, we observe problems with the spinodals of the Hyb truncation. At high chemical potential, we find a saturation of the Nambu and Wigner spinodal and a subsequent unphysical increase of the Nambu spinodal. Additionally, there is no intersection with the chemical potential axis. At this point, we have to note that for such high chemical potentials and low temperatures, the truncation and calculation method neglects color-superconducting phases and effects. To include them, a Nambu-Gorkov formalism would be necessary. See Refs. [95, 96] for studies of the super-conducting phases using the Nambu-Gorkov formalism. We infer that we cannot apply the two truncations presented in previous sections in this region of phase diagram, also because we expect the numerical calculation to break down in this area of the phase diagram.

Furthermore, the arrow in the figure shows the zero-temperature limit of the Wigner spinodal from the Hyb truncation which is located at $\mu_{\mathrm{B}}^{\mathrm{W},\ell} = 936\,\mathrm{MeV}$. This value is calculated on the chemical potential axis with zero temperature implying that the second approximation (the neglect of the chemical potential dependency of the gluon by using the vacuum gluon) in Sec. 2.2.3 becomes important. In Sec. 4.2, we will discuss the zero-temperature limit of the quark condensate and the corresponding Nambu and Wigner solutions in more detail. If we extrapolate the finite temperature Wigner solution to zero temperature using only the data before

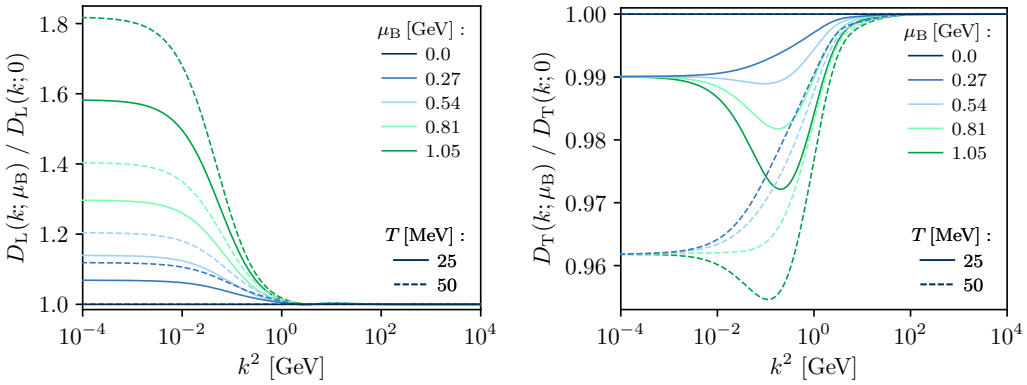

Figure 2.8.: Vacuum normalized longitudinal (left) and transversal (right) gluon propagator $D_{\mathrm{L/T}}(k) = \mathrm{Z}_{\mathrm{L/T}}(k)/k^2$ plotted against the gluon four momentum for different chemical potentials (colors) and temperatures (line-styles). The results are calculated with the Hyb truncation.

saturation takes place, we find a 20 % higher value for the zero-temperature limit of the Wigner spinodal as compared to the calculation on the chemical potential axis. As already mentioned in the last section, the calculation on the chemical potential axis differs from the finite temperature calculation since we use the second (vacuum gluon) approximation from Sec. 2.2.3. Now, there are two possible explanations for the deviation of the Wigner spinodal on the chemical potential axis calculated with the finite temperature and chemical potential method. 1.) The vacuum gluon approximation in this phase diagram area is too strong or 2.) the finite temperature results can not be trusted in an certain area also before saturation. To test the vacuum gluon approximation, we consider the chemical potential dependence of the gluon propagator for two low temperatures.[19] The results are shown in Fig 2.8.

At high momenta, the medium gluon propagators equal the vacuum one. We consequently observe a vanishing chemical potential and temperature dependence for both propagators. For low and moderate momenta, however, the figure shows an increasing behavior for increasing temperature and/or chemical potential. This increase is much more pronounced in the longitudinal gluon propagator than in the transversal one. For chemical potentials up to 1.05 GeV and vanishing temperatures, we expect a maximal change over whole momentum range of 50% and 2% for the longitudinal and transversal gluon propagator, respectively.

[19] We use two temperatures to be able to expect the behavior of the gluon propagator for vanishing temperature. The effect of using a vacuum gluon instead of a medium gluon in the DSE calculation is also discussed in Ref. [115].

To go into more detail, we consider the different contributions to the gluon propagator. The gluon propagator is constructed from the chemical potential independent Yang-Mills part $D_{\mu\nu}^{\mathrm{YM}}$ and the quark loop Π^{QL}. The quark loop itself can be decomposed in a regular part $\tilde{\Pi}^{\mathrm{QL}}$ and a screening mass m^{sc} as discussed in App. C.1.1. The regular part of the quark loop shows a maximal change of 5% up to a chemical potential of 1.05 GeV for the transversal and longitudinal part. Consequently, the regular part has to play a sub-leading role for the chemical potential dependence of the longitudinal gluon propagator. The dominant medium effect of the gluon propagator results from the screening mass m^{sc}.

Since the transversal screening mass or Meissner mass $m_{\mathrm{M}}^{\mathrm{sc}}$ is zero in our calculation[20], the transversal gluon propagator is only weakly chemical potential dependent. The longitudinal screening mass or Debye mass $m_{\mathrm{D}}^{\mathrm{sc}}$ has a much stronger influence. It decreases for decreasing temperatures at low chemical potential and should vanish for vanishing temperatures. In our calculation, however, the screening mass becomes negative above a certain chemical potential (also for non-vanishing but low temperatures) which is unphysical and an artifact of our truncation. This behavior is applicable to 1BC calculations, too.

As we can see, the treatment of the gluon propagator at finite chemical potential and vanishing temperatures has to be improved in future works. The same is true for the appearing negative screening masses. In this work, we will, however, keep the vacuum gluon approximation due to the numerical complexity of the calculation and the high computational runtime experienced otherwise.

[20] The Meisner mass can become non-zero in color-superconducting phase if we use the Nambu-Gorkov formalism.

3. Mesonic bound states in QCD

In the last chapter, we discussed the properties of the fundamental particles of QCD: the quarks and gluons. In nature, these particles do not exist as free particles due to their own color structure and the color confinement. Only hadrons as color-neutral bound states of quarks and gluons which interact via the strong interaction appear as observable particles. Thereby, we define physical particles as irreducible representations of the Poincaré group with fixed quantum numbers such as spin, parity, mass, flavor. Using these quantum numbers we can categorize the observable (composite) particles via

(i) the classes of bound states (mesons, baryons, glueballs, tetraquarks, ...) which result from the requirement of a color singlet state,

(ii) the quantum numbers[1] J^{PC} of the invariant subspace of the Poincaré group with the total spin of the meson J, the parity P and the charge conjugation parity C and

(iii) the quark flavor content.

In this chapter, we consider the important features of mesons as bound states of quarks and antiquarks described by the Dyson-Schwinger approach in vacuum and medium. More specifically, we will consider scalar (S), pseudo-scalar (PS), vector (V) and axial-vector (AV) mesons with the quantum numbers $J^{\mathrm{PC}} = 0^{-+}$, 0^{++}, 1^{--} and 1^{++}, respectively. Now only the flavor content remains to be discussed.

A practical classification scheme for composite particles of QCD according to the quark flavor content is the constituent quark model introduced by Gell-Mann and Zweig in Refs. [116, 117]. In App. B.3, we take this model into account considering the global flavor transformations of the flavor symmetry groups $\mathrm{U_V}(1) \times \mathrm{SU_V}(\mathrm{N_f}) \times \mathrm{SU_A}(\mathrm{N_f}) \times \mathrm{U_A}(1)$ and derive flavor and baryon numbers as conserved quantum numbers. These can be used to derive the meson multiples shown in Fig. 3.1.

In this work, we will concentrate on Pion, Kaon, Sigma/ f_0, Rho, Phi and a_1 mesons. Since we use the isospin-symmetric limit of equal up- and down-quark

[1] See App. B.2.2 for more information to the irreducible representations and the transformations of the Poincaré group and App. B.2.3 for more information of the discrete symmetries of parity, time-reversal and charge-conjugation.

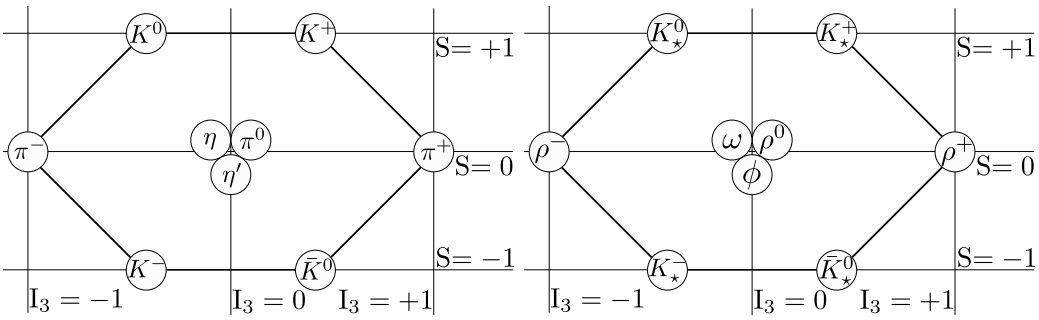

Figure 3.1.: Graphical notation of the pseudo-scalar ($J^{\mathrm{P}} = 0^-$, left) and vector ($J^{\mathrm{P}} = 1^-$, right) mesons in so-called multiplets showing their strangeness S and isospin I_3 quantum numbers. The representation of the mesons in flavor space can be found in App. A.3.

masses and neglect the electromagnetic interaction, there is no further distinction[2] between the charged and uncharged Pions. The same holds for the Rho mesons. In addition, due to the use of a Rainbow-Ladder interaction we also do not distinguish between isoscalar (ω/η) and isovector (ρ/π) mesons.

In the following, we will introduce the Bethe-Salpeter framework and derive the (on-shell) equations necessary to describe the mesonic bound states. Then, we will show the features of their solutions. In the end, we will conclude by discussing general properties of the meson bound states. Thereby, we will pay special attention to the modifications resulting from the introduction of the medium.

3.1. Bethe-Salpeter framework

The Bethe-Salpeter framework is a functional method to calculate bound states consisting of a quark and an antiquark based on their quantum equations of motion, the so-called Bethe-Salpeter equations (BSEs). For this purpose, we need the Green functions of the constituents as input. Analog to the fundamental particles, we can derive the quantum equations of motion of the bound states from the generating functional using two-particle irreducibiliy (2PI).[3] Since the procedure is quite similar, we will only mention the most important relations.

[2] No distinction means that the mesons are identical up to their flavor structure and are therefore calculated in the same way. This is due to the fact that the flavor structure is not important for the bound state wave-function calculation as we will see later on.

[3] Cutting two internal lines does not disconnect a 2PI diagram.

3.1.1. Derivation

To start the derivation, we express the effective action defined in Eq. (2.6) by bilocal sources $J^{[2]}(x,y)$ and fields $\tilde{\varphi}^{[2]}(x,y)$ depending on two space-time points and get the 2PI version of the effective action $\Gamma^{[2]}[\tilde{\varphi}^{[2]}]$. We use the upper index $'[2]'$ here and further on to indicate the 2PI nature of a variable. For a vanishing bilocal source $J^{[2]}(x,y)$ the conjugate bilocal field $\tilde{\varphi}^{[2]}(x,y)$ corresponds to the 1PI two-point Green function or propagator $G_2(x,y) = \tilde{\varphi}^{[2]}(x,y)\Big|_{J^{[2]}(x,y)\to 0}$. The related bilocally connected 2PI two-point Green function $G_2^{[2]} = \left(\frac{\delta^2\Gamma^{[2]}[\tilde{\varphi}^{[2]}]}{\delta\tilde{\varphi}^{[2]}\delta\tilde{\varphi}^{[2]}}\right)^{-1}\Big|_{\tilde{\varphi}^{[2]}\to G_2}$ represents the propagator of a particle pair. In the following we are interested in bound states consisting of quarks. Consequently, we only need the quark part of the 2PI effective action. In Ref. [118] this part was determined and for Green functions evaluated at the stationary point ($\frac{\delta\Gamma^{[2]}[S]}{\delta S} = 0$) it can be written as:

$$\Gamma^{[2]}[S] = \mathrm{Tr}_{\mathcal{F}} \log S^{-1} - \mathrm{Tr}_{\mathcal{F}}\left[\mathbb{1} - S_0^{-1}S\right] + \Gamma^{[2]}_{\mathrm{Int}}[S] \tag{3.1}$$

where S and S_0 are the dressed and bare quark propagators with suppressed quark flavor, color, Dirac and momentum dependence. $\mathrm{Tr}_{\mathcal{F}}$ represents a trace in the functional sense, which means that we trace over the flavor, color and Dirac indices as well as the momentum space. The considered interaction part of the 2PI effective action $\Gamma^{[2]}_{\mathrm{Int}}[S]$ contains all 2PI diagrams w.r.t. the quark propagator S. Analog to the 1PI version, we can now derive all 2PI n-point Green functions from the 2PI effective action by applying functional derivatives w.r.t. the bilocal source and subsequently setting this source to zero similar as shown in Eq. (2.2). If we use the effective action shown in Eq. (3.1) for this procedure, we get the expression

$$\left(G^{[2]}_{2,S}\right)^{-1} = \frac{\delta^2\Gamma^{[2]}[S]}{\delta S\delta S} = S^{-1}S^{-1} + \underbrace{\frac{\delta^2\Gamma^{[2]}_{\mathrm{Int}}[S]}{\delta S\delta S}}_{=:-K} \tag{3.2}$$

for the 2PI two-point Green function or propagator $G^{[2]}_{2,S}$ with quark content. By reshuffling this relation, we obtain the bound state equation of motion

$$G^{[2]}_{2,S} = SS + SSKG^{[2]}_{2,S}\,. \tag{3.3}$$

Strictly speaking the derivation of this equation is only valid for equal quark and antiquark flavor but it can be extended for different flavors as discussed in [118]. If we introduce the 'inhomogeneous' Bethe-Salpeter amplitude $\tilde{\Gamma} = S^{-1}S^{-1}G^{[2]}_{2,S}\Gamma_0$ with the renormalized vertex Γ_0 (see Eq. (B.2) with renormalization constants), we can again rewrite this equation to a general quark-antiquark-meson-vertex

connecting a quark and an antiquark to a color-singlet meson-current channel. We obtain the so-called inhomogeneous Bethe-Salpeter equation

$$\tilde{\Gamma} = \Gamma_0 + KSS\tilde{\Gamma} \tag{3.4}$$

which entails all off-shell information and the pole structure of the Green function $G^{[2]}_{2,S}$. The included BSE kernel K resulting from the interacting part of the 2PI effective action $\Gamma^{[2]}_{\text{Int}}[S]$ is given by[4]

$$\begin{aligned} K^f_{\alpha\beta,\gamma\delta}(p,q,P) = & -\frac{\delta^2\Gamma^{[2]}_{\text{Int}}[S]}{\delta[S^f(q)]_{\beta\delta}\delta[S^f(p)]_{\alpha\gamma}} = -\frac{\delta[\Sigma^f[S](p)]_{\alpha\gamma}}{\delta[S^f(q)]_{\beta\delta}} \\ & \stackrel{!}{=} [\Gamma^{f,\epsilon,h}_{\text{qg},0}]_{\alpha\beta} D_{\nu\epsilon}(k) [\tilde{\Gamma}^{f,\nu,h}_{\text{qg}}(p,q,k)]_{\gamma\delta} \,. \end{aligned} \tag{3.5}$$

Here we used the momentum routing $k = p - q$ and the super-indices α, β, γ and δ to summarize the color, flavor and Dirac structure. The second line is derived similarly as in Ref. [56] and results from our truncation. Consequently, it is not valid in general. In addition to the connection between the quark self energy and the BSE kernel shown in this equation, the two quantities Σ and K have to fulfill the non-singlet axial-vector-Ward-Takahashi identity (AxWTI) in chiral limit [119] (see App. B.4 for a derivation). A possible notation for this AxWTI is

$$\left\{\gamma_5\Sigma^f(p_-) + \Sigma^f(p_+)\gamma_5\right\}_{\alpha\delta} = -\int_q K^f_{\alpha\beta,\gamma\delta}(p,q,P)\left\{\gamma_5 S^f(p_-) + S^f(p_+)\gamma_5\right\}_{\beta\gamma} . \tag{3.6}$$

By relating the quark self energy and the quark-antiquark scattering kernel, this identity ensures the correct implementation of chiral symmetry and its dynamical breaking in the bound state approach. It ensures that the Pion as Goldstone Boson[5] is mass-less in chiral limit enforcing a binding energy of the pseudo-scalar mesons which exactly cancel the quark and antiquark masses.

To avoid a complicated calculation of the meson, especially in medium, we want to be able to write the kernel in form of the second line in Eq. (3.5) without any additional term but fulfilling the AxWTI at the same time. Due to the discussed connection between the quark self energy $\Sigma^f(p)$ and the BSE kernel K, this is only possible if the quark-gluon vertex $\tilde{\Gamma}^{f,\nu,h}_{\text{qg}}(p,q,k)$ in the quark DSE does not

[4] In the 2PI approach the quark self energy results from the effective action via $\Sigma^f(p) = \delta\Gamma^{[2]}_{\text{Int}}[S]/\delta S^f(p)$.

[5] The dichotomous nature of the Pions as almost mass-less (pseudo) Goldstone Bosons and bound state of massive quarks is discussed from first principles in Ref. [31]. More information about the Goldstone theorem and the BSE properties under the chiral symmetry can be found in Refs. [120, 121].

depend on the quark propagator at the momenta p and q. The simplest way to achieve this property is to use a Rainbow-Ladder(-like) truncation for the quark-gluon vertex in the quark DSE. Indeed, the truncation discussed in Sec. 2.2.3 was intentionally constructed such that we can describe the BSE kernel by the second line in Eq. (3.6) and we see that the AxWTI is fulfilled. As a result, we use the same one-gluon exchange interaction and especially the same dressed quark-gluon vertex $\tilde{\Gamma}^{f,\nu,h}_{\mathrm{qg}}(p,q,k)$ in the BSE as applied in the quark DSE.

If we want to go beyond the Rainbow-Ladder(-like) truncation in the interaction of the quark DSE and meson BSE, e.g. by including further terms of the Ball-Chiu vertex in Eq. (B.34), we can no longer express the kernel via the second line of Eq. (3.5). The introduction of the first two terms of the Ball-Chiu vertex leads to a further term in the BSE kernel, where we take the functional derivative of the quark-gluon vertex w.r.t. the quark propagator in the quark self energy into account: $\int_l [\gamma_\mu S(l)]_{\alpha\epsilon} \frac{\delta[\Gamma^\nu_{\mathrm{qg}}(l,p)]_{\epsilon\gamma}}{\delta[S(q)]_{\beta\delta}} D_{\mu\nu}(l-p)$. The AxWTI remains fulfilled. Adding the third Ball-Chiu vertex, too, is only possible via the method explained in Ref. [82]. The functional derivative of the gluon w.r.t. the quark propagator is neglected here because its dependence is only implicit.

Next we want to describe a meson bound state x of mass m_{x} and total momentum P at the on-shell momentum $P^2 = -m_{\mathrm{x}}^2$. For this purpose we derive the on-shell analogon to Eq. (3.4), the so-called homogeneous Bethe-Salpeter equation (hBSE). To keep the chapter concise we will only mention the most important relations while the detailed derivations are shifted to App. C.2.1. There, we use the fact that hadrons produce poles in QCD Green functions, scattering amplitudes and cross sections. As result, by inserting a complete set of hadron eigenstates we can express the 2PI two-point Green function in the pole representation

$$G^{[2]}_{2,S}(P,p,l) = \sum_{\mathrm{x}} \frac{i\chi^\alpha_{\mathrm{x}}(P,p)\bar{\chi}^\alpha_{\mathrm{x}}(-P,l)}{P^2 + m_{\mathrm{x}}^2 + i\epsilon} + R(P,p,l) \tag{3.7}$$

where we sum over the different pole contributions of the various bound states. The second term $R(P,p,l)$ on the other hand is regular. The individual pole terms resemble a free propagator multiplied with a bound state wave-function $\chi^\alpha_{\mathrm{x}}(P,p)$ and its charge conjugated equivalent $\bar{\chi}^\alpha_{\mathrm{x}}(P,p) = \left[C\chi^\alpha_{\mathrm{x}}(P,-p)C^{-1}\right]^\top$.[6] These wave-functions are defined via

$$\chi^\alpha_{\mathrm{x}}(P,x_1,x_2) := \left\langle 0 \left| \hat{T}\left\{\hat{\bar{\Psi}}(x_1)\hat{\Psi}(x_2)\right\} \right| P,\mathrm{x},\alpha \right\rangle \overset{\mathrm{U}_\Lambda(\mathbb{1}_{\mathrm{D}},X)}{=} e^{-iPX}\chi^\alpha_{\mathrm{x}}(P,x) \tag{3.8}$$

and represent the transition probability of a quark-antiquark-system $\left\langle \bar{\Psi}\Psi \right|$ to turn into an on-shell meson bound state $|P,\mathrm{x},\alpha\rangle$ with momentum P, hadron type x

[6] $C = \gamma_2\gamma_4$ is the charge-conjugation matrix and the superscript $\top$ denotes a matrix transpose.

and further quantum numbers which we summarize by α. The second equality results from the invariance under Poincaré translation $\mathrm{U}_\Lambda(\mathbb{1}_\mathrm{D}, X)$ with $X = \frac{x_1+x_2}{2}$ and $x = x_1 - x_2$ (see Eq. (B.14) for the definition of Poincaré transformations onto specific states). In the pole representation the Fourier transformed wave-functions depend on the total momentum of the meson P and the relative momentum between the two constituents p or l. If we now insert the pole representation of the 2PI two-point Green function into Eq. (3.3) and compare the residues for a specific meson x we get the homogeneous Bethe-Salpeter equation (hBSE)

$$S^{-1}(p_+)\chi^\alpha_\mathrm{x}(P,p)S^{-1}(p_-) = \int_q K(p,q,P)\chi^\alpha_\mathrm{x}(P,q) \tag{3.9}$$

for the Bethe-Salpeter wave-functions

$$\chi^\alpha_\mathrm{x}(P,p) = S(p_+)\Gamma^\alpha_\mathrm{x}(P,p)S(p_-)\,. \tag{3.10}$$

Here, $\Gamma^\alpha_\mathrm{x}(P,p)$ is the Bethe-Salpeter amplitude (BSA). In the next sections we will reformulate the hBSE for this amplitude and will discuss its properties under discrete symmetries and in medium.

3.1.2. Homogeneous Bethe-Salpeter equation

In full glory, the general hBSE for different spin-parity-states is given by

$$\Gamma^{(\mu)}_{\mathrm{x},e}(P,p) = \int_q \Gamma^{\epsilon,h}_{\mathrm{qg},0} S(q_+)\Gamma^{(\mu)}_{\mathrm{x},\tilde{e}}(P,q)\,S(q_-)\Gamma^{\nu,h}_{\mathrm{qg}}(p,q,k)\,D_{\nu\epsilon}(k) \tag{3.11}$$

or in a graphical representation as shown in Fig. 3.2. We again use the integral abbreviation $\int_q = \int \frac{d^4q}{(2\pi)^4}$ and represent the bosonic total momentum of the meson by P. The fermionic relative momenta between the quark and the antiquark are denoted by p externally and q inside the loop. We furthermore use the momentum routing $k = q - p$ for the gluon momentum which enters the dressed gluon propagator $D_{\nu\epsilon}$ from Eq. (2.20) and the dressed quark-gluon vertex of the quark flavor f. Since we use the Hyb truncation from Sec. 2.2.3 for the vertex, we can write the dressed quark-gluon vertex via $\Gamma^{f,\nu,h}_{\mathrm{qg}}(p,q,k) = ig_\mathrm{s}\tilde{Z}_3 Z_2^f \gamma^\nu t^h \Gamma(k^2)$. The bare equivalent is again defined via $\Gamma^{f,\epsilon,h}_{\mathrm{qg},0} = ig_\mathrm{s} Z_{1\mathrm{F}}^f \gamma^\epsilon t^h$. In these expressions g_s, $Z_{1\mathrm{F}}^f$ and Z_2^f are the strong coupling constant, the quark-gluon vertex and quark wave-function renormalization constants for the quark flavor f, respectively. They are defined in Sec. 2.1.2. The Dirac γ_μ and color matrices t^h definitions along with useful relations can be found in the Apps. A.1 and A.2, respectively.

The dressed quark propagator in flavor space is given by $S = \mathrm{diag}\left(S^\mathrm{u}, S^\mathrm{d}, \ldots\right)$ with the individual quark flavor propagators defined in Eq. (2.19). Since we use the

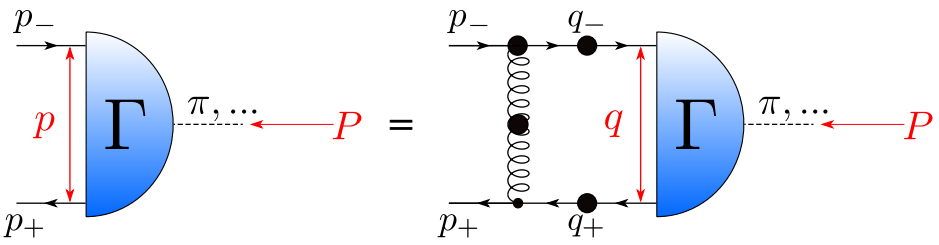

Figure 3.2.: Graphical representation of the homogeneous Bethe-Salpeter equation with the appropriate momentum routing. The blue quantity is called the quark-antiquark-meson vertex or Bethe-Salpeter amplitude. While quark propagators are denoted as solid lines, gluon propagators are represented as curly lines. The intersection of quark and gluon lines are quark-gluon vertices. Dressed quantities are marked by big dots. The remaining quantities are bare.

isospin-symmetric limit $S^{\mathrm{u}} = S^{\mathrm{d}}$. In the hBSE, the dressed quark propagators need to be evaluated at the complex momenta $q_\pm = q \pm \eta_\pm P$. See App. C.1.3 for more information regarding the calculation of quarks at complex momenta. The included momentum partitioning parameters $0 \leq \eta_\pm \leq 1$ fulfill the relation $\eta_+ + \eta_- = 1$. In general, P satisfies the on-shell condition $P^2 = [i(m_{\mathrm{x}} \pm i\Gamma^{\mathrm{x}}_{\mathrm{w}}/2)]^2$ with the mass m_{x} and the width $\Gamma^{\mathrm{x}}_{\mathrm{w}}$ of the meson x [122]. In this work, we do not consider resonances. Consequently, the width is zero and P is a purely imaginary time-like momentum. Since we furthermore consider all mesons to be in rest frame $P = (\vec{0}, im_{\mathrm{x}})$.[7] More technical details can be found in App. C.2 and Ref. [123]. Now, it only remains to discuss the Bethe-Salpeter amplitude (BSA) or quark-antiquark-meson vertex amplitude $\Gamma^{(\mu)}_{\mathrm{x},e}$. This will be done in more detail in the following.

Bethe-Salpeter amplitude

To calculate the Bethe-Salpeter amplitudes for all considered meson kinds, we use the Dirac tensor structure decomposition

$$\Gamma^{(\mu)}_{\mathrm{x},e}(P,p) = \begin{cases} \sum_i f^i_{\mathrm{x}}(P,p) \quad \tau^{(\mu)}_i(P,p) \otimes \mathbb{1}_{\mathrm{C}} \otimes r^e_{\mathrm{x}} & \text{for } J^{\mathrm{P}} = 0^+, 1^- \\ \sum_i f^i_{\mathrm{x}}(P,p)\gamma_5 \tau^{(\mu)}_i(P,p) \otimes \mathbb{1}_{\mathrm{C}} \otimes r^e_{\mathrm{x}} & \text{for } J^{\mathrm{P}} = 0^-, 1^+ \end{cases} \tag{3.12}$$

where the dressing function $f^i_{\mathrm{x}}(P,p)$ of the i^{th} Dirac covariant $\tau^{(\mu)}_i(P,p)$ entails the non-perturbative momentum dependence. Throughout the whole work, we use the meson type index x to indicate a specific degenerated meson flavor $\mathrm{x} \in$

[7] Going beyond the rest frame assumption (in vacuum and medium) is connected with some difficulties. See App. C.2.4 for more information.

$\{\pi, K, \bar{K}, \sigma/f_0, \rho, \phi, a_1\}$ or an invariant subspace of the multiple hadrons, e.g. the spin-parity-states $\mathrm{x} \in \{\mathrm{S}, \mathrm{PS}, \mathrm{V}, \mathrm{AV}\}$. e furthermore represents the meson "flavor" index and is connected to the flavor matrix r^e_{x} which entails the quark content and is defined in App. A.3.

To define the Dirac covariants $\tau_i^{(\mu)}(P,p)$, we first have to consider the Dirac structure of a general vertex. This vertex is constraint by the Clifford algebra of the Dirac matrices. A general Fermion-scalar vertex $\Gamma(P,p)$ depending on the momenta P and p allows four independent matrices $\{\mathbb{1}_{\mathrm{D}}, \not{P}, \not{p}, \not{P}\not{p}\}$, while a general Fermion-vector vertex $\Gamma^\mu(P,p)$ depending on the same momenta results in twelve independent Lorentz covariants consisting of the three vectors γ_μ, P_μ and p_μ each multiplied with the four matrices from the Fermion-scalar vertex $\{\gamma_\mu, P_\mu, p_\mu\} \times \{\mathbb{1}_{\mathrm{D}}, \not{P}, \not{p}, \not{P}\not{p}\}$. Due to the vector WTI shown in App. B.4, there exists a conserved current linking the four longitudinal elements of the vector vertex ($\propto P^\mu$) with quark dressing functions. The eight remaining transversal tensor structures are not constraint. Eventually, the on-shell vector and axial-vector mesons are transverse to their total momentum and their allowed number of covariants reduced to eight. Furthermore, the Dirac covariants are constraint by their transformation property under CPT [124]. The invariance of the considered BSA under parity transformation

$$\mathrm{U}_{\mathbf{P}}^{-1}\Gamma_{\mathrm{x}}^{(\mu)}(P,p)\mathrm{U}_{\mathbf{P}} = (-1)^J(\delta_{J,0} + g_-^{\mu\nu}\delta_{J,1})\gamma_0\Gamma_{\mathrm{x}}^{(\nu)}(g_-P, g_-p)\gamma_0 \stackrel{!}{=} \mathbf{P}\Gamma_{\mathrm{x}}^{(\mu)}(P,p) \tag{3.13}$$

requires the inclusion of a γ_5 into the BSA of pseudo-scalar and axial-vector mesons. In the parity transformation, J and $\mathbf{P} \in \{+,-\}$ are the total spin and the multiplicative parity quantum number of the meson, respectively. $g_- = \mathrm{diag}(1,-1,-1,-1)$ is the metric tensor of the Minkowski space. If we consider equal quark constituents, also the charge conjugation is a valid quantum number. The corresponding charge conjugation invariance condition for the considered BSA is

$$\mathrm{U}_{\mathbf{C}}^{-1}\Gamma_{\mathrm{x}}^{(\mu)}(P,p)\mathrm{U}_{\mathbf{C}} = \bar{\Gamma}_{\mathrm{x}}^{(\mu)}(P,p) = \left[C\Gamma_{\mathrm{x}}^{(\mu)}(P,-p)C^\top\right]^\top \stackrel{!}{=} \mathbf{C}\Gamma_{\mathrm{x}}^{(\mu)}(P,p) \tag{3.14}$$

with $C = \gamma_0\gamma_2$ and the multiplicative charge conjugation quantum number $\mathbf{C} \in \{+,-\}$. This operation exchanges particles with their corresponding antiparticles.[8] Although the choice of the basis for the Dirac covariants $\tau_i^{(\mu)}$ is constraint, the representation is not unique. For our calculations we use the vacuum Dirac basis from previous works [125–127] shown in Tab. 3.1. The signs of the pseudo-scalar

[8] See App. B.2.3 for further information to the discrete symmetries and the transformation properties of meson BSA's and their basis elements.

Table 3.1.: Vacuum Dirac tensor structure basis elements necessary for the description of mesons of spin $J = 0, 1$. The pseudo-scalar $J^{\mathrm{PC}} = 0^{-+}$ and axial-vector $J^{\mathrm{PC}} = 1^{+\pm}$ states have to be multiplied with a γ_5 factor to account for the correct parity transformation. The subscript $\top$ indicates transversality with respect to the total momentum P. For an arbitrary vector v^μ the transverse vector is defined via $v^\mu_\top = T_{\mu\nu}(P)v^\nu$, where $T_{\mu\nu}$ represents the transverse projector in Eq. (2.21). Ref. [126] showed that the axial-vector components in parenthesis are sub-leading and can be neglected. The tensor structure components are multiplied by the factors $\bullet = (p\cdot P)$ and $\circ = \mathbb{1}_{\mathrm{D}}$ which ensure the correct behavior under charge conjugation transformation in case of equal quark constituents.

Name	Component		0^{-+}	0^{++}	
E^{x}	$\tau_1(P,p):$	$\mathbb{1}_{\mathrm{D}}$	$\circ$	$\circ$	
F^{x}	$\tau_2(P,p):$	$-i\not{P}$	$\circ$	$\bullet$	
G^{x}	$\tau_3(P,p):$	$-i\not{p}$	$\bullet$	$\circ$	
H^{x}	$\tau_4(P,p):$	$\left[\not{p},\not{P}\right]$	$\circ$	$\circ$	
Name	Component		1^{--}	1^{++}	1^{+-}
$\mathrm{F}^{\mathrm{x}}_1$	$\tau^\mu_1(P,p):$	$i\gamma^\mu_\top$	$\circ$	$\circ$	$(\bullet)$
$\mathrm{F}^{\mathrm{x}}_2$	$\tau^\mu_2(P,p):$	$\gamma^\mu_\top\not{P}$	$\circ$	$\bullet$	$(\circ)$
$\mathrm{F}^{\mathrm{x}}_3$	$\tau^\mu_3(P,p):$	$-\gamma^\mu_\top\not{p} + p^\mu_\top\mathbb{1}_{\mathrm{D}}$	$\bullet$	$\circ$	$(\bullet)$
$\mathrm{F}^{\mathrm{x}}_4$	$\tau^\mu_4(P,p):$	$i\gamma^\mu_\top\left[\not{P},\not{p}\right] + 2ip^\mu_\top\not{P}$	$\circ$	$\circ$	$(\bullet)$
$\mathrm{F}^{\mathrm{x}}_5$	$\tau^\mu_5(P,p):$	$p^\mu_\top\mathbb{1}_{\mathrm{D}}$	$\circ$	$(\bullet)$	$\circ$
$\mathrm{F}^{\mathrm{x}}_6$	$\tau^\mu_6(P,p):$	$ip^\mu_\top\not{P}$	$\bullet$	$(\bullet)$	$\circ$
$\mathrm{F}^{\mathrm{x}}_7$	$\tau^\mu_7(P,p):$	$-ip^\mu_\top\not{p}$	$\circ$	$(\circ)$	$\bullet$
$\mathrm{F}^{\mathrm{x}}_8$	$\tau^\mu_8(P,p):$	$p^\mu_\top\left[\not{P},\not{p}\right]$	$\circ$	$(\bullet)$	$\circ$

covariants are chosen such that all BSA components are positive and the vector basis elements are transversal to total momentum P. The additional $P\cdot p$ factors ensure that all BSA's transform similarly under CPT.

Chebychev representation of the BSA

The BSA $\Gamma^{(\mu)}_{\mathrm{x}}$ and its components depend on the total momentum of the meson P^2, the relative momentum between the quark and the antiquark p^2 and the angle $z_p = \cos(\sphericalangle(P,p)) = \hat{P}\cdot\hat{p}$ in between those two momenta. In vacuum, the dependence on the angle turns out to be mild. This allows the representation of

the BSA with Chebychev polynomials

$$f_{\mathrm{x}}^{i}(P,p) \approx \sum_{k=0}^{N_{\mathrm{cheby}}} \tilde{f}_{\mathrm{x}}^{i,k}(P^2,p^2)\tilde{T}_k(z_p)\,i^k\,. \tag{3.15}$$

In this representation we utilize modified Chebychev polynomials of first kind: $\tilde{T}_0(z_p) = 1/\sqrt{2}$, $\tilde{T}_k(z_p) = \cos(k\arccos(z_p))$. Since the sum converges rapidly, we only need four polynomials for (pseudo-)scalar and six for (axial-)vector mesons.

If we consider a charge conjugation eigenstate (uncharged meson with equal quark constituents) and a symmetric momentum partitioning ($\eta_\pm = 0.5$), we can study the necessary transformation properties of the scalar meson dressing functions $f_{\mathrm{x}}^{i}(P,p)$. Taking the charge conjugation transformation properties of the full BSA $\Gamma_{\mathrm{x}}^{(\mu)}$ and its basis elements $\tau_i^{(\mu)}$ in Eqs. (3.14) and (B.19) into account, we can deduce the constraints

$$\begin{aligned} \mathrm{U}_{\mathbf{C}}^{-1}(f_{\mathrm{x}}^{i}(P,p))\,\mathrm{U}_{\mathbf{C}} = f_{\mathrm{x}}^{i}(P,-p) &\overset{!}{=} f_{\mathrm{x}}^{i}(P,p) \\ &= \sum_k \tilde{f}_{\mathrm{x}}^{i,2k}(P^2,p^2)\tilde{T}_{2k}(z_p)(-1)^k - i\sum_k \underbrace{\tilde{f}_{\mathrm{x}}^{i,2k+1}(P^2,p^2)}_{\overset{!}{=}0}\,\tilde{T}_{2k+1}(z_p)(-1)^k \end{aligned} \tag{3.16}$$

for the Chebychev coefficients of the meson dressing function $f_{\mathrm{x}}^{i,k}(P,p)$.[9] The minus sign of the second term thereby results from the asymmetry of the odd Chebychev polynomials $\tilde{T}_{2k+1}(-z_p) = -\tilde{T}_{2k+1}(z_p)$. We see that the BSA should only depend on even powers of the angle z_p. Otherwise, there is no well defined charge conjugation eigenvalue any more. We will see in Sec. 4.4 that the introduction of chemical potential breaks the charge conjugation symmetry. To remember, the charge conjugation exchanges particles with their corresponding antiparticles and vice versa. Consequently, we can easily understand that due to the energy offset which is introduced by the chemical potential, antiparticles and particles are no longer energetically degenerated and the C-parity is broken.[105]

We can only study the C-parity breaking using a symmetric momentum partitioning $\eta_\pm = 0.5$, where the calculable meson mass is maximized and the BSA in vacuum is simplified since it is purely real. Asymmetric values introduce imaginary components and lead to non-vanishing odd Chebychev coefficients. Physical observables, however, should be independent from the value of the partitioning parameter. In loop diagrams a shift in the value of $\eta_\pm$ is equivalent to a shift in the integration variables. Ref. [128] shows that as long as we consider non-anomalous processes, the loop integrals are independent of these shifts, although with the condition that all approximated variables in the integral respect Poincaré covariance.

[9] Note that the meson BSA basis elements are intentionally constructed such that the breaking of the C-parity is easily visible in a Chebychev expansion.

3.1.3. Norm

Due to the structure of the homogeneous Bethe-Salpeter equation, the corresponding amplitude is only determined up to a constant factor. To determine this factor a normalization condition is necessary. There are two options for the normalization procedure, the standard Leon-Cutkosky and the Nakanishi normalization method. They can be written via

$$\pm \frac{d}{dP^2} Q^{(T)}_{\mathrm{x},el}(P,Q)\Big|_{P^2=Q^2=-m_\mathrm{x}^2} = \delta_{el}\mathcal{N}_\mathrm{x}^2\,, \tag{3.17}$$

$$\pm \left(\frac{d\ln(\lambda_\mathrm{x})}{dP^2}\right) Q^{(T)}_{\mathrm{x},el}(P,P)\Big|_{P^2=-m_M^2} = \delta_{el}\mathcal{N}_\mathrm{x}^2\,. \tag{3.18}$$

In general, both methods are applicable to Rainbow-Ladder and beyond. But in the first line, we only show the Leon-Cutkosky normalization method for a Rainbow-Ladder kernel which can be obtained by evaluating the derivative of Dyson's equation at the on-shell momentum (See App. C.2.1).[10] The Nakanishi normalization method [129] in the second line is applicable to Rainbow-Ladder and beyond. The sign in both equations depend on the meson type. Furthermore, the loop term $Q^{(T)}_{\mathrm{x},el}$ is defined via

$$\begin{aligned} Q^{(\mu\nu)}_{\mathrm{x},el}(P,Q) &= \int_q \mathrm{Tr}_\mathrm{DCF}\left[\bar{\Gamma}^{(\mu)}_{\mathrm{x},e}(-Q,q)\,S(q_+(P))\,\Gamma^{(\nu)}_{\mathrm{x},l}(Q,q)\,S(q_-(P))\right]\,, \\ Q^{T}_{\mathrm{x},el}(P,Q) &= \frac{1}{\mathrm{N_{pol}}} T_{\mu\nu}(P)\,Q^{\mu\nu}_{\mathrm{x},el}(P,Q) \end{aligned} \tag{3.19}$$

with the charge conjugated BSA defined in Eq. (3.14). Note that the flavor has to be transposed, too. The flavor trace especially is important for multi-flavor configuration mesons states, where different quark flavor propagators of the diagonal flavor matrix $S = \mathrm{diag}\left(S^\mathrm{u}, S^\mathrm{d}, \dots\right)$ contribute to the calculation. Due to the summation over the polarization tensor, we have to include the factor $\mathrm{N_{pol}} = 3$ in case of (axial-)vector mesons.

After discussing the properties of the meson BSA in vacuum we are now interested in the changes resulting from the introduction of a finite chemical potential (and temperature).

[10] In general the Leon-Cutkosky normalization method includes an additional term shown in Eq. (C.20) and can be used for beyond Rainbow-Ladder truncations, too. Due to our Ladder like truncation in the BSE and the total momentum P independence of the kernel the additional term vanishes.

3.1.4. Medium changes

Due to the introduction of finite temperature T and quark chemical potential μ_{q}^f the quark part of the 2PI effective action changes to $\Gamma^{[2]}[S] = \mathrm{Tr}_{\mathcal{F}} \log \frac{S^{-1}}{T} - \mathrm{Tr}_{\mathcal{F}} \left[\mathbb{1} - S_0^{-1} S\right] + \Gamma^{[2]}_{\mathrm{Int}}[S]$. In consequence, the homogeneous BSE and the norm remain structurally unchanged but the dressed quark and gluon propagator representations change as discussed in Sec. 2.1.3. Additionally, the functional trace entails the same changes to the momenta and integral representation at finite temperature and/or chemical potential as mentioned in the first chapter. Since we consider the mesons to be in rest frame $P = (\vec{0}, im_{\mathrm{x}})$, the total momentum and the assigned direction of the medium $v_{\mathrm{med}} = (\vec{0}, 1)$ align in the energy component of the four momentum. As a result, there are no additional momentum or angular dependencies of the BSA but the quark propagators are now evaluated at $q_\pm = q \pm \eta_\pm P$ with $q = (\vec{q}, \tilde{q}_4)$ implying $\tilde{q}^f_{4\pm} = q_4 + i(\mu_{\mathrm{q}}^f \pm \eta_\pm m_{\mathrm{x}})$.

Similar as for the quark and gluon propagator, the assigned direction of the medium and the connected breaking of O(4) symmetry lead to changes in the Dirac structure of the BSA. Instead of four independent matrices in a general scalar vertex we now have eight $\{\mathbb{1}_{\mathrm{D}}, \not{P}, \not{p}, \not{\psi}, \not{P}\not{p}, \not{P}\not{\psi}, \not{\psi}\not{p}, \not{P}\not{p}\not{\psi}\}$ and 32 in a general vector vertex $\{\gamma_\mu, P_\mu, p_\mu, v_\mu\} \times \{\mathbb{1}_{\mathrm{D}}, \not{P}, \not{p}, \not{\psi}, \not{P}\not{p}, \not{P}\not{\psi}, \not{\psi}\not{p}, \not{P}\not{p}\not{\psi}\}$. Here we erased the subscript 'med' from the assigned direction of the medium for a more compact notation. If we again neglect all longitudinal contributions due to the vector WTI, 24 transversal tensor structures remain. Since this increased number of Dirac basis elements also increase the computational complexity, we use the tensor structures detailed in Tab. 3.2 in medium.

In the table, we indicate that the vector meson in medium splits into a spatial and a temporal part w.r.t. the assigned direction of the medium. These two parts of the vector do not mix and fulfill separate BSE and norm relations which probably leads to different masses for the two orientations, c.f. with Ref. [63, 128]. Although the charge conjugation symmetry gets broken by the presence of chemical potential (as we will see later in Sec. 4.4) and there consequently is no unique charge conjugation eigenvalue, we utilize the $P \cdot p$ factors to compare with the vacuum. Since we know from vacuum [28] that E^{x} is dominant, F^{x} has a considerable impact on the mass and decay constant and G^{x} is at least important for the decay constant while H^{x} is negligible, we will restrict our-self to these first three (pseudo-)scalar basis elements to describe the mass and decay constant as accurate as possible. Due to the rest frame, we furthermore neglect $\mathrm{F}^{\mathrm{x}}_{\mathrm{s}}$ and $\mathrm{H}^{\mathrm{x}}_{\mathrm{s}}$ in our calculations. In case of the (axial-)vector mesons, we restrict our-self to $\mathrm{F}^{\mathrm{x}}_1$ and $\mathrm{F}^{\mathrm{x}}_4$ since these are the dominant structures for the vector and the 1^{++}-axial-vector mesons, respectively. By using both we have a direct comparison between these two meson types.

Table 3.2.: Medium Dirac tensor structure basis elements necessary for the description of mesons of spin $J = 0, 1$. The pseudo-scalar $J^{\mathrm{PC}} = 0^{-+}$ and axial-vector $J^{\mathrm{PC}} = 1^{++}$ states have to be multiplied with a γ_5 factor to account for the correct parity transformation. The subscripts "$\top$T" and "$\top$L" indicate vectors defined by $v^{\mu}_{\top(\mathrm{T/L})} = \mathcal{P}^{\mathrm{T/L}}_{\mu\nu}(P)v^{\nu}$ where $\mathcal{P}^{\mathrm{T/L}}_{\mu\nu}$ represents the medium projectors in Eqs. (2.31) and (2.32). Like in vacuum, the tensor structure components are multiplied by the factors $\bullet = (p \cdot P)$ and $\circ = \mathbb{1}_{\mathrm{D}}$.

Name	Component		0^{-+}	0^{++}	
E^{x}	$\tau_1(P,p):$	$\mathbb{1}_{\mathrm{D}}$	$\circ$	$\circ$	
$\mathrm{F}^{\mathrm{x}}_{\mathrm{s}}$	$\tau_2(P,p):$	$-i\vec{\not{P}}$	$\circ$	$\bullet$	
$\mathrm{G}^{\mathrm{x}}_{\mathrm{s}}$	$\tau_3(P,p):$	$-i\vec{\not{p}}$	$\bullet$	$\circ$	
I^{x}	$\tau_4(P,p):$	$-i\gamma_4$	$\circ$	$\circ$	
$\mathrm{H}^{\mathrm{x}}_{\mathrm{s}}$	$\tau_5(P,p):$	$\left[\vec{\not{p}}, \vec{\not{P}}\right]$	$\circ$	$\circ$	
Name	Component		1^{--}	1^{++}	Orientation
$\mathrm{F}^{\mathrm{x}}_{1\mathrm{s}}$	$\tau^{\mu}_{1\mathrm{s}}(P,p):$	$i\gamma^{\mu}_{\top\mathrm{T}}$	$\circ$	$\circ$	Spatial
$\mathrm{F}^{\mathrm{x}}_{4\mathrm{s}}$	$\tau^{\mu}_{4\mathrm{s}}(P,p):$	$i\gamma^{\mu}_{\top\mathrm{T}}\left[\not{P}, \not{p}\right] + 2ip^{\mu}_{\top\mathrm{T}}\not{P}$	$\circ$	$\circ$	Spatial
$\mathrm{F}^{\mathrm{x}}_{1\mathrm{t}}$	$\tau^{\mu}_{1\mathrm{t}}(P,p):$	$i\gamma^{\mu}_{\top\mathrm{L}}$	$\circ$	$\circ$	Temporal
$\mathrm{F}^{\mathrm{x}}_{4\mathrm{t}}$	$\tau^{\mu}_{4\mathrm{t}}(P,p):$	$2ip^{\mu}_{\top\mathrm{L}}P_4\gamma_4$	$\circ$	$\circ$	Temporal

It has to be mentioned that the I^{x} medium BSA component corresponds to the temporal part of F^{x} and G^{x} and consequently gets contributions from both. The vacuum limit therefore is not clear and ambiguous. The same is also true for $\mathrm{F}^{\mathrm{x}}_{1\mathrm{t}}$ and $\mathrm{F}^{\mathrm{x}}_{4\mathrm{t}}$. Note that until now there only exist finite temperature zero Matsubara frequency studies for mesons with $\mathrm{F}^{\mathrm{x}}_{1\mathrm{s}}$ and $\mathrm{F}^{\mathrm{x}}_{1\mathrm{t}}$, see e.g. Ref. [32, 63, 128].

For the calculation of the norm the same medium modifications as for the BSE apply. In addition to those modifications the loop term has to be replaced by $Q^{T(T/L)}_{\mathrm{x},el}(P,Q) = \mathcal{P}^{\mathrm{T/L}}_{\mu\nu}(P)Q^{\mu\nu}_{\mathrm{x},el}(P,Q)/\mathrm{N}^{\mathrm{s/t}}_{\mathrm{pol}}$ for the spatial/temporal part of the vector meson by exchanging the projector $T_{\mu\nu}(P)$ by $\mathcal{P}^{\mathrm{T/L}}_{\mu\nu}(P)$ in Eq. (3.19). There the polarization factor for the spatial and temporal part of the vector meson furthermore reduces to $\mathrm{N}^{\mathrm{s}}_{\mathrm{pol}} = 2$ and $\mathrm{N}^{\mathrm{t}}_{\mathrm{pol}} = 1$, respectively.

With this we can conclude the discussion of the wave-function and amplitude of the meson bound states and can turn our interest to meson properties like the meson mass and decay constant.

3.2. Meson properties

In this section, we will discuss the determination of the meson mass(es) and electroweak decay constant(s) in vacuum and medium, which we then use to construct the meson propagator. At the end, we introduce and explain the Silver-Blaze property (SBP) that all (meson) observables have to fulfill. We will begin with the determination of the meson mass from the homogeneous Bethe-Salpeter equation.

3.2.1. Mass and decay constant in vacuum and medium

When we consider the homogeneous BSE we not only have direct access to the meson wave-function but also to the meson mass. This can be seen in a functional notation, where we suppress all discrete and continuous indices. Then, we can write the hBSE via

$$\tilde{K}(P)\Gamma_{\mathrm{x}}(P) = \lambda_{\mathrm{x}}(P)\Gamma_{\mathrm{x}}(P)\,. \tag{3.20}$$

Although the hBSE is only valid for the on-shell momentum $P^2 = -m_{\mathrm{x}}^2$, we added a total momentum dependent function $\lambda_{\mathrm{x}}(P)$ to describe also off-shell momenta close to the on-shell momentum. In this representation, it is clearly visible that the hBSE is an eigenvalue equation with an eigenvalue of one at the on-shell momentum, i.e. $P^2 = -m_{\mathrm{x}}^2 \Leftrightarrow \lambda_{\mathrm{x}}(P) = 1$. To study the total momentum dependence of the eigenvalue function $\lambda_{\mathrm{x}}(P)$ and thus to determine the on-shell momentum, we vary the total momentum. The resulting eigenvalue function of the Pion is exemplarily displayed in Fig. 3.3 for the vacuum and different chemical potentials. In our calculation, we search for the ground state of the meson which is identified by the largest eigenvalue and calculated using the power iteration method. See App. C.2.4 for more information.

Due to the pole structure of the quark and the numerical problems connected to it (discussed in App. C.1.3), there only is a certain total momentum or meson mass interval which is numerically accessible in our bound state calculation. For heavy mesons with a mass which is outside this interval or close to its border, the eigenvalue functions have to be extrapolated from the accessible region. Because of the alignment of the chemical potential and the total momentum in rest frame, the addition of the meson mass and the chemical potential $|\mu_{\mathrm{q}}^f \pm \eta_{\pm} m_{\mathrm{x}}|$ has to remain in the aforementioned interval. Consequently, the mass interval becomes chemical potential dependent and we can use the partitioning parameter $\eta_{\pm}$ to maximize the accessible chemical potential and mass region. See App. C.2.3 for more information to this topic.

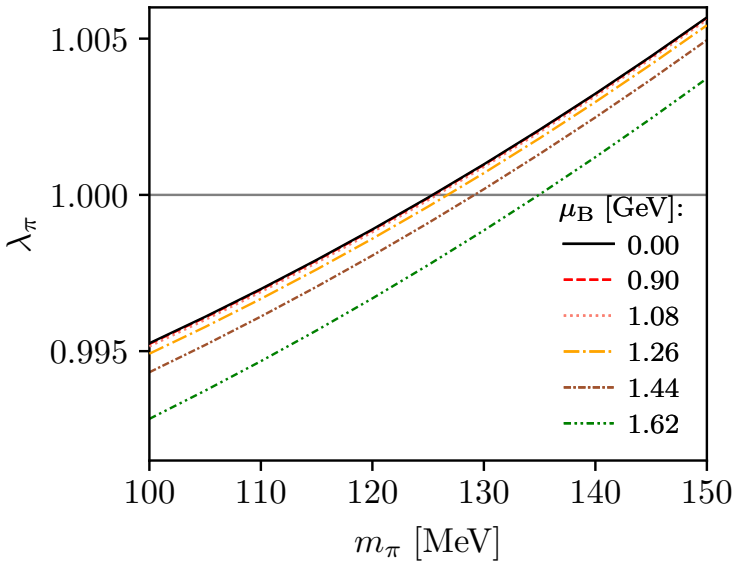

Figure 3.3.: The eigenvalue λ_x is plotted against the meson mass m_x for a Pion meson and different chemical potentials including the vacuum. The results are calculated using only the E^x Dirac tensor structure shown in Tab. 3.2.

The vacuum meson mass of all considered mesons, calculated within this work, are detailed in Tab. 3.3 in comparison to experimental values from Ref. [122]. The π and K meson masses are in good agreement with the experimental values, but this is due to the fact that we fix our truncation and the QCD parameters accordingly. While the σ meson mass lies above the experimental range, the ρ, ϕ and a_1 differ by about $10 - 20\%$. It is, however, possible to improve the agreement with a more elaborate truncation [33, 34].

For a rigorous treatment of bound state resonances above the strong decay threshold (e.g. the $\pi\pi$ production threshold at $P^2 = -4m_\pi^2$), it is important to include possible other (hadronic) decay channels. If we consider the decay channels in Ref. [122], the π and K mesons decay mainly leptonic ($l_f\nu_f$) or electromagnetic ($\gamma\gamma$) but the ρ and ϕ mesons decay mainly hadronic in $\pi\pi$ and KK modes, respectively. For σ/f_0 and a_1 the decay properties are not settled since the branching ratios are unknown but the importance of hadronic decays is plausible. These hadronic decays have to be included into our BSE calculation and enter by a new light meson loop term. This coupling to lighter meson modes then give rise to non-zero meson widths Γ_w^x [128]. As a result, the total momentum becomes now complex valued and has to be parameterized in terms of its resonant mass m_x (pole mass in second Riemann sheet) and width Γ_w^x via $P^2 = [i(m_x \pm i\Gamma_w^x/2)]^2$. The meson is

Table 3.3.: Comparison of the calculated vacuum meson masses and decay constants with the experimental or lattice values given in Ref. [122] and [130] for all considered meson types in this work. Since there are different conventions defining the decay constant differing by a factor of $\sqrt{2}$, the experimental decay constant values were divided by a factor of $\sqrt{2}$ to be comparable to our convention. The mesons are calculated with the most elaborated vacuum Dirac tensor basis shown in Tab. 3.1.

Particles	m_{x} [MeV]		f_{x} [MeV]	
x	This work	Exp. (PDG [122])	This work	Exp./Lat. (PDG [122])
π^0	135.13	134.9768(5)	109.8	92(6)
K^0	494.93	497.611(13)	132.5	110(5)
σ/f_0	633.37	$400-550$	–	–
ρ^0	854.95	775.26(25)	165.4	156(1)
ϕ	1230.62	1019.461(16)	218.1	162(3)
a_1	1016.55	1230(40)	134.1	144(13)[130]

now a resonance and no longer a bound state particle. Note that this effect can only be studied using beyond Rainbow-Ladder truncations.

If we include the decay channel $\rho \to \pi\pi$ into the BSE calculation as shown in Ref. [58], the ρ-meson mass decreases. In addition, Ref. [128] indicates that this coupling is also important for the isoscalar-scalar meson (σ/f_0) due to the large σ width. Without the coupling the σ properties equal those of an idealized chiral partner of the π. Furthermore, it is mentionable that low mass scalar mesons are typical for too attractive Rainbow-Ladder truncation. A beyond Rainbow-Ladder truncation is necessary to describe the observed scalar mesons since a Rainbow-Ladder vertex cannot capture all essentials of the dynamical chiral symmetry breaking [74, 94]. However, concerning the σ meson, we have to keep in mind that after Ref. [131] proposed a possible four-quark description of light scalar mesons, multiple theoretical studies showed that four-quark descriptions deliver a more consistent picture than two-quark descriptions do [132–135].

In this work, we have to neglect these kinds of hadronic and beyond Rainbow-Ladder effects since they would increase the computational effort drastically, especially in medium. We will, however, study other hadronic backcoupling effects in the Chaps. 5 and 6. Next, we will consider the calculation of the meson decay constants.

The meson decay constant(s)

In vacuum, we determine the leptonic or electromagnetic meson decay constant for pseudo-scalar and (axial-)vector mesons [32, 136] via

$$i\delta_{el}\, f_{\mathrm{x}}\, m_{\mathrm{x}} = \int_q \mathrm{Tr}_{\mathrm{DCF}}\Big[j^{(\mu)}_{\mathrm{x},e}(P)\, S(q_+)\, \hat{\Gamma}^{(\mu)}_{\mathrm{x},l}(P,q)\, S(q_-)\Big] \tag{3.21}$$

where $\hat{\Gamma}^{(\mu)}_{\mathrm{x},l}(P,q) = \Gamma^{(\mu)}_{\mathrm{x},l}(P,q)/\mathcal{N}$ describes the normalized BSA and the current is given by

$$j^{(\mu)}_{\mathrm{x},e}(P) = \begin{cases} Z_2\gamma_5 \hat{\not{P}} & \otimes \frac{r^e_{\mathrm{x}}}{\mathrm{N_f}} \otimes \mathbb{1}_{\mathrm{C}} & J^{\mathrm{PC}} = 0^{-+} \\ Z_2 \quad \gamma^\mu \frac{1}{\mathrm{N_{pol}}} & \otimes \frac{r^e_{\mathrm{x}}}{\mathrm{N_f}} \otimes \mathbb{1}_{\mathrm{C}} & J^{\mathrm{PC}} = 1^{--} \\ Z_2\gamma_5\gamma^\mu \frac{1}{\mathrm{N_{pol}}} & \otimes \frac{r^e_{\mathrm{x}}}{\mathrm{N_f}} \otimes \mathbb{1}_{\mathrm{C}} & J^{\mathrm{PC}} = 1^{+\pm} \end{cases} \tag{3.22}$$

with the momentum abbreviation $\hat{\not{P}} = \not{P}/\sqrt{P^2}$. The equation is evaluated at the on-shell momentum $P^2 = -m_{\mathrm{x}}^2$ and is exact as long as the quark propagator and the BSA are exact. Z_2 and $\mathrm{N_{pol}}$ again represent the quark wave-function renormalization constant and the polarization factor.

Since the decay constant for the scalar meson (σ/f_0) is zero (also numerically) we will not consider it in this work. A comparison of the calculated vacuum meson decay constant with the experiment is given in Tab. 3.3 for the remaining mesons. But since only the masses of the π and K are comparable to the experimental values, we only discus their corresponding decay constants. Both are 20% larger compared to the experimental values. Since other truncation methods show better agreements, the reason can only be the employed truncation. An improvement of the employed truncation of the DSE and/or BSE is advisable, e.g. an improvement of the quark-gluon vertex by introducing or using more Ball-Chiu terms.

If we now consider the medium, the introduction of an assigned direction and the connected O(4) symmetry breaking lead to further changes in the decay constant equation, in addition to the arguments in Sec. 3.1.4. Refs. [137–139] showed that the introduction of an assigned direction splits the Pion decay constant into two parts: A part temporal f^{t}_π and another spatial f^{s}_π to the assigned direction of the medium $v_{\mathrm{med}} = (\vec{0}, 1)$. Although this splitting was only shown for the Pion, we expect it to be true for all pseudo-scalars. Taking into account the derivation of the meson decay constant in App. C.2.1, the splitting of the pseudo-scalar meson decay constant

$$f_{\mathrm{P}}\, P^\mu \quad \xrightarrow{\text{medium}} \quad \Big[f^{\mathrm{t}}_{\mathrm{P}}\, \mathcal{P}^{\mathrm{L}}_{\mu\nu}(v) + f^{\mathrm{s}}_{\mathrm{P}} \mathcal{P}^{\mathrm{T}}_{\mu\nu}(v) \Big]\, P^\nu \tag{3.23}$$

now enters on the LHS of the equation. Henceforth, we will denote these two decay constants as temporal $f_{\mathrm{x}}^{\mathrm{t}}$ and spatial $f_{\mathrm{x}}^{\mathrm{s}}$ meson decay constant. Due to the use of the rest frame, we do not have access to the spatial decay constant for pseudo-scalar mesons. If we consider the (axial-)vector mesons, we also have temporal and spatial decay constants which are connected to the corresponding temporal and spatial part of BSA. With this we can define the generalized decay constant equation in medium

$$\delta_{el} f_{\mathrm{x}}^{\mathrm{s/t}} = \int_q \mathrm{Tr}_{\mathrm{DCF}} \left[j_{\mathrm{x},e}^{\mathrm{s/t},(\mu)}(P) S(q_+) \hat{\Gamma}_{\mathrm{x},l}^{(\mu)}(P,q) S(q_-) \right] \tag{3.24}$$

for pseudo-scalar and (axial-)vector mesons. Here the current is defined via

$$j_{\mathrm{x},e}^{\mathrm{s/t},(\mu)}(P) = \begin{cases} Z_2 \gamma_5 \not{\vec{P}}/\vec{P}^2 & \otimes \frac{r_{\mathrm{x}}^e}{\mathrm{N_f}} \otimes \mathbb{1}_{\mathrm{C}} & J^{\mathrm{PC}} = 0^{-+}, \text{ spatial} \\ Z_2 \gamma_5 \gamma_4 / P_4^2 & \otimes \frac{r_{\mathrm{x}}^e}{\mathrm{N_f}} \otimes \mathbb{1}_{\mathrm{C}} & \text{temporal} \\ -iZ_2 \quad \gamma_{\top T}^{\mu}/m_{\mathrm{V}} \frac{1}{\mathrm{N}_{\mathrm{pol}}^{\mathrm{s}}} & \otimes \frac{r_{\mathrm{x}}^e}{\mathrm{N_f}} \otimes \mathbb{1}_{\mathrm{C}} & J^{\mathrm{PC}} = 1^{--}, \text{ spatial} \\ -iZ_2 \quad \gamma_{\top L}^{\mu}/m_{\mathrm{V}} \frac{1}{\mathrm{N}_{\mathrm{pol}}^{\mathrm{t}}} & \otimes \frac{r_{\mathrm{x}}^e}{\mathrm{N_f}} \otimes \mathbb{1}_{\mathrm{C}} & \text{temporal} \\ -iZ_2 \gamma_5 \gamma_{\top T}^{\mu}/m_{\mathrm{V}} \frac{1}{\mathrm{N}_{\mathrm{pol}}^{\mathrm{s}}} & \otimes \frac{r_{\mathrm{x}}^e}{\mathrm{N_f}} \otimes \mathbb{1}_{\mathrm{C}} & J^{\mathrm{PC}} = 1^{+\pm}, \text{ spatial} \\ -iZ_2 \gamma_5 \gamma_{\top L}^{\mu}/m_{\mathrm{V}} \frac{1}{\mathrm{N}_{\mathrm{pol}}^{\mathrm{t}}} & \otimes \frac{r_{\mathrm{x}}^e}{\mathrm{N_f}} \otimes \mathbb{1}_{\mathrm{C}} & \text{temporal} \end{cases} . \tag{3.25}$$

In the following, we will use the discussed meson masses and decay constants to define the meson propagation necessary for the meson backcoupling in Sec. 5.

3.2.2. Propagation

The propagation of mesons, described in this section, is based on the findings of Ref. [138, 139]. In these references, the real part of the dispersion relation of "soft" Pions in the symmetry broken phase is given by $\omega^2 = u_\pi^2(\vec{P}^2 + m_\pi^2)$ with the Pion velocity[11] u_π and m_π being the Pion screening mass and the energy of the Pion at $\vec{P} = 0$. $\tilde{m}_\pi = u_\pi m_\pi$ represents the Pion pole mass. In vacuum, the pole and screening mass coincide and the velocity equals one $u_\pi = 1$ but in medium the velocity in general differs from one due to the missing Lorentz invariance and can be expressed by the ratio of the spatial and temporal Pion decay constant

$$u_\pi = \frac{f_\pi^{\mathrm{s}}}{f_\pi^{\mathrm{t}}} . \tag{3.26}$$

[11] Normally it is only a velocity if $m_\pi = 0$.

For the Pion propagator in medium, we use the same ansatz

$$D_\pi(P) = \frac{1}{P_4^2 + u_\pi^2(\vec{P}^2 + m_\pi^2)} \tag{3.27}$$

as outlined in previous works, e.g. in Ref. [38]. In vacuum, this representation reduces to $D_\pi(P) = \frac{1}{P^2+m_\pi^2}$, while at finite temperature the fourth momentum component has to be replaced by a bosonic Matsubara frequency. The propagation corresponds to a classical one without any widths. Although the dispersion relation is only shown for the Pion at finite temperature, we expect this propagator to be valid for all considered pseudo-scalar and assume it to be valid for scalar mesons in vacuum and medium, too. The propagation of the vector mesons is similar but multiplied by a spin state dependent function $\Lambda_{\mathrm{x}}^{\mu\nu}(P)$. To conclude this section, we have to mention that since the calculation of the spatial part of the decay constant is not possible in the rest frame, we have to set $u_{\mathrm{x}} = 1$. A Pion velocity of a Pion at rest does not make sense.

3.2.3. Silver-Blaze property

In this section, we will discuss the so-called Silver-Blaze property (SBP) which is relevant for observables at zero temperature and small chemical potential. It states that the system has to stay in its vacuum ground state until the baryon chemical potential μ_{B} is large enough to create physical excitations. Since the introduction of finite temperature leads to excitations too, the property is only considered at vanishing temperature. On the chemical potential axis of the QCD phase diagram, the first physical excitation corresponds to the lightest nucleon, the proton. Consequently, the SBP is valid as long as $\mu_{\mathrm{B}} < m_{\mathrm{N}}^{\mathrm{med}} = m_{\mathrm{N}} - E_{\mathrm{bind}}$ with $m_{\mathrm{N}}^{\mathrm{med}} = 928\,\mathrm{MeV}$ being the mass of the lightest nucleon in medium. The nucleon mass in medium results from the corresponding vacuum mass $m_{\mathrm{N}} = 939\,\mathrm{MeV}$ and the binding energy E_{bind}. It is possible to show the SBP analytically for finite isospin chemical potential μ_{I} but it is also plausible for baryon chemical potential [61, 62]. It was furthermore shown in a lattice formulation with heavy quark masses [140].

To clarify, the SBP states that all observables have to remain constant in the Silver-Blaze region which is given by $\mu_{\mathrm{B}} \in [0, m_{\mathrm{N}}^{\mathrm{med}}]$. Above this region, states can be exited and observables change. In this work, we basically consider only the meson masses and decay constants as observables. Since the QCD Lagrangian and non-observable colored quantities derived from it like the Green functions show more or less strong (explicit) chemical potential dependencies, a complex cancellation of internal chemical potential dependencies is necessary to fulfill the

SBP and to obtain constant observables. Therefore, it is understandable that a careless truncation can easily violate the SBP.

To further discuss the SBP, we consider Refs. [101, 141]. There, it was analytically shown that the Quark propagator and different vertices at finite chemical potential can easily be calculated from their vacuum equivalent by evaluating the vacuum pendant at a shifted momentum. For the quark propagator this means $S_{[\mu]}(p) = S_{\mathrm{vac}}(\tilde{p})$ with $\tilde{p} = \left(\vec{p}, p_4 + i\mu_{\mathrm{q}}^f\right)$. As long as the SBP is fulfilled or as long as there is no pole included in our calculation, this would furthermore imply that all quark dressing functions develop an imaginary part and that the two quark vector dressing functions A_f and C_f are identical. In the next chapter, we will observe exactly this behavior and will be able to verify the analytic findings of Refs. [101, 141] with our numerical calculation. If we generalize this property to the main equations which we consider in this work, we get

$$f_{[\mu]}(P,p,k) = \int_q K((P),\tilde{p},\tilde{q}_{(\pm)},k) \overset{\mathrm{I}}{=} f_{\mathrm{vac}}(P,\tilde{p},k)\,, \tag{3.28}$$

$$K((P),\tilde{p},\tilde{q}_{(\pm)},k) \subset \{S(\tilde{q}_{(\pm)}), S(\tilde{p}), D_{\mu\nu}(k), \Gamma_{\mathrm{qg}}(x), \Gamma_{\mathrm{x}}^{(\nu)}(P,\tilde{q})\}\,,$$

$$f(P,p,k) \in \{S(p), \Gamma_{\mathrm{x}}^{(\nu)}(P,p), D_{\epsilon\gamma}(k), \left\langle \hat{\bar{\Psi}}\hat{\Psi} \right\rangle, \mathcal{N}_{\mathrm{x}}, f_{\mathrm{x}}\}$$

with the substitution I: $q_4 \to \tilde{q}_4 = q_4 + i\mu_{\mathrm{q}}^f$ and the momentum routing $k = \tilde{q} - \tilde{p} = q - p$. The substitution holds as long as there is no singularity in the area defined by $q_4 + it$ with $t \in [0, \mu_{\mathrm{q}}^f]$ and $q_4 \in [-\infty, \infty]$. Considering the different quantities appearing in $K((P),\tilde{p},\tilde{q}_{(\pm)},k)$, only $\Gamma_{\mathrm{qg}}(x)$ in the gluon DSE could exhibit singularities in the defined area. We know that $\Gamma_{\mathrm{qg}}(x)$ entails factors like $\frac{a}{b+x}$ with $x \propto p^2 + q^2$ in the gluon DSE and $x \propto k^2 = (p-q)^2$ in the quark DSE. While the chemical potentials of the momenta p and q cancel each other in the momentum $x \propto k$ of the quark DSE, we have an explicit chemical potential dependency in the gluon DSE. Ref. [142] showed that this chemical potential violates the SBP weakly. In consequence, a consistent implementation of the chemical potential in the vertex of the gluon DSE requires a dependence on $p_4 + i\mu_{\mathrm{q}}^f$ and $q_4 + i\mu_{\mathrm{q}}^f$. Since the observed SBP violation in the gluon is only weak and especially since we approximate the gluon propagator at finite chemical potential and vanishing temperature by its vacuum equivalent, we neglect this violation in our calculation and do not modify the vertex dressing.

To clarify again: The relation in Eq. (3.28) does not mean that our considered function $f_{[\mu]}(P,p,k)$ at finite chemical potential can simply be replaced by its vacuum counterpart at the same momenta P, p and k. Instead, we have to evaluate the vacuum counterpart at a shifted momentum $\tilde{p} = \left(\vec{p}, p_4 + i\mu_{\mathrm{q}}^f\right)$. Consequently,

as mentioned above, the relation implies that the number of dressing functions of the quark, gluon and meson at finite chemical potential is the same as in vacuum and all dressing functions develop an imaginary part, at least if the SBP is still valid.

4. Quarks and mesons at finite chemical potential

As a basis for the remaining work, we will now show and discuss the results for quarks and mesons at finite chemical potential but vanishing temperature. The results are obtained with the Hyb truncation presented in Sec. 2.2.3 without hadronic backcoupling, considering $N_f = 2 + 1$ dynamical quark flavors and equal light- and strange-quark chemical potentials $\mu_q^s = \mu_q^\ell$.[1] With our calculation, we go beyond previous works by (i) taking into account the dynamics of the gluon rather than simply modeling it, solving the homogeneous Bethe-Salpeter equation at finite chemical potential with (ii) more than the leading BSA component and (iii) using quark propagators explicitly evaluated in the complex momentum plane.

At first, we will consider the quark dressing functions and the related chiral order parameter and number density. Then, we discuss some restrictions and the necessary input (quarks at complex momenta) for the bound state calculation. Finally, we use the received data to determine the meson wave-functions and properties. These results were also published in Refs. [105, 143].

4.1. Quark dressing functions

We begin the discussion by plotting the first vector and the scalar light-quark dressing function A_ℓ and B_ℓ for different baryon chemical potentials in Fig. 4.1. The spread of the different line types results from the angle between the four momentum p and the assigned direction of the medium $v_{\text{med}} = (\vec{0}, 1)$. Consequently, the spread represents the angular dependence of the considered quark dressing functions resulting from the chemical potential. Note that the second vector dressing function C_ℓ is identical to the first vector dressing function A_ℓ for the chemical potentials shown in the plot. We will discuss this property in more detail later on.

[1] In previous works, we set $\mu_s = 0$. The change to a non-vanishing strange-quark chemical potential only influences the strange-quark condensate and mesons with strange-quark content.

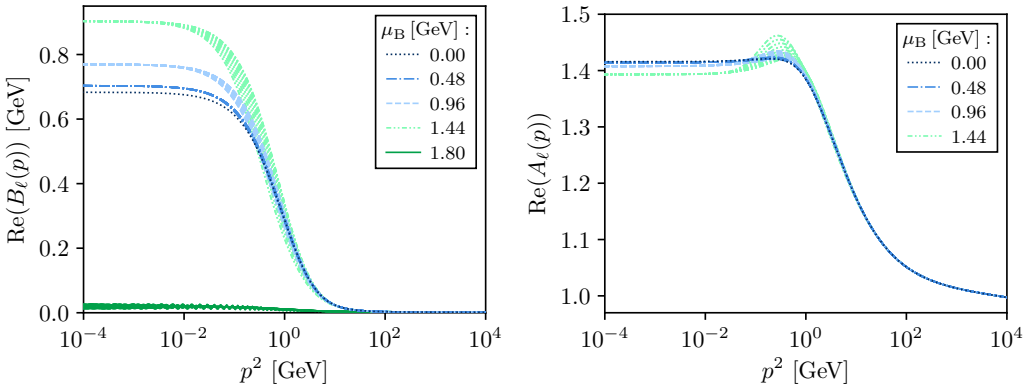

Figure 4.1.: Real part of the scalar B_ℓ (left) and first vector A_ℓ (right) light-quark dressing functions for different baryon chemical potentials μ_B plotted against real and space-like four momenta p^2. The spread of the dressing functions represent their angular dependency resulting from the assigned direction of the medium. Only the $\mu_B = 1.80\,\mathrm{GeV}$ data correspond to the Wigner solution while all remaining values result from the Nambu solution.

We observe that all dressing functions are (almost) independent from the chemical potential for momenta much larger than the scale of the considered chemical potential. In the mid-momentum region, however, the spread of the dressing functions, i.e. their angular dependence, increase with increasing chemical potentials. For small momenta, the scalar dressing function increase drastically with the chemical potential before it drops instantaneously to a much smaller magnitude at high chemical potential, indicating a restoration of chiral symmetry. The scalar dressing function then remains with almost no dynamical contribution. Overall, the first vector dressing function is much less chemical potential dependent than the scalar dressing function but effects can be seen. For baryon chemical potentials in the figure up to 1.44 GeV, the quark dressing functions correspond to the Nambu solution while they represent the Wigner solution above this value. The Nambu and Wigner solutions were already introduced and discussed in Sec. 2.2.4 and represent two types of stable quark solutions. The detected sharp transition between the Nambu and Wigner solution of the scalar dressing function already hints at a first-order transition for a certain chemical potential between 1.44 GeV and 1.8 GeV which we will discuss in the next section.

As indicated before, the first and second vector dressing function A_ℓ and C_ℓ are identical for the Nambu solution but become different for the Wigner solution. While the scalar dressing function almost vanishes in the Wigner solution, one vector dressing function decreases and the other increases strongly. A similar

behavior was found in Ref. [144]. The degeneracy of the vector dressing functions and the connected reduction of the tensor structure of the quark propagator to the vacuum case is not new but was shown analytically for a Rainbow-Ladder truncation in Ref. [141]. It was outlined that the quark propagator at finite chemical potential can be obtained from the vacuum equivalent by an analytical continuation of the form $S_{[\mu]}(p) = S_{[0]}(\tilde{p})$ with $\tilde{p} = p + i\mu_{\mathrm{q}}^{f} v_{\mathrm{med}}$.[2] This holds until the first pole in the complex momentum plane (of the quark) is reached.[3] Knowing the Silver-Blaze property (SBP) which we introduced and discussed in Sec. 3.2.3, one could assume that this pole results from a bound state pole in our calculation that breaks the SBP and would be located at the mass of the lightest baryon, i.e. the proton. But it is still an open question how the breaking of the SBP actually takes place. The backcoupling of the baryon does not necessarily imply a pole in the quark propagator. For the meson, this was shown in Ref. [57]. In Chap. 6, we will however see that the introduction of baryon backcoupling leads to a discontinuity in form of oscillations in the quark propagator if we pass a baryon chemical potential equal to the nucleon mass in medium.

As can be seen in Fig. 4.1, the scalar dressing function shows a mildly oscillating behavior for the Wigner solution. The two vector dressing functions oscillate even stronger and are therefore not shown for the Wigner solution. To find the origin of this behavior, we have to consider the analytic structure of the quark propagator for the Wigner solution. In Ref. [57], the analytic structure of the quark propagator was studied and the authors found that the Wigner solution in vacuum features a pair of complex-conjugated poles close to the time-like real momentum axis at very low quark masses. Since the introduction of chemical potential leads to a shift of the quark momenta into the complex plane, the integration path in the quark DSE is shifted beyond these poles if we consider large chemical potentials. In our calculation, this poses numerical problems[4] and leads to the oscillating behavior. To solve the oscillation problem in our calculation, we would need to dynamically determine the pole positions and their rank in every iteration step to be able to take into account the residues properly. This is not yet done and since we are mainly interested in the Nambu solution, it will not be considered further. But as we will discuss later, we will not be able to calculate mesons for the Wigner phase due to this behavior.

[2] This property is obtained under the assumption of a chemical potential independent gluon and an analytic behavior of the quark for low chemical potential. Whether the property holds when chemical potential effects in the gluon propagator are considered in our numerical calculation or the analytic derivation remains to be investigated.

[3] In Ref. [145], it was proposed that the appearance of poles is connected to a phase transition.

[4] For example, the Cauchy method, used in this work and discussed in App. C.1.2, is affected.

4.2. Quark condensate and number density

In this section, we will first discuss the chemical potential dependence of the quark condensate and will indicate some important regions, before we consider the quark number density $n_f = \langle \Psi^\dagger \Psi \rangle$ reaction on chemical potential. In Sec. 2.2.3, we introduced the approximation of the finite chemical potential gluon propagator through the vacuum gluon propagator if we consider finite chemical potentials and vanishing temperatures. Due to this additional approximation, finite chemical potential effects in the quark loop of the gluon DSE are ignored. In consequence, the light and strange quarks are no longer coupled and do not influence each other any more.[5] The regularization of the quark condensate by subtracting an appropriate amount of the strange quark as in Eq. (2.37) consequently does not make sense anymore. Instead, we regularize the light- and strange-quark condensate by subtracting the appropriate amount of the light-quark condensate evaluated at an high chemical potential where the dynamical part is expected to vanish. We now define the regularized quark condensate via

$$\langle \bar{\Psi}\Psi \rangle_f^{\mathrm{reg}}(\mu_\mathrm{B}) = \langle \bar{\Psi}\Psi \rangle_f (\mu_\mathrm{B}) - \frac{Z_m^f m_\mathrm{q}^f}{Z_m^\ell m_\mathrm{q}^\ell} \langle \bar{\Psi}\Psi \rangle_\ell (\infty) \,. \tag{4.1}$$

In Fig. 4.2, we display this vacuum-normalized and regularized quark condensate plotted against the baryon chemical potential μ_B. We differentiate between light and strange quarks and the two types of stable solutions: The chirally-broken Nambu and chirally-symmetric Wigner solution. If we consider the appearance and disappearance of these Nambu and Wigner solutions for the light and strange quark in the figure, we find different stability regions. Thereby, we observe the same pattern for light and strange quarks: For small chemical potentials only the Nambu solution can be found in the numerical iteration.[6] For large chemical potentials the Nambu solution disappears and only the Wigner solution remains. In a certain chemical potential interval in between, both solutions can be found as stable and attractive solutions.[105] We will refer to this interval as coexistence region or metastable area. The corresponding boundaries of the light- and strange-quark coexistence regions are given by

$$\mu_\mathrm{B} = \begin{array}{lll} \text{Wigner:} & \text{Nambu:} & \\ 0.936\,\mathrm{GeV}\,, & 1.730\,\mathrm{GeV} & (\text{light})\,, \\ 2.149\,\mathrm{GeV}\,, & 2.516\,\mathrm{GeV} & (\text{strange})\,. \end{array} \tag{4.2}$$

[5] In Ref. [115], the influence of this approximation was studied in the case of two color QCD.

[6] The Wigner solution is present too but neither iteratively attractive nor thermodynamically favored. See Refs. [57, 108, 109] for more information and explanations to the appearance and disappearance of the different solutions.

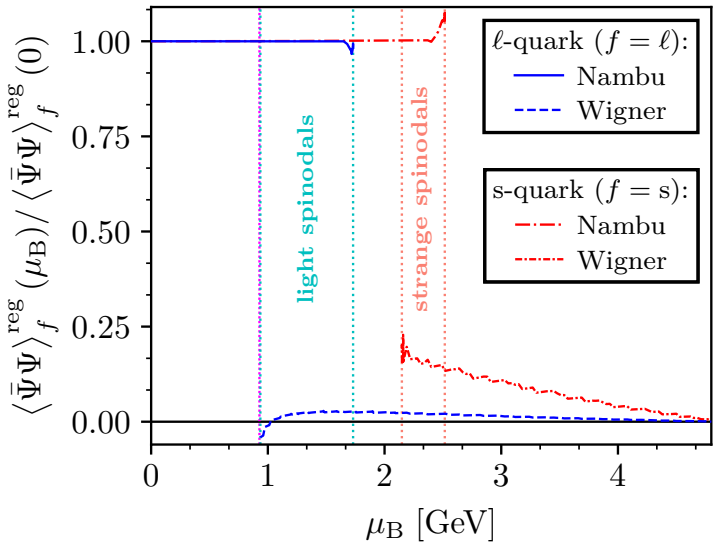

Figure 4.2.: Vacuum-normalized and regularized light (blue) and strange (red) quark condensate for the chirally-broken Nambu (solid and dashed lines) and chirally-restored Wigner (differently dashed dotted lines) solution plotted against the baryon chemical potential μ_B. The boundaries for the appearance/ disappearance of the Nambu and Wigner solution are denoted by vertical dotted lines in the corresponding color of the flavor and called light and strange spinodal points. The densely dotted magenta line corresponds to the mass of the nucleon in medium m_N and therefore represents the end of the Silver-Blaze region.

In Fig. 4.2, these so-called spinodal points are indicated by vertical dotted lines in the color of the considered quark flavor. The question which solution in the coexistence region is thermodynamically favored for a certain chemical potential has to be determined from thermodynamic considerations. It is clear that the physical first-order phase transition happens in this coexistence region but the exact value of the chemical potential where the Wigner solution is thermodynamically favored over the Nambu solution for the first time remains an open question. In the functional Dyson-Schwinger approach, the determination of the thermodynamic potential and consequently the first-order phase transition is tremendously difficult and mostly limited to Rainbow-Ladder truncations, see e.g. Refs. [40, 146, 147]. While it is applicable to our Hyb truncation, we cannot use it for the more elaborated 1BC truncation. A truncation independent way of determining the thermodynamic potential and the equation of state was introduced in Ref. [43]. But the problem is that this method relies on input data for the Wigner phase which are still missing. Since the thermodynamic calculations are out of the scope of the present work, we

will not consider it further.

Another interesting question is whether the chiral symmetry breaking of the light and strange quarks react similarly to chemical potential or if we even find different first-order phase transitions for the quark flavors. In a fully backcoupled system of equations, the first-order transition appearing in the light-quark sector at some critical chemical potential inevitably leads to non-analytic changes in the strange-quark propagator (see Ref. [148] for an explicit calculation of this effect). It is, however, not clear if the corresponding loss in interaction strength due to the almost mass-less (and screening) light quarks is sufficient to reduce the strange quark immediately to its Wigner solution. Instead, there possibly is a chemical potential interval where the strange quark still feels chiral symmetry breaking, however with reduced strength, while the light quarks are already in the Wigner phase. Then, at higher chemical potential, a second first-order transition in the strange-quark sector appears. The plausibility of this scenario, certainly, remains to be studied.[143] In our calculation, because of the vacuum gluon propagator approximation and the resulting lack of backcoupling of the light and strange quarks onto the respective other quarks, we expect and indeed find two different coexistence regions for the light and strange quarks.

After discussing the different quark solutions, we can now take a closer look at the actual behavior of the quark condensates. The light- and strange-quark condensates belonging to the respective Nambu solution remain constant for chemical potentials far into the coexistence regions. The quark condensate therefore fulfills the Silver-Blaze property (SBP), although it is strictly speaking not an observable quantity. In addition, the precision is astonishing: Up to the chemical potential $\mu_{\mathrm{SB}} = 928\,\mathrm{MeV}$ the quark condensate only increases by 0.001 %. This value corresponds to the mass of the nucleon m_{N} in medium with subtracted binding energy and marks the end of the validity of the SBP. In Fig. 4.2, we highlight the end of the Silver-Blaze region by a vertical, magenta and densely dotted line. This line is very close to the lower light-quark spinodal point and therefore shortly below the light-quark coexistence region. Deviations from the constant behavior can only be found shortly before the end of the corresponding coexistence region. For the Wigner solution, we observe that the light-quark condensate increases for lower chemical potentials and settles for higher ones whereas the strange equivalent decrease steadily. Both quark flavors show oscillatory behavior which is due to the fact that the quark dressing functions oscillate, too. As result, it is unknown if we can actually trust the Wigner results.

We remark that we are in qualitative good agreement with simpler truncations in Refs. [63, 96, 141, 144, 149, 150] which all fulfill the Silver-Blaze property at least approximately. The first-order transitions found in these works also correspond to our light-quark coexistence region. An important observation of Ref. [96],

furthermore, is that a full (self-consistent) quark backcoupling is necessary to fulfill the SBP. Hard dense loop calculations with bare quark propagators in the quark loop are not sufficient.

To conclude, we shortly consider the non-observable quark number density $n_f = -Z_2^f \operatorname{Tr}_{\mathcal{F}} \gamma_4 S^f$. For finite chemical potential and vanishing temperature, we find a linear increase with increasing chemical potential which coincides with results at finite but low temperatures in Ref. [42]. This behavior represents the fact that more quarks exist the more energy is present in the system. Deviations from the linear behavior cannot be found. This could either be the actual physical behavior or due to the fact that the quark number density calculation at finite chemical potential but vanishing temperature is strongly cutoff dependent and needs to be regularized properly. Unfortunately, our present regularization method introduced in Ref. [42] is not applicable for this calculation. As result, further studies are necessary to investigate the behavior of the quark number density.

For the following investigations of the meson properties, we will display the light and strange coexistence regions by the spinodal points similar as in Fig. 4.2. The same is true for the indication of the end of the Silver-Blaze region.

4.3. General remarks for the meson results

Before we can discuss the results for the meson properties and wave-functions, we have to mention some features and problems of the bound state calculation. As already mentioned in Sec. 3.1.2 and discussed in App. C.1.3, it is necessary to evaluate the quark propagator at complex momenta for the bound state calculation. If we consider the Wigner solution, the oscillatory behavior of the quark dressing functions found in the last two sections aggravates for this "complex quark" calculation and prevent the iteration from converging. Up to now, this problem with the analytic structure of the quark propagator is beyond current solution techniques. Due to this technical problem and because we expect to encounter super-conducting phases in this region of the phase diagram for chemical potentials above the physical phase transition[7], we refrain from using the Wigner solution and calculate bound state results only with the Nambu solution.[8]

[7] The inclusion of super-conducting phases into our calculation requires a substantial extension of the framework to the Nambu-Gorkov formalism studied in Refs. [95, 96].

[8] The determination of mesons for the Wigner solution has only been accomplished in the vacuum [151].

Since we consider mesons in the rest frame, the chemical potential and the time-like total momentum of the meson add up[9] and as a consequence we need to provide the quark further out in the complex momentum plane. This property, together with the inability to calculate the "complex quark" for the Wigner solution, implies that we can only calculate the meson if $|\mu_{\mathrm{q}}^{f} \pm \eta_{\pm} m_{\mathrm{x}}| < \mu_{\mathrm{q,N}}^{f}$ is fulfilled. Here, m_{x}, $\eta_{\pm}$, and $\mu_{\mathrm{q,N}}^{f}$ denote the meson mass, the quark momentum partitioning parameter, and the upper spinodal point of the quark flavor f, respectively. As a result of this restriction, for fixed m_{x} and μ_{q}^{f}, there exists a certain chemical potential dependent partitioning parameter η_{+} interval where calculations of "complex quarks" and mesons are possible. The higher the meson mass, the smaller this interval becomes. More information on this interval and how we calculate heavy mesons until the end of the coexistence region are deepened in App. C.2.3. Since the coexistence region of strange quarks appears at higher chemical potentials than the one of light quarks, we are able to calculate mesons with strange-quark content for higher chemical potentials.

4.4. Bethe-Salpeter amplitudes

In this section, we will discuss the behavior of all considered mesons under chemical potential and momentum partitioning parameter changes. All Bethe-Salpeter amplitudes are always plotted on-shell and normalized. Derived quantities are based on these normalized and on-shell BSAs. At first we will consider the properties of the (pseudo-)Goldstone Bosons, the Pions, and its chiral partner, the Sigma meson. Then, the remaining mesons will be discussed. In Fig. 4.3, we show a collection of the most important properties of the Pion and Sigma meson BSAs which will be important for the meson backcoupling in the next chapter. We will now begin by discussing the chemical potential dependence of the Pion BSA with a symmetric ($\eta_{\pm} = 0.5$) momentum partitioning parameter (upper row) before we continue with the Pion and Sigma BSA properties for an asymmetric momentum partitioning parameter (lower two rows).

In the upper left panel of Fig. 4.3, the real part of the first normalized BSA component of the on-shell Pion (E^{π}) is plotted against the relative four-momentum for a symmetric momentum partitioning parameter and different chemical poten-

[9] The chemical potential and the total momentum of the meson in rest frame are aligned and only contribute to the energy component of the four momentum, which is at the same time the assigned direction of the medium. Due to this alignment, we can, in a certain extent, map the chemical potential and the partitioning parameter onto another. If we stop using the rest frame, the momentum partitioning parameter dependence, which we will show in the next two sections, could decrease but the calculation is much more complicated.

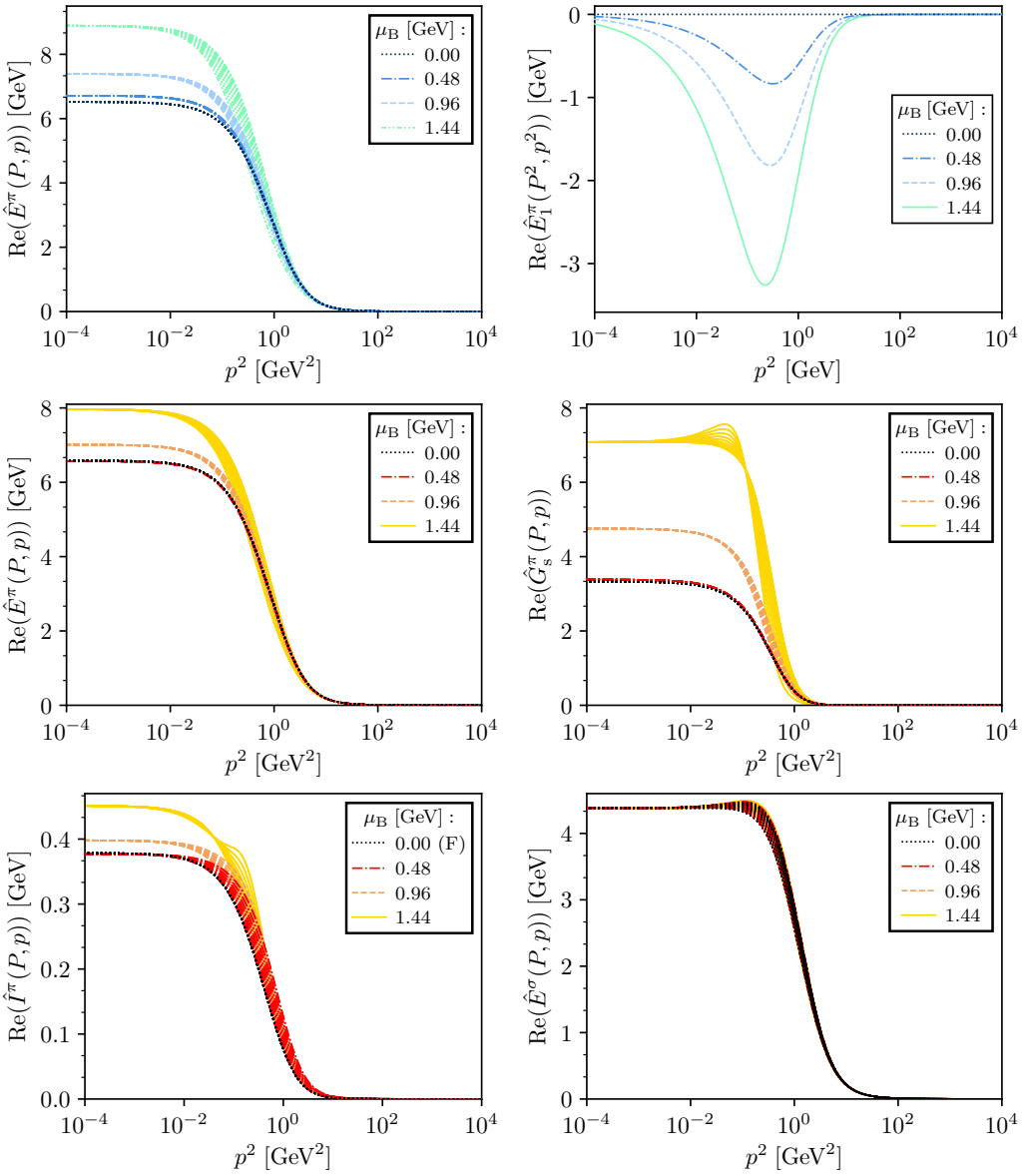

Figure 4.3.: Upper row: Real part of the first normalized on-shell Pion BSA component $\hat{E}^\pi$ (left) and its corresponding first Chebychev coefficient $\hat{E}_1^\pi$ (right) plotted against the relative four-momentum p^2 between the quarks for various baryon chemical potentials μ_B and a symmetric momentum partitioning. Center and lower row: Corresponding data for the real part of the first three normalized on-shell Pion BSA components ($\hat{E}^\pi, \hat{G}_s^\pi, \hat{I}^\pi$) and the first normalized on-shell Sigma BSA component ($\hat{E}^\sigma$) for an asymmetric momentum partitioning $\eta_+ = 0$. The spread of the amplitudes represent their dependence on the angle between the total and the relative momentum of the considered meson.

tials. For a given chemical potential, we further display amplitudes with different angles $\cos(\sphericalangle(P,p)) = \hat{P}\hat{p}$ between the total momentum of the meson P and the relative momentum between the quarks p. Consequently, the spread of the different line types represents the angular dependence. If we compare the chemical potential dependence of this BSA with the one of the scalar quark dressing function in Fig. 4.1, we detect a similar behavior for both quantities. This means that we observe a vanishing chemical potential dependence at large momenta, an increasing angular dependence in the mid momentum region and a strong increase of the BSA at low momenta. But in contrast to the scalar quark dressing function, this increase with the chemical potential experiences a saturation at high chemical potential. This saturation is not visible in the plot since it happens in a small chemical potential interval.

For an explanation of this similarity to the scalar quark dressing function, we have to consider the chiral limit. In chiral limit all Pion BSA components can exactly be represented by generalized Goldberger-Treiman like relations as shown in Ref. [31] for the vacuum. This relation is approximately true also for finite quark masses and expected to persist in medium. For this purpose, this relation was used as approximation in previous vacuum [56–58, 152] and medium [63, 101, 145] studies. For the first Pion BSA component E^π, the relation is given by $\hat{E}^\pi(0,p) = \mathrm{B}(p)/f_\pi$ which explains the similarity of the scalar quark dressing function and the first Pion BSA component. But as we will see in the next section, the Pion decay constant decreases at high chemical potential which would normally lead to a further increase but instead we observe a saturation of the BSA. This disagreement can have different reasons. For example, the approximation is no longer valid for physical quark masses and very high chemical potentials or our calculation breaks down at very high chemical potentials in the coexistence region. As mentioned earlier, at high chemical potentials, our framework should be replaced by a Nambu-Gorkov formalism. However, at low chemical potential the relation seems to hold.

Now we can take a closer look at the angular dependency by making use of the Chebychev expansion representation of the BSA in Eq. (3.15). The zeroth Chebychev coefficient is the only one with a non vanishing contribution at low momenta, since it equals the angular average of the full BSA component. At small chemical potential it therefore gives the largest contribution to the full amplitude. All higher coefficients contribute to the chemical potential dependency in the mid-momentum region, yielding the angular dependence of the BSA. Thereby, the importance of the Chebychev coefficients decrease by one order of magnitude for every order of Chebychev polynomials. The importance of the higher Chebychev coefficients, however, increase with increasing chemical potential as can be seen in the upper right panel of Fig. 4.3 for the first Pion BSA component. In vacuum

the second Chebychev coefficient is more important than the first one. This is due to the fact that in vacuum the neutral Pion is an invariant state under charge conjugation. As explained in Sec. 3.1.2 this causes all odd Chebychev coefficients to vanish for a symmetric momentum partitioning. Therefore: $\mathrm{E}_1^\pi(\mu_\mathrm{B} = 0) = 0$. When the chemical potential is switched on, this property disappears and all odd coefficients begin to contribute as can be seen in the upper right panel of Fig. 4.3. At a certain point, the first Chebychev coefficient even becomes more significant than the second one. To remember, the charge conjugation exchanges particles with their corresponding antiparticles and vice versa. Due to the energy offset which is introduced by the chemical potential, antiparticles and particles are no longer energetically degenerated and the charge conjugation symmetry gets broken.[105]

To study the influence of the momentum partitioning parameter on the first Pion BSA component, we compare the upper and center left panel in Fig. 4.3. As already mentioned the results in the upper left panel are calculated with a symmetric momentum partitioning ($\eta_\pm = 0.5$). The center left panel is calculated with an asymmetric momentum partitioning of $\eta_+ = 0$. While the vanishing chemical potential dependence at large momenta remains the same, the angular dependence at mid momentum and the increase at low momenta are less pronounced for the asymmetric momentum partitioning. The reaction of the BSA on a reduced η_+ parameter is similar to a reduction of the chemical potential. We would like to emphasize, that the BSAs can depend on the partitioning parameter since they are no observables. The partitioning parameter of all other mesons, especially the high-mass mesons, are much less pronounced, since their dependence on chemical potential is much smaller. We will see this behavior in a bit. From now on we will consider only the asymmetric momentum partitioning.

Considering the center panels and the lower left panel of Fig. 4.3, we see that all three Pion BSA components (E^π, $\mathrm{G}_\mathrm{s}^\pi$ and I^π) show a similar behavior. This means: All BSA components increase with the chemical potential at low momenta, spread more in mid-momentum region and do not react to chemical potential at large momenta. The strength of the infrared increase and the spreading, however, is different for the BSA components. The $\mathrm{G}_\mathrm{s}^\pi$ component almost doubles its magnitude and therefore becomes comparable in strength to the leading BSA component E^π at large chemical potential. This shows the importance of taking $\mathrm{G}_\mathrm{s}^\pi$ into account. The I^π component, however, increases only weakly but shows a much stronger chemical potential dependence in the mid momentum.[143] Additionally, the two sub-leading BSA components do not show a saturation of the increase at low momenta. Furthermore, all Pion BSA components connect smoothly to the corresponding vacuum limit. For the vacuum limit of the medium I^π BSA component in the lower left panel, we have to plot $\mathrm{F}^\pi/\sqrt{p^2}$. This agreement

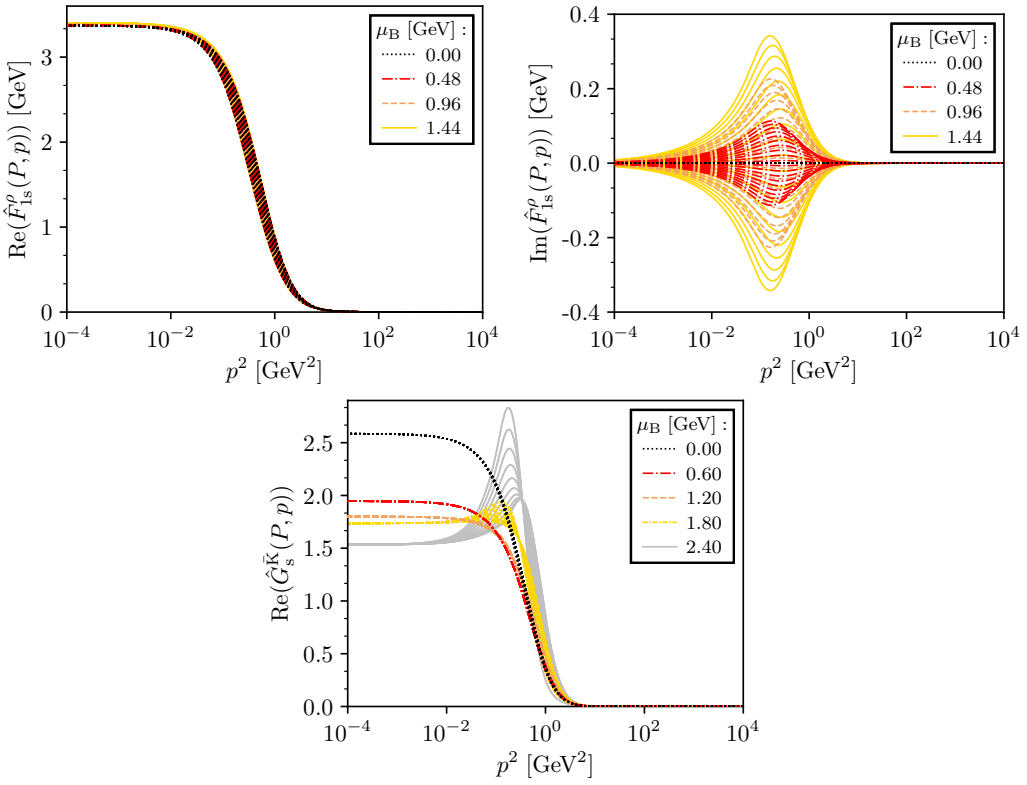

Figure 4.4.: Upper row: Real (left) and imaginary (right) part of the spatial part of the first normalized on-shell Rho BSA component $\hat{F}^{\rho}_{1s}$ plotted against the relative four-momentum p^2 between the quarks for various baryon chemical potentials μ_B and a asymmetric momentum partitioning $\eta_+ = 0$. Lower row: Similar results for the second normalized on-shell $\bar{K}$ meson BSA component $\hat{G}^{\bar{K}}_{s}$.

between the vacuum BSA F^{π} and I^{π} is surprising since I^{π} gets contributions from both vacuum BSA components F^{π} and G^{π}.

Finally considering the Sigma meson in the lower right panel of Fig. 4.3, we see that the real part of the Sigma BSA component shows almost no chemical potential dependence. The same is true for the other two BSA components. They only decrease marginally at low momenta and increase their spread in the mid-momentum for increasing chemical potential. All other high-mass meson BSAs, in particular those of the (axial-)vector mesons, show a very weak chemical potential dependence in the real part of the BSAs, too. Nevertheless, all mesons develop a significant chemical potential dependence in the imaginary part as demonstrated exemplary in the upper panels of Fig. 4.4 for the Rho meson. Thus,

the imaginary parts of the amplitudes that all mesons show, are important to balance the variations in the quark propagator w.r.t. the chemical potential and to provide the Silver-Blaze property as we will see later on.

As final mesons, we will consider the special case of light-strange quark mixed mesons, the Kaons. It is important to note that the momentum partitioning dependence of the Kaons is no longer symmetric since they consist of light ℓ and strange s quarks. This results in a different chemical potential behavior of the amplitudes for the kaons (K,K^+) with quark content $\ell\,\bar{\mathrm{s}}$ and the antikaons ($\bar{K}$,K^-) with quark content $\bar{\ell}\,\mathrm{s}$. In the following, we will only discuss K and $\bar{K}$ since $K^{+/-}$ is degenerated to $K/\bar{K}$ due to the use of the isospin-symmetric limit. The meson BSA components of both Kaon types behave qualitatively similar as the one of the π but the changes are much less pronounced. Most importantly, the G_s^K BSA component of the K meson remains weak and does not become comparable to the leading BSA E^K. For the $\bar{K}$ meson, the $\mathrm{G}_\mathrm{s}^{\bar{K}}$ BSA component even decreases as shown in the lower panel of Fig. 4.4 whereas $\mathrm{I}^{\bar{K}}$ shows a stronger increase as compared to the K meson.[143]

Before we continue with the meson properties, we conclude the BSA discussion mentioning an analytic requirement for the BSAs. In Ref. [101], it was shown that every type of quark-meson vertex at finite chemical potential can be obtained from the vacuum pendant by an analytic continuation of the form $\Gamma_{[\mu]}(P,p,\ldots) = \Gamma_{[0]}(P,\tilde{p},\ldots)$ similar as for the quark propagator, also with the same requirements (see Sec. 4.1). As a consequence, the number of independent Dirac tensor structures of the BSA at finite chemical potential should be equal to the one of the vacuum until the first pole appears. Unfortunately, due to the use of the rest frame we cannot include $\mathrm{F}_\mathrm{s}^\mathrm{x}$ to check this property.

4.5. Meson properties

In this section, we will use the quark and meson BSA results from the previous sections to determine and study the meson properties. We will consider the meson mass(es) and decay constants at finite chemical potential and vanishing temperature. Since we consider the mesons to be in the rest frame, the spatial decay constants of pseudo-scalar mesons are not accessible. The scalar Sigma mesons does not have a leptonic decay constant. To remember, the determination of the meson for the Wigner solution is not possible. Therefore, we will only show results for the Nambu solution. At first, we will discuss the tensor structure and momentum partitioning parameter dependency for the Pion in detail. Then we consider all meson properties in a compact form for the most elaborated approximation of the

BSA. To guide the eye, we will indicate the spinodal points and the end of the Silver-Blaze region in the same way as in Sec. 4.2.

In the upper panels of the Fig. 4.5, the Pion mass and temporal Pion decay constant are shown in vacuum and for finite chemical potential and different levels of approximation of the BSA (different set of BSA components used in the bound state calculation). In vacuum, we display these different levels of approximation as colored symbols. As one can see, the vacuum limit of the Pion mass and decay constant is fulfilled within the numerical precision.[10] If we consider the overall behavior under chemical potential, the addition of the I^π BSA component to the calculation leads to qualitative and quantitative changes of the Pion mass and decay constant. On the one hand, the mass and decay constant are increased and on the other hand, the behavior in the coexistence region is affected. The addition of the G_s BSA component, however, has only a small effect on the Pion mass but a significant quantitative and qualitative effect for Pion decay constant. It leads to a strong decrease in the coexistence region. As expected in Sec. 3.1.4, the I^π BSA component is important for the Pion mass and decay constant whereas G_s is of importance mostly for the Pion decay constant. We refrain from adding more tensor structures to the calculation due to the resulting numerical complexity and since we do not expect a significant qualitative or quantitative change of the properties.

Within the numerical precision, the Pion mass and decay constant for the different levels of BSA approximations remain constant also beyond the end of the Silver-Blaze region. Therefore, the Silver-Blaze property is clearly satisfied. The deviations from the vacuum are smaller than 0.5 % for the Pion mass and 2 % for the temporal Pion decay constant up to the end of the Silver-Blaze region. We are able to trace the existence of the Pion as (pseudo-)Goldstone Boson almost to the end of the coexistence region. For larger chemical potentials it is, for numerical reasons, not possible to identify solutions of BSE. Until the numerical stability decreases drastically and we are no longer able to obtain solutions (shortly before the end of the coexistence region), the Pion mass increases up to 14% compared to the vacuum value. For the temporal Pion decay constant we find a 20% decrease compared to the vacuum value.

After the discussion of the dependence on the used BSA approximation, we now consider the partitioning parameter dependence of the Pion mass. In the central panel of Fig. 4.5, we display the Pion mass plotted against the chemical potential for the symmetric ($\eta_\pm = 0.5$) and a certain asymmetric ($\eta_+ = 0$) momentum partitioning. The difference between the asymmetric and the symmetric solution increases up to 7% for the Pion mass and 5% for the Pion decay constant. But a

[10] Since I^π gets contribution from the vacuum F^π and G^π BSA component, its limit is ambiguous.

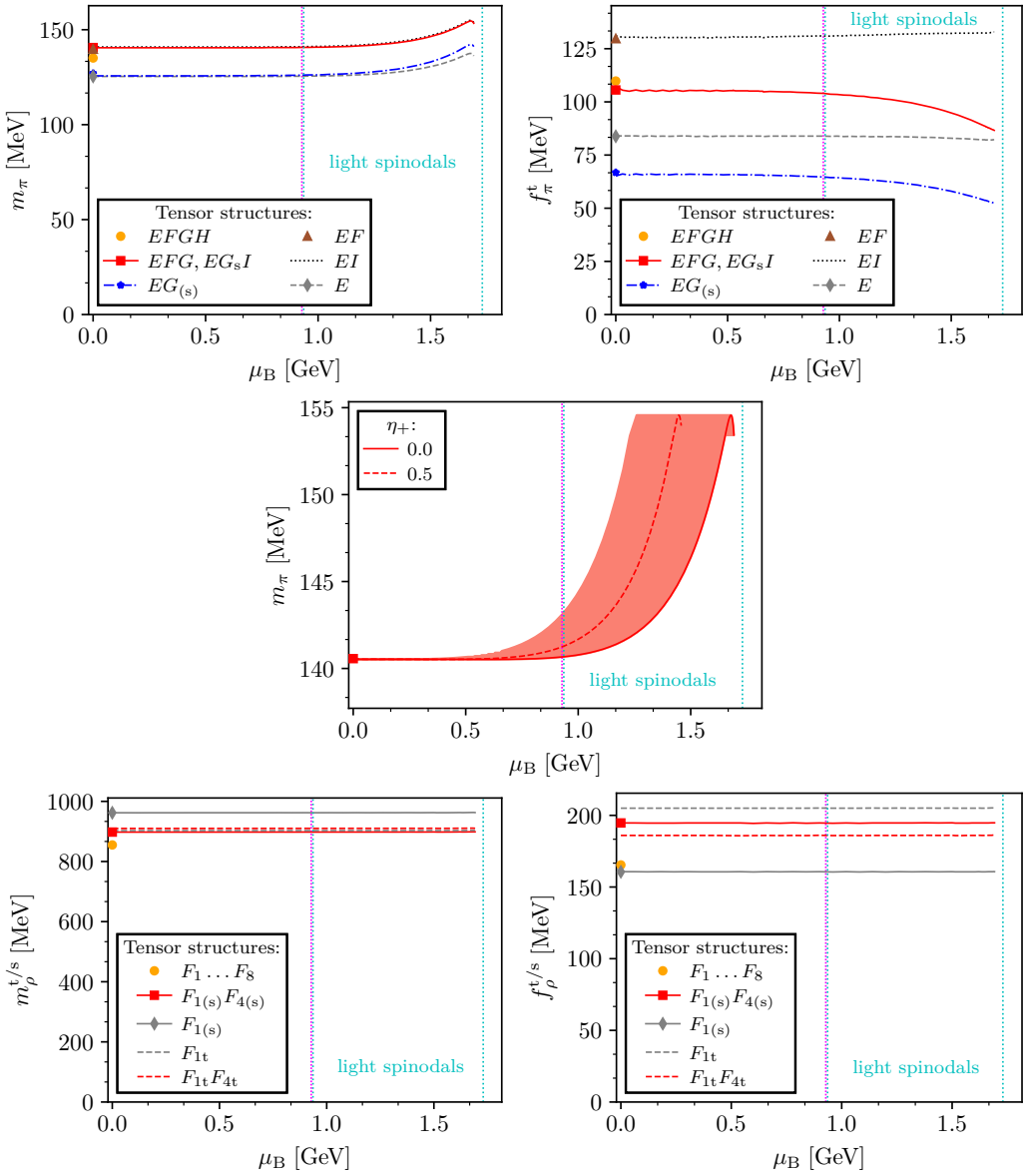

Figure 4.5.: Upper row: Pion mass m_π (left) and temporal decay constant f_π^{t} (right) plotted against the baryon chemical potential μ_{B} for different combinations of tensor-structures used in the BSE calculation. The results are obtained using an asymmetric momentum partitioning $\eta_+ = 0$. Lower row: Similar results for the spatial and temporal Rho mass $m_\rho^{\mathrm{t/s}}$ (left) and decay constant $f_\rho^{\mathrm{t/s}}$ (right). For these results the momentum partitioning has to be varied as explained in App. C.2.3. Center row: Momentum partitioning parameter dependence of the Pion mass in dependence of the baryon chemical potential for the most elaborated tensor-structure combination of the BSE calculation. The meaning of the shaded area is explained in the text. The vertical dotted lines are adopted from Fig. 4.2. The colored symbols represent the vacuum results.

comparison is only possible up to a chemical potential of $\mu_{\mathrm{B}} = 1.4\,\mathrm{GeV}$. Up to the end of the Silver-Blaze region, the partitioning parameter dependence is much weaker. While the mass deviates by less than 0.6%, the decay constant differs by maximally 1.5%. Consequently, we can safely assume that the Silver-Blaze property is not affected. Nonetheless, the partitioning parameter dependence is much stronger than in vacuum. There, the difference between the symmetric and asymmetric partitioning is less than 0.3% for all meson kinds and levels of BSA approximations. In vacuum, this dependence clearly is a numerical artifact.

As already mentioned in Sec. 4.3 and indicated for the transition between the symmetric and asymmetric partitioning representation of the Pion BSA in Sec. 4.4, there is a connection between the chemical potential and momentum partitioning parameter if we use the meson in the rest frame. For the meson properties, we find that we can obtain the Pion mass for a certain momentum partitioning parameter $\eta_{\pm}^{'}$ from another momentum partitioning parameter $\eta_{\pm}$, at least approximately, via the relation $m_\pi(\mu_{\mathrm{B}}', \eta_{\pm}^{'}) = m_\pi(\mu_{\mathrm{B}}, \eta_{\pm})$ and $\mu_{\mathrm{B}}' = \mu_{\mathrm{B}} \pm 3(\eta_{\pm} - \eta_{\pm}^{'}) m_{\mathrm{x}}(\mu_{\mathrm{B}}, \eta_{\pm})$.[11] In the figure, we used this relation to show the possible Pion mass values for the whole interval of partitioning parameter values as a shaded area. As one can see, the shaded area shows larger deviations from the vacuum of the order of 1.8% already at the end of the Silver-Blaze region. We assume that this larger deviation is an artifact of the rest frame calculation which originates from the alignment of the chemical potential and the total momentum of the meson in rest frame. Consequently, it is advisable to study the mesons also using the moving frame to check the corresponding partitioning parameter dependence. Because of the almost perfectly constant behavior of heavy mesons which we will discuss later, the momentum partitioning parameter dependence of these mesons is much weaker and can be neglected.

After discussing the Pion properties in detail, we can now discuss the other considered mesons. In Fig. 4.6, we show the meson mass(es) and decay constants for multiple light- and strange-quark mesons at finite chemical potential and for the respective most elaborated approximation of the BSA. Interesting aspects for the influence of different levels of BSA approximations will only be discussed in the text. The K and $\bar{K}$ meson properties behave similarly as the one of the π meson (for all levels of the BSA approximation). But while the observed decrease of the decay constant is much less pronounced for the K meson and almost constant, it is only modified marginally for the $\bar{K}$ meson. The chemical potential dependence of the two Kaon masses is reduced, too. Furthermore, due to the quark content of the two mesons, the K meson can only be calculated up to the end of the light-

[11] The Pion decay constant in a certain momentum partitioning cannot be approximated by another partitioning since it further depends on the on-shell mass itself.

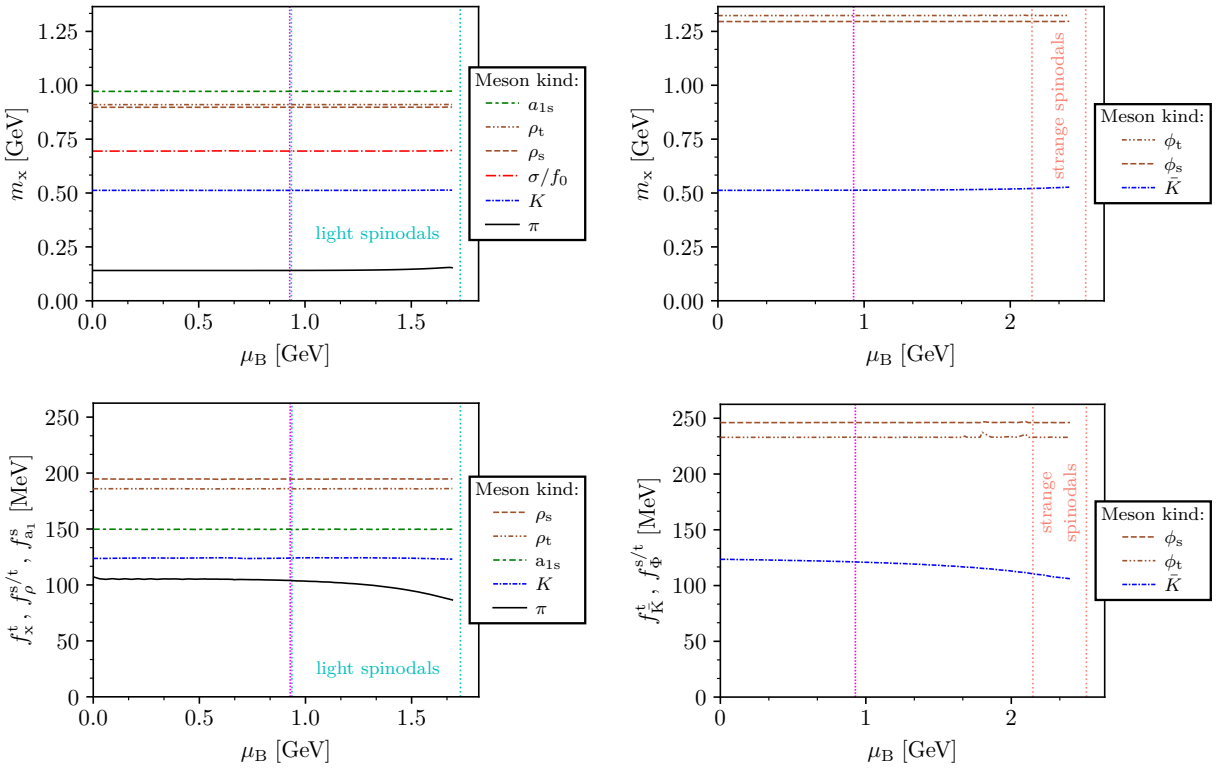

Figure 4.6.: Masses (upper) and decay constants (lower) for different light-quark (left) and strange-quark (right) mesons plotted against the baryon chemical potential for the most elaborated tensor-structure combination of the BSE in medium. The results are calculated using the chirally-broken Nambu solution. Again, the vertical dotted lines represent the end of the Silver-Blaze region (magenta) whereas the light (blue) and strange (red) spinodal points indicate the corresponding coexistence region.

quark coexistence region while the $\bar{K}$ meson is calculable into the strange-quark coexistence region. Until the end of the corresponding coexistence regions (or the breakdown of the numerical stability) the K and $\bar{K}$ meson mass increase by 0.25% and 3%, respectively, whereas the corresponding temporal decay constants decrease by 0.5% and 15%. If we consider the deviations of the K and $\bar{K}$ meson properties from their respective vacuum value only up to the end of the Silver-Blaze region, we can safely state that the Silver-Blaze property is fulfilled within the numerical precision. The deviations are below 0.5% and 2% for the meson masses and decay constants, respectively.

The mass of the σ meson as well as the longitudinal and transversal ρ and ϕ properties remains perfectly constant until the end of the corresponding coexistence regions with a maximal deviation of less than 0.5%. Consequently, we can state that the SBP is fulfilled for these mesons, too. If we consider the temporal and spatial projections of the ρ and ϕ properties, we observe different values for the two orientations of the mass and decay constants. This is shown exemplary for the Rho meson in the lower panel of Fig. 4.5. As we can see, only the spatial Rho meson quantities have a smooth vacuum limit. The reason is that the temporal counterpart receives contributions from several vacuum BSA components. The vacuum limit therefore becomes ambiguous. By including the sub-leading second tensor structure F_4, the difference between the two orientations of the vector meson properties decrease drastically. The wiggly behavior of the ϕ meson properties in Fig. 4.6 is due to the numerics. Also because of numerical reasons, only the spatial projection of the a_1 meson is calculable. Like all heavy-mass mesons, the mass and decay constant of the spatial projection of a_1 remain perfectly constant until the end of the light-quark coexistence region fulfilling the Silver-Blaze property.

We would like to emphasize that the observation of a constant behavior for all meson masses and decay constants until the end of the Silver-Blaze region (and beyond) is a highly non-trivial matter. That the Silver-Blaze property is fulfilled in our calculation relies on subtle cancellations between the chemical potential dependence of the quarks, their interactions inside the mesons and the BSAs. These quantities have to interplay such that they produce constant masses and decay constants. It is quite satisfying to see that this happens in our functional approach.[143]

The observation of the Silver-Blaze property, however, is not new but was observed, at least approximately, in previous works using the functional Dyson Schwinger or FRG approaches, see e.g. Ref. [63, 101, 145, 150, 153–156] or Ref. [157–159], respectively. Most of these works use effective models like the NJL or QM model or apply quite strong truncations for the equations (of the elementary particles) like contact or so-called Maris-Tandy interactions [32]. Even if the elementary particles are properly calculated by solving their corresponding DSEs, the bound state calculation mostly relies on approximations. Apart from Ref. [63], all previous Dyson-Schwinger works did not calculate the meson BSA from the BSE at finite chemical potential but used e.g. generalized Goldberger-Treiman like relations [31] as approximations for the BSAs. The corresponding meson masses and decay constants then have to be obtained from the Pagel-Stokar [160] and GMOR equations. But the usage of these approximations lead to an over- or underestimation of the vacuum Pion properties up to 30% [160]. Furthermore, Ref. [150] is the only work taking the splitting of the decay constant into account. In addition, effects of sub-leading BSA components have not been studied so far at

finite chemical potential. While the pion mass and decay constant at finite chemical potential are often studied in these works, the corresponding chemical potential dependence of the wave-function is mostly neglected. The same applies to the other mesons calculated in this work, at least if they are considered. Although these works used effective interactions and further approximations for the bound state calculation, they deliver qualitatively similar results, at least up to the coexistence region. In the coexistence region there is no unique statement regarding the behavior of the meson properties.

To our knowledge, this work is the first to study not only the meson masses and decay constants until the end of the corresponding coexistence region but also the corresponding BSAs. (Almost) no work has calculated the BSAs, especially not for such an elaborated truncation of the BSAs themselves and of the whole set of equations. In addition, most works restrict themselves to the (pseudo-)Goldstone bosons and possibly vector mesons in addition while we studied a great variety of different mesons. We are quite satisfied to see that our complex calculation of explicitly solving the quark DSE in the complex momentum plane (by taking into account the full momentum dependence of the gluon) and the meson BSE, norm and decay constant worked and yields such convincing results. Nevertheless, as discussed in the last sections and the Sec. 3.2.1, there is still room for improving our calculation.

To conclude the discussion of the meson properties, we mention that there are few lattice studies at very low temperature to compare with. For example in Ref. [161] Pion properties are analytically continued from imaginary to real chemical potentials. For decreasing temperatures the chemical potential dependency of the Pion mass becomes weaker yielding an almost constant behavior up to high chemical potentials where the mass increase monotonically. This coincides with our observations.

5. Meson backcoupling at finite chemical potential and temperature

In this chapter, we are interested in the influence that mesonic (backcoupling) effects have on the QCD phase diagram. For this purpose, we have to mention that the physics of the QCD phase diagram and the meson properties in medium are closely connected in different ways. Especially for the DχSB and its restoration, pseudo-scalar and scalar mesons are important.[1] On the one hand, the pseudo-scalar mesons are the (pseudo-)Goldstone Bosons of chiral symmetry breaking and the scalar mesons are their chiral partners. On the other hand, the two meson types are important for the universal behavior if they are backcoupled.[105]

In the vicinity of second-order chiral phase transitions the relevant degrees of freedom (dof) are associated with long-range correlations. The pseudo-scalar and scalar mesons constitute to these effective long-range dof that control the universal behavior of QCD at second-order chiral phase transition points. If we consider the two-flavors theory in chiral limit, we may observe a second-order phase transition in the O(4) universality class with isovector Pions and an isoscalar scalar meson as driving dof. This however also depends on the fate of the $U_A(1)$-symmetry. At physical quark masses and at the second-order critical endpoint (CEP) this is expected to turn into a Z(2) universality class of the Ising model in three dimensions driven by an isoscalar scalar meson [52].[2] That the mesonic backcoupling contributions become dominant for the universality properties of the CEP, was observed in a corresponding analytic scaling analysis in our framework [38], too. There, the introduction of Pion and Sigma meson backcoupling diagrams lead to a change of the universality class from a mean field to an O(4) scaling.[55, 105] Furthermore, it is clear that the critical region around the CEP, where the (meson) fluctuations are large, is quite small [52]. But we do not know to what extent these meson fluctuations are able to influence the location of the CEP. Consequently, the purpose of this chapter is a quantitative study of this effect. Preliminary work

[1] The Refs. [162, 163] also argued that Pion effects in the quark propagator may even be responsible for quark confinement.

[2] While the Pions remain massive the Sigma mesons become mass-less and therefore important for the scaling of the universality class.

was already done in Ref. [89]. The determination of the universality properties of the CEP will not be considered.

Now the question remains which mesons should be backcoupled. We already saw that the Pion and Sigma mesons are important for the correct scaling properties of the CEP but we are rather interested in the overall changes of the whole phase diagram. Considering the meson backcoupling term of the quark-gluon vertex in Fig. 2.4 at vanishing temperature and physical quark mass, it transpires that the meson exchange is dominated by the exchange of the lightest mesons, the Pions. The other hadrons are suppressed by a factor of $\Lambda_{\mathrm{QCD}}^2/m_{\mathrm{x}}^2$ relative to the Pion [56]. Although the vector mesons would be important for the observed dilepton spectrum[3] and together with the axial-vectors they could have a certain impact on the phase diagram if they are backcoupled, we will only use the Goldstone Bosons (Pions) and their chiral partners (Sigma meson) for the meson backcoupling. We expect that they have the biggest influence on the phase diagram and the location of the CEP. However, in future works the backcoupling of (axial-)vector and further (pseudo-)scalar mesons is desirable.

With the results from the previous sections we now want to improve our truncation by including mesonic backcoupling effects into the calculation. In previous works such effects were studied in the Nambu-Jona-Lasinio (NJL) model [164–166] but also in the functional approach [23, 24, 38, 56, 57, 167] often by including mesons as external degrees of freedom. In the Dyson-Schwinger approach, based on the description of pseudo-scalar and vector mesons with Bethe-Salpeter equations in vacuum [31, 32, 168] and at finite temperature [65], the meson backcoupling onto light quarks and mesons was introduced in vacuum [56, 58], in the CFL phase at large chemical potentials [169] and for finite temperature [38, 170]. Additionally in Ref. [171] Pion cloud effects on the baryon masses were studied in an exploratory vacuum calculation. In all studies the meson backcoupling effects are of the order of $10 - 20\%$ compared to the other components of the quark-gluon interaction. We will build upon these works studying the effects of the meson backcoupling introduced in Sec. 2.2.1. As shown in Ref. [128], other mesonic effects like the inclusion of hadronic decays are also important for the correct description of the meson phenomenology for mesons above the strong decay threshold. But in this work, we will neglect them due to the complexity of the corresponding calculation in medium. In the following, we will introduce a meson backcoupling truncation which is orientated on Ref. [56]. The results were already published in Ref. [55].

[3] The vector mesons, especially the light ones (ρ, ω, and ϕ), are expected to contribute substantially to the observed dilepton spectrum since they couple to the electromagnetic current due to their quantum numbers. Since the photons are produced in the reaction and escape the medium almost undistorted, they can therefore serve as a probe for the state of matter in the early stages of the collision.[143]

5.1. Meson backcoupling truncation

As already mentioned in Sec. 2.2.1, we want to solve the non-hadronic and hadronic part of the quark-gluon vertex separately by inserting them into the equations of the quark, gluon, and mesons. In this section, we will do so for the mesonic part. The baryonic part will be neglected. Inserting the quark-gluon vertex decomposition given by Fig. 2.4 without the baryon diagram into the quark DSE yields the equation shown in Fig. 5.1. For simplicity and since the mesonic contribution

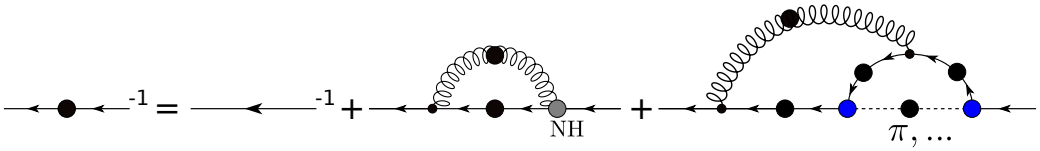

Figure 5.1.: Quark DSE with a dressed quark-gluon vertex separated into a non-hadronic part and an one-meson exchange diagram as shown in Fig. 2.4. Quark, gluon, and meson propagators are denoted by solid, curly, and dashed lines, respectively. The intersection of two quarks and a gluon or a meson represent a quark-gluon or a Bethe-Salpeter vertex, respectively. Dressed quantities are indicated by big colored dots. The remaining ones are bare. The arrows indicate the direction of the quark flavor and the momentum. The signs and prefactors are absorbed into the diagrams.

is suppressed in a large N_c-expansion of the gluon DSE[4], we neglect the one-meson exchange and insert only the non-hadronic part of the quark-gluon vertex into the gluon DSE. By inserting the quark-gluon vertex decomposition into the homogeneous BSE, we get an additional (meson exchange) diagram in the hBSE. This implies that we have to re-ensure that the Bethe-Salpeter kernel fulfills the AxWTI shown in Eq. (3.6). Since, in the considered case, this is quite complicated, we rather approximate the interaction such that the AxWTI is exactly fulfilled by the approximated interaction. To approximate the interaction, we consider the mesonic two-loop diagram with two full Bethe-Salpeter vertices in Fig. 5.1. One loop resembles the homogeneous BSE with only non-hadronic contributions shown in Fig. 3.2. By inserting this homogeneous BSE, we can replace the corresponding loop by an 'effective' Bethe-Salpeter amplitude and get the quark DSE shown in Fig. 5.2. The corresponding new interaction kernel[5] has the correct charge

[4] In the gluon DSE the vertex decomposition has to be inserted into the quark loop, which itself is already suppressed by a factor of $1/N_c$ compared to the Yang-Mills part. Overall the mesonic contribution in the gluon DSE is suppressed by a factor of $1/N_c^2$.

[5] The additional kernel for the meson exchange diagram can be derived from the quark self-energy by taking a functional derivative w.r.t. a quark propagator as discussed in Sec. 3.1.1.

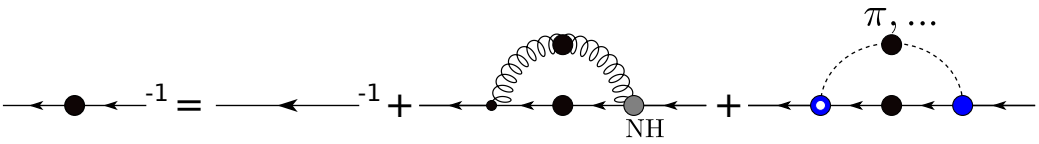

Figure 5.2.: Approximated quark DSE with a gluon (indicated as non-hadronic NH) and meson (last term) backcoupling term. The components are defined in the same way as in Fig. 5.1. The blue dot with a white center represents an effective Bethe-Salpeter vertex, which will be discussed in the text.

conjugation properties and respects the multiplicative renormalizability of the BSE as shown in Ref. [56]. With this approximation we are able to reduce the numerically demanding two-loop diagram to a one-loop diagram. The approximation is justified as long as the Bethe-Salpeter amplitudes, resulting from the two hBSE calculations with and without a meson exchange diagram, do not differ strongly. In Ref. [56] this was proven explicitly for the Pion. To simplify the calculation and since the inclusion of the meson exchange diagram does not strongly change the BSA of the considered mesons, we consequently neglect the mesonic contribution and calculate the homogeneous BSE with the non-hadronic part of the vertex alone.

Let's consider the one-loop approximation in more detail. As stated before, we replaced the second loop in Fig. 5.1 which consists of two dressed quark propagators, a gluon propagator and two bare quark-gluon vertices by an effective BSA since the replaced loop resembles a hBSE. But why is it an effective one? Here, we have to emphasize that the two quark-gluon vertices in the loop that we approximated by the hBSE are bare, while one quark-gluon vertex is fully dressed in the hBSE. Consequently, it is questionable to approximate the loop by a full BSA and we rather introduced an effective Bethe-Salpeter vertex instead, as indicated in Fig. 5.2. Two possible expressions of this effective Bethe-Salpeter vertex were studied in previous works: The use of a fully dressed or a bare Bethe-Salpeter vertex. The initial work in Ref. [56] used two fully dressed Bethe-Salpeter vertices in the one-loop meson exchange diagram but Ref. [57] showed that the resulting strong back-reaction is overestimated and in disagreement with corresponding lattice results. The usage of a bare Bethe-Salpeter vertex in the latter reference, however, yields a quantitatively correct description of the mesonic effect and Ref. [58] additionally showed good results for the meson phenomenology[6] by using the bare vertex. The downside of the use of the bare quark-meson vertex, on the other hand, is that the correct

Considering Fig. 5.2, the non-hadronic and mesonic kernels are obtained by simply cutting the remaining dressed quark propagator in the last two diagrams.

[6]The inclusion of the mesonic backcoupling leads to better results for the meson masses and decay constants in vacuum.

scaling behavior at the (pseudo)critical temperature gets destroyed since the two vertices do not have the same scaling anymore, as shown in the scaling analysis of Ref. [38]. Since we are not interested in the scaling behavior in this work but rather want to estimate the impact of meson effects correctly, we use only one fully dressed Bethe-Salpeter vertex and set the effective Bethe-Salpeter vertex to a bare one. Ref. [89] checked, for a simplified calculation of the BSA, that this choice does not affect the results on a qualitative level.

Now, before we can discuss the mesonic backcoupling term in Fig. 5.2 in more detail, we have to discuss the formulation of the meson exchange kernel. In the backcoupling diagram, the meson exchange is needed in the t-channel. But we only know the meson contribution to the quark-antiquark scattering kernel in the s-channel [31], which is given by

$$M^{\mathrm{x}}_{\alpha\beta,\gamma\delta}(p,q,P) = \left[\hat{\bar{\Gamma}}_{\mathrm{x}}(-P,p)\right]_{\gamma\delta} D_{\mathrm{x}}(P) \left[\hat{\Gamma}_{\mathrm{x}}(P,q)\right]_{\alpha\beta} + R^{\mathrm{x}}_{\alpha\beta,\gamma\delta}(p,q,P) \tag{5.1}$$

with M^{x} representing the mesonic part of the renormalized and fully-amputated quark-antiquark scattering amplitude which is connected to the BSE kernel via $M = K + K(SS)K + \ldots$ [172]. In this scattering kernel, $\hat{\Gamma}_{\mathrm{x}}$ and $\hat{\bar{\Gamma}}_{\mathrm{x}}$ describe the normalized Bethe-Salpeter amplitude and its charge conjugation for the meson type $\mathrm{x} \in \{\pi, \sigma\}$ as discussed in Sec. 3.1.2. The corresponding meson propagator $D_{\mathrm{x}}(P)$ is described in Sec. 3.2.2. The remaining term R^{x} describes the sub-leading contribution and is a regular term in contrast to the first term which has a pol at the meson mass m_{x} in the meson propagator.

The corresponding expression for the t-channel is normally directly related through the crossing symmetry by taking the incoming and outgoing momenta on-shell. But since we only consider the dominant first term of Eq. (5.1), the crossing symmetry gets broken. As a result, the transformation from the s-channel to the t-channel is no longer unique and depends on the choice of the incoming and outgoing momenta. To find an expression for the mesonic part of the BSE kernel and the related mesonic part of the quark self-energy that furthermore fulfills the AxWTI, we take an arithmetic mean over the possible contributions (permutations of the incoming and outgoing momenta leading to the two terms in the curly brackets of Eq. (5.2)). The corresponding mesonic backcoupling part of the quark self-energy $\Sigma^{\mathrm{M}}_f(p)$ for the quark flavor f in the quark DSE is given by

$$\Sigma^{\mathrm{M}}_f(p) = -\sum_{\mathrm{x}\subset\{\pi,\sigma\}} N^f_{\mathrm{x}} \int\!\!\!\!\!\!\sum_q \frac{D_{\mathrm{x}}(P)}{2} \bar{\Gamma}^{\mathrm{bare}}_{\mathrm{x}} S^{f'}(q) \left\{ \hat{\Gamma}_{\mathrm{x}}(P,l) + \hat{\Gamma}_{\mathrm{x}}(-P,l) \right\} \tag{5.2}$$

which contains a sum over the considered mesons (π and/ or σ/f_0) [38, 58]. Thereby, the three isovector Pions are counted as one contribution. As mentioned in Sec. 3,

some of the mesons are degenerated due to our approximations. N_{x}^f takes account for this degeneration and describes the number of times the different degenerated mesons couple to the considered quark flavor f. We will call this quantity meson flavor factor and calculate it via

$$N_{\mathrm{x}}^f = \sum_{e\in\mathrm{x}} v_f^\top \left(r_{\mathrm{x}}^e\right)^\top r_{\mathrm{x}}^e v_f = \begin{cases} 3\,\delta_{f\ell} + 0\,\delta_{f\mathrm{s}} & \text{for } \mathrm{x} = \pi \\ 1\,\delta_{f\ell} + 0\,\delta_{f\mathrm{s}} & \text{for } \mathrm{x} = \sigma \end{cases} . \tag{5.3}$$

In this expression we sum over the degenerated mesons ($\mathrm{x} = \pi \in \{\pi^\pm, \pi^0\}$ and $\mathrm{x} = \sigma$). Thereby the meson flavor matrices r_{x}^e originate from the BSAs in Eq. (3.12) and their representations are discussed in App. A.3. This representation also includes a normalization factor $\sqrt{2}$. Due to the charge conjugation in Eq. (5.2) one meson flavor matrix has to be transposed. We further multiply these flavor matrices by the unit vectors of the quark flavor space v_f to project the (inverse) quark propagator $S = \mathrm{diag}\left(S^{\mathrm{u}}, S^{\mathrm{d}}, \ldots\right)$ onto a specific quark flavor f. If we consider the contributions of the different quark flavors, it is noteworthy that only two Pions interact with the light quarks although there are three of them. This is because the external quark flavor has to run through the meson to archive a coupling between the quark and the meson. If we, e.g., consider the up-quark, we sum over $e \in \{\pi^+, \pi^0\}$. Thereby, π^+ couples to the quark once but π^0 only to a half. The Pion and Sigma mesons, furthermore, only influence the light quarks as indicated by $\delta_{f\ell}$. For the strange quark to couple to a meson we would need to backcouple mesons with open or hidden strangeness, i.e. K or ϕ mesons.[7] Additionally, the quark flavor projection described above also implies that the quark propagator which is integrated over can have another quark flavor f'.

The meson backcoupling self-energy further depends on the meson propagator $D_{\mathrm{x}}(P)$ and one fully dressed and normalized BSA $\hat{\Gamma}_{\mathrm{x}}(P,l)$ of the meson type x as well as a charge conjugated bare Bethe-Salpeter vertex defined by

$$\bar{\Gamma}_{\mathrm{x},e}^{\mathrm{bare}} = \begin{cases} Z_2^f \gamma_5 \otimes \mathbb{1}_{\mathrm{C}} \otimes \left(r_{\mathrm{x}}^e\right)^\top & \text{for } \mathrm{x} = \pi \\ Z_2^f \mathbb{1}_{\mathrm{D}} \otimes \mathbb{1}_{\mathrm{C}} \otimes \left(r_{\mathrm{x}}^e\right)^\top & \text{for } \mathrm{x} = \sigma \end{cases} . \tag{5.4}$$

In this expression, we included the meson flavor matrix for the sake of completeness. The dressed BSA depends on the relative momentum $l = \frac{p+q}{2}$ and the off-shell total momentum $P = q - p$, implying a symmetric momentum partitioning. The off-shell meson BSAs needed in the the meson backcoupling term can be extracted from the inhomogeneous BSE. Since these off-shell BSAs are, for the momenta relevant in our calculation, almost identical to the on-shell amplitudes obtained

[7] The proper inclusion of the Kaon would further introduce another coupling between the light and the strange quarks in addition to the unquenching of the gluon.

from the hBSE, we will use the on-shell BSAs presented in the last chapter as an approximation. Consequently, temperature effects are neglected.[8] The inclusion of finite temperature in the considered truncation by evaluating the complex quark and BSE explicitly is far too complicated and beyond the scope of this work. But through the data, we incorporate the effects of chemical potential in the BSAs and meson properties which are, as we will see later, mandatory to preserve the Silver-Blaze property of QCD. In addition to the use of the on-shell data from the last chapter, we have to apply a further approximation, which is related to the meson propagator. As already mentioned in Sec. 3.2.2, the spatial decay constant and the meson velocity cannot be calculated since we consider the mesons to be in rest frame. Although the velocity would also be important for the scaling behavior, we set $f_{\mathrm{x}}^{\mathrm{t}} = f_{\mathrm{x}}^{\mathrm{s}}$ and $u_{\mathrm{x}} = 1$.

In summary, in this chapter we calculate a coupled set of quark and gluon DSEs and a meson hBSE, neglecting hadronic backcoupling terms in the gluon DSE and the meson hBSE and adding an hadronic backcoupling self-energy given by Eq. (5.2) to the non-hadronic part in the quark DSE:

$$\left(S^f(p)\right)^{-1} = \left(S_0^f(p)\right)^{-1} + \Sigma_f^{\mathrm{NH}}(p) + \Sigma_f^{\mathrm{M}}(p)\,. \tag{5.5}$$

In the gluon DSE, the meson hBSE and the non-hadronic part of the quark DSE we use the Hyb truncation detailed in Sec. 2.2.2 (and following) with $\mathrm{N_f} = 2+1$ quark flavors. How the iterative procedure of the coupled quark and gluon DSEs and meson BSE precisely works is detailed in App. C.1.2. With the (meson backcoupling) truncation fixed, we can now investigate the chiral order parameters.

5.2. Influence on the chiral order-parameters

We start by studying the impact of backcoupled mesons on the dynamical (light-) quark mass function and the corresponding wave-function renormalization function in vacuum. Therefore, in Fig. 5.3, we plot these two quantities against the four momentum. To see the effect of the different mesons individually and in combination, we consider different sets of backcoupled mesons. Compared to the calculation without any backcoupled mesons, the inclusion of Pion backcoupling reduces the dynamical quark mass over the whole momentum range with a maximal reduction of around 7% at vanishing momentum. The Sigma meson backcoupling behaves similarly but is weaker in its chiral restoration effect with a maximal reduction of 5%. The combined effect of both backcouplings trivially is the sum of

[8] In App. C.1.2 we will however try to estimate the the impact of the missing temperature effects.

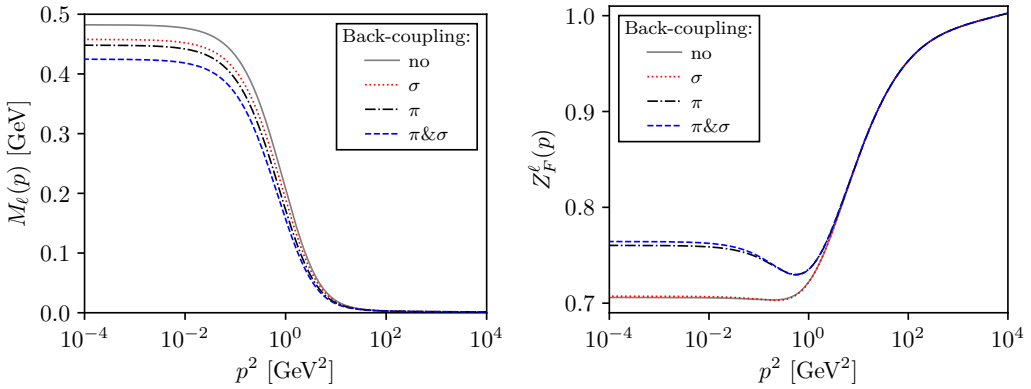

Figure 5.3.: Dynamical quark mass function $M_\ell(p) = B_\ell(p)/A_\ell(p)$ (left) and corresponding quark wave-function renormalization function $Z_{\mathrm{F}}^\ell(p) = 1/A_\ell(p)$ (right) plotted against the four-momentum for light quarks and different numbers of backcoupled mesons in vacuum. All results are obtained with the parameters of the Hyb truncation given in Tab. 2.2.

the individual parts. As we can see in the figure, the wave-function renormalization function also shows a much stronger reaction on the Pion than on the Sigma meson.

Since the introduction of the meson backcoupling terms reduces the (pseudo)critical temperature for all chemical potentials, the truncation parameters have to be re-scaled to match the lattice pseudocritical temperature at vanishing chemical potential [4, 104] again. For this purpose we only need a change of the vertex interaction strength parameter d_1^{q} in the quark DSE as discussed in Sec. 2.2.3. The resulting regularized and normalized quark condensate is plotted in Fig. 5.4 in comparison with corresponding lattice results for finite temperature but vanishing chemical potential. In this plot, we consider two types of meson backcoupling: On the one hand we backcouple only the Pion and use only the leading BSA component ($+\pi$) to later compare with the results presented in Ref. [89]. On the other hand we backcouple the Pion and Sigma meson with all possible BSA components ($+\pi\&\sigma$). In the plot, we furthermore compare with the results without meson backcoupling (Hyb). Since the π backcoupling is introduced to compare with an older QCD phase diagram, the vertex strength parameter naturally is fixed to the same pseudocritical lattice temperature as in previous works [4]. For the $\pi\&\sigma$ backcoupling we however take account of newer lattice results [104] with an pseudocritical temperature which is 2 MeV higher. The corresponding parameters resulting from the new parameter fixings are recorded in Tab. 5.1 together with the resulting pseudocritical temperature at vanishing chemical potential.

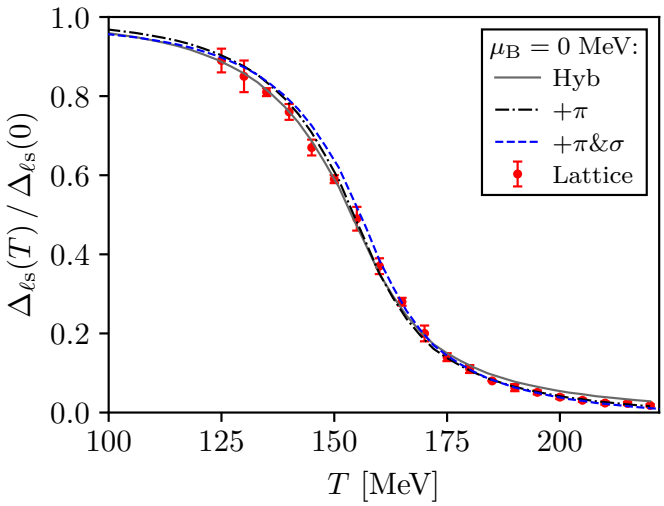

Figure 5.4.: Vacuum-normalized regularized quark condensate (2.37) of the Hyb DSE truncation without meson backcoupling (solid gray) [105], with Pion backcoupling (dashed dotted black) and with Pion and Sigma backcoupling (dashed blue) compared to the corresponding continuum-extrapolated lattice results (solid red circles) from Ref. [4]. The results are considered at finite temperature and vanishing chemical potential.

In the figure we, furthermore, see that the π parameter set coincides quite well with previous data without meson backcoupling and (within the error bars) the lattice, too. At high temperatures the already previously observed and discussed overestimation of chiral symmetry breaking of the truncation without meson backcoupling (see Sec. 2.2.3) vanishes for the two meson backcoupling parameter sets. For the $\pi\&\sigma$ parameter set, it is obviously visible that the condensate does

	d_1^{q} [GeV^2]	d_1 [GeV^2]	m_{q}^{ℓ} [MeV]	$m_{\mathrm{q}}^{\mathrm{s}}$ [MeV]	T_{pc} [MeV]
Hyb $+\,\pi$	13.54	8.49	1.47	37.8	156(1)
Hyb $+\,\pi\&\sigma$	14.18	8.49	1.47	37.8	157(1)

Table 5.1.: Vertex strength parameter(s) $d_1^{(\mathrm{q})}$, quark masses m_{q}^f and the pseudocritical temperature T_{pc} at vanishing chemical potential for the Hyb truncation with Pion as well as Pion and Sigma backcoupling. The error of the pseudocritical temperature is purely numerical and its determination from the vacuum-normalized, regularized quark condensate is discussed in App. C.1.2.

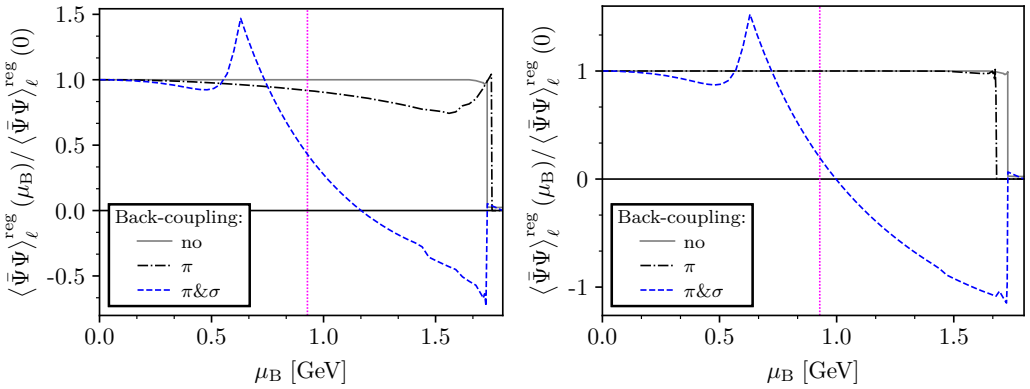

Figure 5.5.: Vacuum-normalized and regularized light-quark condensate of the Hyb DSE truncation without meson backcoupling (solid gray), with Pion backcoupling (dash dotted black) and with Pion and Sigma backcoupling (dashed blue). The results are considered at finite chemical potential and vanishing temperature. The jump represents the transition from the Nambu to the Wigner solution and corresponds to the upper border of the light-quark coexistence region. The densely dotted magenta line corresponds to the end of the Silver-Blaze area. The regularized quark condensate $\langle\bar{\Psi}\Psi\rangle_f^{\rm reg}$ is defined by Eq. (4.1). Due to the average over the possible incoming and outgoing momenta, the imaginary part of the meson BSA components vanishes (left side). We reinsert the imaginary part of the BSA on the right side. More information in the text.

not coincide equally well with the lattice for intermediate temperatures. This, although, is not astonishing since it is fixed to match newer lattice results with a higher pseudocritical temperature. At low and high temperatures the agreement with the other presented data is, however, satisfying. It has to be mentioned that after backcoupling the mesons, the quark masses should be re-scaled, too, potentially yielding a better agreement with the lattice data (at high temperatures). But this requires a much more complicated truncation and calculation since we would need to solve a coupled set of quark and gluon DSEs and the homogeneous BSE simultaneously and in the complex momentum plane.

After introducing the two parameter sets, we can now consider the corresponding results at finite chemical potential and vanishing temperature, before we study the impact on the QCD phase diagram. We therefore display the vacuum-normalized and regularized quark condensate against the baryon chemical potential in Fig. 5.5 for the two parameter sets in comparison with the truncation without any backcoupling. At first, we consider the panel on the left side which directly results from our calculation. As one can see, the results with meson backcoupling show a strong

chemical potential dependence, in contrast to the constant results of the truncation without meson backcoupling. Although the quark condensate is not an observable quantity, the strong dependence on chemical potential and the connected violation of the Silver-Blaze property could hint at a violation of the SBP of an (other) observable. Especially the peak of the $\pi\&\sigma$ backcoupling results seems unphysical.

At this point, we remember one of the most important observations from the last chapter: At finite chemical potential and vanishing temperature, the Bethe-Salpeter amplitudes of all mesons develop an imaginary part. For high-mass mesons this imaginary part is also almost the only reaction of the amplitude to chemical potential. Furthermore we mentioned, at the end of the last chapter, that there is a non-trivial cancellation between the chemical potential dependencies of the quark and meson quantities happening, that provides a constant behavior of the observables. Consequently, all parts of the BSAs which depend on the chemical potential should be included in the calculation. But if we take a closer look at the implemented kernels for the meson backcoupling, the procedure of taking the average over all possible combinations of the incoming and outgoing momenta yields that the imaginary part of all BSAs vanish in the calculation. If we reinsert the imaginary part of the BSAs manually we get the results presented on the right side of the figure. Now at least the quark condensate for the π parameter set is constant and fulfills the SBP. It seems that our approach of just taking the average of the possible permutations of the incoming and outgoing momenta (included to fulfill the AxWTI) is not the optimal choice and has to be replaced. For the behavior of the condensate for Pion and Sigma meson backcoupling, we mention that we had to extrapolate the Sigma meson properties and BSAs for baryon chemical potentials above $\mu_\mathrm{B} = 630\,\mathrm{MeV}$ since we are restricted to use a symmetric momentum partitioning parameter. For simplicity we use a constant extrapolation for both, the Sigma meson properties and BSAs. Due to the resulting missing chemical potential dependence, we expect that the latter approximation leads to the dip and the subsequent decrease of the quark condensate in both figures. In vacuum, we observed that the importance of the H and G BSA components interchange if we go from the Pion to the Sigma meson. This means that H is much more important than G if we consider the Sigma meson instead of the Pion. In our calculation the H BSA component is however neglected. We consequently assume that the SBP violating behavior below $\mu_\mathrm{B} = 630\,\mathrm{MeV}$ could result from the missing H contribution. In future works, we have to include the H contribution and to improve upon the constant extrapolation. To achieve both, we have to go beyond the rest frame description of the mesons.

If we reinsert the imaginary part of the BSAs, also the upper border of the coexistence region is affected. The calculation of the lower border is numerically not feasible since we do not have access to the mesons BSAs for the Wigner

solution.[9] The influence of the imaginary part, for the π parameter set, can also be seen if we consider the quark dressing functions. Before reinserting the imaginary part of the BSAs, all quark dressing functions show a strongly oscillatory behavior already at low chemical potential. Furthermore, the two quark vector dressing functions behave similarly but are not identical. If we reinsert the imaginary part, the oscillations vanish almost completely and only a weak oscillation remains in the second vector dressing function. Additionally, the two vector dressing functions differ by less than 1% over the whole momentum range and for all chemical potential values of the Nambu solution. But in the Wigner phase they are different. Overall, the quark dressing functions react on chemical potential similar as discussed in Sec. 4.1.

5.3. Influence on the QCD chiral phase-diagram

In this section, we will study the impact of the meson backcoupling on the chiral-symmetry QCD phase diagram. Therefore, in Fig. 5.6, we show the QCD phase diagram calculated for the two parameter sets with backcoupled mesons in comparison with the corresponding phase diagram of the Hyb truncation without meson backcoupling. The difference between the phase diagram of the Hyb truncation without meson backcoupling and the phase diagram of previous works (1BC truncation), was already discussed in Sec. 2.2.4. Since the Hyb truncation inherits much stronger approximations than the 1BC truncation, the absolute values for the curvature and the location of the CEP, in this section, should not be regarded as best results. Instead, it only serves to highlight the relative difference resulting from suppressing and including the different mesonic effects.

In the figure, we observe (for all three cases) a crossover at low chemical potential which increases its steepness until it ends in a second-order critical endpoint (CEP). The coexistence region which we observed for the 1BC and Hyb truncation in Sec. 2.2.4 cannot be determined if we include mesonic backcoupling. As already mentioned in the last section, the reason is that we do not have access to the mesons corresponding to the Wigner solution. Consequently, we are only able to determine the upper spinodal.

As one can see, the phase diagram is only affected marginally through the inclusion of the Pion and Sigma backcoupling terms. The most prominent effect is the shift of the CEP to lower chemical potential and higher temperatures along the previous coexistence crossover line. For the π parameter set we find a chemical potential

[9] The results above the upper border of the coexistence region are calculated with mesons from the Nambu solution and therefore have to be considered with caution.

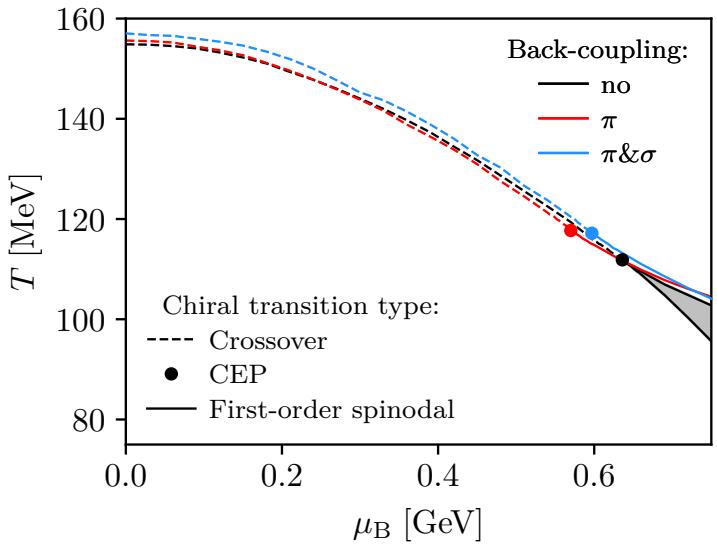

Figure 5.6.: Chiral symmetry QCD phase diagram for the Hyb truncation detailed in Sec. 2.2.3 without meson backcoupling (black) and with different numbers of additionally backcoupled mesons. For the meson backcoupling we consider the Pion (red) as well as the Pion and Sigma (blue) parameter sets. Dashed lines correspond to crossover transitions while strait lines represent a first-order spinodal. The big dots show the location of the second-order critical endpoint of the corresponding truncation. The shaded area represents the coexistence region where the physical first-order phase transition takes place. To be comparable with previous calculations of the QCD phase diagram [42], we set the strange-quark chemical potential to $\mu_q^s = 0$.

shift of 10% while the shift of the $\pi\&\sigma$ parameter set turn out to be smaller of the order of 6%. A similar result was found for baryonic backcoupling in Ref. [44].[10] We have to remember that the π parameter set was calculated using only the dominant Pion BSA component whereas the $\pi\&\sigma$ parameter set uses all possible BSA components mentioned in Sec. 3.1.4. In consequence, the question whether the reduced shift of the $\pi\&\sigma$ parameter set is due to the inclusion of the Sigma backcoupling term or more Bethe-Salpeter amplitude components or a mixture of these two additions, needs to be evaluated in a future (computational expensive) investigation. The corresponding locations of the three critical endpoints are detailed in Tab. 5.2.

[10] However, the results in this work originate from a much more elaborated calculation. In Ref. [44], vacuum quantities were used for the baryon whereas in this work we explicitly include the chemical potential dependency of the mesons.

Table 5.2.: Critical endpoint (CEP) and curvature κ of the two meson backcoupling parameter sets introduced above and corresponding values for the truncation without meson backcoupling (Hyb). The errors of the CEPs are purely numerical.

	$(\mu_B, T_c)_{CEP}$ [MeV]	κ
Hyb	(636(1), 111.9(1))	0.0173
$+\pi$	(570(1), 117.7(1))	0.0210
$+\pi\&\sigma$	(597(1), 117.2(1))	0.0167

In the table, we also show the curvature values obtained from a fit to Eq. (2.42) up to a baryon chemical potential of $\mu_B = 240\,\text{MeV}$. In our calculation, we find an increase of the curvature for the π parameter set and a slight decrease for the $\pi\&\sigma$ parameter set.

Finally, we can state that we are consistent with Ref. [89] where a similar effect on the CEP and the curvature was found using only the Pion backcoupling term and a generalized Goldberger-Treiman like relation as approximation for the leading BSA component (See Sec. 4.4 and Ref. [31] for more details). Since this relation replaces the BSAs by quark dressing functions, also temperature effects are considered properly in this approximation, at least if the relation holds also for finite temperature. Since we see a similar behavior in our calculation we are confident that our results are meaningful even though we neglect the temperature dependence of the meson properties and wave-functions. Although this truncation is only comparable to the π parameter set, we have now seen that the $\pi\&\sigma$ parameter set does behave in the same way.

To conclude, we can state that if we combine our results with the results of the Refs. [38, 44, 89], we find strong evidence that the location of the CEP is mainly driven by the non-resonant part of the quark-gluon vertex, i.e. by the microscopic degrees of freedom of QCD (the quarks and gluons), whereas macroscopic dof (in particular the σ meson) are expected to take over if we consider the properties of the CEP like the critical exponents/ the universal behavior. The latter feature is expected for a system in the Z(2) universality class and was explored in detail in effective models of QCD [52, 59, 60].[11] The corresponding analytic scaling analysis in our framework is straightforward along the lines of Ref. [38] but requires a tremendous additional numerical effort.[55] To study the scaling behavior, the behavior of the meson velocity and decay constant in the dispersion relation is

[11] Indications for the correct scaling behavior in lattice and functional methods can be found in Refs. [173–176] and [177, 178], respectively.

crucial [38]. Consequently, we have to consider the meson in the moving frame which would enable the possibility to properly calculate the spatial meson decay constant. In addition to the decay constant, we need to find a better description of the effective BSA and to include temperature effects to be able to study the critical scaling. Apart from the scaling analysis, the inclusion of mesonic decays into the calculation and a proper study of baryon properties and backcouplings in medium could be done in future investigations.

6. Baryon backcoupling effects at finite chemical potential

Similar to the last chapter with meson backcoupling, we want to investigate the influence of baryon (and diquark) backcoupling in this chapter. In Refs. [44, 80], the qualitative impact of this baryon backcoupling onto the QCD phase diagram was already studied in a rather simple way for a $N_f = 2$ quark flavor calculation and a 1BC truncation (description see Sec. 2.2.3). A strong influence on the QCD phase diagram and the critical endpoint could not be found.[1] However, since it would be important that the truncation shows the desired nuclear matter liquid-gaseous phase transition [18], we now extend this investigation to the chemical potential axis of the QCD phase diagram. Because the baryon backcoupling provides us a connection between the chiral observables and the baryon wave-function, we hope to find an indication of this transition if we properly included the baryon backcoupling effects onto the quark propagator. Changes in the baryon wave-function, e.g. through the sharp (first-order) nuclear liquid-gaseous transition, then influence the quark condensate directly.

In the next section, we will introduce the applied truncation and show the equations to solve. Since Refs. [44, 80] already discussed the derivation of the baryon (and diquark) backcoupling in detail and since this derivation is quite similar to the one for meson backcoupling in the last chapter, we will mention only the most important aspects. Then, we will consider the impact of the baryon and diquark backcoupling onto the quark dressing functions and the quark condensate.

6.1. Approximations

We include the baryonic contributions in the same way as we did it for the mesons in the last chapter. This means that we include the baryon diagram of the quark-gluon vertex decomposition in Fig. 2.4 into the quark DSE but neglect the meson backcoupling. This yields a three-loop diagram which is far too complicated to

[1] In a two color version of QCD, the FRG studies in Ref. [179, 180] found that baryon backcoupling effects are even crucial for the existence of CEP.

be solved numerically, especially if we consider the calculation of the three-quark Faddeev amplitude in medium.[2] To reduce the complexity, we apply a commonly used approximation of the baryon, the so-called quark-diquark approximation: Due to the dynamical formation of diquark correlations inside the baryon, quark-diquark degrees of freedom can be seen as a satisfying approximations for the three-body framework. This approximation converts the three-quark Faddeev amplitude into a quark-diquark BSA for baryons. The corresponding Bethe-Salpeter equation can be found in Ref. [44]. By applying this approximation with simple models for the quark and diquark propagators and ansätze for diquark amplitudes [186–189] or with more fundamental approaches similar to our calculation [190–193], previous works were able to show satisfying descriptions of nucleon and Δ-baryon ground-state properties and a good agreement with the three-quark Faddeev calculation of the nucleon, see e.g. in Ref. [181].[44]

By inserting the quark-diquark ansatz into each three-body Faddeev amplitude of the three-loop diagram, we can rearrange the resulting diagrams into two groups which can be represented by the two one-loop diagrams shown in the lower row of Fig. 6.1. We will refer to the diagram where the quark couples to a diquark ampli-

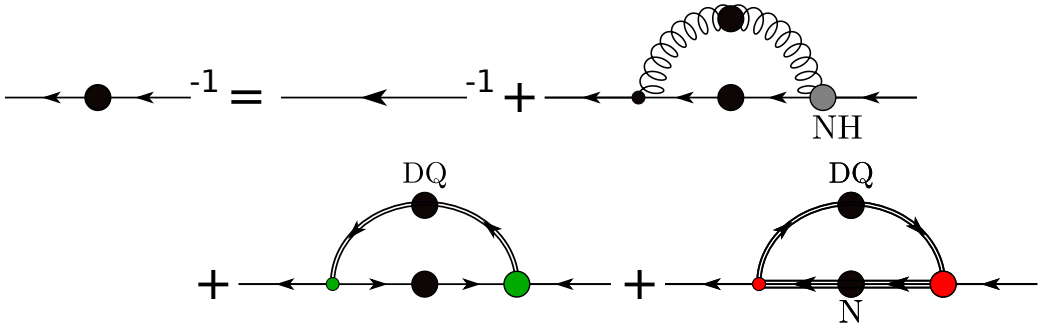

Figure 6.1.: Approximated quark DSE with a gluon (indicated as non-hadronic NH), diquark (first term in second row) and baryon (last term in second row) backcoupling. Quark, gluon, diquark, and baryon propagators are denoted by solid, curly, double, and triple lines, respectively. The intersection of two quarks and a gluon or a diquark represent a quark-gluon or a diquark Bethe-Salpeter vertex, respectively. The intersection of a baryon, a diquark and a quark is a Faddeev-type amplitude in the quark-diquark approximation. Dressed quantities are indicated by big colored dots. The remaining ones are bare. The arrows indicate the direction of the quark, diquark, and baryon flavor and the momentum. The signs and prefactors are absorbed into the diagrams.

[2] The calculation of the three-body Faddeev equation in vacuum as shown in Refs. [171, 181–185] is already quite complicated.

tude as diquark loop, while we denote the diagram where the quark couples to a diquark-baryon amplitude as baryon loop. Each of the two diagrams has one proper amplitude/ vertex and an effective one which absorbs the remaining objects of the set of graphs. Analogous to the treatment of the Pion loop in the quark DSE in Sec. 5.1, we use a bare vertex instead of an effective vertex since dressing both vertices would overestimate the strength of the backcoupling by far [44]. This is due to the normalization factor of the dressed amplitudes which we will introduce later on. The resulting truncated quark DSE with diquark and baryon backcoupling and bare instead of effective vertices is shown in Fig. 6.1 and given by

$$\left(S^f(p)\right)^{-1} = \left(S_0^f(p)\right)^{-1} + \Sigma_f^{\mathrm{NH}}(p) + \Sigma_f^{\mathrm{DQ}}(p) + \Sigma_f^{\mathrm{BA}}(p) \tag{6.1}$$

with the non-hadronic (X=NH), diquark (X=DQ), and baryon (X=BA) self-energies Σ_f^{X}. Similar to the meson backcoupling, the inclusion of the baryon vertex term into the gluon DSE is neglected since the baryonic contribution to the quark loop is suppressed by a factor of $1/\mathrm{N_c^2}$. To be comparable to Refs. [44, 80], we use the 1BC truncation discussed in Sec. 2.2.3 with $\mathrm{N_f} = 2$ quark flavors and modified vertex interaction strength $d_1 = 8.05\,\mathrm{GeV}^2$ for the non-hadronic part of the interaction. Since we consider $\mathrm{N_f} = 2$ quark flavors and use the isospin-symmetric limit, only the isospin-singlet scalar and isospin-triplet axial-vector diquarks and the degenerated isospin-doublet of nucleons remain in the calculation. Like in the Refs. [44, 80], we omit axial-vector diquarks in the calculation. Finally, we obtain the nucleon (BA) and the scalar diquark (DQ) backcoupling quark self-energies via

$$\Sigma_f^{\mathrm{DQ}}(p) = \int_q \bar{\Gamma}^0_{\mathrm{DQ}} \left(S^{f'}(q)\right)^{\top} \Gamma_{\mathrm{DQ}}(P,l)\, D_{\mathrm{DQ}}(k)\,, \tag{6.2}$$

$$\Sigma_f^{\mathrm{BA}}(p) = \int_q \bar{\Gamma}^0_{\mathrm{BA}}(P)\, S_{\mathrm{BA}}(2l)\, \Gamma_{\mathrm{BA}}(P,r)\, D_{\mathrm{DQ}}(2l) \tag{6.3}$$

where we use the abbreviation $\int_q = \int \frac{d^4q}{(2\pi)^4}$ and the transposition $\top$. The momenta appearing in the vertices are the total P and relative momenta $l = (q-p)/2$ and $r = q/2 - p$. The remaining momentum routing is given by $k = q + p$. The corresponding bare quark-diquark and diquark-baryon vertices are given by

$$\Gamma^0_{\mathrm{DQ}} = \gamma_5\, C \quad \otimes \frac{\epsilon_{\mathrm{ABC}}}{\sqrt{2}} \otimes s^0\,, \tag{6.4}$$

$$\Gamma^0_{\mathrm{BA}}(P) = \Lambda_+(P) \otimes \frac{\mathbb{1}_{\mathrm{C}}}{\sqrt{3}} \quad \otimes d^0 \tag{6.5}$$

with the charge conjugation matrix $C = \gamma_0\gamma_2$ as well as the diquark and baryon flavor matrices $s^0 = \frac{i}{\sqrt{2}}\sigma_2$ and $d^0 = \mathbb{1}_{\mathrm{B}}$. The color matrices are normalized.

Furthermore, the projection operator onto positive-energy states $\Lambda_+(P)$ will be omitted in the baryon loop because its purpose is already fulfilled by the baryon propagator. The dressed quark-diquark and diquark-baryon vertices are approximated by their leading tensor structures which correspond to the bare tensor structures. Consequently, the amplitudes are given by $\Gamma_{\mathrm{DQ}}(P,q) = f_{\mathrm{DQ}}(q^2)\Gamma^0_{\mathrm{DQ}}$ and $\Gamma_{\mathrm{BA}}(P,q) = f_{\mathrm{BA}}(q^2)\Gamma^0_{\mathrm{BA}}(P)$ where f_{DQ} and f_{BA} represent the leading diquark and baryon dressing functions. Since little is known about in-medium properties of baryons, we use an exploratory ansatz for these dressing functions. They are taken from explicit solutions of the diquark and nucleon amplitudes in a vacuum Rainbow-Ladder quark-diquark calculation with an effective interaction [191–193].[3] In Ref. [73] the results were parameterized in the form

$$f_{\mathrm{DQ}}(q^2) = N_{\mathrm{DQ}}\left(e^{-\alpha_{\mathrm{DQ}}x} + \frac{\beta_{\mathrm{DQ}}}{1+x}\right), \tag{6.6}$$

$$f_{\mathrm{BA}}(q^2) = N_{\mathrm{N}}\left(e^{-\alpha_{\mathrm{N}}x} + \frac{\beta_{\mathrm{N}}}{(1+x)^3}\right). \tag{6.7}$$

The momentum $x = q^2/\Lambda^2$ includes the scale $\Lambda = 0.7\,\mathrm{GeV}$ and the amplitudes are normalized by the normalization factors $N_{\mathrm{DQ}} = 15.6$ and $N_{\mathrm{N}} = 28.4$. The remaining parameters for the exponentials and the ultraviolet behavior are given by $\alpha_{\mathrm{DQ}} = 0.85$, $\alpha_{\mathrm{N}} = 1.0$, $\beta_{\mathrm{DQ}} = 0.02$, and $\beta_{\mathrm{N}} = 0.03$. Finally, as the last quantities, the off-shell diquark and baryon propagators are approximated by free propagators

$$D_{\mathrm{DQ}}(q) = \frac{1}{\vec{q}^2 + (q_4 + 2/3 i\mu_{\mathrm{B}})^2 + m^2_{\mathrm{DQ}}}, \tag{6.8}$$

$$S_{\mathrm{BA}}(q) = \frac{-i\vec{\not{q}} - i\gamma_4(q_4 + i\mu_{\mathrm{B}}) + m_{\mathrm{N}}}{\vec{q}^2 + (q_4 + i\mu_{\mathrm{B}})^2 + m^2_{\mathrm{N}}} \tag{6.9}$$

where we use the vacuum diquark and nucleon mass $m_{\mathrm{DQ}} = 0.85\,\mathrm{GeV}$ and $m_{\mathrm{N}} = 0.938\,\mathrm{GeV}$. By the use of vacuum masses and wave-functions, we neglect important temperature and chemical potential dependencies. On the one hand, we do so to keep the calculation simple and fast, but on the other hand there are only a few investigations about baryon mass and wave-function in medium [194–197]. We know from Ref. [195] that the amplitude is almost independent of the temperature while the mass depends strongly on it, especially at the critical temperature. This can have important effects on the quark propagator and the chiral observable. For finite chemical potential and vanishing temperature, the liquid-gas transition

[3] Due to the use of another interaction for the calculation of the baryon and diquark amplitude as compared to the quark DSE, we have to pay special attention to the renormalization as shown in App. C.1.1.

represents a sharp change in the behavior of the nucleon mass and wave-function. This, however, is neglected in our ansatz.

In our calculation, we only take the lowest lying $J^P = \frac{1}{2}^+$ baryon multiplet for two quark flavor into account. All other baryons 'b' are suppressed by powers of $m_{\mathrm{N}}^2/m_{\mathrm{b}}^2$, except for the parity partner of the nucleon which becomes (almost) mass degenerated when chiral symmetry is restored. By projecting the baryon loops of the nucleon and its parity partner onto the quark dressing functions by applying appropriate Dirac traces, the contribution of the nucleon and its partner cancel in the scalar part of the self energy $(\Sigma_f^{\mathrm{BA}})_B$ and add up in the vector parts $(\Sigma_f^{\mathrm{BA}})_{A/C}$ in the chirally restored phase. We take this feature into account by introducing an extra factor into the calculation. As this extra factor, we use

$$C_{\mathrm{X}} = \begin{cases} 2 - \frac{M_\ell(T,\mu_{\mathrm{B}};0)}{M_\ell(0,0;0)} & \mathrm{X} \in \{A, C\} \\ \frac{M_\ell(T,\mu_{\mathrm{B}};0)}{M_\ell(0,0;0)} & \mathrm{X} = B \end{cases} \tag{6.10}$$

with $M_\ell(T,\mu_{\mathrm{B}};p) = \mathrm{B}_\ell(T,\mu_{\mathrm{B}};p)/\mathrm{A}_\ell(T,\mu_{\mathrm{B}};p)$ representing the renormalization point independent dynamical quark mass function in medium at the four momentum p. This factor has no effect in vacuum but mimics the cancellation of the multiplets in the chirally restored phase.[44, 80] This completes our discussion of the applied (baryon and diquark loop) truncation. Now, we can determine the quark dressing functions and the corresponding quark condensate.

6.2. Quark dressing functions

In Fig. 6.2, we display the dynamical (light-)quark mass and the corresponding quark wave-function renormalization function in vacuum. The two quantities are plotted against the four-momentum for different combinations of baryon and diquark backcouplings: We consider the diquark and baryon backcoupling separately and in combination and compare them to the case of no backcouplings (1BC). The backcoupling terms have the largest impact at small momenta but are of no importance for large momenta. Consequently, we will concentrate on the infrared part only. While the wave-function renormalization function is almost independent of the applied backcoupling, the dynamical quark mass shows a strong decrease for each loop contribution separately. But this chiral restoration effect is differently pronounced for the different contributions. The diquark term only yields a reduction of dynamical mass generation of 3% whereas the baryon term results in a reduction of 11%. We see that the baryon influence is much stronger than the one of the diquark. The combined effect is just the sum of the individual

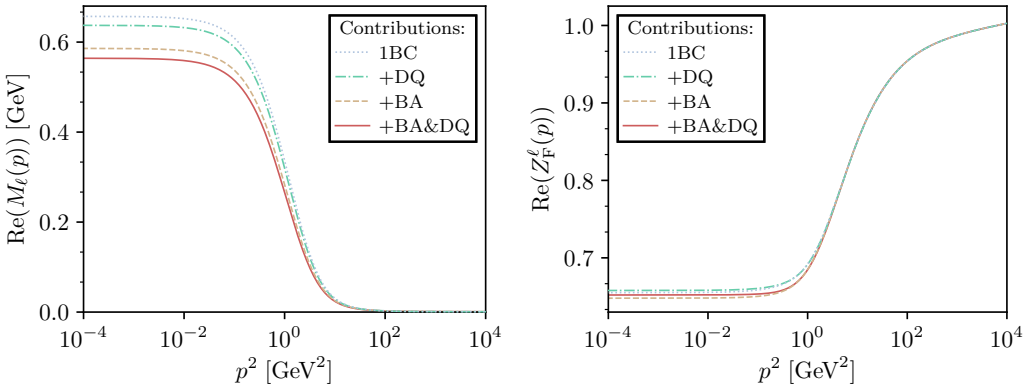

Figure 6.2.: Dynamical quark mass $M_\ell = B_\ell/A_\ell$ (left) and corresponding quark wave-function renormalization function $Z_\mathrm{F}^\ell = 1/A_\ell$ (right) plotted against the four-momentum for light quarks and different combinations of diquark and baryon backcouplings in vacuum.

effects and is in the same ballpark as the meson backcoupling effect discussed in the last chapter. Overall, the dynamical quark mass reacts similar on baryons and diquarks as on mesons. The wave-function renormalization function, however, is much less affected by baryons and diquarks as can be seen in comparison to Fig. 5.3.

For the discussion of the chemical potential dependency, we will concentrate on the combined effects of diquark and baryon backcoupling. In Fig. 6.3, we therefore show again the dynamical (light-)quark mass and the quark wave-function renormalization function plotted against the four-momentum but now for different chemical potentials. The resulting chemical potential dependence is similar to the one presented in Sec. 4.1. This means that we observe an increase at low momenta and an increase of the spreading in mid-momentum region indicating more angular dependence as well as a vanishing chemical potential dependencies for large momenta. The wave-function renormalization function, however, shows a weaker chemical potential dependence compared to the case without baryon and diquark backcoupling. There only is a marginal decrease at low momenta. The difference between the two vector dressing functions in case of baryon and diquark backcoupling is less than 0.3% over the whole momentum range for chemical potentials in the Silver-Blaze region. Above, the difference increases strongly. We can trace back this behavior to the baryon mass which is now explicitly included into the calculation and yields some numerical problems, too.

As one can see in both panels of Fig. 6.3, there is a strong oscillatory behavior at

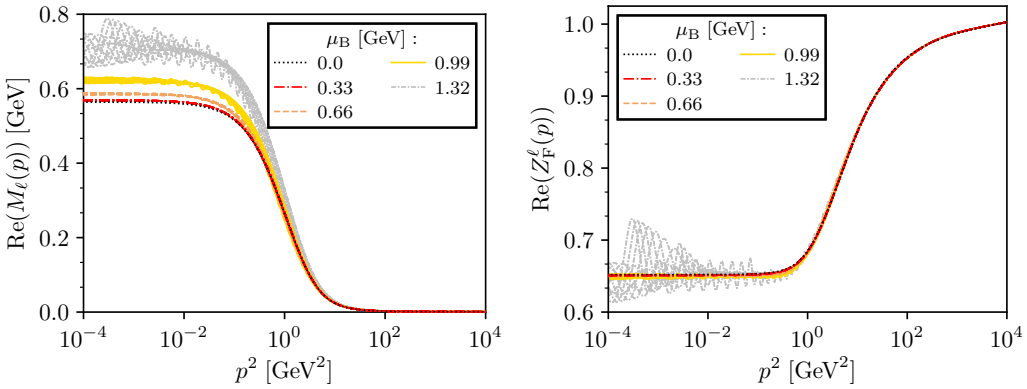

Figure 6.3.: Chemical potential dependency of the dynamical (light-)quark mass (left) and the quark wave-function renormalization function (right) for the combined effects of diquark and baryon backcoupling. The results are obtained with the Nambu solution only.

low and mid momenta for $\mu_B = 1.32\,\mathrm{GeV}$. This behavior is already visible for lower chemical potential but much less pronounced. To get insights into the origins of this oscillatory behavior, we consider the different self energy components of Eq. (6.1) in dependence of the chemical potential. While the baryon component Σ_f^{BA} already shows a weak oscillatory behavior at low chemical potential[4], the stronger oscillations enter near specific chemical potentials. If we consider the diquark Σ_f^{DQ} and baryon Σ_f^{BA} components separately, we observe that these chemical potentials are around $\mu_B = \frac{3}{2} m_{DQ} = 1.275\,\mathrm{GeV}$ and $\mu_B = m_N = 0.928\,\mathrm{GeV}$, respectively. We assume that they are connected to the poles of the diquark and baryon. Due to the poles in the integration area, our numerical calculation, e.g. the applied Cauchy method, breaks down and cannot be trusted any longer.

To conclude the dressing function discussion, we mention that neither the baryon nor the diquark contribution show a discontinuity in form of a jump in their behavior when passing the end of the Silver-Blaze region which corresponds to a baryon chemical potential equal to the baryon mass. We only find such a jump when passing from the Nambu to the Wigner phase. We however find a discontinuity in form of oscillations when passing both the specific chemical potentials mentioned before which are connected to the nucleon and scalar diquark mass. Since these oscillation originate from a numerical breakdown, we can neither confirm nor deny the existence of a liquid-gaseous phase transition. We assume that if we repair the numerical calculation by including the dynamically evaluated residues of the

[4] We expect the complex numerical evaluation or the strong approximations to be the reason.

bound state poles, we could possibly find an indication for such a transition. But unless these calculations are done, the situation remains unclear. Nevertheless, it is clear that our truncation lacks important chemical potential dependencies in the baryon and diquark propagators and vertices. We expect that an explicit calculation of the diquark Bethe-Salpeter equation and the three-quark Faddeev equation (possibly in the quark-diquark picture) in medium and with more than the leading amplitudes similar to the calculation in the last chapter, could improve the description of the baryon and could lead to a more visible indication of the liquid-gaseous phase transition.

6.3. Quark condensate

In this section, we will consider the reaction of the chiral observable on the introduction of diquark and baryon backcoupling terms at finite chemical potential. For this purpose, we display the vacuum-normalized and regularized light-quark condensate plotted against the baryon chemical potential in Fig. 6.4. In the figure, we display different combinations of backcouplings: We consider the diquark and baryon backcoupling separately and in combination and compare the results to the case without backcoupling (1BC). Since we consider only $N_f = 2$ quark flavors, we use a heavy quark 'h' instead of the strange quark to regularize the quark condensate. In the following, we will first consider the results of the Nambu solution before we continue with the Wigner solution.

As we saw already in previous chapters, the condensate without backcoupling remains constant until the end of the coexistence region. If we include only the diquark backcoupling, the condensate remains constant until the aforementioned value of $\mu_B = \frac{3}{2} m_{DQ} = 1.275\,\text{GeV}$ indicated by a vertical gray dotted line in the figure. The condensate results with baryon backcoupling on the other hand show a weak linear increase until the end of the Silver-Blaze region (marked as vertical magenta dotted line) and a stronger linear increase up to $\mu_B = \frac{3}{2} m_{DQ}$.[5] Although the quark condensate is, strictly speaking, not an observable quantity, the fact that the condensate with baryon backcoupling does not remain constant until the end of the Silver-Blaze region could hint at the violation of the Silver-Blaze property of other observables. We can imagine two origins of this behavior:

[5] Because of the chemical potential in the denominator, the diquark and baryon loop get weaker. Therefore, the chiral restoration effect of the two backcoupling terms is reduced, leading to increased values for the condensate.

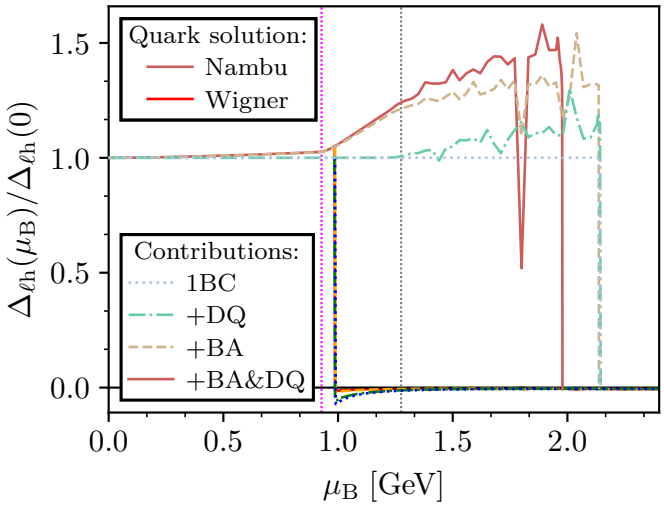

Figure 6.4.: Chemical potential dependence of the vacuum-normalized and regularized light-quark condensate for the chirally-broken Nambu (lines of muted colors) and chirally-restored Wigner (lines of bright colors) solution as well as for different combinations of considered diquark and baryon backcoupling terms (different line types). We consider results with the diquark and baryon backcoupling term included separately and in combination. In addition, we show the corresponding results without any backcoupling (1BC truncation). The densely dotted magenta and gray vertical lines correspond to the end of the Silver-Blaze region at $\mu_B = m_N$ and to the specific chemical potential $\mu_B = \frac{3}{2} m_{DQ}$.

(i) In the last section, we saw that the numerical complexity of the baryon loop calculation leads to small oscillations of the baryon contribution Σ_f^{BA} at low chemical potentials. This numerical instability could harm the SBP.

(ii) We saw in the last chapter that the correct way of meson backcoupling (with contained imaginary part of the BSAs) is important to obtain a constant behavior of the condensate. In this chapter, the correct chemical potential dependence of the diquark and baryon vertex is possibly missing (since we consider vacuum quantities) and cannot compensate the corresponding chemical potential dependence of the quark.

Above the baryon chemical potential $\mu_B = \frac{3}{2} m_{DQ}$, we see strong numerical artifacts which we trace back to the diquark and baryon poles which are now included into the integral calculation. Due to this behavior, it is not clear if the results can be trusted above $\mu_B = \frac{3}{2} m_{DQ}$ or even above $\mu_B = m_N$. Another observation is that the lower border of the coexistence region is unaffected by the backcoupling terms

while the upper border shows a stronger dependence. The results of the Wigner solution are only marginally affected by the inclusion of different backcoupling terms.

To conclude, we can furthermore mention that we were not able to find a finite but small jump in the light-quark condensate for all backcoupling types. Such a jump would however be a clear sign indicating a nuclear matter liquid-gaseous phase transition. But as already motivated in the last section, the absence of such a jump could be due to an insufficient calculation where the residues of the bound state poles are neglected. Consequently, to make a proper statement regarding the confirmation or denial of a liquid-gaseous phase transition, further calculations with improved numerics are necessary. In addition, we assume that the explicit calculation of the baryon and diquark in medium could provide us a chemical potential dependent nucleon mass, possibly with a discontinuity at a certain chemical potential indicating the liquid-gaseous phase transition.

7. Summary and conclusion

In this work, we studied the chemical potential dependence of quark and meson properties at vanishing temperature and investigated the impact of mesonic and baryonic backcoupling effects on different areas of the QCD phase diagram. For this purpose, we applied the functional framework of Dyson-Schwinger equations and explicitly calculated the meson bound state properties and the quark-meson Bethe-Salpeter vertex from their homogeneous Bethe-Salpeter equation. We used a well studied truncation [17, 35–38, 75, 76] to reduce the infinite tower of coupled integral equations to a coupled set of truncated DSEs for the Landau gauged quark and gluon propagators with $N_f = 2\,(+1)$ dynamical quark flavors. In this truncation, we expressed the Yang-Mills part of the gluon DSE by a temperature dependent fit to quenched lattice data [76, 97] and unquenched the equation by explicitly calculating the backcoupling of the quark onto the gluon. To keep the bound state calculation manageable and to be able to simultaneously calculate the phase diagram, we modified the infrared enhanced perturbative quark-gluon vertex ansatz used in previous works. To this end, the tensor structure of the vertex in the quark DSE, originally guided by the Slavnov-Taylor identity, is adjusted such that the axial-vector Ward-Takahashi identity is simply fulfilled. In addition, the gluon propagator at finite chemical potential and vanishing temperature is approximated by the vacuum equivalent. With these approximations, the newly defined truncation shows a qualitatively identical phase diagram but the critical endpoint is shifted to much higher chemical potentials and the curvature is decreased. Although this new truncation is less evolved than the previous one, the curvature (and the location of the CEP) agrees better with extrapolated lattice [104, 110, 111] and FRG [47–49] results.

With our calculations of quark and meson properties at finite chemical potential and vanishing temperature, we improved previous calculations by (i) taking into account the dynamics of the gluon rather than simply modeling it and (ii) solving the hBSE at finite chemical potential with more than the leading tensor structure as well as (iii) using quark propagators explicitly calculated in the complex momentum plane.[105] We identified the chirally-broken Nambu-Goldstone and the chirally-restored Wigner-Weyl solution of the quark and observed different coexistence regions (without overlap) for the light and strange quarks. Possibly this is due to the missing coupling between the quark flavors resulting from the new approximations

but could also be physically realized. The necessary thermodynamic calculations [43] to locate the physical first-order phase transition in this coexistence region could not be performed. Furthermore, we observed a strong chemical potential dependence of the quark dressing functions and meson Bethe-Salpeter amplitudes, especially for the light mesons. Interestingly, all mesons developed a significant chemical potential dependence in the imaginary part of the BSAs, which turned out to be crucial to balance the variations of the quark propagator w.r.t. the chemical potential and to provide the Silver-Blaze property. In fact, the meson mass and decay constant of all considered (light and strange quark) mesons and the quark condensate remain constant within the numerical precision and fulfill therefore the SBP. Only the light mesons showed a stronger chemical potential dependence at large chemical potentials in the coexistence regions. The existence of all mesons could be traced up to the end of the corresponding coexistence regions but the determination of mesons for the Wigner solution was not possible because of numerical problems connected to the pole structure of the quarks in the complex momentum plane. By applying a Chebychev expansion to the BSAs, we were also able to trace the breaking of the charge conjugation parity back to the introduction of chemical potential. This property is expected since the quark and the antiquark are no longer energetically degenerated due to the energy offset induced by the chemical potential.

For the hadronic backcoupling, we extended the truncation by introducing hadron degrees of freedom into the quark-gluon vertex DSE and reducing the vertex to a decomposition of a non-hadronic, a mesonic and a bosonic contribution. We did not solve the vertex DSE but inserted the decomposition into the quark DSE, instead. In the gluon DSE and the meson BSE, however, only the non-hadronic part is used which we identify with the vertex ansatz introduced before. We studied the meson and baryon backcoupling separately and neglected the respective other contribution. In case of the meson backcoupling, we introduced further approximations to obtain a calculable one-loop one-meson exchange diagram. These approximations originate from a series of previous works [38, 56–58, 89] and are guided by the AxWTI and comparisons to corresponding lattice results. Unfortunately, the approximations prevent a study of the universal properties (of the CEP). Instead of using ansätze or approximations for the mesons like in previous works [38, 56, 58, 89, 169, 170], we used explicitly calculated meson properties and wave-functions as input. If we backcouple these explicitly calculated Pion and Sigma mesons, we find a similar chiral restoration effect for both of them. Furthermore, both violate the SBP at finite chemical potential but, at least for the Pion backcoupling, this violation can be repaired by a modification of the approximations introduced for the meson backcoupling. Thereby, the importance of the imaginary part of the meson BSAs for the SBP is observed once again and it is shown that the applied

approximations have to be improved. Our study of the phase diagram implies that mesonic backcoupling effects are qualitatively irrelevant and quantitatively small. Through the meson backcoupling the CEP is shifted marginally to smaller chemical potentials and higher temperatures. Furthermore, backcoupling Pions and Sigma mesons decreases the curvature to a small extent. A similar effect could be found for the baryon backcoupling in Ref. [44]. Together with Refs [38, 44, 89], we therefore find strong evidence that the location of the CEP is mainly driven by the non-resonant part of the quark-gluon vertex, i.e. by the microscopic degrees of freedom of QCD, the quarks and gluons. The macroscopic dof, in particular the Sigma meson, are expected to be dominant for the properties of the CEP [52, 59, 60].[55]

Oriented to the truncation detailed in Ref. [44], we used a quark-diquark approximation and baryon and diquark properties and wave-functions obtained from a vacuum calculation as input to study the baryon backcoupling effects at finite chemical potential. The baryon and diquark backcoupling effects lead to chiral restoration effects in the same order as the meson but the applied numeric and possibly the strong approximations are insufficient to properly describe the baryon backcoupling. On the one hand, the SBP is violated while, on the other hand, unconsidered residues of poles in the bound state propagators lead to an oscillating behavior of the quark dressing functions and the quark condensate. We assume that a proper calculation of these bound state pole residues is necessary to get rid of the numerical oscillations and to possibly find a proper indication of the liquid-gaseous nuclear matter phase transition. Furthermore, we expect that a proper calculation of the baryon properties and wave-functions at finite chemical potential, as we performed for the meson, could improve the description of the SBP and lead to a more visible indication of the liquid-gaseous phase transition.

To conclude, we would like to emphasize that the observation of a constant behavior for all meson masses and decay constants (as well as the quark condensate with and without Pion backcoupling) until the end of the Silver-Blaze region and beyond is a highly non-trivial matter. The fact that the SBP is fulfilled, relies on subtle cancellations between the chemical potential dependencies of the quarks and mesons. These quantities have to interplay such that they produce constant masses and decay constant. It is quite satisfying to see that this happens in our functional approach.[143]

A. Conventions

In this chapter, we will introduce the used conventions and abbreviations. We will begin with general remarks before we continue with the Dirac, color and (meson) flavor space representations and relations. Then, we introduce the Euclidean and momentum space and show how the are related to the Minkowski and coordinate space. In the last two sections, we will reformulate the QCD action in the corresponding spaces.

In general, we use the Einstein sum convention $a \cdot b = a_\mu b^\mu = \sum_\mu a_\mu b^\mu$ and natural (Planck) units, i.e. the speed of light $c = 1$, the Planck constant $\hbar = 1$, the Boltzmann constant $k_\mathrm{B} = 1$ and the electrical charge $e = 1$ are set to one. For the integral representation we normally introduce abbreviations. The four dimensional momentum and space-time integrals are represented by $\int_p = \int \frac{d^4p}{(2\pi)^4}$ and $\int_x = \int d^4x$, respectively. At finite temperature, the temporal integral is furthermore only a finite interval integration. For the finite temperature momentum integral, we use the shorthand notation $\fint_p = \sum_{\omega_p} \int \frac{d^3p}{(2\pi)^3}$. In the following the Pauli

$$\sigma_1 = \begin{pmatrix} 0 & 1 \\ 1 & 0 \end{pmatrix}, \qquad \sigma_2 = \begin{pmatrix} 0 & -i \\ i & 0 \end{pmatrix}, \qquad \sigma_3 = \begin{pmatrix} 1 & 0 \\ 0 & -1 \end{pmatrix} \tag{A.1}$$

and Gell-Mann matrices

$$\lambda_1 = \begin{pmatrix} 0 & 1 & 0 \\ 1 & 0 & 0 \\ 0 & 0 & 0 \end{pmatrix}, \ \lambda_2 = \begin{pmatrix} 0 & -i & 0 \\ i & 0 & 0 \\ 0 & 0 & 0 \end{pmatrix}, \ \lambda_3 = \begin{pmatrix} 1 & 0 & 0 \\ 0 & -1 & 0 \\ 0 & 0 & 0 \end{pmatrix}, \ \lambda_4 = \begin{pmatrix} 0 & 0 & 1 \\ 0 & 0 & 0 \\ 1 & 0 & 0 \end{pmatrix},$$

$$\lambda_5 = \begin{pmatrix} 0 & 0 & -i \\ 0 & 0 & 0 \\ i & 0 & 0 \end{pmatrix}, \ \lambda_6 = \begin{pmatrix} 0 & 0 & 0 \\ 0 & 0 & 1 \\ 0 & 1 & 0 \end{pmatrix}, \ \lambda_7 = \begin{pmatrix} 0 & 0 & 0 \\ 0 & 0 & -i \\ 0 & i & 0 \end{pmatrix}, \ \lambda_8 = \frac{1}{\sqrt{3}} \begin{pmatrix} 1 & 0 & 0 \\ 0 & 1 & 0 \\ 0 & 0 & -2 \end{pmatrix} \tag{A.2}$$

are important. These are traceless ($\mathrm{Tr}[A_i] = 0$), Hermitian ($A_i^\dagger = A_i$) and orthogonal ($\mathrm{Tr}[A_i A_j] = 2\delta_{ij}$) matrices for each case $A \in \{\sigma, \lambda\}$.

A.1. Dirac space

The most important basis elements of the Dirac space are the so-called Dirac matrices γ^μ. They are defined by the Clifford algebra which is inherited from the Pauli matrices and in Minkowski space given by

$$\{\gamma^\mu, \gamma^\nu\} = 2g_-^{\mu\nu} \mathbb{1}_\mathrm{D} \tag{A.3}$$

with the unit matrix $\mathbb{1}_\mathrm{D} = \mathrm{diag}(1,1,1,1)$ and the metric tensor of the Minkowski space $g_- = \mathrm{diag}(1,-1,-1,-1)$ in the mostly minus convention. The latter quantity defines the connection between covariant and contravariant Lorentz vectors $p^\mu = g_-^{\mu\nu} p_\nu$. In the standard Dirac representation, the Dirac matrices are given by

$$\gamma^0 = \begin{pmatrix} \mathbb{1} & 0 \\ 0 & -\mathbb{1} \end{pmatrix}, \qquad \gamma^k = \begin{pmatrix} 0 & \sigma_k \\ -\sigma_k & 0 \end{pmatrix}, \qquad \gamma^5 = i\gamma^0\gamma^1\gamma^2\gamma^3 = \begin{pmatrix} 0 & \mathbb{1} \\ \mathbb{1} & 0 \end{pmatrix} \tag{A.4}$$

with $k \in \{1,2,3\}$. Other representations are possible but have to be unitary transformations $\gamma_\mu^{'} = U\gamma_\mu U^\dagger$ of the Dirac representation. One of these other representations is the Weyl or chiral representation received by the unitary transformation $U = \frac{1}{\sqrt{2}}\left(\begin{smallmatrix} \mathbb{1} & -\mathbb{1} \\ \mathbb{1} & \mathbb{1} \end{smallmatrix}\right)$. This representation is important, since in this notation the $\mathrm{Weyl}(\gamma^5) = -\mathrm{Dirac}(\gamma^0)$ matrix is diagonal and used to project onto left- and right-handed particles. This is relevant in the chiral or ultra-relativistic limit where the quark masses are neglectable. In each representation, the Dirac matrices γ^μ and the special Dirac matrix γ^5 are related by

$$\left\{\gamma^\mu, \gamma^5\right\} = 0 \tag{A.5}$$

which means that they anticommute. To conclude, we have to mention the Feynman slash notation $A_\mu\gamma^\mu = \not{A}$, where A_μ is an arbitrary Lorentz vector.

A.2. Color space

For the color space, we have to consider two representations of the $\mathrm{SU_C(N_c)}$-group[1]: the fundamental representation for quarks and the adjoint representation for the gluons as gauge Bosons which mediate the strong interaction. In both cases, the $\mathrm{N_c^2} - 1$ generators t_a fulfill the Lie algebra

$$[t_a, t_b] = i f_{abc} t_c \tag{A.6}$$

[1] Throughout the whole work, We always use $\mathrm{N_c} = 3$ colors flavors.

where the quantities f_{abc} are the totally antisymmetric structure constants defined in Tab. A.1 together with the totally symmetric structure constants d_{abc} which in turn result from the anticommutation relation of the generators in the fundamental representation $\{t_a, t_b\} = \frac{1}{2\mathrm{N_c}}\delta_{ab}\mathbb{1}_\mathrm{C} + \frac{1}{2}d_{abc}t_c$.

Table A.1.: Totally antisymmetric (left) and symmetric (right) real structure constants for the color gauge group $\mathrm{SU_C(N_c)}$ with three colors $\mathrm{N_c} = 3$. All indices resulting from permutations have the same structure constant value. The structure constants of the remaining indices are zero

f_{abc}	abc
1	123
1/2	147, 246, 257, 345
−1/2	156, 367
$\sqrt{3}/2$	458, 678

d_{abc}	abc
$1/\sqrt{3}$	118, 228, 338
1/2	146, 157, 256, 344, 355
−1/2	247, 366, 377
$-1/\sqrt{6}$	448, 558, 668, 778
$-1/\sqrt{3}$	888

In addition, the generators fulfill the relations

$$\mathrm{Tr_C}[t_a t_b] = T(R)\delta_{ab} \qquad \text{and} \qquad \left(\sum_{a=0}^{\mathrm{N_c^2}-1} t_a^2\right)_{ij} = C(R)\delta_{ij} \tag{A.7}$$

with $T(R)$ and $C(R)$ representing the Dynkin index and Casimir factor in the representation R. The values of these two objects are detailed in Tab. A.2 for the fundamental and adjoint representation together with the representation of the matrices and their dimension. In the fundamental representation, the matrices $t_a = \frac{\lambda_a}{2}$ are defined through the Gell-Mann matrices λ_a in Eq. (A.2).

Table A.2.: Fundamental and adjoint representation of the $\mathrm{SU_C(N_c)}$-group generators and corresponding properties.

Representation R	$(t_a)_{ij}$	$\dim(t_a)$	$T(R)$	$C(R)$
Fundamental	$(\lambda_a/2)_{ij}$	$\mathrm{N_c}$	$\frac{1}{2}$	$\frac{\mathrm{N_c^2}-1}{2\mathrm{N_c}}$
Adjoint	$-if_{aij}$	$\mathrm{N_c^2}-1$	$\mathrm{N_c}$	$\mathrm{N_c}$

A.3. Flavor space

In this section, we consider the meson flavor matrices in the quark flavor space of $N_f = 3$ quark flavors. In Sec. 3, we already mentioned the considered mesons of the different spin-parity-states. In Tab. A.3, the different representations of these mesons are shown together with their quark-antiquark content. It has to be mentioned that the ϕ-meson normally is a mixing of $u\bar{u}$, $d\bar{d}$ and $s\bar{s}$ but due to the experimentally observed mixing angle of $\theta_V = 39°$ we can safely assume that the meson only consists out of $s\bar{s}$. In the equations, we will use $r_x^e = \sqrt{N_f}\, b_x^e$ instead

Table A.3.: Meson bound-state flavor structure for different spin-parity states $x \in \{PS, S, V, AV\}$ and contained mesons $e \in \{\pi^\pm, \pi^0, K^0, \bar{K}^0, K^\pm, \sigma, \rho^\pm, \rho^0, \phi, a_1\}$. The second to fourth column are different representations of the meson flavor structure in the considered $N_f = 3$ dimensional quark flavor space. The second column shows the quark and antiquark content where the antiquarks are given by $\bar{u} = (100)$, $\bar{d} = (010)$, $\bar{s} = (001)$ and the corresponding quarks via $\{u, d, s\} \ni x = \bar{x}^\top$. The fourth column is the representation of the meson flavor using the Gell-Mann matrices defined in Eq. (A.2).

b_x^e	$q\bar{q}$	$(\dot{\cdot}\dot{\cdot})$	λ
$b_{PS}^{\pi^+}$, $b_V^{\rho^+}$	$u\bar{d}$	$\left(\begin{smallmatrix}0&1&0\\0&0&0\\0&0&0\end{smallmatrix}\right)$	$\frac{1}{2}(\lambda_1 + i\lambda_2)$
$b_{PS}^{\pi^-}$, $b_V^{\rho^-}$	$d\bar{u}$	$\left(\begin{smallmatrix}0&0&0\\1&0&0\\0&0&0\end{smallmatrix}\right)$	$\frac{1}{2}(\lambda_1 - i\lambda_2)$
$b_{PS}^{\pi^0}$, $b_V^{\rho^0}$	$\frac{1}{\sqrt{2}}(u\bar{u} - d\bar{d})$	$\left(\begin{smallmatrix}1&0&0\\0&-1&0\\0&0&0\end{smallmatrix}\right)$	$\frac{1}{2}\lambda_3$
b_S^{σ}, $b_{AV}^{a_1}$	$\frac{1}{\sqrt{2}}(u\bar{u} + d\bar{d})$	$\left(\begin{smallmatrix}1&0&0\\0&1&0\\0&0&0\end{smallmatrix}\right)$	$\frac{\sqrt{2}}{3}\mathbb{1}_F + \frac{1}{\sqrt{6}}\lambda_8$
$b_{PS}^{K^0}$	$d\bar{s}$	$\left(\begin{smallmatrix}0&0&0\\0&0&1\\0&0&0\end{smallmatrix}\right)$	$\frac{1}{2}(\lambda_6 + i\lambda_7)$
$b_{PS}^{K^+}$	$u\bar{s}$	$\left(\begin{smallmatrix}0&0&1\\0&0&0\\0&0&0\end{smallmatrix}\right)$	$\frac{1}{2}(\lambda_4 + i\lambda_5)$
$b_{PS}^{K^-}$	$s\bar{d}$	$\left(\begin{smallmatrix}0&0&0\\0&0&0\\0&1&0\end{smallmatrix}\right)$	$\frac{1}{2}(\lambda_6 - i\lambda_7)$
$b_{PS}^{\bar{K}^0}$	$s\bar{u}$	$\left(\begin{smallmatrix}0&0&0\\0&0&0\\1&0&0\end{smallmatrix}\right)$	$\frac{1}{2}(\lambda_4 + i\lambda_5)$
b_V^{ϕ}	$s\bar{s}$	$\left(\begin{smallmatrix}0&0&0\\0&0&0\\0&0&1\end{smallmatrix}\right)$	$\frac{1}{3}\mathbb{1}_F - \frac{1}{\sqrt{3}}\lambda_8$

of the normalized meson flavor structures of the table. These modified matrices fulfill the orthogonality relation $\mathrm{Tr}_F\left[(r_x^e)^\top r_x^l\right] = N_f\delta_{el}$ and similar commutation and anticommutation relations as in App. A.2 for the fundamental representation.

A.4. Euclidean space

All our calculations are done in the Euclidean space. Therefore, in this section, we will introduce the Euclidean space as a counterpart to Minkowski space and show the connection between them. All quantities with index "E" are given in the Euclidean space, while the Minkowski quantities are shown without index. As notional remark, we have to mention that in Euclidean space we refer to the energy component with index 4 instead of 0 in Minkowski space. The main property of the Euclidean space is that the difference between the co- and contra-variant vectors vanishes and the metric is now given by $g_{-}^{\mu\nu} \to \delta_{\mu\nu}$. Consequently, the scalar products and the Clifford-algebra now given by

$$a_{\mathrm{E}} \cdot b_{\mathrm{E}} = \sum_{\mu} a_{\mathrm{E}}^{\mu} b_{\mathrm{E}}^{\mu} = \vec{a}_{\mathrm{E}} \vec{b}_{\mathrm{E}} + a_{\mathrm{E}}^{4} b_{\mathrm{E}}^{4} \qquad \text{and} \qquad \{\gamma_{\mathrm{E}}^{\mu}, \gamma_{\mathrm{E}}^{\nu}\} = 2\delta_{\mu\nu} \mathbb{1}_{\mathrm{D}} \,. \tag{A.8}$$

Note that this is applicable to the Feynman slash notation by exchanging a or b with γ, too. We achieve this property via Wick rotation and the resulting redefinition of the Lorentz-vectors, -tensors and gamma matrices. The Euclidean counterparts are defined via

$$a_{\mathrm{E}}^{\mu} = \begin{pmatrix} \vec{a} \\ i a_0 \end{pmatrix} , \qquad \gamma_{\mathrm{E}}^{\mu} = \begin{pmatrix} -i\vec{\gamma} \\ \gamma_0 \end{pmatrix} , \qquad T_{\mathrm{E}}^{\mu\nu} = \begin{pmatrix} T^{00} & iT^{i0} \\ iT^{0j} & -T^{ij} \end{pmatrix} , \qquad \gamma_{\mathrm{E}}^{5} = \gamma^{5} \,. \tag{A.9}$$

The Dirac matrices in the Euclidean standard representation are now Hermitian ($\gamma_{\mathrm{E}}^{\mu} = (\gamma_{\mathrm{E}}^{\mu})^{\dagger}$) and are represented by

$$\gamma_{\mathrm{E}}^{0} = \begin{pmatrix} \mathbb{1} & 0 \\ 0 & -\mathbb{1} \end{pmatrix} , \qquad \gamma_{\mathrm{E}}^{k} = \begin{pmatrix} 0 & -i\sigma_k \\ i\sigma_k & 0 \end{pmatrix} , \qquad \gamma_{\mathrm{E}}^{5} = \begin{pmatrix} 0 & \mathbb{1} \\ \mathbb{1} & 0 \end{pmatrix} . \tag{A.10}$$

The overall replacement rules between the Minkowski and Euclidean space, which follow from the representations above, are

$$a_{\mathrm{E}} \cdot b_{\mathrm{E}} = a \cdot b \,, \qquad \not{a}_{\mathrm{E}} = i\not{a} \,, \qquad (\partial \cdot a)_{\mathrm{E}} = (\partial \cdot a) \,, \qquad \not{\partial}_{\mathrm{E}} = -i\not{\partial} \,, \qquad \Box_{\mathrm{E}} = -\Box \,. \tag{A.11}$$

The Wick rotation also influences the fourth component of the integral such that we get the connection

$$\lim_{t \to \infty - i\epsilon} i \int_{-t}^{t} dx_0 = \lim_{\tau \to \infty} \int_{-\tau}^{\tau} dx_4 \tag{A.12}$$

between Minkowski and Euclidean time integral. In Minkowski space, the infinitesimal ϵ parameter was necessary due to poles of the propagator in the integration

interval. Using the rules presented in this section, we can rewrite the Euclidean QCD action in Landau gauge to

$$
\begin{aligned}
S^{\mathrm{E}}_{\mathrm{QCD}}[A,\bar{\Psi},\Psi,c,\bar{c}] = \int_x \Big[& Z_2 \bar{\Psi}(x) \left(\not{\partial} + Z_m m_{\mathrm{q}}\right) \Psi(x) + \\
& + Z_{1F}^f i g_{\mathrm{s}} \bar{\Psi}(x) \not{A}(x) \Psi^f(x) - Z_3 \frac{1}{2} A^g_\mu(x) \left(\Box \delta_{\mu\nu} - \partial_\nu \partial_\mu\right) A^g_\nu(x) + \\
& - Z_1 \frac{g_{\mathrm{s}}}{2} f_{ghl} \left[\partial_\mu A^g_\nu(x) - \partial_\nu A^g_\mu(x)\right] A^h_\mu(x) A^l_\nu(x) + \tilde{Z}_3 \bar{c}(x) \Box c(x) + \\
& - Z_4 \frac{g_{\mathrm{s}}^2}{4} f_{gko} f_{ghl} A^\mu_k(x) A^\nu_o(x) A^h_\mu(x) A^l_\nu(x) + i g_{\mathrm{s}} \tilde{Z}_1 \left(\partial_\mu \bar{c}(x)\right) \mathcal{A}^\mu(x) c(x) \Big]
\end{aligned}
\tag{A.13}
$$

where we suppress the index E except for the action itself. Overall, the the Euclidean and Minkowski action are connected via $iS = -S_{\mathrm{E}}$. The index 'E' will no longer be used in this work. The considered space will be clear in the context.

A.5. Momentum space

On top of the Euclidean space, we always calculate in the momentum space. For this purpose, we now show the connection between the coordinate and momentum space. A transformation between the two spaces is possible via the Fourier transformations

$$
\varphi(x) = \int \frac{d^4p}{(2\pi)^4} e^{-ipx} \varphi(p)\,, \qquad \varphi(p) = \int d^4x\, e^{ipx} \varphi(x) \tag{A.14}
$$

where φ stands for an arbitrary variable, e.g. a certain field in the QCD action. At finite temperature, we have to take the changes of the four dimensional integrals mentioned in Sec. 2.1.3 into account. This means that the time integral is finite in the coordinate space implying a sum over discrete Matsubara frequencies for the energy component in the momentum space. For the transformation into momentum space, we, furthermore, have to apply the substitutions

$$
\partial \cdot v(x) \to ip \cdot v(p)\,, \qquad \Box s(x) \to -k^2 s(k)\,, \qquad \not{\partial} s(x) = i \not{q} s(q)\,. \tag{A.15}
$$

with the Lorentz vector v and the Lorentz scalar s. The Fourier transformation implies that we have to integrate over a new four-momentum for every transformed variable. Applied onto Eq. (A.13), the Euclidean QCD action in Landau-gauge in

momentum space is given by

$$
\begin{aligned}
S^{\mathrm{E}}_{\mathrm{QCD}}[A,\bar{\Psi},\Psi,c,\bar{c}] = \int_{\vec{p}} \Big[& Z_2 \bar{\Psi}(p_1)\left(i\not{p}_2 + Z_m m_{\mathrm{q}}\right)\Psi(p_2) + \\
& + Z_{1F}^f i g_{\mathrm{s}} \bar{\Psi}(p_1) \not{A}(p_2) \Psi^f(p_3) + Z_3 \frac{1}{2} A^g_\mu(p_1)\left(p_2^2 \delta_{\mu\nu} - p_2^\nu p_2^\mu\right) A^g_\nu(p_2) + \\
& - Z_1 i \frac{g_{\mathrm{s}}}{2} f_{ghl}\left[p_1^\mu A^g_\nu(p_1) - p_1^\nu A^g_\mu(p_1)\right] A^h_\mu(p_2) A^l_\nu(p_3) - \tilde{Z}_3 \bar{c}(p_1) p_2^2 c(p_2) + \\
& - Z_4 \frac{g_{\mathrm{s}}^2}{4} f_{gko} f_{ghl} A^\mu_k(p_1) A^\nu_o(p_2) A^h_\mu(p_3) A^l_\nu(p_4) - g_{\mathrm{s}} \tilde{Z}_1 \left(p_1^\mu \bar{c}(p_1)\right) \mathcal{A}^\mu(p_2) c(p_3) \Big]
\end{aligned}
\tag{A.16}
$$

with shorthand notation $\int_{\vec{p}} = \int_{p_1} \ldots \int_{p_n} \delta(p_1 + \ldots p_n)$. In this notation, the variables p_i $i \in [1, n]$ represent the n four-momenta of the n fields of the considered term. The delta-distribution ensures the four-momentum conservation and results from the space-time integral of the action.

B. Transformations and symmetries

In this section, we consider invariances of the QCD (action) under certain symmetry-transformations. Symmetries, which we identify with invariances, imply conserved quantities. We are interested in finding these conserved quantities for the considered transformations. We will begin with the Lorentz and Poincaré transformations which are the basic symmetries of all theories. Then we consider symmetries under quark flavor transformations and conclude with resulting quantum mechanical current conservations (identities). But to begin, we introduce some basic relations and naming conventions which we will need later on.

B.1. Basic relations and notations

For simplicity, we define the quark bilinears

$$\begin{aligned} j^{(\mu)}_{\Gamma,a}(x) &= \bar{\Psi}(x)\Gamma^{(\mu)}\tau_a\Psi(x)\,, \\ j^{(\mu)}_{\Gamma}(x) &= \bar{\Psi}(x)\Gamma^{(\mu)}\Psi(x) \end{aligned} \tag{B.1}$$

with the quark spinor Ψ and antispinor $\bar{\Psi}$ as well as the Dirac matrices $\Gamma^{(\mu)} \in \{\mathbb{1}_{\mathrm{D}}, i\gamma_5, \gamma^\mu, \gamma^\mu\gamma_5\}$. Based on these quark bilinears, we introduce the notation of scalar $\mathrm{S}_{(a)}(x)$ and pseudo-scalar $\mathrm{P}_{(a)}(x)$ densitys as well as vector $\mathrm{V}^\mu_{(a)}(x)$ and axial-vector $\mathrm{A}^\mu_{(a)}(x)$ currents via

$$\begin{aligned} \mathrm{S}_{(a)}(x) &\leftrightarrow \Gamma^{(\mu)} = \mathbb{1}_{\mathrm{D}}\,, & \mathrm{V}^\mu_{(a)}(x) &\leftrightarrow \Gamma^{(\mu)} = \gamma^\mu \quad , \\ \mathrm{P}_{(a)}(x) &\leftrightarrow \Gamma^{(\mu)} = i\gamma_5\,, & \mathrm{A}^\mu_{(a)}(x) &\leftrightarrow \Gamma^{(\mu)} = \gamma^\mu\gamma_5 \end{aligned} \tag{B.2}$$

with $j^{(\mu)}_{\Gamma,(a)}(x) \in \{\mathrm{S}_{(a)}(x), \mathrm{P}_{(a)}(x), \mathrm{V}^\mu_{(a)}(x), \mathrm{A}^\mu_{(a)}(x)\}$. We will see in the next section that these densities and currents correspond to spin-parity states. In the following, we will consider color ($\tau_a = t_a$ in the fundamental representation) and meson flavor ($\tau_a = r^a_{\mathrm{x}}$) currents and densities with the matrix elements defined in Apps. A.2 and A.3, respectively.

By applying Eq. (2.7), we can express classical relations of these currents and densities as quantum mechanical identities. For this purpose, we have to consider

the quark fields and bilinears as operators, before we take the vacuum expectation value. As result of this procedure, we get quantum mechanical relations between Green functions. To shorten future relations, we therefore introduce the naming conventions

$$\begin{aligned} G_{2n,S}(x_1,\ldots,x_{2n}) &= \left\langle 0 \left| \hat{T} \left\{ \hat{\bar{\Psi}}(x_1)\hat{\Psi}(x_2)\ldots\hat{\bar{\Psi}}(x_{2n-1})\hat{\Psi}(x_{2n}) \right\} \right| 0 \right\rangle , \\ G^{(\mu)}_{2n,\Gamma,(a)}(y;x_1,\ldots,x_{2n}) &= \left\langle 0 \left| \hat{T} \left\{ \hat{j}^{(\mu)}_{\Gamma,(a)}(y)\hat{\bar{\Psi}}(x_1)\hat{\Psi}(x_2)\ldots\hat{\bar{\Psi}}(x_{2n-1})\hat{\Psi}(x_{2n}) \right\} \right| 0 \right\rangle , \\ G^{(\mu\nu)}_{\Gamma\Gamma',(ab)}(y;x) &= \left\langle 0 \left| \hat{T} \left\{ \hat{j}^{(\mu)}_{\Gamma,(a)}(y)\hat{j}^{(\nu)}_{\Gamma',(b)}(x) \right\} \right| 0 \right\rangle . \end{aligned} \tag{B.3}$$

for quark Green functions (compare with Eq. (2.2)). The indices S and $\Gamma \in \{\mathrm{S},\mathrm{P},\mathrm{V},\mathrm{A}\}$ indicate the corresponding quark and bilinear content. The first Green function describes a correlation function of n incoming and n outgoing quark fields and the second one corresponds to a transition element between the current $\hat{j}^{(\mu)}_{\Gamma,(a)}(y)$ and a n quark and n antiquark state while the last one is a correlation of two densities or currents of the kinds Γ and Γ'. For two identical (spin-parity) quark bilinears the latter Green function describes a 2PI two-point Green function or propagator

$$G^{(\mu\nu)}_{\Gamma\Gamma,(ab)}(x;y) = \delta_{ab}\int_P e^{-iPz} D^{(\mu\nu)}_{F,\Gamma}(P,m) = \delta_{ab} G^{[2],(\mu\nu)}_{2,S,\Gamma}(z) \tag{B.4}$$

with $z = x - y$ and the Feynman propagator $D^{(\mu\nu)}_{F,\Gamma}(P,m) = \frac{i\Lambda^{(\mu\nu)}_{\Gamma}(P)}{P^2 - m^2 + i\epsilon}$ where m and P are the mass and the total momentum of the particle and $\Lambda^{(\mu\nu)}_{\Gamma}(P)$ defines a spin state dependent function.[1] Additionally, the Green function $G^{(\mu\nu)}_{\Gamma\Gamma,(ab)}(y;x)$ can be seen as a projected version of a four-point 1PI quark Green function $G^{\mathcal{P}}_{4,S}$

$$G^{(\mu\nu)}_{\Gamma\Gamma,(ab)}(y;x) = \left\langle 0 \left| \hat{T} \left\{ \hat{\bar{\Psi}}(x)\Gamma^{(\mu)}\tau_a\hat{\Psi}(x)\hat{\bar{\Psi}}(y)\Gamma^{(\mu)}\tau_b\hat{\Psi}(y) \right\} \right| 0 \right\rangle = G^{\mathcal{P}}_{4,S}(y,y,x,x) \tag{B.5}$$

where projected means that the quark-antiquark state is projected onto a certain spin-parity and (meson) flavor or color subspace by introducing Dirac and (meson) flavor or color matrices. If we return to the quark bilinears in Eq. (B.1) and consider them as operators, the quark bilinear and field operators fulfill the commutation

[1] If we consider meson flavor densities or currents ($\tau_a = r^a_{\mathrm{x}}$) the 2PI two-point Green function can be seen as effective meson propagator of the bound state mass m_{x} and the total momentum P.

relations

$$\begin{aligned}
\left[\hat{j}^{(\mu)}_{\Gamma,a}(y), \hat{\Psi}(x)\right] &= -\tau_a \gamma^0 \Gamma^{(\mu)} \hat{\Psi}(x) \delta^3(\vec{x}-\vec{y})\,, \\
\left[\hat{j}^{(\mu)}_{\Gamma,a}(y), \hat{\bar{\Psi}}(x)\right] &= \hat{\bar{\Psi}}(x) \Gamma^{(\mu)} \gamma^0 \tau_a \delta^3(\vec{x}-\vec{y})\,, \\
\left[\hat{j}^{(\mu)}_{\Gamma,a}(y), \hat{j}^{(\nu)}_{\Gamma',b}(x)\right] &= \frac{1}{2} \hat{\bar{\Psi}}(x) \left(\Gamma^{(\mu\nu)}_{+} \left[\tau_a, \tau_b\right] + \Gamma^{(\mu\nu)}_{-} \left\{\tau_a, \tau_b\right\}\right) \hat{\Psi}(x) \delta^3(\vec{x}-\vec{y})\,, \\
\left[\hat{j}^{(\mu)}_{\Gamma,a}(y), \hat{j}^{(\nu)}_{\Gamma'}(x)\right] &= \hat{\bar{\Psi}}(x) \Gamma^{(\mu\nu)}_{-} \tau_a \hat{\Psi}(x) \delta^3(\vec{x}-\vec{y})
\end{aligned} \tag{B.6}$$

with $\Gamma^{(\mu\nu)}_{\pm} = \Gamma^{(\mu)}\gamma_0\Gamma'^{(\nu)} \pm \Gamma'^{(\nu)}\gamma_0\Gamma^{(\mu)}$. Before we start to discuss some specific transformations, let us discuss two different symmetry representations of an arbitrary continuous global symmetry group.

Symmetry representations

This section follows the lines of Ref. [73]. We begin by considering a continuous global symmetry group G which acts non-trivially on the fields φ_i (eventually describing bound states/ composite particles). The quantum mechanical transformation and its infinitesimal version are given by

$$e^{i\epsilon_a \hat{Q}_a} \hat{\varphi}_i e^{-i\epsilon_a \hat{Q}_a} = D^{-1}_{ij}(\epsilon) \hat{\varphi}_j \qquad \text{and} \qquad \left[\hat{Q}_a, \hat{\varphi}_i\right] = -(\hat{\tau}_a)_{ij} \hat{\varphi}_i \tag{B.7}$$

where $e^{i\epsilon_a \hat{Q}_a}$ is an element of the symmetry group G and $D^{-1}_{ij}(\epsilon) = \left[e^{i\epsilon_a \hat{\tau}_a}\right]_{ij}$ is the representation matrix corresponding to the representation to which the field φ_i belongs. $\hat{Q}_a$ is a charge operator which forms a representation of the algebra on Hilbert space, whereas ϵ_a and $\hat{\tau}_a$ are the group parameters and generators of the Lie algebra of G in the representation of the field φ_i.

If the symmetry group leaves the vacuum invariant, i.e. $e^{i\epsilon_a \hat{Q}_a} |0\rangle = |0\rangle$, the generator annihilates the vacuum $\hat{Q}_a |0\rangle = 0$. Considering the vacuum expectation value of the general transformation in Eq. (B.7), the fields transform non-trivially under G, implying that $D^{-1}_{ij}(\epsilon)$ is not the identity matrix. Consequently, if the symmetry group leaves the vacuum invariant, $\langle 0 | \hat{\varphi}_i | 0 \rangle$ must vanish for all i to fulfill the equation. This is called the Wigner-Weyl representation of the symmetry.

If, however, an operator $\hat{\varphi}$ which is not invariant under G develops a non-zero vacuum expectation value, the symmetry G is spontaneously broken. We call this the Nambu-Goldstone realization of the symmetry. In consequence the charge operators do not annihilate the vacuum but produce another energy-degenerated vacuum state $|\eta\rangle = \hat{Q}_a |0\rangle$ instead. Since the symmetry is classically conserved the charge operator commutes with the Hamiltonian and therefore $\hat{H} |\eta\rangle = 0$.

B.2. Poincaré and Lorentz transformations

In Sec. 3, we introduced particles as irreducible representations of the Poincaré group with fixed quantum numbers. In this section, we are interested to find the irreducible representations and their connected quantum numbers which describe and classify our (fundamental and composite) particles. In addition, we will derive transformation properties necessary for the description of bound states. At first, we will consider the properties of the Lorentz group before we deepen this investigation when studying the Poincaré group. Throughout this section, we work in the Minkowski space with the metric g_- defined in App. A.1.

B.2.1. Lorentz group

The Lorentz transformations are defined as the transformations

$$\mathrm{U}_\Lambda(\Lambda): \qquad x' = \Lambda x \qquad \Leftrightarrow \qquad x'_\mu = \Lambda^\nu{}_\mu x_\nu \tag{B.8}$$

that leave the scalar product $x \cdot y = x^\top g_- y = g_-^{\mu\nu} x_\mu y_\nu$ invariant. This leads to the defining condition

$$\Lambda^\top g_- \Lambda = g_- \qquad \Leftrightarrow \qquad g_-^{\mu\nu} \Lambda^\alpha{}_\mu \Lambda^\beta{}_\nu = g_-^{\alpha\beta} \tag{B.9}$$

which constrains the 4×4 matrix Λ with 10 conditions due to the symmetric metric g_-. The Lorentz group is an orthogonal group $\mathrm{O}(3,1)$.[2] The group axioms are fulfilled with the unit element $\Lambda = \mathbb{1}_\mathrm{D}$ and the inverse element $\Lambda^{-1} = g_- \Lambda^\top g_-$. From Eq. (B.9), furthermore, follows $\det \Lambda = \pm 1$ and $(\Lambda^0{}_0)^2 \geq 1$. Depending on the sign of $\Lambda^0{}_0$ and $\det \Lambda$, we can define four disconnected irreducible subgroups of the Lorentz group shown in Fig. B.1.

The six-dimensional Lorentz transformation $\mathrm{SO}(3,1)^\uparrow \ni \Lambda = L(\vec{\beta}) R(\vec{\alpha})$ can be reconstructed from three-dimensional Lorentz boosts $L(\vec{\beta})$ with the velocity $\vec{\beta} = \vec{v}/c$ and spatial rotations $R(\vec{\alpha}) \in \mathrm{SO}(3)$ in three dimensions with the rotation angle $\vec{\alpha}$. Thereby, only the rotation group forms an irreducible subgroup. The whole Lorentz group is a) not compact (due to the boosts all unitary representations are infinite-dimensional) and b) not simply connected due to the rotations.

To find all irreducible unitary representations of the Lorentz group $\mathrm{SO}(3,1)^\uparrow$, we have to consider the universal covering group $\mathrm{SL}(2,\mathbb{C})$ of it. The covering group has the same Lie algebra, which reflects the property of the group close to its identity,

[2] In general, a transformation of coordinates $\{x_1 \dots x_n, y_1 \dots y_m\}$ that leaves the quadratic form $(x_1^2 + \dots + x_n^2) - (y_1^2 + \dots + y_m^2)$ invariant constitute the orthogonal group $\mathrm{O}(m,n)$.

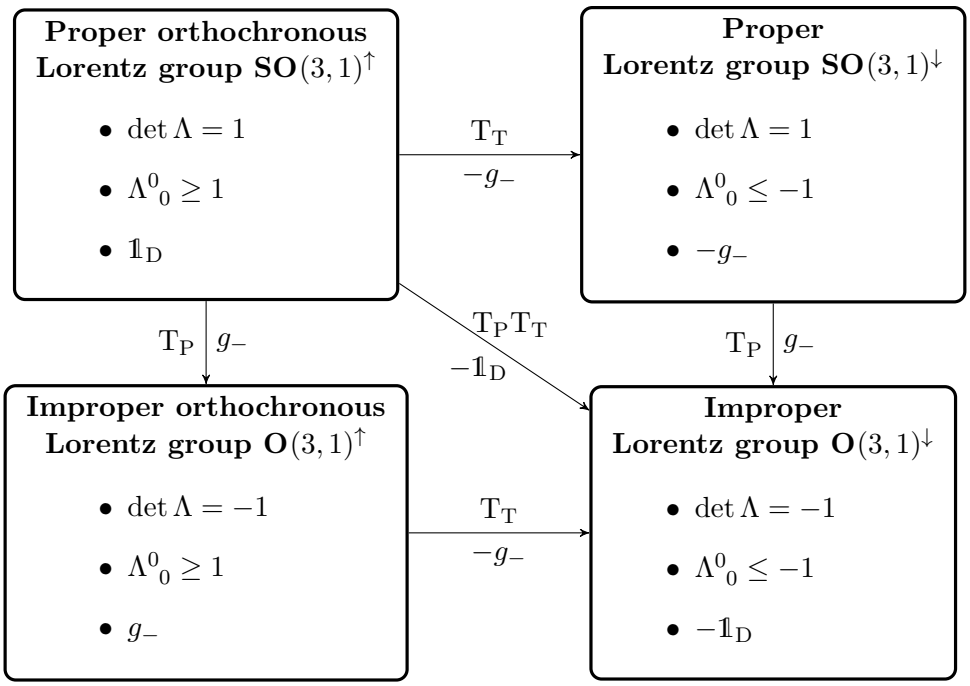

Figure B.1.: The four disconnected irreducible subgroups or components of the Lorentz group $\mathrm{O}(3,1) = \mathrm{SO}(3,1)^{\uparrow} \cup \mathrm{SO}(3,1)^{\downarrow} \cup \mathrm{O}(3,1)^{\downarrow} \cup \mathrm{O}(3,1)^{\uparrow}$ including their properties and relations. Lorentz transformations that preserve the direction of time are called orthochronous and have ${\Lambda^0}_0 \geq 1$. The transformations that preserve orientation are denoted as proper and have a determinant of 1. The corresponding improper ones have a determinant of -1. Time-reversal $\mathrm{T_T} \widehat{=} -g_-$ and parity inversion $\mathrm{T_P} \widehat{=} g_-$ transform orthochronous in non-orthochronous and proper into improper groups, respectively. The last entry of the disconnected components of the Lorentz group represents the group-identity to which all subgroup elements are continuously connected.

but is simply connected. Furthermore, $\mathrm{SL}(2,\mathbb{C})$ is a double cover of $\mathrm{SO}(3,1)^{\uparrow}$. The use of the covering group is necessary to find the spinor representations beside the tensor representations which we find also with the Lorentz group itself.

B.2.2. Poincaré group

The Poincaré group or inhomogeneous Lorentz group $\mathrm{IO}(1,3)$ is a ten dimensional Lie group consisting of the Lorentz group and translations in four dimensions. It has the same disconnected components as the Lorentz group. The proper

orthochronous Poincaré group $\mathrm{ISO}^{\uparrow}(1,3)$ with the group identity $\mathbb{1}_{\mathrm{D}}$, thereby, represents the basic symmetry group of the space-time for the whole physics. The Poincaré transformation $\mathrm{U}_{\Lambda}(\Lambda, a) \in \mathrm{IO}(1,3)$ of four-vectors is given by

$$\mathrm{U}_{\Lambda}(\Lambda, a) x_{\mu} = \lambda_{\mu}^{\nu} x_{\nu} + a_{\mu} \,. \tag{B.10}$$

This transformation leaves the line element $(dx)^2 = c^2(dt)^2 - (d\vec{x})^2$ invariant and guarantees that the speed of light c is equal in all inertial systems. The group axioms are again fulfilled:

a) Group multiplication: $\mathrm{U}_{\Lambda}(\Lambda_1, a_1)\mathrm{U}_{\Lambda}(\Lambda_2, a_2) = \mathrm{U}_{\Lambda}(\Lambda_1\Lambda_2, \Lambda_1 a_2 + a_1)$

b) Inverse element: $\mathrm{U}_{\Lambda}(\Lambda^{-1}, -\Lambda^{-1}a)$

c) Neutral element: $\mathrm{U}_{\Lambda}(\mathbb{1}_{\mathrm{D}}, 0)$

Furthermore, the decomposition in pure translation $\mathrm{U}_{\Lambda}(a) = \mathrm{U}_{\Lambda}(\mathbb{1}_{\mathrm{D}}, a)$ and pure four dimensional "rotations" $\mathrm{U}_{\Lambda}(\Lambda) = \mathrm{U}_{\Lambda}(\Lambda, 0)$ is possible and can be represented by

$$\mathrm{U}_{\Lambda}(\Lambda, a) = \mathrm{U}_{\Lambda}(\Lambda)\mathrm{U}_{\Lambda}(a) = e^{\frac{i}{2}\omega_{\mu\nu}\hat{M}^{\mu\nu}} e^{ia_{\sigma}\hat{P}^{\sigma}} \tag{B.11}$$

with the generators of translations $\hat{P}^{\mu}$ (momentum operator) and the generator of spatial rotations and boots $\hat{M}^{\mu\nu}$.[3] These generators form a Lie algebra, the so-called Poincaré algebra

$$\begin{aligned} i\left[\hat{M}^{\mu\nu}, \hat{M}^{\rho\sigma}\right] &= g_{-}^{\mu\sigma}\hat{M}^{\nu\rho} + g_{-}^{\nu\rho}\hat{M}^{\mu\sigma} - g_{-}^{\mu\rho}\hat{M}^{\nu\sigma} - g_{-}^{\nu\sigma}\hat{M}^{\mu\rho} \,, \\ i\left[\hat{P}^{\mu}, \hat{M}^{\rho\sigma}\right] &= g_{-}^{\mu\rho}\hat{P}^{\sigma} - g_{-}^{\mu\sigma}\hat{P}^{\rho} \\ \left[\hat{P}^{\mu}, \hat{P}^{\nu}\right] &= 0 \end{aligned} \tag{B.12}$$

which we get from the infinitesimal transformation (only the linear terms) of $\mathrm{U}_{\Lambda}^{-1}(\Lambda, a)\mathrm{U}_{\Lambda}(\Lambda', a')\mathrm{U}_{\Lambda}(\Lambda, a)$. The explicit form of the generators and the transformation itself depend on the representation. To discuss the irreducible unitary representations, we wish do describe the system through eigenvalues of a set of commuting observables which also commute with the generators. For this purpose, we use the Casimir operators of the Poincaré Lie group, which are defined as

[3] The Lorentz group generators can be expressed by $\frac{i}{2}\omega_{\mu\nu}\hat{M}^{\mu\nu} = i\vec{\alpha}\hat{\vec{J}} + i\vec{\beta}\hat{\vec{K}}$ where $\hat{J}^k = \frac{1}{2}\epsilon^{kij}\hat{M}^{ij}$ are the generators of spatial rotations and $\hat{K}^k = \hat{M}^{k0}$ represent the generators of boosts $(k, i, j \in \{1, 2, 3\})$.

operators commuting with all generators and build by a product of generators. The Casimir operators of the Poincaré group are $\hat{P}^2$ and $\hat{W}^2$ where

$$\hat{W}_\mu = -\frac{1}{2}\epsilon_{\mu\rho\sigma\lambda}\hat{M}^{\rho\sigma}\hat{P}^\lambda \qquad \Leftrightarrow \qquad \hat{W} = \begin{pmatrix} \hat{\vec{P}} \cdot \hat{\vec{J}} \\ \hat{P}_0\hat{\vec{J}} + \hat{\vec{P}} \times \hat{\vec{J}} \end{pmatrix} \tag{B.13}$$

is the so-called Pauli-Lubanski vector. Since the generators of the translation commute, the translation operators have common eigenvectors $|P, \mathrm{x}, \alpha\rangle$ with the total momentum P, other quantum numbers α and x as an identifier of the particle. We use these eigenvectors as basis for our physical Hilbert space. Considering the two cases a) $P^2 = m^2 > 0$ in rest frame $\vec{P} = 0$ and b) $P^2 = 0$ ($P \neq 0$) for the momentum, we can directly extract conserved quantum numbers from the Casimir operators, which we then use to classify the irreducible unitary representations.

In case a) the Casimir operators take the form $\hat{W}^2 = -\hat{P}^2\hat{\vec{J}}$ and $\hat{P}^2 = \hat{P}_0^2$ with the eigenvalues $-m^2 j(j+1)$ and m^2 respectively. While $\hat{\vec{J}}$ represents the spin operator, its eigenvalue j is the total spin of the particle and m is the corresponding mass of the particle. In case b) the Pauli-Lubanski vector is given by $\hat{W}^\mu = \lambda\hat{P}^\mu$ where λ is the helicity which defines the direction or sign of the projection of the spin onto the momentum. The irreducible unitary representations in both cases are labeled with the spin and the mass of the particle (in the latter case the mass is zero).

In the following we take a closer look at the Poincaré transformations in these irreducible unitary representations (spin states). The general Poincaré transformation of i) a field operator $\hat{\Phi}^{\mu_1\cdots\mu_n}(x)$, ii) the eigenstate $|P, \mathrm{x}, \alpha\rangle$ defined above and iii) the vacuum state $|0\rangle$, are defined by

$$\begin{aligned} \mathrm{U}_\Lambda^{-1}(\Lambda, a)\hat{\Phi}^{\mu_1\cdots\mu_n}(x)\mathrm{U}_\Lambda(\Lambda, a) &= \left\{ \left[D(\mathrm{U}_\Lambda(\Lambda)) \right]_{\mu_1\ldots\mu_n}^{\nu_1\ldots\nu_n} \right\}^{-1} \hat{\Phi}^{\nu_1\ldots\nu_n}(\Lambda x + a)\,, \\ \mathrm{U}_\Lambda(\Lambda, a)\,|P, \mathrm{x}, \alpha\rangle &= e^{iPa}\,|\Lambda P, \mathrm{x}, \alpha\rangle\ , \\ \mathrm{U}_\Lambda(\Lambda, a)\,|0\rangle &= |0\rangle \end{aligned} \tag{B.14}$$

where $D(\mathrm{U}_\Lambda(\Lambda))$ is the finite dimensional representation-matrix of the Lorentz group for the considered irreducible unitary representation. The irreducible unitary representations considered in this work are (pseudo-)scalars, spinors and (axial-)vectors particles. The corresponding representation matrices for Lorentz scalars, vectors and Dirac spinors are given in Tab. B.1. Axial-vectors and pseudo-scalar particles result via parity transformation from the vectors and scalar particles.

If we consider the Poincaré transformation for composite scalar and vector particles consisting of a quark and an antiquark, we have to study the transformation

Table B.1.: Representation matrix $D(\mathrm{U}_\Lambda(\Lambda))$ of the double cover $\mathrm{SL}(2,\mathbb{C})$ of the Proper orthochronous Lorentz group $\mathrm{SO}(3,1)^\uparrow$ for different irreducible unitary representations (spin states). In the Dirac spinor case the generator is given by $\sigma^{\mu\nu} = -\frac{1}{2}[\gamma^\mu, \gamma^\nu]$.

Spin	0	$\frac{1}{2}$	1
Type	scalar s	Dirac spinor Ψ	vector v^μ
$D(\mathrm{U}_\Lambda(\Lambda))$	1	$\exp(\frac{i}{2}\omega_{\mu\nu}\sigma^{\mu\nu})$	Λ

properties of the transition probability of a quark-antiquark-system to become a meson bound state. This transition probability is given by Eq. (3.8) and transforms like the Green function

$$G^{(\mu)}_{2,\Gamma}(x; x_1, x_2) = \left\langle 0 \left| \hat{T} \left\{ \hat{j}^{(\mu)}_\Gamma(x) \hat{\bar{\Psi}}(x_1) \hat{\Psi}(x_2) \right\} \right| 0 \right\rangle \tag{B.15}$$

with $\hat{j}_\mathrm{S}(x)$ representing a scalar density and $\hat{j}^\mu_\mathrm{V}(x)$ a vector current. The corresponding Poincaré transformation is given by

$$G^{(\mu)}_{2,\Gamma}(x; x_1, x_2) = \left\langle 0 \left| \hat{T} \left\{ \mathrm{U}_\Lambda^{-1} \underbrace{\mathrm{U}_\Lambda \hat{j}^{(\mu)}_\Gamma(x) \mathrm{U}_\Lambda^{-1}}_{=:\left[D^{(\mu\nu)}_{(\mathrm{vec})/\mathrm{sc}}(\mathrm{U}_\Lambda)\right]^{-1} \hat{j}^{(\mu)}_\Gamma(x')} \overbrace{\mathrm{U}_\Lambda \hat{\bar{\Psi}}(x_1) \mathrm{U}_\Lambda^{-1}}^{=:\hat{\bar{\Psi}}(x_1') D_\mathrm{sp}(\mathrm{U}_\Lambda)} \underbrace{\mathrm{U}_\Lambda \hat{\Psi}(x_2) \mathrm{U}_\Lambda^{-1}}_{=:D^{-1}_\mathrm{sp}(\mathrm{U}_\Lambda)\hat{\Psi}(x_2')} \mathrm{U}_\Lambda \right\} \right| 0 \right\rangle$$

$$= \left[D^{(\mu\nu)}_{(\mathrm{vec})/\mathrm{sc}}(\mathrm{U}_\Lambda(\Lambda))\right]^{-1} D_\mathrm{sp}(\mathrm{U}_\Lambda(\Lambda)) G^{(\nu)}_{2,\Gamma}(\Lambda x + a; \Lambda x_1 + a, \Lambda x_2 + a) D^{-1}_\mathrm{sp}(\mathrm{U}_\Lambda(\Lambda))\,. \tag{B.16}$$

The Bethe-Salpeter wave-function of Eq. (3.8) in momentum space then transforms like

$$\chi^{(\mu)}(P, q) = \left[D^{(\mu\nu)}_{(\mathrm{vec})/\mathrm{sc}}(\mathrm{U}_\Lambda(\Lambda))\right]^{-1} D_\mathrm{sp}(\mathrm{U}_\Lambda(\Lambda)) \chi^{(\nu)}(\Lambda P, \Lambda q) D^{-1}_\mathrm{sp}(\mathrm{U}_\Lambda(\Lambda))\,. \tag{B.17}$$

The Poincaré transformation of the Bethe-Salpeter amplitude results from the decomposition in Eq. (3.10) and the fact that the quark propagator S transforms like $G_{2,S}(x, y) = D_\mathrm{sp}(\mathrm{U}_\Lambda(\Lambda)) G_{2,S}(\Lambda x + a, \Lambda y + a) D^{-1}_\mathrm{sp}(\mathrm{U}_\Lambda(\Lambda))$. A more detailed description of the Lorentz and Poincaré group transformations and representations can be found in the Refs. [70, 73].

B.2.3. CPT-transformations

Besides of rotations in three dimensions and the transition between inertial systems moving with constant velocity relative to each other (boots), the Lorentz group contains space-time reflections. They preserve the scalar product but cannot be represented via continuous transformations. These so-called time-reversal and parity symmetries define, together with the charge conjugation, the three discrete symmetries. In Tab. B.2, we show the transformation properties of different variables, quantum numbers and field operators under the parity $\mathrm{U}_{\mathbf{P}}$, time reversal $\mathrm{U}_{\mathbf{T}}$, and charge conjugation $\mathrm{U}_{\mathbf{C}}$ transformations.

Table B.2.: Transformation of different variables, quantum numbers and field operators under parity $\mathrm{U}_{\mathbf{P}}$, time reversal $\mathrm{U}_{\mathbf{T}}$, and charge conjugation $\mathrm{U}_{\mathbf{C}}$ transformation. Considered variables are the space time x, the four-momentum p, the spin $\vec{s}$ and the helicity $h = \frac{\vec{p}\cdot\vec{s}}{|\vec{p}||\vec{s}|}$. The quantum numbers are the electrical charge Q_{el} and the baryon B and flavor F numbers. The scalar $\hat{\mathrm{S}}$, Dirac $\hat{\Psi}$, and vector $\hat{\mathrm{V}}^{\mu}$ field operators transform corresponding to $\mathrm{U}_{\mathbf{X}}^{-1}\hat{\Phi}^{(\mu)}(\cdot)\mathrm{U}_{\mathbf{X}} = \left[D^{(\mu\nu)}_{\mathrm{type}}(\mathrm{U}_{\mathbf{X}})\right]^{-1}\hat{\Phi}^{(\nu)}(\cdot')$ with $D^{(\mu\nu)}_{\mathrm{type}}(\mathrm{U}_{\mathbf{X}})$ in the corresponding representation shown in Tab. B.1.

	$\mathrm{U}_{\mathbf{P}}$	$\mathrm{U}_{\mathbf{T}}$	$\mathrm{U}_{\mathbf{C}}$
x	$g_- x$	$-g_- x$	x
p	$g_- p$	$g_- p$	p
$\vec{s}$	$\vec{s}$	$-\vec{s}$	$\vec{s}$
h	$-h$	h	h
Q_{el}	Q_{el}	Q_{el}	$-Q_{\mathrm{el}}$
B, F	B, F	B, F	$-B, -F$
$\hat{\mathrm{S}}(\cdot)$	$\hat{\mathrm{S}}(\cdot')$	$\hat{\mathrm{S}}(\cdot')$	$\hat{\mathrm{S}}^{*}(\cdot')$
$\hat{\Psi}(\cdot)$	$\gamma_0\hat{\Psi}(\cdot')$	$\gamma_1\gamma_3\hat{\Psi}(\cdot')$	$-i\gamma_2\hat{\Psi}^{*}(\cdot')$
$\hat{\mathrm{V}}^{\mu}(\cdot)$	$-g_-^{\mu\nu}\hat{\mathrm{V}}_{\nu}(\cdot')$	$g_-^{\mu\nu}\hat{\mathrm{V}}_{\nu}(\cdot')$	$\hat{\mathrm{V}}^{\mu\dagger}(\cdot')$

The parity transformation, which is defined by the reflection of the spatial position $\vec{x}$, is a unitary operation that flips the left- and right-handed parts of a quark spinors. For the time reversal on the other hand is important to note that it is an

antiunitary operation and the charge conjugation exchanges particles with their corresponding antiparticles implying also that the electric charge, the flavor and baryon numbers of the particle flip. For the charged conjugated Dirac spinor we define $-i\gamma_2\Psi^* = (\bar{\Psi}C)^\top$ with $C = -i\gamma_0\gamma_2$.

For the Bethe-Salpeter amplitude of a general meson shown in Eq. (3.12), we get the discrete transformations

$$\begin{aligned} \mathrm{U}_{\mathbf{P}}^{-1}\Gamma_{\mathrm{x}}^{\mu_1\cdots\mu_n}(P,q)\mathrm{U}_{\mathbf{P}} &= (-1)^{\mathrm{J}} g_{-\nu_1}^{\mu_1}\cdots g_{-\nu_n}^{\mu_n} \quad \gamma_0\Gamma_{\mathrm{x}}^{\nu_1\cdots\nu_n}(g_-P,g_-q)\gamma_0\,, \\ \mathrm{U}_{\mathbf{C}}^{-1}\Gamma_{\mathrm{x}}^{\mu_1\cdots\mu_n}(P,q)\mathrm{U}_{\mathbf{C}} &= \left[C \;\; \Gamma_{\mathrm{x}}^{\mu_1\cdots\mu_n}(P,-q) \quad C^\top\right]^\top . \end{aligned} \tag{B.18}$$

Changing to the Euclidean space only the definition of the charge conjugation matrix changes to $C = \gamma_0\gamma_2$. The corresponding vacuum basis elements shown in Tab. 3.1 transform under charge conjugation and parity transformation via

$$\begin{aligned} \mathrm{U}_{\mathbf{P}}^{-1}(\mathbb{1}_{\mathrm{D}} + \gamma_5)\tau_i^{(\mu)}(P,p)\mathrm{U}_{\mathbf{P}} &= (-1)^{\mathrm{J}}(\mathbb{1}_{\mathrm{D}} - \gamma_5)\tau_i^{(\mu)}(P,p) \\ \mathrm{U}_{\mathbf{C}}^{-1}(\mathbb{1}_{\mathrm{D}} + \gamma_5)\tau_i^{(\mu)}(P,p)\mathrm{U}_{\mathbf{C}} &= \quad \mathbf{C} \quad (\mathbb{1}_{\mathrm{D}} + \gamma_5)\tau_i^{(\mu)}(P,p) \end{aligned} \tag{B.19}$$

where $\mathbf{C}$ is the charge conjugation eigenvalue or quantum number.

B.3. Quark flavor transformations

For discussing the quark flavor transformations, we have to introduce the Noether theorem first. This theorem tells us that any continuous local or global symmetry transformation that leaves the action invariant implies the existence of a conserved Noether current and a corresponding Noether charge which is a constant of motion. If we consider the variation of the super-field φ induced by the symmetry transformation U: $\varphi' = \varphi + \delta\varphi$, the invariance of the action $S = \int d^4x \mathscr{L}(\varphi, \partial_\mu\varphi)$ under U leads to the equation of motion

$$\frac{\partial\mathscr{L}}{\partial\varphi} - \partial_\mu\frac{\partial\mathscr{L}}{\partial(\partial_\mu\varphi)} = 0 \tag{B.20}$$

on the one hand and to the Noether current $-\epsilon_{(a)}j_{(a)}^\mu(x) = \frac{\partial\mathscr{L}}{\partial(\partial_\mu\varphi)}\delta\varphi$ and its conservation

$$\partial_\mu j_{(a)}^\mu(x) = 0 \tag{B.21}$$

on the other hand. In the definition of the Noether current, $\epsilon_{(a)}$ is a group parameter and a represents an index for the generator of the symmetry group. There is one

conserved current for each generator. These Noether currents take the form of the Lorentz vectors of the quark bilinears defined in Eq. (B.1). Their corresponding Noether charges are defined by

$$Q^{\Gamma}_{(a)}(t) = \int d^3x j^0_{\Gamma,(a)}(x) \tag{B.22}$$

and describe a constant of motion if

$$\frac{d}{dt}Q^{\Gamma}_{(a)}(t) = \int d^3x \frac{\partial}{\partial t} j^0_{\Gamma,(a)}(x) \overset{(B.21)}{=} -\int d^3x \vec{\nabla}\vec{j}_{\Gamma,(a)}(x) = 0 \tag{B.23}$$

which is fulfilled if the Noether current vanishes sufficiently fast on the surface in infinity. Now let's consider the quark flavor dependent part of the QCD action $\int d^4x \bar{\Psi}(x)(i\partial\!\!\!/ + g_{\mathrm{s}}\mathcal{A}\!\!\!/ - m_{\mathrm{q}})\Psi(x)$ in Eq. (2.15) where the vector $\mathcal{A}_\mu$ is the gauge field mediating the interaction and g_{s} is the strong coupling constant. The quark mass matrix for the three considered quark flavors, is given by

$$m_{\mathrm{q}} = \mathrm{diag}(m^u_{\mathrm{q}}, m^d_{\mathrm{q}}, m^s_{\mathrm{q}}) = \frac{m^u_{\mathrm{q}} + m^d_{\mathrm{q}} + m^s_{\mathrm{q}}}{3}\mathbb{1}_{\mathrm{F}} + \frac{m^u_{\mathrm{q}} - m^d_{\mathrm{q}}}{2}\lambda_3 + \frac{m^u_{\mathrm{q}} + m^d_{\mathrm{q}} - 2m^s_{\mathrm{q}}}{\sqrt{12}}\lambda_8 \tag{B.24}$$

with the Gell-Mann matrices λ_a defined in Eq. (A.2). In the following, we are interested in the global quark flavor symmetry transformations $\Psi' = \mathrm{U}\Psi$ of QCD which are described by the groups $\mathrm{U_V}(1)\times\mathrm{SU_V}(\mathrm{N_f})\times\mathrm{SU_A}(\mathrm{N_f})\times\mathrm{U_A}(1)$. In Tab. B.3, the unitary representation of the groups, their Noether currents and charges as well as their conservation conditions are mentioned. To receive the conservation condition mentioned in the Tab. B.3, we use the equation of motion

$$\partial\!\!\!/\Psi(x) = i(g_{\mathrm{s}}\mathcal{A}\!\!\!/(x) - m_{\mathrm{q}})\Psi(x), \qquad \bar{\Psi}(x)\overleftarrow{\partial\!\!\!/} = i\bar{\Psi}(x)(g_{\mathrm{s}}\mathcal{A}\!\!\!/(x) - m_{\mathrm{q}}) \tag{B.25}$$

of the quark fields $\Psi(x)$ and $\bar{\Psi}(x)$ which result from Eq. (B.20). In the following, we will take a closer look at the different quark flavor symmetry groups. The $\mathrm{U_V}(1)$ group represents a global phase transformation and entails the baryon number $B := \frac{Q^{\mathrm{V}}}{3}$ as constant of motion. Furthermore, the current conservation condition in momentum space

$$\partial_\mu \mathrm{V}^\mu(x) = 0 \qquad \Leftrightarrow \qquad k_\mu \mathrm{V}^\mu(k) = 0 \tag{B.26}$$

will be important for later discussions. The $\mathrm{SU_V}(\mathrm{N_f})$ symmetry is explicitly broken by a mass matrix $m_{\mathrm{q}} \neq m^f_{\mathrm{q}}\mathbb{1}_{\mathrm{F}}$ but there still are conserved Noether currents and charges for the diagonal generators $\lambda_3/2$ and $\lambda_8/2$ which are also present in the mass matrix in Eq. (B.24). From these conserved Noether currents and charges, we obtain the Isospin $I_3 = Q^{\mathrm{V}}_3$ and Hypercharge $Y = (2/\sqrt{3})Q^{\mathrm{V}}_8$ as constants of

Table B.3.: Global quark flavor transformations of the QCD action in Eq. (2.15). The first and second column show the group and the corresponding unitary representation. The third and fourth column are the Noether current $j^{\mu}_{(a)}(x)$ and charge $Q^{\Gamma}_{(a)}(t)$ defined in Eqs. (B.1) and (B.22), respectively. The last column demonstrates the condition necessary to fulfill the Noether current conservation of Eq. (B.21). The flavor matrix is given by $\tau_a = \lambda_a/2$ with the Gell-Mann matrices λ_a defined in Eq. (A.2).

Group	**Representation**	$j^{\mu}_{\Gamma,(a)}$	$Q^{\Gamma}_{(a)}$	**Conservation condition**
$\mathrm{U_V(1)}$	$\exp(i\epsilon)$	V^{μ}	Q^{V}	$\partial_{\mu}\mathrm{V}^{\mu}(x) = 0$
$\mathrm{SU_V(N_f)}$	$\exp(i\sum_a \epsilon_a \tau^a)$	V^{μ}_a	Q^{V}_a	$\partial_{\mu} V^{\mu}_a(x) = i\bar{\Psi}(x)\left[m_{\mathrm{q}}, \tau_a\right]\Psi(x)$
$\mathrm{SU_A(N_f)}$	$\exp(i\gamma_5\sum_a \epsilon_a \tau^a)$	A^{μ}_a	Q^{A}_a	$\partial_{\mu} A^{\mu}_a(x) = i\bar{\Psi}(x)\left\{m_{\mathrm{q}}, \tau_a\right\}\gamma_5\Psi(x)$
$\mathrm{U_A(1)}$	$\exp(i\epsilon\gamma_5)$	A^{μ}	Q^{A}	$\partial_{\mu} A^{\mu}(x) = i2\bar{\Psi}(x) m_{\mathrm{q}}\gamma_5\Psi(x)$+an.

motion. Together with the constants of motion of the $\mathrm{U_V(1)}$ group, we, finally, get the conserved quantum numbers

$$\begin{aligned} B &= \sum_f \frac{n_f}{3}\,, \\ I_3 &= n_{\mathrm{u}} - n_{\mathrm{d}}\,, \\ Y &= \frac{n_{\mathrm{u}} + n_{\mathrm{d}} - 2n_{\mathrm{s}}}{3}\,, \\ S &= Y - B = -n_{\mathrm{s}}\,, \\ Q_{\mathrm{el}} &= I_3 + \frac{Y}{2} = \frac{2}{3}n_{\mathrm{u}} - \frac{1}{3}n_{\mathrm{d}} - \frac{1}{3}n_{\mathrm{s}} \end{aligned} \tag{B.27}$$

where $n_f = \int d^3x \Psi^{\dagger}_f(x)\Psi_f(x) = $ nr. of quarks $-$ nr. of antiquarks with the quark flavor $f \in \{\mathrm{u}, \mathrm{d}, \mathrm{s}\}$. In these expressions, S and Q_{el} represent the strangeness and the electrical charge of state. Even if the flavor symmetry in $\mathrm{SU_V(N_f)}$ is broken in general, we can use these quantum numbers to arrange hadrons, as composite particles of quarks of a certain (quark) flavor, into $\{I_3, S\}$ multiplets[4] of different invariant subspaces. In Sec. 3, we did so for pseudo-scalar and vector mesons.

The $\mathrm{SU_A(N_f)}$ symmetry is explicitly broken by a mass matrix $m_{\mathrm{q}} \neq 0$. But for $m_{\mathrm{q}} = m^f_{\mathrm{q}}\mathbb{1}_{\mathrm{F}}$, we can consider a special relation. In this case, the divergence of the

[4]Multiplets are graphical representation of particles depending on their quantum numbers.

axial-vector current is a pseudo-scalar density

$$\partial_\mu \mathrm{A}^\mu_a(x) = 2m^f_\mathrm{q} \mathrm{P}_a(x) \tag{B.28}$$

which is known as partially conserved axial-vector current (PCAC). The $\mathrm{U_A}(1)$ symmetry is classically conserved for $m_\mathrm{q} = 0$ but no longer preserved after quantization since the $\mathrm{U_A}(1)$ Noether current gets broken by the QCD anomaly $an. = -\frac{g_\mathrm{s}^2 \mathrm{N_f}}{32\pi^2} \tilde{F}^{\mu\nu}_a F^a_{\mu\nu}$.

B.4. Ward-Takahashi identities

In this section, we consider the current conservation discussed in App. B.3 at the level of Green functions. For this purpose, the currents and fields become operators and we consider their vacuum expectation value. If we consider the Green function in second line of Eq. (B.3) and use the abbreviations $\hat{\varphi}(x_i) = \hat{\bar{\Psi}}(x_i)$ for odd i and $\hat{\varphi}(x_i) = \hat{\Psi}(x_i)$ for even i, we can derive

$$\begin{aligned}
\frac{\partial}{\partial y^\mu} G^\mu_{2n,\Gamma,(a)}(y; x_1, \ldots, x_{2n}) &= \frac{\partial}{\partial y^\mu} \left\langle 0 \left| \hat{T} \left\{ \hat{j}^\mu_{\Gamma,(a)}(y) \hat{\varphi}(x_1) \ldots \hat{\varphi}(x_{2n}) \right\} \right| 0 \right\rangle \\
&= \left\langle 0 \left| \hat{T} \left\{ \left(\partial_\mu \hat{j}^\mu_{\Gamma,(a)}(y) \right) \hat{\varphi}(x_1) \ldots \hat{\varphi}(x_{2n}) \right\} \right| 0 \right\rangle + \\
&\quad + \sum_{k=1}^{2n} \delta(y_0 - x_{k,0}) \left\langle 0 \left| \hat{\varphi}(x_1) \ldots \left[\hat{j}^0_{\Gamma,(a)}(y), \hat{\varphi}(x_k) \right] \ldots \hat{\varphi}(x_{2n}) \right| 0 \right\rangle
\end{aligned} \tag{B.29}$$

where we used the derivative $\partial_\mu \theta(x_0 - y_0) = -\partial_\mu \theta(y_0 - x_0) = \delta(x_0 - y_0)\delta_{0\mu}$ of the time-ordering operator $\hat{T}(f(x)g(y)) = \theta(x_0 - y_0) f(x)g(y) \pm \theta(y_0 - x_0) g(y) f(x)$. By considering the three-point Green function ($n = 1$) in Eq. (B.29) and using the commutation relations of current operators with quark field operators defined in Eq. (B.6) as well as the current conservation relations in Eqs. (B.26) and (B.28), we get

$$\begin{aligned}
\partial_\mu G^\mu_{2,\mathrm{V},a}(x; x_1, x_2) &= \delta^4(x - x_1) G_{2,S}(x_1, x_2)\tau_a - \delta^4(x - x_1)\tau_a G_{2,S}(x_1, x_2) \\
\partial_\mu G^\mu_{2,\mathrm{A},a}(x; x_1, x_2) &= \delta^4(x - x_1) G_{2,S}(x_1, x_2)\gamma_5\tau_a - \delta^4(x - x_1)\tau_a\gamma_5 G_{2,S}(x_1, x_2) \\
&\quad + 2m_\mathrm{q} G_{2,\mathrm{P},a}(x; x_1, x_2)
\end{aligned} \tag{B.30}$$

Transferred into the momentum frame this relation becomes

$$\begin{aligned}
k_\mu G^\mu_{2,\mathrm{V},a}(p_1, p_2) &= S(p_2)\tau_a - \tau_a S(p_1) \\
k_\mu G^\mu_{2,\mathrm{A},a}(p_1, p_2) &= S(p_2)\gamma_5\tau_a - \tau_a\gamma_5 S(p_1) + 2m_\mathrm{q} G_{2,\mathrm{P},a}(x; x_1, x_2)
\end{aligned} \tag{B.31}$$

with $k = p_1 - p_2$ and identifying $G_{2,S}(p)$ with the quark propagator $S(p)$. $\tau_a = \lambda_a/2$ is defined by the Gell-Mann matrices λ_a in Eq. (A.2). These relations are the so-called Ward-Takahashi-identities (WTIs) and relate the vector and axial-vector vertices with quark propagators and the pseudo-scalar vertex. In the flavor-singlet case ($\tau_a \to 1$), the axial-vector vertex is related to an additional term, the anomaly. In general the WTIs relate n-point and $(n+1)$-point Green functions. In the following, we will discuss some important implications of these WTIs.

Applications of the WTIs

Two important applications are i) the axial-vector Ward-Takahashi-identity (AxWTI) constraining the connection of the BSE kernel K and the quark self energy Σ^f (in chiral limit) and ii) the Ball-Chiu vertex as approximation for the longitudinal part of the quark-gluon vertex.

For i), we rewrite the flavor singlet version ($\tau_a \to \mathbb{1}_\mathrm{D}$) of the second line of Eq. (B.31) in chiral limit in terms of quark-antiquark-meson vertices defined in Eq. (3.4) (multiply with $S^{-1}S^{-1}$) and consider on-shell momenta. We therefore get

$$P_\mu \Gamma^\mu_\mathrm{A}(P,p) = S^{-1}(p_+)\gamma_5 + \gamma_5 S^{-1}(p_-) \tag{B.32}$$

with the total and relative momenta P and p as well as the quark momenta $p_\pm = p \pm \frac{P}{2}$. Furthermore, $\Gamma^\mu_\mathrm{A}(P,p)$ represents the inhomogeneous Bethe-Salpeter amplitude which fulfills the Eq. (3.4). Inserting the quark DSE $S^{-1}(p) = S_0^{-1}(p) + \Sigma(p)$ and the inhomogeneous BSE defined in Eqs. (2.16) and (3.4) into the AxWTI (and the AxWTI in the representation of Eq. (B.32) again into the resulting equation) yields the more prominent version shown in Eq. (3.6).

For ii) we consider the vertex of two quarks and the gauge Boson of QCD (gluon) and calculate properties of the correlation of the gauge Boson current with a quark-antiquark system. The resulting quantum mechanical color current conservation is called vector Slavnov-Taylor identity. It constrains the longitudinal part of the quark-gluon vertex by relating it to the quark and ghost propagators as well as the quark-ghost scattering kernel, similar as in Eq. (B.31). So far, this could not be solved in QCD, but we approximate it by the Abelian vector Ward-Takahashi identity shown in the first line of Eq. (B.31) multiplied with a non-Abelian factor $\mathrm{NA}(k)$ and rewritten in the same way as for i). This means that we consider the flavor singlet case and multiply the equation with $S^{-1}S^{-1}$. In the end, we get

$$k_\mu \Gamma^\mu_\mathrm{qg}(p,q,k) = \mathrm{NA}(k)\left[S^{-1}(p_+) - S^{-1}(p_-)\right] \tag{B.33}$$

for the approximated quark-gluon vertex. Neglecting the non-Abelian factor, this is solved by the Ball-Chiu vertex construction

$$\begin{aligned}
\Gamma^{\mu}_{\mathrm{BC}}(p,q) &= \gamma^{\mu}\frac{\mathrm{A}(p)+\mathrm{A}(q)}{2} + 2\not{k}k^{\mu}\frac{\mathrm{A}(p)-\mathrm{A}(q)}{p^2-q^2} + 2ik^{\mu}\frac{\mathrm{B}(p)-\mathrm{B}(q)}{p^2-q^2}\,, \\
\Gamma^{\mu}_{\mathrm{BC}}(p,q) &= \vec{\gamma}^{i}(1-\delta_{\mu 0})\frac{\mathrm{A}(p)+\mathrm{A}(q)}{2} + \gamma_4\delta_{\mu 0}\frac{\mathrm{C}(p)+\mathrm{C}(q)}{2} + \\
&\quad + 2\vec{\not{k}}k^{\mu}\frac{\mathrm{A}(p)-\mathrm{A}(q)}{p^2-q^2} + 2\tilde{k}_4\gamma_4 k^{\mu}\frac{\mathrm{C}(p)-\mathrm{C}(q)}{p^2-q^2} + 2ik^{\mu}\frac{\mathrm{B}(p)-\mathrm{B}(q)}{p^2-q^2}\,.
\end{aligned} \tag{B.34}$$

in vacuum (first line) and medium (second line). In this relation we used the abbreviation $k = (p+q)/2$.

C. How to solve ...

In this chapter, we will discuss the numerical background for the calculation of fundamental particles with the help of the Dyson-Schwinger equations and of mesonic bound states by using the Bethe-Salpeter approach. We will begin with the description of the fundamental particles.

C.1. ... the DSE

For the description of the DSE calculations, we will, at first, detail the regularization and renormalization of the quark and the gluon in vacuum and medium. Then, we consider all facets of the numerical implementation of the DSE. Next, we discuss the determination of the (pseudo)critical temperatures for the QCD phase diagram and the changes to the quark calculation necessary due to the introduction of complex momenta.

C.1.1. Regularization and renormalization of the quark and gluon

For the numerical calculation of the DSEs, the radial part of the momentum integrals has to be truncated. For this purpose, we use a momentum subtraction (MOM) regularization scheme and introduce two different kinds of ultraviolet O(4) momentum regulators for the quark and the gluon. In the gluon DSE, we use a hard cutoff $\Lambda_{\mathrm{UV}} = 200\,\mathrm{GeV}$ for the radial part of the four-momentum. For the quark DSE, on the other hand, we utilize a translational invariant momentum regulator in form of a Pauli-Villars regulator $R(q^2) = \frac{1}{1+q^2/\Lambda_{\mathrm{PV}}^2}$ to truncate the radial part of the four-momentum. The regulator thereby entails the Pauli-Villar scale $\Lambda_{\mathrm{PV}} = 200\,\mathrm{GeV}$. It is mentionable that we use these O(4) regulators for the four-momentum, also in case of finite temperatures where the O(4) symmetry, actually, is broken down to a O(3) symmetry.

To cancel the divergences appearing with the regulator, we impose renormalization conditions at the renormalization points ξ_{x} with $\mathrm{x} \in \{\mathrm{q}, \mathrm{g}\}$. This transfers the regulator dependency into a renormalization point dependency, implies the need of an external input given at this renormalization point and fixes the renormalization

constants. Since the medium do not introduce new divergences [198], we renormalize in vacuum and use the resulting renormalization constants or self energies at the renormalization points as input for the medium. In the following, we will consider the renormalization of the quark in vacuum and medium, before we move on to the gluon. For the quark in vacuum, we use the renormalization condition

$$\left(S^f(\xi_\mathrm{q})\right)^{-1} = i\not{p} + m_\mathrm{q}^f(\xi_\mathrm{q}) \tag{C.1}$$

at the quark renormalization point $\xi_\mathrm{q} = 80\,\mathrm{GeV}$.[1] This renormalization condition can be rewritten into conditions for the quark dressing functions which are given by $\mathrm{A}_f(\xi_\mathrm{q}) = 1$ and $\mathrm{B}_f(\xi_\mathrm{q}) = m_\mathrm{q}^f(\xi_\mathrm{q})$. The renormalized quark mass $m_\mathrm{q}^f(\xi_\mathrm{q})$ has to be fixed externally. But due to the confinement, there is no experimental values for it. Consequently, we fix the quark mass by matching the Pion and Kaon mass as explained in Sec. 2.2.3. In case of real momenta, we determine the quark wave-function Z_2^f and quark mass Z_m^f renormalization constants from the quark self energy $\Sigma_f(\xi_\mathrm{q})$ at the quark renormalization point ξ_q in vacuum and insert them into the medium equations. The changes to the renormalization procedure due to the use of complex momenta are detailed in App. C.1.3.

For the renormalization of the diquark and baryon backcoupling in Chap. 6, we need special attention. All self energies in Eq. (6.1) are proportional to the quark wave-function renormalization constant Z_2. The diquark and baryon loop self energies depend on $\Gamma S S \Gamma$ and $\Psi_\mathrm{B} S S S \Psi_\mathrm{B}$, respectively. Here, Γ and Ψ_B represent the diquark and baryon amplitudes which are proportional to $Z_2^{1/2}$ and $Z_2^{3/4}$. Since the diquark and baryon amplitudes are calculated with another truncation and regularization than the quark, we have to insert the factors $Z_2/Z_2^{\mathrm{eff.}}$ and $Z_2/(Z_2^{\mathrm{eff.}})^{3/2}$ for the diquark and baryon loop, respectively. Here, $Z_2^{\mathrm{eff.}}$ represents the quark wave-function renormalization constant evaluated with an effective interaction, no hadronic backcoupling, a hard cutoff instead of a Pauli-Villars regulator and at a renormalization point of $\xi_\mathrm{q} = 19\,\mathrm{GeV}$. More information on this topic can be found in Ref. [80].

The numerical need to introduce a hard cutoff in the gluon DSE leads to quadratic divergences in the quark loop, which break the translational and gauge invariance. On the one hand, we have spurious quadratic divergences transversal to the gluon four-momentum and on the other hand there arises an unphysical quadratic divergent component longitudinal to the gluon four-momentum. In Landau gauge, this component should vanish. If we consider the medium case, the divergences transversal to the gluon four-momentum are furthermore accompanied by screening

[1] We use such a high value for the renormalization point to be sufficiently far in the perturbative regime.

mass like quantities in the form[2] $\frac{aT^2+b\mu_\mathrm{B}^2}{k^2}$. The contribution to these screening masses is the dominant medium effect of the gluon. Therefore, the unphysical and spurious quadratic divergences have to be removed without spoiling these screening mass like terms. We do so by introducing the regularized quark loop

$$\Pi_{\epsilon\nu}^{\mathrm{QL,reg}}(k) = \left(\delta_{\epsilon\alpha}\delta_{\nu\beta} - \delta_{\epsilon\nu}L_{\alpha\beta}(k)\right)\Pi_{\alpha\beta}^{\mathrm{QL}}(k) \tag{C.2}$$

where the two divergent parts cancel each other. Here, $\Pi_{\alpha\beta}^{\mathrm{QL}}(k)$ is the quark loop and the longitudinal projector $L_{\alpha\beta}(k)$ w.r.t. the gluon four-momentum is defined by Eq. (2.22). Due to this procedure, it only remains a logarithmic divergent term in direction longitudinal to the assigned direction of the medium. By fixing the quark loop with the renormalization condition $\Pi_{\epsilon\nu}^{\mathrm{QL,ren}}(\xi_\mathrm{g}) = 0$ at the gluon renormalization point $\xi_\mathrm{g} = 10\,\mathrm{GeV}$, we can derive the gluon wave-function renormalization constant Z_3, and get the renormalized quark loop

$$\Pi_{\epsilon\nu}^{\mathrm{QL,ren}}(k) = \Pi_{\epsilon\nu}^{\mathrm{QL,reg}}(k) - \frac{k^2}{\xi_\mathrm{g}^2}\Pi_{\epsilon\nu}^{\mathrm{QL,reg}}(\xi_\mathrm{g})\,. \tag{C.3}$$

It is sufficient to calculate the quark loop $\Pi_{\epsilon\nu}^{\mathrm{QL,reg}}(\xi_\mathrm{g})$ at the gluon renormalization point ξ_g once in vacuum. In medium we use the vacuum value as input. With Eq. (C.3) we still have infrared divergences due to the screening mass. For this purpose, we split the regularized quark loop into a divergence free (regular) part $\tilde{\Pi}_{\mathrm{T/L}}^{\mathrm{QL}}(k)$ and a screening mass term $m_{\mathrm{T/L}}^{\mathrm{sc}}(T,\mu_\mathrm{B})$. With this procedure, the regularized quark loop and the screening mass can be written by

$$\begin{aligned}\Pi_{\epsilon\nu}^{\mathrm{QL,reg}}(k) = \quad & \left\{\tilde{\Pi}_{\mathrm{T}}^{\mathrm{QL}}(k) + 2\frac{\left[m_{\mathrm{T}}^{\mathrm{sc}}(T,\mu_\mathrm{B})\right]^2}{k^2}\right\}\mathcal{P}_{\epsilon\nu}^{\mathrm{T}}(k) + \\ & + \left\{\tilde{\Pi}_{\mathrm{L}}^{\mathrm{QL}}(k) + 2\frac{\left[m_{\mathrm{L}}^{\mathrm{sc}}(T,\mu_\mathrm{B})\right]^2}{k^2}\right\}\mathcal{P}_{\epsilon\nu}^{\mathrm{L}}(k)\,,\end{aligned}$$

$$\left[m_{\mathrm{T/L}}^{\mathrm{sc}}(T,\mu_\mathrm{B})\right]^2 = \left.\frac{k^2}{2N_{\mathrm{pol}}^{\mathrm{s/t}}}\mathcal{P}_{\epsilon\nu}^{\mathrm{T/L}}(k)\Pi_{\epsilon\nu}^{\mathrm{QL,reg}}(k)\right|_{k\to 0}\,. \tag{C.4}$$

The screening mass is strongly sensitive to high accuracy and needs to be calculated with the full Matsubara sum, an analytically solved angular part and by numerically/ manually restoring the O(4) invariance via

$$\mathrm{C}_f(q) \to \left(1 - e^{-x}\right)\mathrm{A}_f(q) + e^{-x}\mathrm{C}_f(q) \tag{C.5}$$

with $x = q^2/\Lambda_{\mathrm{AC}}^2$ and $\Lambda_{\mathrm{AC}}^2 = 40\,\mathrm{GeV}^2$. We consequently calculate the regular part and the screening mass separately and with different numeric.

[2] k is the gluon four-momentum, T is the temperature and μ_B is the baryonic chemical potential. a and b are arbitrary parameters.

C.1.2. Numerical implementation

For the numerical implementation, we have to discuss the momentum and integral representation and handling. Then, we continue with the dressing function and (pseudo)critical temperature determination and the way how the iterative procedure works.

Momentum parametrization:

The parametrization of the external p and internal q quark momentum at finite chemical potential and vanishing temperature is based on hyper-spherical coordinates and given by

$$p = (0, 0, |\vec{p}|, \tilde{p}_4), \qquad q = (0, |\vec{q}|\bar{y}_q, |\vec{q}|y_q, \tilde{q}_4) \tag{C.6}$$

where the abbreviation for the fourth momentum component $\tilde{l}_4 = l_4 + i\mu_{\mathrm{q}}^f$ with $l \in \{p, q\}$ entails the quark chemical potential of the quark flavor f. The parametrization of the gluon momentum k equals the one of the external quark momentum p without the chemical potential. In this parametrization the vector part $|\vec{l}| = \sqrt{l^2}\bar{z}_l$ and the fourth momentum component $l_4 = \sqrt{l^2}z_l$ for the momenta $l \in \{p, q, k\}$ include the angles $\bar{z}_l = \sqrt{1 - z_l^2}$ and z_l. Thereby, $z_l = \cos(\sphericalangle(l, v_{\mathrm{med}}))$ represents the angle between the momentum l and the assigned direction of the medium $v_{\mathrm{med}} = (\vec{0}, 1)$ or energy direction (fourth momentum component). $\bar{y}_l$ and y_l are defined in the same way. The vacuum (a) and finite temperature (b) parametrization results from Eq. (C.6) by setting (a) the angle $y_l = 1$ and the quark chemical potential $\mu_{\mathrm{q}}^f = 0$ and (b) exchanging the fourth momentum component $l_4 = \omega_l$ with the appropriate discrete Matsubara frequencies.

Integral parametrization:

We already discussed the regularization of the quark and gluon equations in App. C.1.1 and the momentum parametrization in the previous App. C.1.2. The corresponding integrals for vanishing (first line) and finite (second line) temperatures are given by

$$\begin{aligned} \int_q^\Lambda &= \int_{\epsilon^2}^{\Lambda^2} dq^2 \frac{q^2}{2} \int d\Omega_{4\mathrm{D}}^q \,, \\ \sum\!\!\!\!\!\!\int_q^\Lambda &= T \sum_{n_q}^{|\omega_q|<\Lambda} \int_{\epsilon^2}^{\vec{\Lambda}^2_{\omega_q}} d|\vec{q}|^2 \frac{|\vec{q}|}{2} \int d\Omega_{3\mathrm{D}}^q \end{aligned} \tag{C.7}$$

with the four and three dimensional angular integral

$$\int d\Omega^q_{\mathrm{4D}} = \frac{1}{(2\pi)^4}\int_0^{2\pi} d\phi_q \int_{-1}^{1} dy_q \int_{-1}^{1} dz_q \sqrt{1-z_q^2}\,,$$
$$\int d\Omega^q_{\mathrm{3D}} = \frac{1}{(2\pi)^3}\int_0^{2\pi} d\phi_q \int_{-1}^{1} dy_q \tag{C.8}$$

and the three-momentum squared ultraviolet cutoff $\vec{\Lambda}^2_{\omega_q} = \Lambda^2 - \omega_q^2$. The angles in Eq. (C.8) not appearing in the corresponding vacuum, finite temperature, and finite chemical potential but vanishing temperature parametrization cases of App. C.1.2, can directly be analytically evaluated. While we describe the z_q angular integral with a linear Gauss-Chebychev integration, the remaining angular integrals and the radial part are described by a linear and logarithmic Gauss-Legendre integration, respectively.[3] It remains the discussion of the Matsubara sum. We treat the Matsubara sum differently in the quark self energy and the quark loop. The reason is the necessary precision and the low number of necessary calculations (see App. C.1.2) of the quark loop compared to the quark self energy. In the quark loop we perform the whole Matsubara sum explicitly. For the Matsubara sum in the quark self energy we assume continuity above a Matsubara index $N_{\max}$ and use the integral approximation

$$\begin{aligned} T\sum_{n_q}^{|\omega_q|<\Lambda} &= T\int_{-(\frac{\Lambda}{2\pi T}-\frac{1}{2})}^{-N^q_{\mathrm{mats}}+\frac{1}{2}} d\omega_q + T\sum_{n_q=-N^q_{\mathrm{mats}}}^{N^q_{\mathrm{mats}}-1} + T\int_{N^q_{\mathrm{mats}}-\frac{1}{2}}^{\frac{\Lambda}{2\pi T}-\frac{1}{2}} dn_q \\ &= \frac{1}{2\pi}\int_{-\Lambda}^{-\omega_{q,\max}-\pi T} dn_q + T\sum_{n_q=-N^q_{\mathrm{mats}}}^{N^q_{\mathrm{mats}}-1} + \frac{1}{2\pi}\int_{\omega_{q,\max}+\pi T}^{\Lambda} d\omega_q \end{aligned} \tag{C.9}$$

with $\omega_{q,\max} = \pi T(2N^q_{\mathrm{mats}} - 1)$. We have to add $1/2$ and πT to the integral limits due to the validity range of the sum. In the substitution, we used the fact, that the summed Matsubara frequencies of the quark loop and the quark self energy are fermionic Matsubara frequencies. For the quark self energy we calculate $2N^q_{\mathrm{mats}}$ Matsubara frequencies explicitly and approximate the remaining momentum interval by a logarithmic Gauss-Legendre integration (grid). For decreasing temperature and fixed N^q_{mats}, the explicit sum describes a shrinking

[3] Gauss-Legendre or Gauss-Chebychev integration means that we use a Gaussian quadrature and Legendre or Chebychev polynomials of second kind as grid-points. To increase the precision, we always use an equidistant external grid (p or k) and embed the integration grid (q) between the external grid points. Consequently, we need an interpolation routine base on the external grid points. This will be discussed in App. C.1.2.

momentum range. As result, more and more parts of the momentum interval have to be approximated and are therefore less accurate. Consequently, if we want to describe the integral at lower temperatures as accurately as possible, we should increase N^q_{mats} for decreasing temperatures.

Dressing function determination:

As already mentioned before, the external and internal grids differ and consequently we need an interpolation routine to determine the dressing functions of the quark and the gluon on the internal grid. At finite temperature, the heat bath direction yields an additional complication. In this case, the dressing functions are saved for a finite number of discrete external Matsubara frequencies in between $-\omega_{l,\max}$ and $\omega_{l,\max} \in \{\omega_{p,\max}, \omega_{k,\max}\}$ with $\omega_{p,\max} = \pi T(2\tilde{N}^q_{\text{mats}} - 1)$ for the quark and $\omega_{k,\max} = 2\pi T \tilde{N}^g_{\text{mats}}$ for the gluon dressing functions. Usually, we set $\tilde{N}^q_{\text{mats}} = N^q_{\text{mats}}$ with N^q_{mats} being the maximal Matsubara index of the Matsubara frequency integral approximation in Eq. (C.9). This implies that only the approximated Matsubara frequencies are not saved and calculated explicitly. For the quark and gluon Matsubara frequencies that are not saved and calculated explicitly, we need an approximation or determination method for the dressing functions needed on the internal (Matsubara) grid. For this purpose, we use the restoration of the O(4) invariance of the quark and gluon dressing functions at high four-momenta. The dressing function X at the three-momentum $\vec{q}^2$ and the Matsubara-frequency $\omega_q > \omega_{l,\max}$ can be approximated by the same dressing function X but now evaluated at the three-momentum $\vec{q}^2 + \omega_q^2 - \omega_{l,\max}^2$ and the last saved Matsubara frequency $\omega_{l,\max}$. We expressed this in formulas via

$$X(\vec{q}^2, \pm\omega_q) \approx X(\vec{q}^2 + \omega_q^2 - \omega_{l,\max}^2, \pm\omega_{l,\max}) \tag{C.10}$$

where $X \in \{\text{A}, \text{B}, \text{C}, \text{Z}, \text{Z}_{\text{T/L}}\}$ represents the dressing functions and $\{\omega_{p,\max}, \omega_{k,\max}\} \ni \omega_{l,\max} < \omega_q$ the highest saved Matsubara frequency. For the quark, we need at least $\tilde{N}^q_{\text{mats}} = N^q_{\text{mats}} = 5$ Matsubara frequencies before we can use the restoration of the O(4) invariance. For lower temperatures ($< 100\,\text{MeV}$) even more. For the gluon, however, it is sufficient to use the zeroth Matsubara frequency approximation, which means that we only save the first bosonic Matsubara frequency implying $N^g_{\text{mats}} = 0$.

At finite temperature, we still need an interpolation routine for the spatial part of the momentum which means the three-momentum. Therefore, we introduce one cubic spline object per dressing function and for every saved Matsubara frequency. This cubic spline object is based on the logarithmic and equidistant distributed radial part of the external three-momentum. In vacuum, the interpolation is

necessary for the four-momentum. Similar to the finite temperature case, we introduce again one cubic spline object per dressing function. But the cubic splines are now based on the logarithmic and equidistant distributed radial part of the external four-momentum. At finite chemical potential and vanishing temperature, the interpolation is a little bit more complicated. The dressing functions now depend on the four-momentum and an angle between the four-momentum and the assigned direction of the medium. One possibility is a two dimensional cubic-spline interpolation. But this interpolation is quite slow. For this purpose, we use the fact, that the chemical potential extents our four-momentum into the complex plane.

In this work, our (external) four-momentum at finite chemical potential and vanishing temperature can, in general, be represented by $p = (\vec{p}, p_4 + i\tilde{c})$ as discussed in App. C.1.2. Here, we generalized the momentum representation for the ability to describe also complex momenta. This will be discussed in more detail in App. C.1.3. For now, we want to discuss the interpolation routine at finite chemical potential and vanishing temperature and without any further complex momentum. Consequently, the imaginary contribution is given by $\tilde{c} = \mu_{\mathrm{q}}^{f}$. To make things easier to understand, we express the four-momentum including the imaginary contribution by $p_{\mathbb{C}}$ and the four-momentum without the imaginary contribution by $p_{\mathbb{R}}$. Their relation is given by $p_{\mathbb{C}} = p_{\mathbb{R}} + iv_{\mathrm{med}}\tilde{c}$ with the assigned direction of the medium $v_{\mathrm{med}} = (\vec{0}, 1)$. The needed complex momenta can now be represented by

$$p_{\mathbb{C}}^2 = p_{\mathbb{R}}^2 - \tilde{c} + i\sqrt{p_{\mathbb{R}}^2} z_p \tilde{c} \tag{C.11}$$

with the angle $z_p = \cos(\sphericalangle(p, v_{\mathrm{med}}))$ between the external momentum p and the assigned direction of the medium $v_{\mathrm{med}} = (\vec{0}, 1)$. To evaluate the quark propagator in the complex plane or for finite chemical potential we have different interpolation routines available, e.g. the shell- and the Cauchy-method. A review to the numerical techniques in vacuum can be found in Ref. [199]. In this work, we use the Cauchy-method, which was introduced in Ref. [125] and which is based on the Cauchy integral formula

$$f(p) = \frac{\int_\Gamma \frac{f(q)}{q-p}}{\int_\Gamma \frac{1}{q-p}} \tag{C.12}$$

where we obtain the function f at the momentum p interior to the closed contour Γ by a contour integration over the function at Γ. The closed contour thereby describes the edge of the set of necessary momenta in the complex momentum plane. As already mentioned, the necessary momenta can be described by Eq. (C.11). Finally, we only need to evaluate the dressing functions on the corresponding

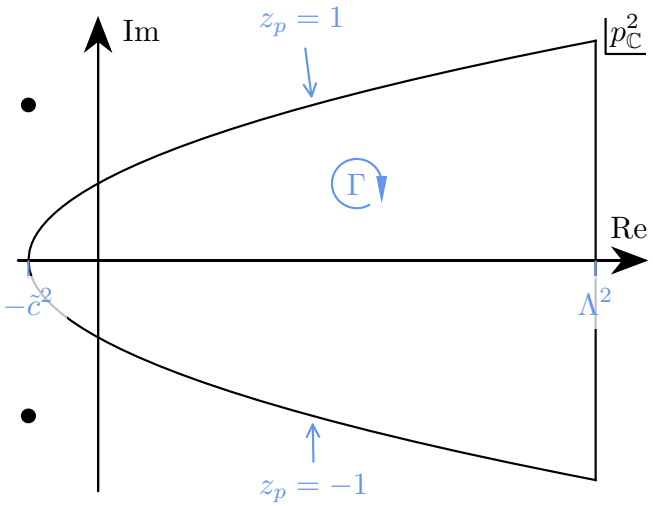

Figure C.1.: Closed path Γ for the complex momenta needed in the finite chemical potential and vanishing temperature as well as in the bound state calculations. We furthermore show poles of the quark propagator marked as dots. The closed path consists of three parts: a vertical line at the UV cutoff Λ, and two parabolas indicated by $z_p = \pm 1$. The direction of the path integral is given by the arrow around the closed path Γ.

closed path which is given in Fig. C.1. The dressing functions for all momenta in between are obtained from the Cauchy integral formula in Eq. (C.12). The edge of the set of complex momenta is defined by the two parabolas $z_p = \pm 1$ in Eq. (C.11) and a vertical line at the UV-cutoff Λ, which connects the two parabolas. The maximal (calculable) value of $\tilde{c}$ is dictated by the appearance of poles or singularities in the quark propagator, which are indicated in the figure as big dots. The parametrization and the grid are chosen in the same as in the review in Ref. [199].

Due to the existence of the quark chemical potential in the external quark four-momentum, we are able to use the Cauchy-method as interpolation routine for the quark dressing functions at finite chemical potential and vanishing temperature. However, there is no chemical potential in the gluon four-momentum. Consequently we would need a slow two dimensional cubic spline interpolation for the gluon interpolation at finite chemical potential and vanishing temperature. To avoid this slowing factor, we introduced the vacuum gluon approximation in Sec. 2.2.3. An improvement through the use of a two dimensional cubic spline interpolation can be done in a future work.

In our calculations, we also need the dressing functions at momenta above the ultraviolet cutoff. Consequently, we implemented two methods for the extrapolation: a constant and a linear extrapolation. For the constant extrapolation, we evaluate the dressing function X at the momentum $|p| > \Lambda$ by simply using the same dressing function evaluated at $|p| = \Lambda$ and keeping the considered angles and Matsubara frequencies unchanged. The mapping onto the saved Matsubara frequencies in Eq. (C.10), however, is still necessary.[4] For the linear extrapolation, we keep the considered angles and Matsubara frequencies fixed and apply the mapping onto the saved Matsubara frequencies. Then, we use the upper two external grid points of the considered angle and Matsubara frequency to determine a linear function from the logarithmic grid. Afterwards, we use this linear function to determine the value of the extrapolated dressing function. The linear extrapolation is especially important for the gluon. There the results show a considerable difference, if the constant extrapolation is used instead. In our calculation of the quark and gluon, we therefore use the linear extrapolation for large momenta and the constant extrapolation for small momenta.

Iterative procedure:

Since the quark and gluon integral equations are coupled, we have to calculate them simultaneously with a fixpoint iteration. If we further include hadrons in the calculation, this quark-gluon system fixpoint iteration has to be repeated once again. A schematic representation of the iterative procedure is shown in Fig. C.2.

If we backcouple baryons and diquarks via Eq. (6.1) instead of mesons, the flow diagram changes a bit. At first, the quarks and gluons are again calculated without the hadron. Then, we repeat the macro cycle with the diquark and baryon backcoupled and therefore included in the quark iteration. For the diquark and baryon, we use precalculated dressing functions, which are discussed in Sec. 6.1. Because of this, we do not need to solve the hadrons with an iterative procedure.

Since we use the same meson at a specific chemical potential for all temperatures as mentioned in Sec. 5.1, we need to consider if this is a good approximation. For this purpose, we now try to estimate the the impact of the missing temperature effects considering the results of previous calculations concerning mesons and meson backcoupling at finite temperature. A characteristic behavior in lattice [200, 201]

[4] At finite temperature, we use the dressing function X at the four-momentum $p = (\hat{\vec{p}}\sqrt{\Lambda^2 - \omega_p^2}, \pm\omega_p)$ instead of the same dressing function at $p = (\vec{p}, \pm\omega_p)$. For vanishing temperatures the corresponding four-momentum p is exchanged by $p = \hat{p}\Lambda$. The three-momentum $\hat{\vec{p}} = \vec{p}/\sqrt{\vec{p}^2}$ represents the normalized three-vector. The normalized four-vector is defined similarly.

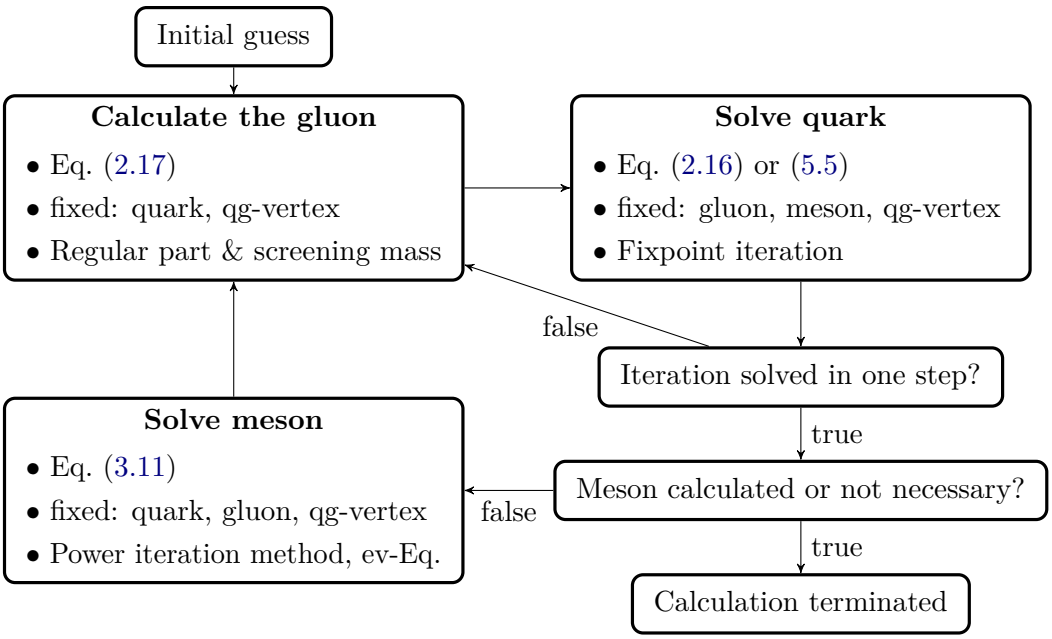

Figure C.2.: Flow diagram showing how the quarks, gluons and mesons are calculated for fixed input parameters (quark masses m_{q}^f and vertex interaction strengths $d_1^{(\mathrm{q})}$) defined in Sec. 2.2.3. The quark is solved iteratively until the propagator converged. The gluon, quark-gluon vertex and mesons (if already calculated) are kept fixed during this iteration which we call micro cycle. If the quark converged, the gluon is updated (we calculate the new regular part and the screening mass). The quark and gluon calculation together is the macro cycle. The quark-gluon system converged if the update of the gluon leads to no changes in the quark propagator. The quark iteration then terminates in one step. If this is the case and the meson is already calculated and included in the quark calculation or the meson is not necessary, the whole calculation is terminated. If the meson is necessary but not calculated so far, it is with a power iteration method and an eigenvalue equation explained in App. C.2.4 and Sec. 3.2.1, respectively. Meanwhile, the quark, gluon and quark-gluon vertex are kept fixed. Afterwards the macro cycle is started again. In this work, the finite temperature mesons are approximated by corresponding mesons with their temperature turned down to zero.

and DSE [63–67] studies is that the Pion mass is almost temperature independent for temperatures below the pseudocritical temperature. Furthermore, Ref. [64] shows that the Pion and sigma mesons do not dissolve into a gas of almost mass-less quarks for temperatures also significantly higher than the chiral and deconfinement

transition. These two features are in accordance with our approximation. However, in disagreement with our approximation, Ref. [128] observed that the sigma meson mass decreases already for temperatures below the pseudocritical temperature and exhibits a dip at the pseudocritical temperature. For temperatures shortly above the pseudocritical temperature the sigma meson degenerates[5] with the Pion meson and their mass increase approaching an asymptotic behavior of $2\pi T$. This linear increase of the Pion and sigma mass w.r.t. the temperature was also observed in lattice in the Refs. [200, 201] and is missing in our approximation.

In summary, the meson properties and the meson propagator depend much stronger on temperature than on chemical potential. But how important are the comparatively small changes in the meson propagator for observables and the QCD phase diagram? In Ref. [169], the influence of the mass of a backcoupled Pion on the dynamical quark mass, the quark condensate and the meson decay constant was studied. As result, we see that the bound state mass variations, certainly, are important for the correct description of the phase diagram. However, the influence of the temperature on the BSAs can play an important part, too. Unfortunately, the BSAs at finite temperature (for our quite evolved truncation) are unknown. Consequently, further investigations are necessary to be able to make qualitative statements. So far, the BSAs and the meson backcoupling at finite temperature were only calculated in a simplified manner. Previous works used an effective interaction, e.g. Ref. [65], and/ or approximated the Bethe-Salpeter amplitude components via generalized Goldberger-Treiman like relation given in Ref. [31].[6] By using the latter approximation, Ref. [89] obtained the first results of meson effects (with temperature dependency) on the QCD phase diagram. In comparison with our results in Sec. 5.3, the observed qualitative impact of the meson effects on the QCD phase diagram is the same. This implies that the neglect of temperature effects on the meson propagator and the BSA do not influence the results on a qualitative basis. Similar as in Ref. [89], we rather expect that the strongest (meson backcoupling) effect results from the number of considered meson flavors or the

[5] In the chiral limit, Ref. [65] discusses that the Pion and sigma mesons even become locally identical above the pseudocritical temperature, meaning that the leading amplitudes become point-wise identical while the remaining amplitudes vanish.

[6] These relations relate the Pion BSA components to quark dressing functions, e.g. via $\mathrm{E}^\pi(p) = \mathrm{B}(p)/f_\pi$. This provides us the opportunity to evaluate the Pion BSA off-shell and for general momenta. However, the relation is only valid in the chiral limit. At finite quark mass, the UV behavior is different. For example the B function has a logarithmic running (see Ref. [202]) while the E^π function retains the chiral power law behavior. This mostly affects the finiteness of integrals. Because of this difference, Ref. [89] introduced an extra factor to repair this behavior. Note that Ref. [65] showed that the Goldberger-Treiman like relation holds at finite temperature, too. Using this relation, the Pion decay constant and the Pion masses have to be obtained by the Pagel-Stokar approximation and the GMOR relation, respectively. But the latter relation is only applicable if all four tensor structures are used.

BSA not from their precise mass.

Furthermore, we have to mention that the correct way to include hadrons into the calculation is to solve a fully coupled system of DSEs and BSEs at the desired phase diagram point. To achieve this, the flow diagram has to be extended. The first two steps are the same: We calculate the quark-gluon system without the hadron. Then in another iterative cycle, we calculate the hadron and include it into the quark-gluon calculation until neither the quark, nor the gluon or the meson change anymore. This is, furthermore, done for fixed input parameters. But we have to repeat this calculation varying the input parameters to find the optimal values for the input parameters, at least in vacuum. The fixing of the parameters is discussed in Sec. 2.2.3. The search of the optimal input parameters itself is again an iterative procedure, since we have to repeat the quark-gluon and meson calculation for every change of the parameters. The problem with this procedure, however, is that we need to calculate the quark in the complex momentum plane to be able to solve the meson. The calculation of the quark in the complex momentum plane and the determination of the meson with a eigenvalue equation and power iteration method leads to extremely time-consuming calculations.

If we calculate the quarks, gluons and hadrons with the flow diagram presented in Fig. C.2, problems with the convergence of the quark fixpoint iteration can appear. To solve them, we introduce a relaxation parameter $0 \leq r \leq 1$ for the calculation of new dressing functions. New dressing functions are then obtained by a certain ratio of the new and the old dressing function via $X'_{\text{new}} = rX_{\text{new}} + (1-r)X_{\text{old}}$.

(Pseudo)critical temperature and CEP location determination:

In this section, we will detail how we determine the (pseudo)critical temperatures and the location of the critical endpoint. For the determination of the (pseudo)critical temperature, we can consider different thermodynamic quantities derived from the thermodynamic potential, e.g. the order parameter or fluctuations/ response functions. Here, we will discuss the order parameter, i.e. the (regularized) quark condensate or the dynamical quark mass, and the response function which (in case of the chiral symmetry) is the chiral susceptibility.

The critical temperature of the sharp first-order phase transition is identical for all ways of determination. This means that all thermodynamic quantities yield the same critical temperature for the first-order phase transition. The critical temperature thereby is determined by the location of the discontinuity of the considered thermodynamic quantity mentioned before. The crossover, as a continuous transition between the two phases, on the other hand, is not an actual

phase transition and does not have a properly defined critical temperature. There is no unique definition. In this section, we will consider two possible definitions of the pseudocritical temperature which work for the first-order phase transition too: The inflection point of the order parameter $\left(T_{\mathrm{pc}}^{f}\right)_{\mathrm{op.}}$ or the maximum of the response function $\left(T_{\mathrm{pc}}^{f}\right)_{\mathrm{rf.}}$. These two quantities are defined via

$$\begin{aligned}\left(T_{\mathrm{pc}}^{f}\right)_{\mathrm{op.}} &= \arg\max_{T}\left|\frac{\partial\Delta_{fh}(T,\mu_{\mathrm{B}})}{\partial T}\right|,\\ \left(T_{\mathrm{pc}}^{f}\right)_{\mathrm{rf.}} &= \arg\max_{T}\left|\frac{\partial\langle\hat{\bar{\Psi}}\hat{\Psi}\rangle_{f}(T,\mu_{\mathrm{B}})}{\partial m_{\mathrm{q}}^{f}}\right|.\end{aligned} \tag{C.13}$$

Both methods give different results in the crossover region but coincide in the discontinuous phase transition region and the location of the CEP. For all results in this work, we use the inflection point definition.

Due to the numerical complexity of the calculation, the obtained regularized quark condensate shows an oscillating behavior around the transition between the hadronic and the quark-gluon plasma phase if we consider the crossover. To compensate this behavior, we fit smoothed splines to the regularized quark condensate and determine the pseudocritical temperatures from them. We do this iteratively in a temperature interval $T \in [T_{\mathrm{pc}} - T_{\mathrm{int}}(\mu_{\mathrm{B}})/2, T_{\mathrm{pc}} + T_{\mathrm{int}}(\mu_{\mathrm{B}})/2]$ until the pseudocritical temperature and therefore also the interval does not change anymore. In this interval, T_{pc} represents the pseudocritical temperature of the last iteration step or the stating guess and $T_{\mathrm{int}}(\mu_{\mathrm{B}})$ defines the range of the temperature interval. As starting guess, we use the pseudocritical temperature from the raw (unsplined) regularized quark condensate which we get from a simple differential quotient. $T_{\mathrm{int}}(\mu_{\mathrm{B}})$ is chemical potential dependent, since the regularized quark condensate becomes steeper, the closer we get to the CEP. Consequently, for numerical reasons, the spline is only able to describe the quark condensate in a shrinking temperature interval. We determine the error of the pseudocritical temperature from this procedure.

We define the location of the second-order CEP as the chemical potential (together with the corresponding critical temperature) where the crossover turns into a first-order phase transition. If we, however, are able to determine the Nambu and Wigner solution, we instead define the location of the CEP as the lowest chemical potential (together with the corresponding critical temperature) where the Nambu and Wigner coexistence lines coincide but the Wigner solution still is a stable and different solution compared to the Nambu solution. We do so since the numerical evaluation does not properly allow to distinguish between finite and infinite jumps

without applying a lot of computing effort. We get the Nambu and Wigner solution by inserting two different initial conditions.

C.1.3. Quark propagators for complex momenta

If we calculate bound states, we need the quark propagator for momenta in the complex plane. For this purpose, we consider the external quark momentum p in the quark DSE in the complex plane. By keeping the momentum routing of the quark DSE the same and using the self consistent solution of the quark propagator at real momenta for a final iteration step, we can perform a simple analytic continuation. This, however, requires the knowledge of the gluon and the quark-gluon-vertex for complex momenta. But if these are not accessible, we have to modify the momentum routing instead.

The imaginary contribution $\tilde{c} = \mu_{\mathrm{q}}^f + \eta_\pm m_{\mathrm{x}} \equiv c_\pm$ to the complex four-momentum $p_{\mathbb{C}} = p_{\mathbb{R}} + \tilde{c}v$ has two origins: On the one hand the chemical potential μ_{q}^f and on the other hand the externally added imaginary momentum. Since we consider bound states at rest, the second term is given by a fraction of the bound state mass $\eta_\pm m_{\mathrm{x}}$ in energy direction $v = v_{\mathrm{med}} = (\vec{0}, 1)$. While the chemical potential is directly connected to the quark propagator and therefore contributes to the quark momenta alone, the second term only affects the external quark momentum. Consequently, we only need to modify the momentum routing presented in Sec. 2.1.2 if we consider externally added imaginary contributions.

By redefining the loop momentum $k = p+q$ and exchanging the momenta q (without chemical potential) and k in the quark DSE, the imaginary contribution is directed through the quark propagator alone. This implies that the quark propagator has to be evaluated iteratively on all points needed in the complex plane. The needed complex momenta can be described by Eq. (C.11) with $\tilde{c} = \mu_{\mathrm{q}}^f + \eta_\pm m_{\mathrm{x}} \equiv c_\pm$. The corresponding quark dressing functions are again calculated with the Cauchy-method discussed in App. C.1.2. Furthermore, a different regularization is necessary. Instead of using the renormalization constants as factor, we now have to subtract the vacuum self energy at the renormalization point. Through this procedure, we get a characteristic (small) drop of the quark dressing functions at large momenta.

C.2. ... the BSE

In this section, we will at first derive the on-shell equations necessary to calculate the mesons and their properties within the Bethe-Salpeter approach. Then, for the

numerical implementation of the BSE calculations, we will discuss the momentum and integral representations, similar as for the DSE. Furthermore, the chemical potential dependence of the momentum partitioning parameter, the BSA component determination and the power iteration method will be detailed at the end.

C.2.1. Derivation of the on-shell equations

For the calculation of on-shell mesons and their properties, we have to derive the homogeneous BSE, norm and decay constants equations. We will do so in Minkowski space. More details to the following derivations can be found in Refs. [124, 203]. We will begin with the derivation of the homogeneous BSE.

As already mentioned in Sec. 3.1.1, n-particle bound states appear as poles (at the bound state masses) in the $2n$-point quark Green functions defined in Eq. (2.2) for the (anti)quark fields $\varphi \in \{\bar{\Psi}, \Psi\}$. Consequently, to describe a meson bound state x of mass m_{x} and momentum P, we will now consider the four-point quark Green function $G_{4,S}$. In addition, we need a complete set of orthogonal hadron eigenstates $|P, \mathrm{x}, \alpha\rangle$ with momentum P, hadron type x (indicating specific hadrons) and further quantum numbers α (angular momentum, parity, hadron flavor, ...). These eigenstates are a basis for the system describing Hamiltonian and fulfill the completeness relation

$$\mathbb{1} = \sum_{\mathrm{x}} \int \frac{d^4P}{(2\pi)^3} \theta(P_0)\delta(P^2 - m_{\mathrm{x}}^2) \, |P, \mathrm{x}, \alpha\rangle \, \langle P, \mathrm{x}, \alpha| = \sum_{\mathrm{x}} \frac{1}{(2\pi)^3} \int \frac{d^4P}{2E_P} \, |\ldots\rangle \, \langle \ldots| \, . \tag{C.14}$$

Due to the Lorentz-invariant integral weight, each hadron on its mass shell $P^2 = m_{\mathrm{x}}^2$ ($\Leftrightarrow E_P^2 = \vec{P}^2 + m_{\mathrm{x}}^2$). If we now insert this completeness relation into the 1PI 4-point quark Green function $G_{4,S}$ given in Eq. (B.3) and use the meson bound state wave-function $\chi_{\mathrm{x}}^{\alpha}$ definition in Eq. (3.8), we get an expression for the 2PI 2-point quark Green function[7] $G_{2,S}^{[2]}$

$$G_{2,S}^{[2]}(P, x, y) = \sum_{\mathrm{x}} \int \frac{d^3P}{(2\pi)^3} \frac{\chi_{\mathrm{x}}^{\alpha}(P, x)\bar{\chi}_{\mathrm{x}}^{\alpha}(-P, y)}{2E_P} e^{-iE_P(X_0 - Y_0) + i\vec{P}(\vec{X} - \vec{Y})} \theta(X_0 - Y_0) \tag{C.15}$$

with $X = \frac{x_1 + x_2}{2}$ and $x = x_1 - x_2$ as well as analogous expressions for Y and y. Since the constituents of the initial state should be chronologically earlier than those of the final state, we introduced $\theta(X_0 - Y_0) = -(i2\pi)^{-1} \int dk (k + i\epsilon)^{-1} \exp(-i(X_0 - Y_0)k)$

[7] In App. B.1, we show that there is a connection between the four-point quark Green functions $G_{4,S}$ and the 2PI two-point meson Green function or meson propagator $G_{2,S,\mathrm{x}}^{[2]}$.

with $k = P_0 - E_P$. By Fourier transforming this relation, adding the contribution of the antiparticle states of $|P, \mathrm{x}, \alpha\rangle$ (this implies a factor of two), and considering the Green function at the Pole $P^2 = m_\mathrm{x}^2$, we get the pole representation

$$G^{[2]}_{2,S}(P,p,l) = \sum_\mathrm{x} \frac{i\chi^\alpha_\mathrm{x}(P,p)\bar{\chi}^\alpha_\mathrm{x}(-P,l)}{P^2 + m_\mathrm{x}^2 + i\epsilon} \tag{C.16}$$

with the total momentum of the meson P, the relative momenta between the two constituents p or l and the on-shell condition $P^2 = m_\mathrm{x}^2$. This equation only represents the pole contribution. As indicated by Eq. (3.7), there additionally exists a regular term $R(P,p,l)$. If we now multiply the bound state equation of motion in Eq. (3.3) with $S^{-1}(p_+) \otimes S^{-1}(p_+)$, insert the pol representation of Eq. (C.16), and take the residue ($\mathrm{Res}_{x_0} \frac{f(x)}{g(x)} = \frac{f(x_0)}{g'(x_0)}$) for a specific meson x, we get

$$S^{-1}(p_+)\chi^\alpha_\mathrm{x}(P,p)S^{-1}(p_-)\bar{\chi}^\alpha_\mathrm{x}(-P,l) = \int_q K(p,q,P)\chi^\alpha_\mathrm{x}(P,q)\bar{\chi}^\alpha_\mathrm{x}(-P,l) \tag{C.17}$$

with the Bethe-Salpeter wave-function $\chi^\alpha_\mathrm{x}(P,\cdot)$ in momentum space defined by Eq. (3.10). By cutting the charge conjugated Bethe-Salpeter wave-function $\bar{\chi}^\alpha_\mathrm{x}(P,l) = [C\chi^\alpha_\mathrm{x}(P,-l)C^{-1}]^\top$, we get the quark-antiquark-meson vertex on-shell equation or homogeneous Bethe-Salpeter equation (hBSE) shown in Eq. (3.9). Since the Bethe-Salpeter amplitude, as solution of the hBSE, is only determined up to constant factor (due to the structure of the hBSE as eigenvalue equation), we need a normalization condition for it.

Norm

We can derive the standard canonical norm (Leon-Cutkosky normalization) from the 2PI 2-point Green function $G^{[2]}_{2,S}$ (restricted to one mesonic channel) by demanding the residue at the bound state pole to equal one. This is necessary for the decomposition of Eq. (3.7) into a pole and a regular term to hold. In the neighborhood of a pole, we can approximate the propagator $G^{[2]}_{2,S}$ by the pole representation in Eq. (C.16) multiplied by an arbitrary residue $\mathcal{R}_\mathrm{x}$. If we, furthermore, consider the general derivative of the equation $G^{[2]}_{2,S} = \left(S^{-1}S^{-1} - K\right)^{-1}$ which is given by $\frac{\partial}{\partial\lambda}G^{[2]}_{2,S} = -G^{[2]}_{2,S}\left(\frac{\partial S^{-1}S^{-1}}{\partial\lambda} - \frac{\partial K}{\partial\lambda}\right)G^{[2]}_{2,S}$ and insert the pole representation, we obtain[8]

$$i\frac{\partial P^2}{\partial\lambda}\sum_\mathrm{x}\mathcal{R}_\mathrm{x}\frac{\chi^\alpha_\mathrm{x}\bar{\chi}^\alpha_\mathrm{x}}{(P^2-m_\mathrm{x}^2)^2} = -\sum_{\mathrm{x}'}\mathcal{R}_{\mathrm{x}'}\frac{\chi^{\alpha'}_{\mathrm{x}'}\bar{\chi}^{\alpha'}_{\mathrm{x}'}}{P^2-m_{\mathrm{x}'}^2}\frac{\partial}{\partial\lambda}\left(S^{-1}S^{-1}-K\right)\sum_\mathrm{x}\mathcal{R}_\mathrm{x}\frac{\chi^\alpha_\mathrm{x}\bar{\chi}^\alpha_\mathrm{x}}{P^2-m_\mathrm{x}^2}\,. \tag{C.18}$$

[8] Keep in mind that χ^α_x is on the mass-shell. This implies $\partial\chi^\alpha_\mathrm{x}(P,p)/\partial P^2 = 0$.

By multiplying with $-i\frac{\partial\lambda}{\partial P^2}(P^2-m_{\mathrm{x}''}^2)/\mathcal{R}_{\mathrm{x}}^2$, $(\bar{\chi}_{\mathrm{x}''}^{\alpha''})^{-1}$ (from the right) and $(\chi_{\mathrm{x}'''}^{\alpha'''})^{-1}$ (from the left) and considering $\lambda = P_\mu$, we can rewrite the equation into

$$\delta_{\alpha\alpha'}\delta_{\mathrm{xx}'}\mathcal{N}_{\mathrm{x}}^2 = \frac{\delta_{\alpha\alpha'}\delta_{\mathrm{xx}'}}{\mathcal{R}_{\mathrm{x}}} = i\frac{P_\mu}{2P^2}\bar{\chi}_{\mathrm{x}'}^{\alpha'}\frac{\partial}{\partial P_\mu}\left(S^{-1}S^{-1}-K\right)\chi_{\mathrm{x}}^{\alpha}\Big|_{P^2=m_{\mathrm{x}}^2} \tag{C.19}$$

If we now take the functional, Dirac, flavor and color trace into account and express the Bethe-Salpeter wave-function by Eq. (3.10), we can reshuffle the equation into

$$\begin{aligned}\delta_{\alpha\alpha'}\delta_{\mathrm{xx}'}\mathcal{N}_{\mathrm{x}}^2 = & -i\frac{P_\mu}{2P^2}\frac{d}{dQ_\mu}\,\mathrm{Tr}_{\mathrm{DCF}}\Big\{\int_q \bar{\Gamma}_{\mathrm{x}'}^{\alpha'}(-P,q)\,S(q_+(Q))\,\Gamma_{\mathrm{x}}^{\alpha}(P,q)\,S(q_-(Q)) + \\ & + \int_q\int_p S(q_-(P))\,\bar{\Gamma}_{\mathrm{x}'}^{\alpha'}(-P,q)\,S(q_+(P))K(p,q,Q)\,S(p_-(P))\cdot \\ & \cdot\,\Gamma_{\mathrm{x}}^{\alpha}(P,p)\,S(p_+(P))\Big\}\Big|_{Q^2=P^2=m_{\mathrm{x}}^2}\end{aligned} \tag{C.20}$$

with the charge conjugated Bethe-Salpeter amplitude $\bar{\Gamma}_{\mathrm{x}}^{\alpha}(P,p) = \left[C\Gamma_{\mathrm{x}}^{\alpha}(P,-p)C^{-1}\right]^\top$. Due to our Ladder like truncation in the BSE and the total momentum P independence of the kernel, the second term vanishes in this work.

Decay constant

To derive the meson decay constant, we consider the transition element between a hadron state defined in Eq. (C.14) and the current $j_{\mathrm{x},e}^{\mu}(x) := \bar{\Psi}(x)\Gamma_{\mathrm{x}}^{\mu}\tilde{r}_{\mathrm{x}}^{e}\Psi(x)$ with the Dirac matrix $\Gamma_{\mathrm{x}}^{\mu} \in \{\gamma^\mu, \gamma_5\gamma^\mu\}$ and the meson flavor matrices $\tilde{r}_{\mathrm{x}}^{e} = r_{\mathrm{x}}^{e}/\mathrm{N_f}$.[9] This transition element is defined by

$$\begin{aligned}&\left\langle 0\left|\hat{j}_{\mathrm{x},e}^{\mu}(0)\right|P,\mathrm{x}',\alpha\right\rangle e^{-iPx} = \left\langle 0\left|\hat{j}_{\mathrm{x},e}^{\mu}(x)\right|P,\mathrm{x}',\alpha\right\rangle = -\left[\Gamma_{\mathrm{x}}^{\mu}\tilde{r}_{\mathrm{x}}^{e}\right]_{\gamma\delta}\left[\chi_{\mathrm{x}'}^{\alpha}(P,x,x)\right]_{\delta\gamma} \\ &= -\lim_{z\to 0}\left[\Gamma_{\mathrm{x}}^{\mu}\tilde{r}_{\mathrm{x}}^{e}\right]_{\gamma\delta}\left[\chi_{\mathrm{x}'}^{\alpha}(P,z)\right]_{\delta\gamma}e^{-iPx} = -\lim_{z\to 0}\int_q \mathrm{Tr}_{\mathrm{DCF}}\left[\Gamma_{\mathrm{x}}^{\mu}\tilde{r}_{\mathrm{x}}^{e}\chi_{\mathrm{x}'}^{\alpha}(P,q)\right]e^{-i(Px+qz)}\,.\end{aligned} \tag{C.21}$$

Considering different current and meson combinations we find (See Refs. [32, 204])

$$\begin{aligned}-\mathrm{Tr}_{\mathcal{F}}\left[\Gamma_{\mathrm{x}}^{\mu}\tilde{r}_{\mathrm{x}}^{e}\chi_{\mathrm{x}',e'}^{(\nu)}(P)\right] &= \left\langle 0\left|\hat{j}_{\mathrm{x},e}^{\mu}(0)\right|P,\mathrm{x}',(\nu),e'\right\rangle \\ &= \begin{cases}\delta_{e,e'}f_{\mathrm{x}'}iP^\mu & \text{for } \mathrm{x}'\in\{\mathrm{PS/S}\} \text{ and } \mathrm{x}\in\{\mathrm{AV/V}\}\\ \delta_{e,e'}f_{\mathrm{x}'}im_{\mathrm{x}'}T_{\mu\nu}(P) & \text{for } \mathrm{x}'\in\{\mathrm{AV/V}\} \text{ and } \mathrm{x}\in\{\mathrm{AV/V}\}\end{cases}.\end{aligned} \tag{C.22}$$

[9] See App. A.3 for the definition of r_{x}^{e} and corresponding relations.

Here, x represents the type of the current and x' the type of the meson. The pseudo-scalar and axial-vector mesons $\mathrm{x}' \in \{\mathrm{PS}, \mathrm{AV}\}$ couple to an axial-vector current $\mathrm{x} = \mathrm{AV}$ while the vector $\mathrm{x}' = \mathrm{V}$ mesons couple to a vector meson current $\mathrm{x} = \mathrm{V}$. We use $T_{\mu\nu}(P)$ instead of the polarization tensor $\epsilon_\mu(P)$ from Refs. [32, 204], to take the open Lorentz index of the meson state under consideration. Through this procedure, we keep the orthogonality of the meson state w.r.t. the total momentum and receive the correct polarization number if we contract the Lorentz indices. After renormalization, a Z_A has to be included into the vertex Γ_0 of Eq. (3.4) and to the RHS of Eq. (C.22) (see Ref.[31]). We can replace Z_A by Z_2 since their ratio is a renormalization-group-invariant quantity (see Ref. [205]).

C.2.2. Momentum and integral parametrization

In the bound state calculation for vanishing temperatures, the momentum parametrizations of the total (P) and relative (p externally and q internally) momenta of the meson are given by

$$P = \left(|\vec{P}|(0,0,1), P_4\right), \quad p = (|\vec{p}|(0, \bar{y}_p, y_p), \tilde{p}_4), \quad q = (|\vec{q}|(\bar{y}_q \sin\phi_q, \bar{y}_q \cos\phi_q, y_q), \tilde{q}_4) \ . \tag{C.23}$$

Like in the DSE momentum parametrization in App. C.1.2, the external and internal relative momenta entail the chemical potential. Also the angles are defined in the same way. The gluon momentum entering in the quark-gluon vertex, is given by $k = p - q$. The quarks are evaluated at the momenta

$$l_\pm = l \pm \eta_\pm P \tag{C.24}$$

with $l \in \{q, p\}$. The parametrization shown in Eq. (C.23) is generalized for the correct determination of the angular dependency of the necessary equations. Ultimately, we consider the mesons in rest frame by setting $|\vec{P}| = 0$. This implies $P_4 = i m_\mathrm{x}$ for the fourth component of the total momentum and $y_p = 1$ and $\cos\phi_q = 1$ for the angles in the relative momenta. The parametrization of the momenta in the bound state approach for finite temperature is much more complicated and not considered in this work. The integrals are described in the same way as in the DSE case detailed in App. C.1.2.

C.2.3. Chemical potential dependence of the partitioning parameter

In the bound state approach, the quark propagators are evaluated at the complex momenta shown in Eq. (C.24). Another representation is $p = \left(\vec{p}, p_4 + i c_\pm^f\right)$ where

$c_\pm^f = \mu_\mathrm{q}^f \pm \eta_\pm m_\mathrm{x}$ is the complex extension which depends on the quark chemical potential[10] μ_q^f, the mass of the considered meson m_x, and the momentum partitioning parameters $0 \leq \eta_\pm \leq 1$ introduced in Sec. 3.1.2. This partitioning parameter has to fulfill the condition $\eta_+ + \eta_- = 1$. The complex extension can be increased until the quark propagator hits a pole. In vacuum and medium, we have to define this position differently. In medium, we identify the pole position with the highest still calculable chemical potential. Since the poles are much closer in the Wigner solution[11], the highest chemical potential of the Nambu solution is the desired value, i.e. the upper border of the considered coexistence region studied in Sec. 4.2. Only at the transition from the Nambu to the Wigner solution a pole enters the complex quark momentum plane in medium. Since we force the vacuum quark propagator to O(4) symmetry by not allowing a distinction between the first and second quark vector dressing function, the calculation of the quark propagator is possible for higher complex extensions than those in medium. In this work, we are mostly interested in the medium, therefore, we have the condition $|c_\pm^f| \leq \mu_{\mathrm{q,c}}^f$ with the chemical potential $\mu_{\mathrm{q,c}}^f$ representing the upper border of the coexistence region for the quark flavor f. Note that the medium quark propagator at complex momenta shows numerical problems already before the Nambu transition.

For high meson masses, we get the problem that we can only access a small chemical potential interval if we do not modify the partitioning parameter in dependence on the chemical potential. To find the best chemical potential dependence for the partitioning parameter, we consider a generalized version of the condition mentioned above.[12] The lower boundary is now given by $-\mu_{\mathrm{q,c}}^f \leq c_-^f = \mu_\mathrm{q}^f - \eta_- m_\mathrm{x} = \mu_\mathrm{q}^f - (1-\eta_+) m_\mathrm{x}$ and the upper one by $\mu_\mathrm{q}^{f'} + \eta_+ m_\mathrm{x} = c_+^{f'} \leq \mu_{\mathrm{q,c}}^{f'}$. By rearranging and expressing the quark chemical potential by the baryonic chemical potential[13], we get the condition

$$\max\left(0.0\,,\, 1.0 - \frac{\mu_{\mathrm{q,c}}^f}{m_\mathrm{x}} - \frac{\mu_\mathrm{B}}{3m_\mathrm{x}}\right) \leq \eta_+(\mu_\mathrm{B}) \leq \min\left(1.0\,,\, \frac{\mu_{\mathrm{q,c}}^{f'}}{m_\mathrm{x}} - \frac{\mu_\mathrm{B}}{3m_\mathrm{x}}\right) \tag{C.25}$$

for the partitioning parameter $\eta_+(\mu_\mathrm{B})$. In Fig. C.3, we show this condition in a graphical way and demonstrate the optimal chemical potential dependence for the partitioning parameter $\eta_+(\mu_\mathrm{B})$. Since numerical artifacts appear near the maximal

[10] For the meson in medium calculation, we can set the quark chemical potential to $\mu_\mathrm{q}^f = \mu_\mathrm{B}/3$.

[11] The quark propagator of the Wigner solution for complex momenta is not calculable since the pole is almost immediately included in the complex plane.

[12] Note that the quark and the antiquark have two different coexistence regions for mesons with mixed quark content like the K and $\bar{K}$ meson. Consequently the quark and the antiquark can be calculated up to different quark chemical potentials: $\mu_{\mathrm{q,c}}^\ell$ and $\mu_{\mathrm{q,c}}^\mathrm{s}$.

[13] Here, we use the fact that we calculate all mesons for $\mu_\mathrm{q}^\mathrm{s} = \mu_\mathrm{q}^\ell$.

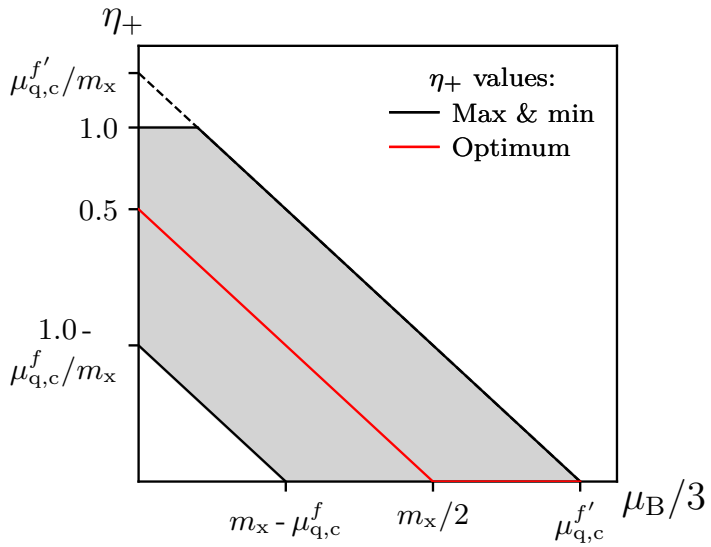

Figure C.3.: Possible values for the partitioning parameter $\eta_+(\mu_{\mathrm{B}}) = \frac{c_+ - \mu_{\mathrm{B}}/3}{m_{\mathrm{x}}}$ are indicated by the gray area in dependence of the considered baryonic chemical potential μ_{B}. More information can be found in the text.

or minimal values of $\eta_+(\mu_{\mathrm{B}})$, we should chose $\eta_+(\mu_{\mathrm{B}})$ for high-mass mesons as shown in the figure.

C.2.4. BSA component determination and power iteration method

Like for the quark and gluon dressing functions we derive equations for the BSA components $f_{\mathrm{x}}^i(P,p)$ by projection. The difference to the quark and gluon dressing functions is that we express these components with Chebychev polynomials like shown in Eq. (3.15). To extract the corresponding Chebychev coefficients, we use the Chebychev orthogonality relation

$$\frac{2}{N}\sum_{n=0}^{N-1}\tilde{T}_i(z_p^n)\tilde{T}_j(z_p^n) = \delta_{ij}\,. \tag{C.26}$$

In this orthogonality relation, the angle $z_p^n = \cos\left(\frac{2n+1}{2N}\pi\right)$ defines the n^{th} of N roots of the N^{th} Chebychev polynomial.[14] For each Chebychev coefficient of all BSA components, we introduce one cubic spline object like for the quark and gluon

[14] The Chebychev polynomials can be calculated by the Chebychev recursive formula $T_j(z_p) = 2z_pT_{j-1}(z_p) - T_{j-2}(z_p)$ with the first polynomials $T_0(z_p) = 1$ and $T_1(z_p) = z_p$.

dressing functions. In vacuum and for finite chemical potential and vanishing temperature, these cubic splines are based on the logarithmic and equidistant distributed radial part of the external relative four-momentum. This, however, is only possible since we consider the rest frame. Going beyond rest frame is connected with some difficulties. Then, we either need a slow three dimensional (spline) interpolation routine or a complicated two dimensional Cauchy interpolator. Moreover, the calculation becomes more difficult due to the more complicated momentum representation shown in Eq. (C.24).

In case of fundamental particles, the tree level term in the DSE represents an inhomogeneity that stabilizes the iteration and plays a major role for its convergence. The same is true for the inhomogeneous BSE in Eq.(3.4). Due to the absence of such an inhomogeneity in the homogeneous BSE, the iteration does not converge and we need another abort criterion for the eigenvalue like equation in Eq. (3.20). Since the ground state of the considered bound state is identified by the largest eigenvalue [199], we can extract the corresponding eigenvector by the so-called power iteration method. In this method, we use the convergence of the eigenvalue as abort criterion. We apply the kernel $\tilde{K}(P)$ iteratively onto the eigenvector (represented by the BSA $\Gamma_{\mathrm{x}}^{n}(P)$) and start with an initial guess $\Gamma_{\mathrm{x}}^{0}(P)$. Consequently, the applied eigenvalue equation is rather given by

$$\tilde{K}(P)\Gamma_{\mathrm{x}}^{n}(P) = \lambda_n(P)\Gamma_{\mathrm{x}}^{n+1}(P) \tag{C.27}$$

with n indicating the iteration step. For increasing orders of application, the iterative eigenvalue trends towards the real eigenvalue

$$\lambda_n(P) = \frac{\Gamma_{\mathrm{x}}^{n+1}(P)}{\Gamma_{\mathrm{x}}^{n}(P)} \xrightarrow{n\to\infty} \lambda(P) \tag{C.28}$$

and the eigenvector $\Gamma_{\mathrm{x}}^{n}(P) \xrightarrow{n\to\infty} \Gamma_{\mathrm{x}}(P)$ to the correct BSA. After every step we normalize the BSA $\Gamma_{\mathrm{x}}^{n+1}(P)$ by the the leading BSA component evaluated at a certain momentum p. Since this momentum p is arbitrary and we choose it to be $p = 0$. For simplicity we use the leading BSA component instead of the full BSA for the definition of the eigenvalue and the normalization of the eigenvector.

D. Eigenständigkeitserklärung

Selbstständigkeitserklärung

Hiermit versichere ich, die vorgelegte Thesis selbstständig und ohne unerlaubte fremde Hilfe und nur mit den Hilfen angefertigt zu haben, die ich in der Thesis angegeben habe. Alle Textstellen, die wörtlich oder sinngemäß aus veröffentlichten Schriften entnommen sind, und alle Angaben die auf mündlichen Auskünften beruhen, sind als solche kenntlich gemacht. Bei den von mir durchgeführten und in der Thesis erwähnten Untersuchungen habe ich die Grundsätze guter wissenschaftlicher Praxis, wie sie in der ‚Satzung der Justus-Liebig-Universität zur Sicherung guter wissenschaftlicher Praxis' niedergelegt sind, eingehalten. Gemäß § 25 Abs. 6 der Allgemeinen Bestimmungen für modularisierte Studiengänge dulde ich eine Überprüfung der Thesis mittels Anti-Plagiatssoftware.

Datum	Unterschrift

E. Acknowledgment

This work has been supported by the Helmholtz Graduate School for Hadron and Ion Research (HGS-HIRe) for FAIR, the GSI Helmholtzzentrum für Schwerionenforschung, the Helmholtz International Center for FAIR within the LOEWE program of the State of Hesse, and the BMBF under contract No. 05P18RGFCA. I acknowledge computational resources provided by the HPC Core Facility and the HRZ of the Justus-Liebig-University Giessen. Furthermore, I would like to thank HGS-HIRe for giving me the opportunity to participate at the different seminars, the summer school and the research travel to the A&M university in Texas. For the latter one, I want to thank Ralf Rapp for including me into his working group for this time.

At the end, it remains me to express my gratitude to some supporters and friends. First of all, I would like to thank my parents Birger and Christine, my bother Olivier and my girlfriend Desiree for their continuous support and patience with me throughout my studies and PhD. I know, I can always count on you and I love you guys for this. Thank you for motivating me, encouraging me, helping me in every way you find and supporting me to pursue all my aspirations, already all my life long. Without you, this work would not have been possible.

Next I want to thank my fellow students and friends, especially Jonas Wilhelm, Jonas Schäfer, Konstantin Otto and Daniel Zink, for an eventful and fascinating time during our studies. Furthermore, my gratitude goes to my office mates and friends Paul Wallbott and Philipp Isserstedt for their support, their advice, the discussions and overall the funny time I had with you two. Additionally, I would like to thank them and the rest of the group for helpful discussions, their well appreciated help and the great time I had at the institute or with the friends I found there. Furthermore, I want to thank Richard Williams for his advises and his support at every time. Finally I would like to express my appreciation for Nico Santowsky and Julian Bernhardt for the careful reading of the manuscript. I conclude by thanking Christian Fischer to give me the opportunity to work in this supportive group.

Bibliography

[1] A. Bzdak et al., *Mapping the Phases of Quantum Chromodynamics with Beam Energy Scan*, Phys. Rept. **853**, 1–87 (2020), arXiv:1906.00936 [nucl-th].

[2] P. Salabura and J. Stroth, *Dilepton Radiation from Strongly Interacting Systems*, (2020), arXiv:2005.14589 [nucl-ex].

[3] B. Friman et al., eds., *The CBM physics book: Compressed baryonic matter in laboratory experiments*, Vol. 814 (2011).

[4] S. Borsanyi et al., *Is there still any T_c mystery in lattice QCD? Results with physical masses in the continuum limit III*, JHEP **09**, 073 (2010), arXiv:1005.3508 [hep-lat].

[5] A. Bazavov et al., *The chiral and deconfinement aspects of the QCD transition*, Phys. Rev. D **85**, 054503 (2012), arXiv:1111.1710 [hep-lat].

[6] T. Bhattacharya et al., *QCD Phase Transition with Chiral Quarks and Physical Quark Masses*, Phys. Rev. Lett. **113**, 082001 (2014), arXiv:1402.5175 [hep-lat].

[7] A. Bazavov et al., *Equation of state in (2+1)-flavor QCD*, Phys. Rev. D **90**, 094503 (2014), arXiv:1407.6387 [hep-lat].

[8] D. J. Gross and F. Wilczek, *Ultraviolet Behavior of Nonabelian Gauge Theories*, Phys. Rev. Lett. **30**, edited by J. C. Taylor, 1343–1346 (1973).

[9] H. D. Politzer, *Reliable Perturbative Results for Strong Interactions?*, Phys. Rev. Lett. **30**, edited by J. C. Taylor, 1346–1349 (1973).

[10] Y. Nambu and G. Jona-Lasinio, *Dynamical Model of Elementary Particles Based on an Analogy with Superconductivity. 1.* Phys. Rev. **122**, edited by T. Eguchi, 345–358 (1961).

[11] G. 't Hooft, *On the Phase Transition Towards Permanent Quark Confinement*, Nucl. Phys. B **138**, 1–25 (1978).

[12] M. Stephanov, *The phase diagram of QCD and the critical point*, Acta Phys. Polon. B **35**, edited by M. Sadzikowski, 2939–2962 (2004).

[13] M. A. Stephanov, *QCD phase diagram: An Overview*, PoS **LAT2006**, edited by T. Blum et al., 024 (2006), arXiv:hep-lat/0701002.

[14] B.-J. Schaefer and M. Wagner, *On the QCD phase structure from effective models*, Prog. Part. Nucl. Phys. **62**, edited by A. Faessler, 381 (2009), arXiv:0812.2855 [hep-ph].

[15] K. Fukushima and V. Skokov, *Polyakov loop modeling for hot QCD*, Prog. Part. Nucl. Phys. **96**, 154–199 (2017), arXiv:1705.00718 [hep-ph].

[16] M. Drews and W. Weise, *Functional renormalization group studies of nuclear and neutron matter*, Prog. Part. Nucl. Phys. **93**, 69–107 (2017), arXiv:1610.07568 [nucl-th].

[17] C. S. Fischer, *QCD at finite temperature and chemical potential from Dyson–Schwinger equations*, Prog. Part. Nucl. Phys. **105**, 1–60 (2019), arXiv:1810.12938 [hep-ph].

[18] W. Weise, *Nuclear chiral dynamics and phases of QCD*, Prog. Part. Nucl. Phys. **67**, edited by A. Faessler and V. Rodin, 299–311 (2012), arXiv:1201.0950 [nucl-th].

[19] P. de Forcrand, *Simulating QCD at finite density*, PoS **LAT2009**, edited by C. Liu and Y. Zhu, 010 (2009), arXiv:1005.0539 [hep-lat].

[20] O. Philipsen, "Lattice QCD at non-zero temperature and baryon density", in Les Houches Summer School: Session 93: Modern perspectives in lattice QCD: Quantum field theory and high performance computing (Sept. 2010), pp. 273–330, arXiv:1009.4089 [hep-lat].

[21] O. Philipsen, *The QCD equation of state from the lattice*, Prog. Part. Nucl. Phys. **70**, 55–107 (2013), arXiv:1207.5999 [hep-lat].

[22] V. Skokov, B. Stokic, B. Friman, and K. Redlich, *Meson fluctuations and thermodynamics of the Polyakov loop extended quark-meson model*, Phys. Rev. C **82**, 015206 (2010), arXiv:1004.2665 [hep-ph].

[23] T. K. Herbst, J. M. Pawlowski, and B.-J. Schaefer, *The phase structure of the Polyakov–quark–meson model beyond mean field*, Phys. Lett. B **696**, 58–67 (2011), arXiv:1008.0081 [hep-ph].

[24] T. K. Herbst, J. M. Pawlowski, and B.-J. Schaefer, *Phase structure and thermodynamics of QCD*, Phys. Rev. D **88**, 014007 (2013), arXiv:1302.1426 [hep-ph].

[25] R.-A. Tripolt, B.-J. Schaefer, L. von Smekal, and J. Wambach, *Low-temperature behavior of the quark-meson model*, Phys. Rev. D **97**, 034022 (2018), arXiv:1709.05991 [hep-ph].

[26] S. Resch, F. Rennecke, and B.-J. Schaefer, *Mass sensitivity of the three-flavor chiral phase transition*, Phys. Rev. D **99**, 076005 (2019), arXiv:1712.07961 [hep-ph].

[27] R. Alkofer and L. von Smekal, *The Infrared behavior of QCD Green's functions: Confinement dynamical symmetry breaking, and hadrons as relativistic bound states*, Phys. Rept. **353**, 281 (2001), arXiv:hep-ph/0007355.

[28] C. D. Roberts and S. M. Schmidt, *Dyson-Schwinger equations: Density, temperature and continuum strong QCD*, Prog. Part. Nucl. Phys. **45**, S1–S103 (2000), arXiv:nucl-th/0005064.

[29] J. M. Pawlowski, *Aspects of the functional renormalisation group*, Annals Phys. **322**, 2831–2915 (2007), arXiv:hep-th/0512261.

[30] B.-J. Schaefer and J. Wambach, *Renormalization group approach towards the QCD phase diagram*, Phys. Part. Nucl. **39**, 1025–1032 (2008), arXiv:hep-ph/0611191.

[31] P. Maris, C. D. Roberts, and P. C. Tandy, *Pion mass and decay constant*, Phys. Lett. B **420**, 267–273 (1998), arXiv:nucl-th/9707003.

[32] P. Maris and P. C. Tandy, *Bethe-Salpeter study of vector meson masses and decay constants*, Phys. Rev. C **60**, 055214 (1999), arXiv:nucl-th/9905056.

[33] C. S. Fischer, S. Kubrak, and R. Williams, *Mass spectra and Regge trajectories of light mesons in the Bethe-Salpeter approach*, Eur. Phys. J. A **50**, 126 (2014), arXiv:1406.4370 [hep-ph].

[34] R. Williams, C. S. Fischer, and W. Heupel, *Light mesons in QCD and unquenching effects from the 3PI effective action*, Phys. Rev. D **93**, 034026 (2016), arXiv:1512.00455 [hep-ph].

[35] C. S. Fischer, J. Luecker, and J. A. Mueller, *Chiral and deconfinement phase transitions of two-flavour QCD at finite temperature and chemical potential*, Phys. Lett. B **702**, 438–441 (2011), arXiv:1104.1564 [hep-ph].

[36] C. S. Fischer and J. Luecker, *Propagators and phase structure of Nf=2 and Nf=2+1 QCD*, Phys. Lett. B **718**, 1036–1043 (2013), arXiv:1206.5191 [hep-ph].

[37] C. S. Fischer, J. Luecker, and C. A. Welzbacher, *Phase structure of three and four flavor QCD*, Phys. Rev. D **90**, 034022 (2014), arXiv:1405.4762 [hep-ph].

[38] C. S. Fischer and J. A. Mueller, *On critical scaling at the QCD N_f = 2 chiral phase transition*, Phys. Rev. D **84**, 054013 (2011), arXiv:1106.2700 [hep-ph].

[39] Y. Jiang, L.-J. Luo, and H.-S. Zong, *A Model study of quark number susceptibility at finite temperature beyond rainbow-ladder approximation*, JHEP **02**, 066 (2011), arXiv:1102.1532 [hep-ph].

[40] F. Gao et al., *Phase diagram and thermal properties of strong-interaction matter*, Phys. Rev. D **93**, 094019 (2016), arXiv:1507.00875 [nucl-th].

[41] S.-x. Qin, L. Chang, Y.-x. Liu, and C. D. Roberts, *Quark spectral density and a strongly-coupled QGP*, Phys. Rev. D **84**, 014017 (2011), arXiv:1010.4231 [nucl-th].

[42] P. Isserstedt, M. Buballa, C. S. Fischer, and P. J. Gunkel, *Baryon number fluctuations in the QCD phase diagram from Dyson-Schwinger equations*, Phys. Rev. D **100**, 074011 (2019), arXiv:1906.11644 [hep-ph].

[43] P. Isserstedt, C. S. Fischer, and T. Steinert, *Thermodynamics from the quark condensate*, Phys. Rev. D **103**, 054012 (2021), arXiv:2012.04991 [hep-ph].

[44] G. Eichmann, C. S. Fischer, and C. A. Welzbacher, *Baryon effects on the location of QCD's critical end point*, Phys. Rev. D **93**, 034013 (2016), arXiv:1509.02082 [hep-ph].

[45] C. S. Fischer, L. Fister, J. Luecker, and J. M. Pawlowski, *Polyakov loop potential at finite density*, Phys. Lett. B **732**, 273–277 (2014), arXiv:1306.6022 [hep-ph].

[46] W.-j. Fu, J. M. Pawlowski, F. Rennecke, and B.-J. Schaefer, *Baryon number fluctuations at finite temperature and density*, Phys. Rev. D **94**, 116020 (2016), arXiv:1608.04302 [hep-ph].

[47] W.-j. Fu, J. M. Pawlowski, and F. Rennecke, *QCD phase structure at finite temperature and density*, Phys. Rev. D **101**, 054032 (2020), arXiv:1909.02991 [hep-ph].

[48] F. Gao and J. M. Pawlowski, *QCD phase structure from functional methods*, Phys. Rev. D **102**, 034027 (2020), arXiv:2002.07500 [hep-ph].

[49] F. Gao and J. M. Pawlowski, *Chiral phase structure and critical end point in QCD*, (2020), arXiv:2010.13705 [hep-ph].

[50] R. Contant, M. Q. Huber, C. S. Fischer, C. A. Welzbacher, and R. Williams, *On the quark-gluon vertex at non-vanishing temperature*, Acta Phys. Polon. Supp. **11**, edited by P. Bicudo, R. Kamiski, M. Krstic Marinkovic, J. Jovicevic, and C. Nuno, 483 (2018), arXiv:1805.05885 [hep-ph].

[51] J. Braun et al., *Chiral susceptibility in (2+1)-flavor QCD*, Phys. Rev. D **102**, 056010 (2020), arXiv:2003.13112 [hep-ph].

[52] B.-J. Schaefer and J. Wambach, *Susceptibilities near the QCD (tri)critical point*, Phys. Rev. D **75**, 085015 (2007), arXiv:hep-ph/0603256.

[53] B.-J. Schaefer, J. M. Pawlowski, and J. Wambach, *The Phase Structure of the Polyakov–Quark-Meson Model*, Phys. Rev. D **76**, 074023 (2007), arXiv:0704.3234 [hep-ph].

[54] F. Rennecke and B.-J. Schaefer, *Fluctuation-induced modifications of the phase structure in (2+1)-flavor QCD*, Phys. Rev. D **96**, 016009 (2017), arXiv:1610.08748 [hep-ph].

[55] P. J. Gunkel and C. S. Fischer, *Locating the critical endpoint of QCD: mesonic backcoupling effects*, (2021), arXiv:2106.08356 [hep-ph].

[56] C. S. Fischer, D. Nickel, and J. Wambach, *Hadronic unquenching effects in the quark propagator*, Phys. Rev. D **76**, 094009 (2007), arXiv:0705.4407 [hep-ph].

[57] C. S. Fischer, D. Nickel, and R. Williams, *On Gribov's supercriticality picture of quark confinement*, Eur. Phys. J. C **60**, 47–61 (2009), arXiv:0807.3486 [hep-ph].

[58] C. S. Fischer and R. Williams, *Beyond the rainbow: Effects from pion back-coupling*, Phys. Rev. D **78**, 074006 (2008), arXiv:0808.3372 [hep-ph].

[59] B. J. Schaefer and M. Wagner, *QCD critical region and higher moments for three flavor models*, Phys. Rev. D **85**, 034027 (2012), arXiv:1111.6871 [hep-ph].

[60] Y.-r. Chen, R. Wen, and W.-j. Fu, *Critical behaviors of the $O(4)$ and $Z(2)$ symmetries in the QCD phase diagram*, (2021), arXiv:2101.08484 [hep-ph].

[61] T. D. Cohen, R. Furnstahl, and D. K. Griegel, *Quark and gluon condensates in nuclear matter*, Phys. Rev. C **45**, 1881–1893 (1992).

[62] T. D. Cohen, *QCD functional integrals for systems with nonzero chemical potential*, edited by M. Shifman, A. Vainshtein, and J. Wheater, 101–120 (2004), arXiv:hep-ph/0405043.

[63] P. Maris, C. D. Roberts, and S. Schmidt, *Chemical potential dependence of pi and rho properties*, Phys. Rev. C **57**, 2821–2825 (1998), arXiv:nucl-th/9801059.

[64] D. Blaschke, G. Burau, Y. L. Kalinovsky, P. Maris, and P. C. Tandy, *Finite T meson correlations and quark deconfinement*, Int. J. Mod. Phys. A **16**, 2267–2291 (2001), arXiv:nucl-th/0002024.

[65] P. Maris, C. D. Roberts, S. M. Schmidt, and P. C. Tandy, *T - dependence of pseudoscalar and scalar correlations*, Phys. Rev. C **63**, 025202 (2001), arXiv:nucl-th/0001064.

[66] C. D. Roberts and S. M. Schmidt, "Dyson-Schwinger equations and the quark gluon plasma", in ECT* International Workshop on Understanding Deconfinement in QCD (Mar. 1999), arXiv:nucl-th/9903075.

[67] D. Blaschke, Y. L. Kalinovsky, A. E. Radzhabov, and M. K. Volkov, *Scalar sigma meson at a finite temperature in a nonlocal quark model*, Phys. Part. Nucl. Lett. **3**, 327–330 (2006).

[68] R. Rapp and J. Wambach, *Chiral symmetry restoration and dileptons in relativistic heavy ion collisions*, Adv. Nucl. Phys. **25**, 1 (2000), arXiv:hep-ph/9909229.

[69] S. Leupold, V. Metag, and U. Mosel, *Hadrons in strongly interacting matter*, Int. J. Mod. Phys. E **19**, 147–224 (2010), arXiv:0907.2388 [nucl-th].

[70] S. Weinberg, *The quantum theory of fields*, Vol. I (Cambridge university press, 2010).

[71] L. D. Faddeev and V. N. Popov, *Feynman Diagrams for the Yang-Mills Field*, Phys. Lett. B **25**, edited by J.-P. Hsu and D. Fine, 29–30 (1967).

[72] W. J. Marciano and H. Pagels, *Quantum Chromodynamics: A Review*, Phys. Rept. **36**, 137 (1978).

[73] G. Eichmann, "Lecture notes in introduction to hadron physics", URL: http://cftp.ist.utl.pt/~gernot.eichmann/ Last visited on 2021/02/05, 2014.

[74] R. Alkofer, C. S. Fischer, F. J. Llanes-Estrada, and K. Schwenzer, *The Quark-gluon vertex in Landau gauge QCD: Its role in dynamical chiral symmetry breaking and quark confinement*, Annals Phys. **324**, 106–172 (2009), arXiv:0804.3042 [hep-ph].

[75] C. S. Fischer, *Deconfinement phase transition and the quark condensate*, Phys. Rev. Lett. **103**, 052003 (2009), arXiv:0904.2700 [hep-ph].

[76] C. S. Fischer, A. Maas, and J. A. Muller, *Chiral and deconfinement transition from correlation functions: SU(2) vs. SU(3)*, Eur. Phys. J. C **68**, 165–181 (2010), arXiv:1003.1960 [hep-ph].

[77] J. Taylor, *Ward Identities and Charge Renormalization of the Yang-Mills Field*, Nucl. Phys. B **33**, 436–444 (1971).

[78] N. P. Landsman and C. G. van Weert, *Real and Imaginary Time Field Theory at Finite Temperature and Density*, Phys. Rept. **145**, 141 (1987).

[79] R. Contant and M. Q. Huber, *Phase structure and propagators at nonvanishing temperature for QCD and QCD-like theories*, Phys. Rev. D **96**, 074002 (2017), arXiv:1706.00943 [hep-ph].

[80] C. Welzbacher, "Quarks and gluons in the phase diagram of quantum chromodynamics", PhD thesis (Giessen U., Aug. 2016).

[81] C. S. Fischer, J. Luecker, and C. A. Welzbacher, *Locating the critical end point of QCD*, Nucl. Phys. A **931**, edited by P. Braun-Munzinger, B. Friman, and J. Stachel, 774–779 (2014), arXiv:1410.0124 [hep-ph].

[82] W. Heupel, T. Goecke, and C. S. Fischer, *Beyond Rainbow-Ladder in bound state equations*, Eur. Phys. J. A **50**, 85 (2014), arXiv:1402.5042 [hep-ph].

[83] S. Borsanyi et al., *Freeze-out parameters: lattice meets experiment*, Phys. Rev. Lett. **111**, 062005 (2013), arXiv:1305.5161 [hep-lat].

[84] J. Braun, L. Fister, J. M. Pawlowski, and F. Rennecke, *From Quarks and Gluons to Hadrons: Chiral Symmetry Breaking in Dynamical QCD*, Phys. Rev. D **94**, 034016 (2016), arXiv:1412.1045 [hep-ph].

[85] A. K. Cyrol, M. Mitter, J. M. Pawlowski, and N. Strodthoff, *Nonperturbative quark, gluon, and meson correlators of unquenched QCD*, Phys. Rev. D **97**, 054006 (2018), arXiv:1706.06326 [hep-ph].

[86] A. C. Aguilar et al., *Gluon propagator and three-gluon vertex with dynamical quarks*, Eur. Phys. J. C **80**, 154 (2020), arXiv:1912.12086 [hep-ph].

[87] M. Q. Huber, *Correlation functions of Landau gauge Yang-Mills theory*, Phys. Rev. D **101**, 114009 (2020), arXiv:2003.13703 [hep-ph].

[88] F. Gao, J. Papavassiliou, and J. M. Pawlowski, *Fully coupled functional equations for the quark sector of QCD*, Phys. Rev. D **103**, 094013 (2021), arXiv:2102.13053 [hep-ph].

[89] J. Lücker, "Chiral and deconfinement phase transitions in $N_f = 2$ and $N_f = 2 + 1$ quantum chromodynamics", PhD thesis (Giessen U., 2013).

[90] G. 't Hooft, *A Planar Diagram Theory for Strong Interactions*, Nucl. Phys. B **72**, edited by J. C. Taylor, 461 (1974).

[91] E. Witten, *Baryons in the 1/n Expansion*, Nucl. Phys. B **160**, 57–115 (1979).

[92] J. Skullerud and A. Kizilersu, *Quark gluon vertex from lattice QCD*, JHEP **09**, 013 (2002), arXiv:hep-ph/0205318.

[93] J. I. Skullerud, P. O. Bowman, A. Kizilersu, D. B. Leinweber, and A. G. Williams, *Nonperturbative structure of the quark gluon vertex*, JHEP **04**, 047 (2003), arXiv:hep-ph/0303176.

[94] R. Alkofer, C. S. Fischer, and F. J. Llanes-Estrada, *Dynamically induced scalar quark confinement*, Mod. Phys. Lett. A **23**, 1105–1113 (2008), arXiv:hep-ph/0607293.

[95] D. Müller, M. Buballa, and J. Wambach, *Dyson-Schwinger approach to color superconductivity at finite temperature and density*, Eur. Phys. J. A **49**, 96 (2013), arXiv:1303.2693 [hep-ph].

[96] D. Müller, M. Buballa, and J. Wambach, *Dyson-Schwinger Approach to Color-Superconductivity: Effects of Selfconsistent Gluon Dressing*, (2016), arXiv:1603.02865 [hep-ph].

[97] A. Maas, J. M. Pawlowski, L. von Smekal, and D. Spielmann, *The Gluon propagator close to criticality*, Phys. Rev. D **85**, 034037 (2012), arXiv:1110.6340 [hep-lat].

[98] C. S. Fischer and R. Alkofer, *Nonperturbative propagators, running coupling and dynamical quark mass of Landau gauge QCD*, Phys. Rev. D **67**, 094020 (2003), arXiv:hep-ph/0301094.

[99] J. S. Ball and T.-W. Chiu, *Analytic Properties of the Vertex Function in Gauge Theories. 1.* Phys. Rev. D **22**, 2542 (1980).

[100] R. Aouane, F. Burger, E.-M. Ilgenfritz, M. Müller-Preussker, and A. Sternbeck, *Landau gauge gluon and ghost propagators from lattice QCD with N_f=2 twisted mass fermions at finite temperature*, Phys. Rev. D **87**, 114502 (2013), arXiv:1212.1102 [hep-lat].

[101] Y. Jiang, Y.-m. Shi, H.-t. Feng, W.-m. Sun, and H.-s. Zong, *Quark-meson vertices and pion properties at finite chemical potential*, Phys. Rev. C **78**, 025214 (2008).

[102] F.-y. Hou, L. Chang, W.-m. Sun, H.-s. Zong, and Y.-x. Liu, *New method for numerically solving the chemical potential dependence of the dressed quark propagator*, Phys. Rev. C **72**, 034901 (2005), arXiv:hep-ph/0504281.

[103] R. Bellwied et al., *The QCD phase diagram from analytic continuation*, Phys. Lett. B **751**, 559–564 (2015), arXiv:1507.07510 [hep-lat].

[104] A. Bazavov et al., *Chiral crossover in QCD at zero and non-zero chemical potentials*, Phys. Lett. B **795**, 15–21 (2019), arXiv:1812.08235 [hep-lat].

[105] P. J. Gunkel, C. S. Fischer, and P. Isserstedt, *Quarks and light (pseudo-)scalar mesons at finite chemical potential*, Eur. Phys. J. A **55**, 169 (2019), arXiv:1907.08110 [hep-ph].

[106] P. J. Gunkel, C. S. Fischer, and P. Isserstedt, *Mesons at finite chemical potential and the Silver-Blaze property of QCD*, J. Phys. Conf. Ser. **1667**, edited by M. Destefanis, T. Galatyuk, A. Bauswein, C. Ratti, and L. Tolos, 012011 (2020), arXiv:1911.04399 [hep-ph].

[107] U. Krey and W. Gebhardt, *Phasenübergänge und kritische Phänomene* (Vieweg, 1980) Chap. 2.1.

[108] R. Williams, C. Fischer, and M. Pennington, *Anti-q q condensate for light quarks beyond the chiral limit*, Phys. Lett. B **645**, 167–172 (2007), arXiv:hep-ph/0612061.

[109] L. Chang, Y.-X. Liu, M. S. Bhagwat, C. D. Roberts, and S. V. Wright, *Dynamical chiral symmetry breaking and a critical mass*, Phys. Rev. C **75**, 015201 (2007), arXiv:nucl-th/0605058.

[110] C. Bonati, M. D'Elia, F. Negro, F. Sanfilippo, and K. Zambello, *Curvature of the pseudocritical line in QCD: Taylor expansion matches analytic continuation*, Phys. Rev. D **98**, 054510 (2018), arXiv:1805.02960 [hep-lat].

[111] S. Borsanyi et al., *QCD Crossover at Finite Chemical Potential from Lattice Simulations*, Phys. Rev. Lett. **125**, 052001 (2020), arXiv:2002.02821 [hep-lat].

[112] L. Fister and J. M. Pawlowski, *Confinement from Correlation Functions*, Phys. Rev. D **88**, 045010 (2013), arXiv:1301.4163 [hep-ph].

[113] L. F. Abbott, *The Background Field Method Beyond One Loop*, Nucl. Phys. B **185**, 189–203 (1981).

[114] L. F. Abbott, *Introduction to the Background Field Method*, Acta Phys. Polon. B **13**, 33 (1982).

[115] R. Contant and M. Q. Huber, *Dense two-color QCD from Dyson-Schwinger equations*, Phys. Rev. D **101**, 014016 (2020), arXiv:1909.12796 [hep-ph].

[116] M. Gell-Mann, *The interpretation of the new particles as displaced charge multiplets*, Nuovo Cim. **4**, 848–866 (1956).

[117] G. Zweig, *An SU(3) model for strong interaction symmetry and its breaking. Version 1*, (1964).

[118] J. M. Cornwall, R. Jackiw, and E. Tomboulis, *Effective Action for Composite Operators*, Phys. Rev. D **10**, 2428–2445 (1974).

[119] G. Eichmann, "Hadron properties from QCD bound-state equations", PhD thesis (Graz U., 2009), arXiv:0909.0703 [hep-ph].

[120] H. J. Munczek, *Dynamical chiral symmetry breaking, Goldstone's theorem and the consistency of the Schwinger-Dyson and Bethe-Salpeter Equations*, Phys. Rev. D **52**, 4736–4740 (1995), arXiv:hep-th/9411239.

[121] A. Bender, C. D. Roberts, and L. Von Smekal, *Goldstone theorem and diquark confinement beyond rainbow ladder approximation*, Phys. Lett. B **380**, 7–12 (1996), arXiv:nucl-th/9602012.

[122] P. Zyla et al., *Review of Particle Physics*, PTEP **2020**, 083C01 (2020).

[123] G. Eichmann, H. Sanchis-Alepuz, R. Williams, R. Alkofer, and C. S. Fischer, *Baryons as relativistic three-quark bound states*, Prog. Part. Nucl. Phys. **91**, 1–100 (2016), arXiv:1606.09602 [hep-ph].

[124] C. Llewellyn-Smith, *A relativistic formulation for the quark model for mesons*, Annals Phys. **53**, 521–558 (1969).

[125] C. Fischer, P. Watson, and W. Cassing, *Probing unquenching effects in the gluon polarisation in light mesons*, Phys. Rev. D **72**, 094025 (2005), arXiv:hep-ph/0509213.

[126] R. Williams, *Bethe-Salpeter studies of mesons beyond rainbow-ladder*, EPJ Web Conf. **3**, edited by E. Epelbaum, H. Hammer, and U.-G. Meissner, 03005 (2010), arXiv:0912.3494 [hep-ph].

[127] C. Llewellyn Smith, "A Relativistic Formulation of the Quark Model for Mesons", 1969.

[128] P. Maris and P. C. Tandy, "Mesons as bound states of confined quarks: Zero and finite temperature", in Research Program at the Erwin Schodinger Institute on Confinement (Sept. 2001), arXiv:nucl-th/0109035.

[129] N. Nakanishi, *Normalization Condition and Normal and Abnormal Solutions of the Bethe-Salpeter Equation*, Phys. Rev. **138**, B1182–B1192 (1965).

[130] J. C. R. Bloch, Y. L. Kalinovsky, C. D. Roberts, and S. M. Schmidt, *Describing a(1) and b(1) decays*, Phys. Rev. D **60**, 111502 (1999), arXiv:nucl-th/9906038.

[131] R. L. Jaffe, *Multi-Quark Hadrons. 1. The Phenomenology of (2 Quark 2 anti-Quark) Mesons*, Phys. Rev. D **15**, 267 (1977).

[132] G. Eichmann, C. S. Fischer, and W. Heupel, *The light scalar mesons as tetraquarks*, Phys. Lett. B **753**, 282–287 (2016), arXiv:1508.07178 [hep-ph].

[133] N. Santowsky, G. Eichmann, C. S. Fischer, P. C. Wallbott, and R. Williams, *σ-meson: Four-quark versus two-quark components and decay width in a Bethe-Salpeter approach*, Phys. Rev. D **102**, 056014 (2020), arXiv:2007.06495 [hep-ph].

[134] F. Giacosa, *Mixing of scalar tetraquark and quarkonia states in a chiral approach*, Phys. Rev. D **75**, 054007 (2007), arXiv:hep-ph/0611388.

[135] H.-X. Chen, A. Hosaka, and S.-L. Zhu, *QCD sum rule study of the masses of light tetraquark scalar mesons*, Phys. Lett. B **650**, 369–372 (2007), arXiv:hep-ph/0609163.

[136] P. C. Tandy, *Hadron physics from the global color model of QCD*, Prog. Part. Nucl. Phys. **39**, 117–199 (1997), arXiv:nucl-th/9705018.

[137] R. D. Pisarski and M. Tytgat, *Propagation of cool pions*, Phys. Rev. D **54**, R2989–R2993 (1996), arXiv:hep-ph/9604404.

[138] D. Son and M. A. Stephanov, *Pion propagation near the QCD chiral phase transition*, Phys. Rev. Lett. **88**, 202302 (2002), arXiv:hep-ph/0111100.

[139] D. Son and M. A. Stephanov, *Real time pion propagation in finite temperature QCD*, Phys. Rev. D **66**, 076011 (2002), arXiv:hep-ph/0204226.

[140] M. Fromm, J. Langelage, S. Lottini, M. Neuman, and O. Philipsen, *Onset Transition to Cold Nuclear Matter from Lattice QCD with Heavy Quarks*, Phys. Rev. Lett. **110**, 122001 (2013), arXiv:1207.3005 [hep-lat].

[141] H.-s. Zong, L. Chang, F.-y. Hou, W.-m. Sun, and Y.-x. Liu, *New approach for calculating the dressed quark propagator at finite chemical potential*, Phys. Rev. C **71**, 015205 (2005).

[142] D. R. Müller, "QCD at finite density with Dyson-Schwinger equations", PhD thesis (Darmstadt, Tech. Hochsch., 2013).

[143] P. J. Gunkel and C. S. Fischer, *Masses and decay constants of (axial-)vector mesons at finite chemical potential*, Eur. Phys. J. A **57**, 147 (2021), arXiv:2012.01957 [hep-ph].

[144] H. Chen et al., *Chemical potential and the gap equation*, Phys. Rev. D **78**, 116015 (2008), arXiv:0807.2755 [nucl-th].

[145] Y. Jiang, Y.-m. Shi, H. Li, W.-m. Sun, and H.-s. Zong, *The Calculation of f(pi) and m(pi) at Finite Chemical Potential*, Phys. Rev. D **78**, 116005 (2008), arXiv:0810.0750 [nucl-th].

[146] D. Blaschke, C. D. Roberts, and S. M. Schmidt, *Thermodynamic properties of a simple, confining model*, Phys. Lett. B **425**, 232–238 (1998), arXiv:nucl-th/9706070.

[147] S.-S. Xu, Y. Yan, Z.-F. Cui, and H.-S. Zong, *2+1 flavors QCD equation of state at zero temperature within Dyson–Schwinger equations*, Int. J. Mod. Phys. A **30**, 1550217 (2015), arXiv:1506.06846 [hep-ph].

[148] K. Otto, M. Oertel, and B.-J. Schaefer, *Hybrid and quark star matter based on a nonperturbative equation of state*, Phys. Rev. D **101**, 103021 (2020), arXiv:1910.11929 [hep-ph].

[149] L. Chang et al., *Chemical potential dependence of chiral quark condensate in Dyson-Schwinger equation approach*, Phys. Lett. B **644**, 315–321 (2007), arXiv:hep-ph/0508094.

[150] W. Detmold, "Nonperturbative approaches to quantum chromodynamics", PhD thesis (University of Adelaide, Australia, 2002).

[151] T. Hilger, *Poincaré covariant pseudoscalar and scalar meson spectroscopy in Wigner-Weyl phase*, Phys. Rev. D **93**, 054020 (2016), arXiv:1510.08288 [hep-ph].

[152] R. Williams, *Vector mesons as dynamical resonances in the Bethe–Salpeter framework*, Phys. Lett. B **798**, 134943 (2019), arXiv:1804.11161 [hep-ph].

[153] A. Bender, G. I. Poulis, C. D. Roberts, S. M. Schmidt, and A. W. Thomas, *Deconfinement at finite chemical potential*, Phys. Lett. B **431**, 263–269 (1998), arXiv:nucl-th/9710069.

[154] Y.-X. Liu, J.-Y. Chao, L. Chang, and W. Yuan, *Density dependence of the mass and decay constant of pion in nuclear matter in the Dyson-Schwinger equation approach of QCD*, Chin. Phys. Lett. **22**, 46–49 (2005).

[155] P. Costa and R. C. Pereira, *Phase Diagram, Scalar-Pseudoscalar Meson Behavior and Restoration of Symmetries in (2 + 1) Polyakov-Nambu-Jona-Lasinio Model*, Symmetry **11**, 507–538 (2019), arXiv:1904.05805 [hep-ph].

[156] D. Ebert, K. G. Klimenko, and V. L. Yudichev, *Pion, sigma-meson and diquarks in the 2SC phase of dense cold quark matter*, Phys. Rev. C **72**, 015201 (2005), arXiv:hep-ph/0412129.

[157] R.-A. Tripolt, C. Jung, L. von Smekal, and J. Wambach, *Vector and Axial-Vector Mesons in Nuclear Matter*, (2021), arXiv:2105.00861 [hep-ph].

[158] C. Jung, "Spectral Functions of Vector Mesons from the Functional Renormalization Group", PhD thesis (Giessen U., 2019).

[159] C. Jung, F. Rennecke, R.-A. Tripolt, L. von Smekal, and J. Wambach, *In-Medium Spectral Functions of Vector- and Axial-Vector Mesons from the Functional Renormalization Group*, Phys. Rev. D **95**, 036020 (2017), arXiv:1610.08754 [hep-ph].

[160] C. S. Fischer, "Power week: functional methods, part 2: dyson-schwinger equations", 2014.

[161] J. Sugano, H. Kouno, M. Yahiro, and J. Takahashi, *Pion and ρ-meson screening masses at finite chemical potential in two-flavor lattice QCD with Wilson fermion*, (2017), arXiv:1709.02198 [hep-lat].

[162] V. N. Gribov, *Orsay lectures on confinement (III)*, edited by J. Nyiri (1992), arXiv:hep-ph/9905285.

[163] V. N. Gribov, *The Theory of quark confinement*, Eur. Phys. J. C **10**, edited by J. Nyiri, 91–105 (1999), arXiv:hep-ph/9902279.

[164] V. Dmitrasinovic, H. J. Schulze, R. Tegen, and R. H. Lemmer, *Chirally symmetric O (1/N(c corrections to the Nambu-Jona-Lasinio model*, Annals Phys. **238**, 332–369 (1995).

[165] M. Oertel, M. Buballa, and J. Wambach, *Meson loop effects in the NJL model at zero and nonzero temperature*, Phys. Atom. Nucl. **64**, 698–726 (2001), arXiv:hep-ph/0008131.

[166] E. N. Nikolov, W. Broniowski, C. V. Christov, G. Ripka, and K. Goeke, *Meson loops in the Nambu-Jona-Lasinio model*, Nucl. Phys. A **608**, 411–436 (1996), arXiv:hep-ph/9602274.

[167] C. S. Fischer and R. Williams, *Probing the gluon self-interaction in light mesons*, Phys. Rev. Lett. **103**, 122001 (2009), arXiv:0905.2291 [hep-ph].

[168] P. Maris and C. D. Roberts, *Pi- and K meson Bethe-Salpeter amplitudes*, Phys. Rev. C **56**, 3369–3383 (1997), arXiv:nucl-th/9708029.

[169] M. D. J. Nickel, "Color-superconductivity from a Dyson-Schwinger perspective", PhD thesis (Darmstadt, Tech. U., May 2007).

[170] J. A. Mueller and C. S. Fischer, *Studying pion effects on the chiral phase transition*, Prog. Part. Nucl. Phys. **62**, edited by A. Faessler, 549 (2009), arXiv:0811.2923 [hep-ph].

[171] H. Sanchis-Alepuz, C. S. Fischer, and S. Kubrak, *Pion cloud effects on baryon masses*, Phys. Lett. B **733**, 151–157 (2014), arXiv:1401.3183 [hep-ph].

[172] C. D. Roberts and A. G. Williams, *Dyson-Schwinger equations and their application to hadronic physics*, Prog. Part. Nucl. Phys. **33**, 477–575 (1994), arXiv:hep-ph/9403224.

[173] A. Ali Khan et al., *Phase structure and critical temperature of two flavor QCD with renormalization group improved gauge action and clover improved Wilson quark action*, Phys. Rev. D **63**, 034502 (2000), arXiv:hep-lat/0008011.

[174] S. Ejiri et al., *On the magnetic equation of state in (2+1)-flavor QCD*, Phys. Rev. D **80**, 094505 (2009), arXiv:0909.5122 [hep-lat].

[175] F. Karsch, *O(N) universality and the chiral phase transition in QCD*, Prog. Theor. Phys. Suppl. **186**, edited by A. Ohnishi et al., 479–484 (2010), arXiv:1007.2393 [hep-lat].

[176] O. Kaczmarek et al., *Phase boundary for the chiral transition in (2+1) -flavor QCD at small values of the chemical potential*, Phys. Rev. D **83**, 014504 (2011), arXiv:1011.3130 [hep-lat].

[177] J. Berges, D. U. Jungnickel, and C. Wetterich, *Two flavor chiral phase transition from nonperturbative flow equations*, Phys. Rev. D **59**, 034010 (1999), arXiv:hep-ph/9705474.

[178] O. Bohr, B. J. Schaefer, and J. Wambach, *Renormalization group flow equations and the phase transition in O(N) models*, Int. J. Mod. Phys. A **16**, 3823–3852 (2001), arXiv:hep-ph/0007098.

[179] N. Strodthoff, B.-J. Schaefer, and L. von Smekal, *Quark-meson-diquark model for two-color QCD*, Phys. Rev. D **85**, 074007 (2012), arXiv:1112.5401 [hep-ph].

[180] N. Strodthoff and L. von Smekal, *Polyakov-Quark-Meson-Diquark Model for two-color QCD*, Phys. Lett. B **731**, 350–357 (2014), arXiv:1306.2897 [hep-ph].

[181] G. Eichmann, R. Alkofer, A. Krassnigg, and D. Nicmorus, *Nucleon mass from a covariant three-quark Faddeev equation*, Phys. Rev. Lett. **104**, 201601 (2010), arXiv:0912.2246 [hep-ph].

[182] H. Sanchis-Alepuz, G. Eichmann, S. Villalba-Chavez, and R. Alkofer, *Delta and Omega masses in a three-quark covariant Faddeev approach*, Phys. Rev. D **84**, 096003 (2011), arXiv:1109.0199 [hep-ph].

[183] H. Sanchis-Alepuz and C. S. Fischer, *Octet and Decuplet masses: a covariant three-body Faddeev calculation*, Phys. Rev. D **90**, 096001 (2014), arXiv:1408.5577 [hep-ph].

[184] H. Sanchis-Alepuz and R. Williams, *Probing the quark–gluon interaction with hadrons*, Phys. Lett. B **749**, 592–596 (2015), arXiv:1504.07776 [hep-ph].

[185] G. Eichmann, *Nucleon electromagnetic form factors from the covariant Faddeev equation*, Phys. Rev. D **84**, 014014 (2011), arXiv:1104.4505 [hep-ph].

[186] M. Oettel, G. Hellstern, R. Alkofer, and H. Reinhardt, *Octet and decuplet baryons in a covariant and confining diquark - quark model*, Phys. Rev. C **58**, 2459–2477 (1998), arXiv:nucl-th/9805054.

[187] M. Oettel, R. Alkofer, and L. von Smekal, *Nucleon properties in the covariant quark diquark model*, Eur. Phys. J. A **8**, 553–566 (2000), arXiv:nucl-th/0006082.

[188] I. C. Cloet, G. Eichmann, B. El-Bennich, T. Klahn, and C. D. Roberts, *Survey of nucleon electromagnetic form factors*, Few Body Syst. **46**, 1–36 (2009), arXiv:0812.0416 [nucl-th].

[189] J. Segovia, I. C. Cloet, C. D. Roberts, and S. M. Schmidt, *Nucleon and Δ elastic and transition form factors*, Few Body Syst. **55**, 1185–1222 (2014), arXiv:1408.2919 [nucl-th].

[190] G. Eichmann, A. Krassnigg, M. Schwinzerl, and R. Alkofer, *A Covariant view on the nucleons' quark core*, Annals Phys. **323**, 2505–2553 (2008), arXiv:0712.2666 [hep-ph].

[191] G. Eichmann, I. C. Cloet, R. Alkofer, A. Krassnigg, and C. D. Roberts, *Toward unifying the description of meson and baryon properties*, Phys. Rev. C **79**, 012202 (2009), arXiv:0810.1222 [nucl-th].

[192] D. Nicmorus, G. Eichmann, and R. Alkofer, *Delta and Omega electromagnetic form factors in a Dyson-Schwinger/Bethe-Salpeter approach*, Phys. Rev. D **82**, 114017 (2010), arXiv:1008.3184 [hep-ph].

[193] G. Eichmann and D. Nicmorus, *Nucleon to Delta electromagnetic transition in the Dyson-Schwinger approach*, Phys. Rev. D **85**, 093004 (2012), arXiv:1112.2232 [hep-ph].

[194] I. Pushkina et al., *Properties of hadron screening masses at finite baryonic density*, Phys. Lett. B **609**, 265–270 (2005), arXiv:hep-lat/0410017.

[195] K.-l. Wang, Y.-x. Liu, L. Chang, C. D. Roberts, and S. M. Schmidt, *Baryon and meson screening masses*, Phys. Rev. D **87**, 074038 (2013), arXiv:1301.6762 [nucl-th].

[196] D. Blaschke, A. S. Dubinin, and D. Zablocki, *NJL model approach to diquarks and baryons in quark matter*, PoS **BaldinISHEPPXXII**, 083 (2015), arXiv:1502.03084 [nucl-th].

[197] H. Zhang, R. Dong, and S. Shu, *The baryon mass calculation in the chiral soliton model at finite temperature and density*, Int. J. Mod. Phys. E **24**, 1550025 (2015), arXiv:1504.02248 [hep-ph].

[198] M. L. Bellac, *Thermal field theory*, Vol. I (Cambridge university press, 2010).

[199] H. Sanchis-Alepuz and R. Williams, *Recent developments in bound-state calculations using the Dyson–Schwinger and Bethe–Salpeter equations*, Comput. Phys. Commun. **232**, 1–21 (2018), arXiv:1710.04903 [hep-ph].

[200] F. Karsch and E. Laermann, *Numerical simulations in particle physics*, Rept. Prog. Phys. **56**, 1347–1396 (1993), arXiv:hep-lat/9304010.

[201] K. D. Born et al., *Hadronic correlation functions in the QCD plasma phase*, Phys. Rev. Lett. **67**, 302–305 (1991).

[202] V. A. Miransky, *ON DYNAMICAL CHIRAL SYMMETRY BREAKING*, Phys. Lett. B **165**, 401–404 (1985).

[203] N. Nakanishi, *A General survey of the theory of the Bethe-Salpeter equation*, Prog. Theor. Phys. Suppl. **43**, 1–81 (1969).

[204] J. Gasser and H. Leutwyler, *Quark Masses*, Phys. Rept. **87**, 77–169 (1982).

[205] G. Preparata and W. I. Weisberger, *Ultraviolet divergences in radiative corrections to weak decays*, Phys. Rev. **175**, 1965–1974 (1968).